

Copyright

by

Jesse Vincent Jokerst

2009

The Dissertation Committee for Jesse Vincent Jokerst Certifies that this is the approved version of the following dissertation:

**Next Generation Transduction Pathways for
Nano-Bio-Chip Array Platforms**

Committee:

John T. McDevitt, Supervisor

Jason B. Shear

James A. Holcombe

C. Grant Willson

Dean P. Neikirk

**Next Generation Transduction Pathways for
Nano-Bio-Chip Array Platforms**

by

Jesse Vincent Jokerst, B.S.

Dissertation

Presented to the Faculty of the Graduate School of
The University of Texas at Austin
in Partial Fulfillment
of the Requirements
for the Degree of

Doctor of Philosophy

The University of Texas at Austin

May, 2009

Dedication

Written with gratitude to my God.

Acknowledgements

It is with no small amount of deep personal satisfaction that I observe this milestone in my fledgling career. Transitioning from venipuncture and collecting pathology samples, to learning conventional biomedical analysis techniques, to devising state-of-the-art clinical methods leaves me forever indebted to those who have so graciously blessed me with their time, talent, and treasure. My interest in using chemistry to improve human health arose through the dual inspiration of a passionate educator and an eccentric pathologist. I owe a permanent debt of gratitude to my high school chemistry teacher, Ms. Nancy Fisher, and my first real boss, Dr. Gordon Johnson, for planting the seeds of clinical analysis in my young mind.

The faculty of Truman State University and their dedication to the art of teaching also deserve high praise. Professors David McCurdy, Anne Moody, Randy Hagerty, and Cole Woodcox showed me the art of instruction, while Dr. Ken Fountain was the first to share with me his joy in performing chemical laboratory research. Upon landing in Texas, the hospitable environment created by Professors Shear, Brodbelt, Holcombe, and Willson helped me settle in before joining Professor John T. McDevitt's research group. I am also deeply thankful for the the initial contributions of Dr. Jason Shear, Dr. Eric Anslyn, and Dr. Dean Neikirk to the "electronic taste chip" which established the fundamental grounds for this work.

The McDevitt group was one of the best things to happen to me in Austin. The enthusiasm and persistence with which John pursues his discipline as well his composure

in discouraging times continues to motivate me. He allowed me to grow at my own pace, with both genuine personal and professional kindness, while graciously opening his healthy coffers. Led by this example, his research team offered a progressive and welcoming laboratory environment. In addition to my formal advisor, I consistently modeled Dr. Pierre Floriano as tangible example of the type of scientist I wished to become, while Dr. Nick Christodoulides was a dependable source of wise counsel and kind support. I'm equally thankful for fellow graduate students, Michael Griffin, Jorge Wong, Shannon Weigum, and Mehnaaz Ali for their aid in giving flight to my clumsy albatross. With the arrival of Alexis Lennart, Amanda Pollard, and Archana Raamanathan, I knew I could continue to enjoy a relationship of friendship as well as an affable collegial rapport. Additional UT members such as Glenn Simmons, Dr. Dwight Romanicviz, Shelley Acosta, and Mitra Mohanty in John's lab, Penny Kile as Graduate Coordinator, and my dear Administratrix, Cindy Thompson, helped to solidify the supportive milieu that launched my career. Although I can no longer extend my time at Texas, I will treasure taking a bit of each one of them with me on departure.

Of course, no retro-sequential litany of gratitude would be complete without mentioning my parents, Tom and Mary Ellen, for raising me in an environment that valued education in tandem with a firm foundation in fundamental integrity. Their love and unselfish interest in my well-being has never wavered. My siblings too, Adam, Hannah, and Rita and their jovial, dependable support, maintained my pursuits in academe. Finally, friends both new—Ron Bowdoin, Christopher Solis, Jon Paul Patrik—and old—Brian Hayes, Stefan Guerra, Apolonio Aguilar, Jake Amato, Ali Fakhreddine—have marched with me on this ever evolving path. Their contributions to intervals hilarious and moments sublime, will never be forgotten.

Next Generation Transduction Pathways for Nano-Bio-Chip Array Platforms

Publication No. _____

Jesse Vincent Jokerst, Ph.D.

The University of Texas at Austin, 2009

Supervisor: John. T. McDevitt

In the following work, nanoparticle quantum dot (QD) fluorophores have been exploited to measure biologically relevant analytes via a miniaturized sensor ensemble to provide key diagnostic and prognostic information in a rapid, yet sensitive manner—data essential for effective treatment of many diseases including HIV/AIDS and cancer. At the heart of this “nano-bio-chip” (NBC) sensor is a modular chemical/cellular processing unit consisting of either a polycarbonate membrane filter for cell-based assays, or an agarose bead array for detection of biomarkers in serum or saliva. Two applications of the NBC sensor system are described herein, both exhibiting excellent correlation to reference methods (R^2 above 0.94), with analysis times under 30 minutes and sample volumes below 50 μL .

First, the NBC sensor was employed for the sequestration and enumeration of T lymphocytes, cells specifically targeted by HIV, from whole blood samples. Several different conjugation methods linking QDs to recognition biomolecules were extensively characterized by biological and optical methods, with a thiol-linked secondary antibody labeling scheme yielding intense, specific signal. Using this technique, the photostability

of QDs was exploited, as was the ability to simultaneously visualize different color QDs via a single light pathway, effectively reducing optical requirements by half. Further, T-cell counts were observed well below the 200/ μ L discriminator between HIV and AIDS and across the common testing region, demonstrating the first reported example of cell counting via QDs in an enclosed, disposable device.

Next, multiplexed bead-based detection of cancer protein biomarkers CEA, Her-2/*Neu*, and CA125 in serum and saliva was examined using a sandwich immunoassay with detecting antibodies covalently bound to QDs. This nano-based signal was amplified 30 times versus molecular fluorophores and cross talk in multiplexed experiments was less than 5%. In addition, molecular-level tuning of recognition elements (size, concentration) and agarose porosity resulted in NBC limits of detection two orders of magnitude lower than ELISA, values competitive with the most sensitive methods yet reported (0.021 ng/mL CEA). Taken together, these efforts serve to establish the valuable role of QDs in miniaturized diagnostic devices with potential for delivering biomedical information rapidly, reliably, and robustly.

Table of Contents

Common Acronyms	xiii
List of Tables	xvi
List of Figures	xviii
Chapter 1: Background for and Introduction to Nano-Bio-Chip Approach to Point-of-Care Diagnostics	1
1.1 Overview	1
1.1 Statement of Problem	2
1.2 Background	3
1.3.1 Biomarkers of Disease	4
1.3.2 Instrumentation Evolves via Microfluidics	6
1.3.3 Nanotechnology	12
1.4 Integrated Systems	17
1.5 McDevitt Group Integrated Approach—The Programmable NBC	23
1.6 Summary and Dissertation Overview	28
Chapter 2: Integration of Semiconductor Quantum Dots into NBC Systems for the Enumeration of CD4+ T Cell Counts	32
2.1 Chapter Overview	32
2.2 Introduction	32
2.3 Materials and Methods	36
2.3.1 Reagents and Samples	36
2.3.2 NBC Construction	38
2.3.3 Optical Station	38
2.3.4 Cell Immunolabeling	39
2.3.5 Image Analysis	40
2.4 Results	41
2.4.1 NBC Device	41
2.4.2 QD Evaluation	44
2.4.3 Expanded Pathway Assessment	50

2.4.4 Optimization and Validation.....	54
2.4.5 Monocyte Discrimination	57
2.4.6 Absolute Determinations	59
2.4.7 Flow Cytometry Correlation	63
2.4.8 Comparison to Molecular Fluorophores	64
2.4.9 Optical Pathway Evaluation.....	67
2.5 Discussion	68
2.5.1 Role in HIV	68
2.5.2 NBC Advantages	69
2.5.3 Fluorophore Considerations.....	70
2.5.4 Quantum Dot Performance	71
2.5.5 Optical Gating.....	72
2.5.6 Limitations and Comparison to Other Miniaturized Techniques	73
2.5.7 Bridging Gaps—Towards a Condensed Analyzer.....	75
2.6 Summary and Conclusions	77
Chapter 3: Utilization of QD Bioconjugates in Nano-Bio-Chip Assemblages for Multiplexed Detection of Oncologic Biomarkers.....	78
3.1 Chapter Overview	78
3.2 Introduction.....	78
3.3 Materials and Methods.....	83
3.3.1 Immunoreagents.....	83
3.3.2 Preparation of Beads	83
3.3.3 IgG-Fluorophore Labeling.....	84
3.3.4 Clinical Sample Acquisition and Preparation	84
3.3.5 NBC System and Assay Conditions	85
3.3.6 LOD and Assay Range.....	86
3.3.7 System Precision.....	87
3.3.8 System Linearity	87
3.3.9 Immunodepletion	87
3.3.10 Method Comparison Studies.....	88

3.3.11 Data Interpretation	89
3.4 Results and Discussion	89
3.4.1 QD Integration into NBC	92
3.4.2 The QD Advantages Relative to Molecular Fluorochromes.....	96
3.4.3 Analytical Performance of NBC Assays.....	99
3.4.4 Analytical Performance of NBC for Clinical Samples	105
3.4.5 Multiplexing Capabilities.....	108
3.5 Conclusion	114
Chapter 4: Molecular Level Programming of NBC Sensor Components for a Universal Approach to Assay Building	119
4.1 Chapter Overview and Goals	119
4.2 Introduction.....	121
4.3 Materials and Methods.....	128
4.3.1 Preparation of Components for CEA Assay	128
4.3.2 Ficin Fragmentation of Whole IgG ₁ Molecules.....	128
4.3.3 Preparation of Beads	129
4.3.4 Microscopy Design	130
4.3.5 Image Analysis.....	131
4.4 Results and Discussion	132
4.4.1 Effect of Antibody Size on Assay Performance	132
4.4.1.1 Characterization of Immobilization Elements	133
4.4.1.2 Preparation of Bead Micro-reactors.....	136
4.4.1.3 Fragment-Based Immunoassays—Signal Intensity	139
4.4.1.4 Characterization of Immunoassay Signal Distribution .	143
4.4.1.5 Further Systemic Characterization.....	145
4.4.1.6 Effect of Capture Antibody Size on Antigen Location.	149
4.4.2 Multiple Color Channel Colocalization.....	151
4.4.3 Effect of Agarose Porosity on Assay Performance.....	154
4.4.3.1 Agarose Permeability.....	155
4.4.3.2 Effects of Agarose Permeability and Antigen Size on Immunoassay	161

4.4.3.3 Antibody Concentration Effects on Immunoassay	164
4.4.3.4 Importance of Pressure Driven Flow	167
4.4.3.5 Confocal Colocalization Imaging Controls	169
4.4.3.5 Occlusion of Agarose Nanochannels	171
4.4 Summary and Conclusion	176
Dénouement: Conclusions, Outlook, and Future-Leaning Perspective	181
Appendix A: Optical Optimization—Emission and Excitation Filters.....	188
Appendix B: Reagent Optimization—Primary and Secondary Antibody Titration Experiments	189
Appendix C: Sample Cellular Analysis Method via Java and ImageJ	190
Appendix D: Reprint Permissions	194
References	196
Vita	216

Common Acronyms

- AF – Alexa Fluor; trademarked brand name for a series of molecular fluorophores
- Agn. – Antigen; often synonymous with the analyte in immunoassay
- AIDS – Acquired Immunodeficiency Syndrome
- B – Background; signal present at a zero analyte concentration
- BSA – Bovine Serum Albumin; a common protein used to stabilize other polypeptides
- c.Ab. – Capture Antibody; immobilization ligand in sandwich immunoassay
- CA125 – Cancer Antigen 125; a cancer biomarker
- CAOI – Circular Area of Interest; describes a collection of pixels
- CCD – Charge Coupled Device; array of photosensitive elements; heart of digital photography
- CD – Cluster of Differentiation or Complementarity Domain; cell surface epitope that defines cellular function and development
- CD3 – a common lymphocyte CD
- CD4 – a CD present in lymphocytes and monocytes
- CD8 – a CD specific to killer lymphocytes
- CEA – Carcinoembryonic Antigen; a common epithelial cancer biomarker
- CFD – Computational Fluid Dynamics; *in silico* approach used to model and optimize reagent transport and liquid delivery in microfluidic systems
- CP – Circular Profile; a collection of pixels defined by deconvolution macro
- CPU – Central Processing Unit or Cellular Processing Unit or Chemical Processing Unit; the reactive core of computers or nano-bio-chip assemblages
- CRP – C-Reactive Protein; a well-studied marker of inflammation
- Ctrl. – Control
- CV – Coefficient of Variation; descriptor of deviation within a collection of measurements
- D – Doughnut; a collection of pixels defined by deconvolution macro
- d.Ab. – Detecting Antibody; the transduction element in sandwich immunoassay
- DTT – Dithiothreitol; a powerful reducing agent
- EDC – 1-Ethyl-3-[3-dimethylaminopropyl]carbodiimide; a popular zero-length cross-linker used to link carboxyls to primary amines.
- ELISA – Enzyme Linked Immunosorbent Assay; well-established approach for protein measurements using a sandwich arrangement of antibodies and a color-changing substrate

- F(ab')₂ – Fragment of whole IgG without Fc region containing both antigen recognition regions
- Fab – Fragment of whole IgG without Fc region containing one antigen recognition region
- Fc – Fragment Crystallizable; portion of IgG forming non-antigen binding stem
- FC – Flow Cytometry; a common bioanalytical technique to counting and sort cells
- FDA – Food and Drug Administration; a government body charged with regulating safety
- FITC – Fluorescein Isothiocyanate; a common green fluorescing molecule
- FOV – Field of View; the amount of space a microscope may view at any given time with a given objective of defined magnification
- FRET – Fluorescence (also Förster) Resonance Energy Transfer; optical phenomenon of non-radiative energy transfer energy from an excited donor molecule to an acceptor, causing emission
- FWHM – Full Width at Half Maximum; descriptor of uniformity in a collection of measurements
- GLP – Good Laboratory Practice; systemic effort to improve the quality of technique
- Her-2/Neu (Her-2 or C-erbB-2) – Human Epithelial Growth Factor Receptor 2; indicator of aberrant smooth tissue growth
- HIV – Human Immunodeficiency Virus; precursor to AIDS; infects CD3+CD4+ lymphocytes
- IgG – Immunoglobulin G; protein used for immunity
- IgG₁ – Immunoglobulin G in mouse; protein used for murine immunity
- IL-1 β – Interleukin 1-beta; cytokine used by circulating WBCs for communication
- ISE – Ion Selective Electrode; chemical/mechanical ensemble for measurement of charged atomic species
- LOC – Lab on a Chip; any type of small, novel analytical tool replacing many aspects of bench-based laboratory
- LOD – Limit of Detection; the lowest amount of analyte that may be reliably measured with a given technique
- LP – Line Profile; a collection of pixels defined by deconvolution macro
- MEMS – Microelectromechanical Structures; micrometer-scale machines
- MW – Molecular Weight; mass of one mole of a substance

- N – Noise; any type of variation in signal
- NBC – Nano-Bio-Chip; an integrated measurement assemblage for medically themed analyte classes
- NHS – N-hydroxy succinimide; carboxylic acid activator and EDC stabilizer
- NK – Natural Killer; class of cytotoxic lymphocytes
- PBS – Phosphate Buffered Saline; a common laboratory diluents; isotonic with serum
- PCR – Polymerase Chain Reaction; nucleic acid amplification procedure
- PDB – Protein Database; repository for polypeptide structures
- PDMS – Poly-dimethylsiloxane; a silicon based organic polymer; plastic
- PEG – Poly-ethyleneglycol; a hydrophilic plastic
- PEO – Poly-ethyleneoxide; synonym for PEG
- PMMA – Poly-methyl-methacrylate; a strong plastic; Plexiglass[®]
- POC – Point-of-Care; a health paradigm focusing on treatment and diagnostic events moving to patient not vice versa
- PVC – Poly-vinyl-chloride; a common, sometimes brittle plastic
- QD – Quantum Dot; a class of fluorescent semiconductor nanoparticles
- QD XXX – QD with emission maximum; e.g. QD 565 has emission peak at 565 nm
- S – Signal; transduction output specific to the analyte in question
- SBR – Signal to Background Ratio; a measure of analyte-specific transduction output quality versus the system's ambient output
- SEM – Scanning Electron Microscopy; powerful technique for gleaning 3D surface imagery
- SERS – Surface Enhanced Raman Spectroscopy; a scatter-based technique
- SMCC - succinimidyl 4-(N-maleimidomethyl) cyclohexanecarboxylate; a PEG-amino activator
- SNR – Signal to Noise Ratio; a measure of analyte-specific transduction output quality versus the system's variation in output
- TAT – Turnaround Time; the temporal difference between initiation of analytical procedure and results
- TEM – Transmission Electron Microscopy; analytical technique with ultra-sensitive resolution
- TIFF (TIF) – Top Image File Format; a data storage paradigm typical of images
- μ TAS – Micro Total Analysis System; any assemblage combing various facets of the analytical process into a small device footprint

List of Tables

Table 1.1. Concentration as a Function of Volume. For a sample type with 250 molecules of analyte, measurement is impossible when volumes are on the order of the benchtop. As the same number of analyte molecules are concentrated into a smaller microfluidic volume, analysis becomes much more realistic as concentrations increase. . 8

Table 1.2. Assays Demonstrated on NBC Device. A wide variety of sample and analyte types have been incorporated into the McDevitt NBC analysis scheme. All of these assays were performed using a traditional molecular fluorophore or a conventional colorimetric assay. This dissertation seeks to detail analytical improvements available via QDs. (Green inset lists all assays with proof-of-principle on NBC) 25

Table 2.1. Extended Evaluation of QD Conjugation Schemes. SMCC (A), EDC (B), and secondary (C) techniques were subjected to an extended evaluation in addition to an avidin/biotin linkage (D) and protein A facilitated pathway (E). Some avidin/biotin labeled cells were subjected to additional biotin amplification (Bt. Amp.) and those values separated by dashed line. These were characterized in terms of path length (as determined by crystal structure and literature reports), antibody to fluorophore ratio, quantum yield, molar extinction coefficient, background, non-specific signal, and signal to background ratio. The superior performance of the secondary antibody scheme remains apparent by its high SBR and low non-specific signal. Note $\Delta\Phi$ is change in quantum yield upon linkage to antibody and ϵ is measured at 350 nm. Other descriptors are explained further in the text of **Section 2.3.3**. 52

Table 2.2. Performance Features of QDs From Various Vendors. QDs were used in conjunction with the EDC method to label CD3+ lymphocytes in the NBC. Invitrogen (A, E) and EvidentTech (B) QDs are carboxy coated and consist of CdSe core and ZnS coat. PlasmaChem (C, D) QDs have a CdTe core which resulted in a much dimmer signal; however, these QDs also had much less problems in terms of aggregation and non-specificity. An additional parameter included here not in **Table 2.1** is macroscopic precipitation (macro ppt) a term used to evaluate how much of the antibody-QD conjugate is in solid form at the end of conjugation. 54

Table 2.3. Performance Features of Covalent QD Linking Techniques. A summation of the shortcomings and highlights of the EDC, SMCC, and secondary antibody conjugation methods reveals that, for this application, secondary antibodies are best suited due their lack of aggregation and intense, specific signal. 71

Table 3.1. Performance features of CEA analysis methods. Comparisons between the NBC, ELISA, and bench-top hospital laboratory analyzers reveals superiority of NBC. Detailed here are coefficient of variation (CV) both within a single experimental run and between assays. The LOD listed here was defined previously while limited of linearity (LOL) is defined classically as the concentration at which a best-fit curve deviates at greater than 10%.^{216, 217} 114

Table 4.1. CEA Capture Antibody and Antibody Fragment Characterization. Absorption at 650 nm and 280 nm was used to calculate the amount of protein and Alexa Fluor 647 fluorophore in various fractions of digested immobilization elements. The ‘647’ indicates fluorophore labeled product while ‘Un’ implies unlabeled antibody. (¥ - concentration provided by manufacturer) 136

Table 4.2. Terminal-amine Containing Amino Acids in Recognition Elements. The major amino acids through which both fluorophore conjugation and immobilization onto agarose substrate are completed include lysine (Lys), arginine (Arg), glutamine (Glu), and asparagine (Asp). As recognition element size decreases, the percentage of amine-containing amino acids tasked with facilitating a bond increases. 142

Table 4.3. Detecting Antibody Concentration Differences Affect Signal. At higher concentrations of capture antibody (A) ~60% of the bead is unused for sandwich immunoassay. No reagents besides capture antibody can penetrate into the bead center. This remains true regardless of bead porosity. (B) At a lower concentration, the distance between antibodies is increased allowing for more of the entire immunocomplex to penetrate. Here, void volumes are reduced to zero; however, note the decreased epifluorescent signal intensity. The * indicates the values is an estimate based on the trend fitting. Data in § comes from Pernodet²⁴⁴ and ¶ is sourced to Narayanan.²⁰⁶ 175

Table 4.4. Size Dependent Diffusion Time and Information Density. The important effect size of reaction vessel has on system performance is illustrated above for a number of diffusion-limited hypothetical systems with dimensions and volumes listed above. Note that the ability to perform an increasingly larger number of assays in a shorter amount of time in a smaller amount of space. (t_d calculated by $t_d = (d^2/2D)$ where D is diffusion coefficient; for this example hemoglobin’s value of $1.75 \times 10^{-7} \text{ cm}^2/\text{s}$ was used.²⁶⁹) Please see Manz reference for additional insight.³⁶ 180

List of Figures

Figure 1.1. Trends Toward Coherent POC Biomedical Devices. Triumvirate advances in areas essential to development of the current NBC design: molecular diagnostic biomarkers, miniaturization of laboratory components via microfluidics, and nanoparticle quantum dots. 4

Figure 1.2. Quantum Dot Essentials.⁶⁷ **A)** Commercially available hydrophilic QDs consist of the fluorescent core semiconductor followed by a shell of passivation material designed to preserve structural integrity of the core and increase fluorescent signal and quantum yield. This is capped by an additional coat of polymer or other material to increase hydrophilicity and allow coordination of any additional chemistry. **B)** TEM images of QDs with peak emission at 495 nm show smaller nanoparticles than those in **C** with λ_{em} of 655 nm. **D)** QDs size determines their λ_{em} with larger particles emitting more red shifted light. Nevertheless, all particles are easily excited in the UV, an ideal arrangement for multiplexed experiments. (Units in relative fluorescence units, RFU.). 13

Figure 1.3. Quantum Dot Electronic Structure. **A)** Bulk semiconductor materials have a small bandgap and closely spaced, continuous energy levels both in the valence and conduction bands. **B)** As the physical dimensions of semiconductor materials are decreased, not only does the bandgap energy increases, but so does the differences between energy levels within valence and conduction bands. These increases eventually make the energy levels *discreet*, rather than *continuous*. **C)** The QDs have physical dimensions smaller than the Böhrr exciton radius, creating a quantum confined situation. 16

Figure 1.4. Nano-bio-chip Design. **A)** The research-grade NBC used these studies consists of an aluminum housing with a central processing unit sealed between PMMA layers designed to direct fluid flow. **B)** The benchtop support equipment used in conjunction with research-grade NBC includes a modified epifluorescent microscope with CCD digital camera as well as a peristaltic pump fluid delivery system. **C)** For membrane-based NBC experiments, a polycarbonate track-etched membrane is used. Pore diameter is determined by analyte size. **D)** In bead-based experiments, agarose microspheres form the underlying infrastructure. Any number of chemistries may be performed to make the beads selective for proteins, ions, or small molecules..... 24

Figure 1.5. Essential Elements of the NBC for POC Assays. The nano-bio-chip contains attributes and design contributions from three key areas: biomarkers of disease

and biological reagents/controls, nanometer size fluorescent tags and the nano-net formed within the agarose microspheres, and the microfluidic cartridges that focus fluid flow and contain reagents and waste. All must synchronize to achieve reliable results that meet the COMMAND QUALS descriptors. 27

Figure 1.6. Motivation and Direction. A) Current laboratory designs include a bench-top instrument with fluid handling, electrical, waste, and refrigeration supporting instrumentation. In contrast, POC-type systems work to condense this entire lab infrastructure into a small, device with COMMAND QUALS descriptors. The strong trend toward POC systems is illustrated in B. C) This dissertation will explore the core subcomponents of the NBC system with work targeting singularity in a truly integrated POC device (D). (Fig. 1.6B constructed via the number of returns on a search for “point of care” in SciFinder Scholar[®] literature service.) 30

Figure 2.1. Distribution of HIV positive individuals. The highest rates of HIV infection are found in sub-Saharan Africa, a region also known for scarcity of biomedical infrastructure. In these areas, the unmet clinical need is access to diagnostic testing. (Reprinted with permission of UNAIDS. Copyright 2008.)..... 34

Figure 2.2. The optical and mechanical requirements of the membrane-based NBC. Typical arrangement in an epifluorescent experiment contains excitation and emission filters as well as beam splitting optics. A) With traditional molecular fluorophores, each dye has its own requirements, and thus, illuminating different color concurrently frequently requires multiple optical sets. Conversely, with a QD arrangement (B), a single UV excitation source, in tandem with a long pass emission filter allows simultaneous excitation and visualization of a number of differently colored QDs. C) The first generation “flow cell” NBC assembly was constructed from an aluminum housing in which PMMA support mechanisms along with plastic gasket material served to immobilize a polycarbonate membrane. This aluminum model was used for preliminary, qualitative experiments. D) The second-generation NBC was constructed entirely of disposable material including vinyl adhesive and precision-cut laminate layers designed for fluid flow. 42

Figure 2.3. Cells immobilized and isolated by NBC. A) SEM image of whole blood sample after NBC processing indicates that the vast majority of erythrocytes and platelets are relegated to waste while leukocytes are preserved on top of membrane. B) Cartoon cross section of membrane illustrates the ability of the NBC to concurrently isolate a cellular fraction and label it by subtype. 43

Figure 2.4. EDC Conjugation. **A-B)** The EDC cross linker was examined both in the presence and absence of the S-NHS stabilizer to link carboxy-coated QDs to IgG antibodies. This technique gave poor results as it non-specifically cross links amines to carboxy groups. **C)** The method to determination signal (S), noise (N), and background (B) is reminiscent of traditional methods in spectroscopy and are created by drawing line profiles through the fluorescently labeled cells (**D**). For the lymphocyte counting application in the NBC, signal to background ratio (SBR) was a particularly important descriptor as it defined an authentic cellular event. White line in **D** indicates line profile leading to optical cross section in **C**. 45

Figure 2.5. SMCC Conjugation. **A)** SMCC coats the surface of amine functionalized QDs with an active maleimide group. **B)** DTT reduces disulfide bonds effectively cleaving whole IgG into smaller fragments with a free sulfhydryl. **C)** This sulfhydryl can then reduce into the maleimide ring structure linking fragment to QD. 46

Figure 2.6 Secondary Antibody QD Linkage Conjugation. **A)** SMCC coats the surface of amine functionalized QDs with an active maleimide group. **B)** Proteolytic digestion DTT reduces disulfide bonds specifically cleaving whole IgG into F(ab')₂ fragments including a free sulfhydryl. **C)** This sulfhydryl can then reduce into the maleimide ring structure linking fragment to QD. This conjugate was purchased in the form of panel **C** from Invitrogen. 48

Figure 2.7. Performance Features of Three QD Linkage Strategies. **A)** SMCC technique non-selectively links fragmented IgG onto QD surface. This strategy consistently gave unacceptable fluorescent precipitate both in the presence and absence of blood sample. **B)** Although the EDC technique was more reliable at giving low backgrounds, its lack of a defined orientation and high fluorophore to antibody ratios resulted in cells with low SBR. **C)** The secondary antibody scheme specifically labeled cells with high specificity and little background. 50

Figure 2.8. Cross Reactivity in Secondary Antibody Labeling Pathway. Panel **A** and **B** are the same sample subjected to CD4 primary antibody raised in rat and then subjected to secondary staining by both goat anti-rat (QD565) and goat anti-mouse (QD655) antibodies. The sample was then imaged with optical settings specific to either green (**A**) or red (**B**) QDs. Only the specific rat-rat interaction elicits a signal. Conversely, panels **C** and **D** employed a CD3 specific primary antibody raised in mouse

and an identical secondary cocktail as employed above. Again, specific signal comes from the iso-species interaction. Images captured at three seconds exposure..... 55

Figure 2.9. Lymphocyte subset profiling via QDs. Representative photomicrographs of whole blood labeled with CD specific antibody and QD fluorescently tagged secondary antibody taken with a 10X objective and 3 seconds of exposure time. The QD 565 labels CD4+ cells including monocytes and T lymphocytes in the green channel (A) while QD 655 stains CD3+ lymphocytes red (B), as observed through separate filter cubes specific to each fluorophore. A digital overlap of the red and green images (C) shows monocytes (CD3+CD4+, green), T lymphocytes (CD3+CD4+, yellow) resulting from signal both in red and green channels, and remaining NK and CD8+CD3+ T-killer lymphocytes (CD3+CD4+, red). An alternative approach (D) utilizes a long-pass emission filter cube (520 nm and longer) allowing a single capture event to produce a similar image to that generated by separate photomicrographs. Insets illustrate highlighted areas with 2X digital zoom; images captured with three seconds of exposure..... 56

Figure 2.10. NBC Gating. Graphical depiction of cells and the spatial and intensity gating procedures used for selected lymphocyte and monocyte populations. A) The CD4+ cells fall into two distinct populations: CD4+ bright, lymphocytes, and CD4+ dim, monocytes as shown in the schematic. The intensity of this CD4-specific signal is an initial descriptor to remove monocytes from analysis. B) The CD3+ cells include T and NK lymphocytes. C) Overlap of the two images results in red, green, and yellow cells. Cells doubly positive for red and green, and thus yellow, are the CD4+ T lymphocytes of interest. Cells remaining green are the interfering monocytes. D) A green color channel 8-bit intensity histogram is shown for the CD4+ cells as analyzed by the membrane-based NBC. The cells are labeled with QD 565. E) A similar 10-bit histogram is shown for the populations as determined by FC. (FC histogram truncated from 1024 to ~550 to maximize plot area.)..... 58

Figure 2.11. Cell Counting and NBC Validation for HIV Studies. Whole blood of varying volume was subjected to the staining process and membrane-based NBC analysis. A) Undiluted blood was stained for CD4+ lymphocytes and counts per field of view translated into total number of cells distributed across the entire membrane. This was interpreted by either a constant (set) or dynamic (auto) threshold value. B) To simulate immunocompromised samples, blood volumes were subjected to PBS/BSA dilution to a total volume of 50 μ L and stained for CD3+CD4+ lymphocytes with total membrane area and dilution correction factors utilized to estimate cells per μ L in the

original 50 μ L sample. C) Small pilot study comparison of the membrane-based NBC method to flow cytometry for %CD4 determinations correlates at $R^2 = 0.97$ 62

Figure 2.12. QD Photostability. CD3+ cells were processed with equimolar concentrations of both primary and secondary-antibody-fluorophore conjugate, which was normalized to fluorophore. This was injected into the NBC, and images captured every 20 sec for 15 min. Intensities from each fluorophore were plotted relative to their individual maximum, initial intensity. Conventional fluorophores exhibit exponential decay versus QD photostability that is critical for capturing a number of FOVs in the NBC system. This stability may also be exploited to add additional reagents for further cell analysis. Images captured at one second exposure. 66

Figure 2.13. QD Filter Optical Properties. Signal to noise and signal to background ratios for individual filter cubes versus a single long pass filter for staining CD3+ cells. Individual cell intensities were evaluated relative to immediate environment in terms of membrane auto-fluorescence and variation in background signal. For this application, SBR proved critical in identifying authentic events. 67

Figure 2.14. Size Regimes Involved in NBC. The NBC uses elements from many different size scales including nano (A), micro (B, C), and macro (D, E). The integration ultimately has the potential to have a global impact (F)..... 76

Figure 3.1. Ratios of Individuals Testing Above CEA Disease Threshold. Cancer and other disease biomarkers are rarely the proverbial “smoking gun” sought by diagnosticians. Rather, they indicate a generalized disturbance in normal body function and may present in both benign, malignant, and even asymptomatic individuals. For CEA, any number of conditions may cause an increase in serum levels. Note too, that no one condition is represented by uniform upregulation of serum CEA. (Data reproduced from Bayer Diagnostics/Siemens white paper.)..... 80

Figure 3.2. Formats of Sandwich Immunoassay. The fundamental components of sandwich immunoassay are retained across all three types of assay designs including underlying assay support (i), capture antibody (ii), antigen or biomarker (iii), and detecting antibody (iv). A) ELISA designs expand further this transduction pathway and include an enzyme (v) and substrate (vi) to affect a color change for a later absorbance measurement. B) The NBC system changes planar substrate in A, for the sponge-like agarose solid-phase support. The transduction pathway is also truncated to fluorophore tagged detecting antibody. C) The QD-based NBC design is typified by a larger

fluorochrome and thus a detecting antibody to fluorophore ratio that inverts relative to **B**.
..... 91

Figure 3.3. Bead-based NBC. **A)** SEM photomicrograph of beads in anisotropically etched silicon chip. **B)** Fluorescent image of beads after immunoassay including negative controls with DVC camera settings of ‘gain’ 10, ‘offset’ 0, and 1 sec. exposure.
..... 92

Figure 3.4. Analysis Methods Used in the Bead-based NBC. A graphic representation of the analysis methods described in **Section 3.3.10**: **(A)** Line profile (LP), **(B)** circular profile (CP), **(C)** integrated density or doughnut (D), **(D)** circular area of interest (CAOI). **E)** Dose response curves of the three different methods of analysis indicates that the LP approaches consistently yields the highest signal and most sensitive response. 93

Figure 3.5. Photomicrographs Show Intensity Differences Between Samples. **A)** Zero-calibrator, negative control, consisting of buffer only gives little signal, while 50 ng/mL **(B)** and 100 ng/mL **(C)** show increasing fluorescent output. Fluorescent signal intensity advantage with QDs **(C)** versus molecular Alexa Fluor dye **(D)** is greater than 30 fold at identical antigen concentration. An additional row of negative control beads with similarly negative output on the photomicrograph right side was digitally cropped. All images procured at DVC camera settings ‘gain’ 10, ‘offset’ 0, with one sec. exposure.
..... 96

Figure 3.6. CEA Dose Response Curves. Curves were constructed by adding recombinant antigen to buffer followed by analysis with the NBC. **A)** Logarithmic figure spanning six orders of magnitude concentration of CEA with sharpest response overlapping physiologically relevant range from 0.1 to 100 ng/mL. Signal is relative to the maximum intensity produced by highest concentration calibration point and expressed as relative fluorescence units (RFU). **B)** Linear and sensitive dose response over region of typical sample concentration. 101

Figure 3.7. Limits of Detection via CEA Dose Response Curves. Both ELISA and NBC methods allow calculation of a LOD and are compared here by maximizing their 12.5 ng/mL signal intensity to unity and scaling the others relative to the most intense point. **A)** ELISA data is indicated by the red points while 3σ above the background (zero calibrator) is indicated by the green circle. The point is then graphically translated via the best fit line, to a point on the ordinate for LOD determination. **B)** This is repeated with

NBC data to give the results in **C** that indicates the enhanced performance of the NBC relative to conventional enzyme-based assays..... 103

Figure 3.8. Validation of authentic CEA signal in saliva. **A)** Assay results of **i)** recombinant antigen at one half calibration curve maximum (50 ng/mL), **ii)** saliva at 1:4 dilution, **iii)** saliva sample spiked with recombinant antigen, **iv)** CEA depleted saliva. One row from each image was digitally sliced to create montage above. **B)** Results after digital image processing indicates the specific nature of CEA signal. (All images have been background corrected and use one second of exposure.)..... 106

Figure 3.9. Analytical Validation of NBC System via Clinical Samples. Saliva (n = 6) (**A**) and serum (n = 24) (**B**) samples correlate well with measurements achieved on reference methods. Saliva samples were validated versus ELISA; serum samples via a Siemens Centaur clinical chemistry analyzer. In addition to best fit line (solid), the 95% confidence interval (short dash) and 95% prediction interval (long dash) are presented. 107

Figure 3.10. Expansion of NBC to Additional Analytes. Dose response curves for CA125 (**A**) and Her-2/Neu (**B**) show linear response across the physiologically relevant range. **C)** Her-2/Neu detection limits calculated for three different detection methods. The NBC-QD approaches yields values five times lower than ELISA methodology, and nearly 14 times lower than NBC-Alexa Fluor 488. This order of magnitude is similar to the intensity advantage seen in **Section 3.4.2.** 109

Figure 3.11. The NBC Multiplexes via the Spatial Arrangement of Beads. **A)** In these experiments, cross-reactivity was evaluated. **(i)** All three antigens, at concentrations near calibration curve maximum, were incubated concurrently followed by a cocktail of all three detecting antibodies. **(ii)** Beads were exposed to only Her-2/Neu antigen, and again, the detecting antibody cocktail. Similarly, assays specific to CA125 **(iii)** and CEA **(iv)** were performed, as well as a zero antigen, negative control **(v)**. **B)** Non-authentic output emanating from untargeted beads plotted as a percentage of specific signal intensity shows strong specificity across all three analytes. Non-specific signal (noise) was less than five percent of the intense, specific signal. (All images have been background corrected and use one second of exposure.)..... 111

Figure 3.12. Intra-bead Multiplexing. **A)** Multi-analyte capabilities of the NBC include intra-bead duplexing in which dually functionalized beads measure two analytes concurrently. Beads sensitized to CEA, CA125, and both biomarkers are used

simultaneously on a single chip and demonstrate independent assay behavior. **B)** Across the physiologically relevant range of concentrations, no statistical difference is seen in fluorescent signal output between sole CEA and dual CEA/CA125 beads. (All images have been background corrected and use one second of exposure.)..... 112

Figure 3.13. Molecular Level Programming of NBC Assay components. The integrated NBC cartridge (**B**) is read with a compact, self-contained analyzer (**A**). This labcard still contains the fundamental agarose bead micro-reactors (**C**) as the research grade NBC (**Fig. 1.4A**) only in tandem with more elegant microfluidic condensations. It is this agarose core (**D**) that contains the nano-net serving as support for immunocomplexes. **E)** Close-up of a single sandwich immunocomplex within the bead gives molecular-level insight not attainable in the typical representations such as those in **Figure 3.2.**²²² 117

Figure 4.1. Contributors to assay performance in NBC. In **A** the location of an agarose microsphere in the MEMS structure is considered from the xz optical plane. Reagent transport into the bead structure is affected by active transport (flow) of material (**B**), diffusion of reactants into the sponge-like bead center (**C**), and the kinetic rate constants of interaction between non-covalently linked antigen and antibody (K_{on} and K_{off} , **D**). In this chapter, work is performed to move beyond a 2D conception (**E**), to an improved 3D appreciation of the agarose bead environment (**F**). Red line in **A** indicates the plane used for fluorescent confocal imaging studies. 120

Figure 4.2. Inconsistent ELISA Capture Antibody Design. **A)** In optimal coating environments, capture antibody is evenly distributed across the surface of a microtiter plate. However, any number of alternative schemes can result in less than ideal antigen capture including IgG linkage through active site (**B**), orthogonal antibody orientation (**C**), insufficient antibody coating (**D**), antibody stacking (**E**), and antibody layering (**F**). In addition, non-covalently linked antibody may disassociate from plate surface upon washing, effectively rinsing away analyte and later decreasing signal (**G**)...... 122

Figure 4.3. Size Considerations of Bead-based NBC Recognition Elements. Both the capture and detection bodies in sandwich immunoassay are typically whole IgG fragments (**A**).^{150, 238} A variety of proteolytic digestion schemes can be used to render this whole antibody into smaller F(ab')₂ (**B**) or Fab (**C**) fragments. Alternatively, scFV (single chain variable fragment, **D**) chains, using recombinant pathways, consist of only the heavy and light antibody target recognition chains. (**E**) Comparison of the molecular weight, maximum distance, radius of gyration (all left axis), as well as total number of

amino acids in the protein (right axis) for different size recognition bodies as well as the CEA antigen.²⁰⁶ 125

Figure 4.4. Characterization of Antibody Fragments. These figures arise from the Fab fragment preparation from Alexa Fluor 647-coated IgG capture antibody. After proteolytic fragmentation, antibody digests were purified using a Protein A affinity chromatography column with agarose solid phase support, in tandem with gradient elution. Yellow highlighted sections indicate pH 8.25 binding buffer, sections in green employ pH 6.02 elution buffer, and pink areas are pH 3.00 0.1 citric acid. **A)** Absorbance values at 647 nm indicate that the antibody fragments elute in basic buffer while Fc regions are not released from Protein A beads until change to acidic liquid phase. **B)** Absorbance at 280 nm shows similar signal increases from Fab fragments and poorly defined increase for Fc pieces. **C)** Similarly, the Coomassie reagent and 595 nm absorption indicates the presence of Fab fragments and vague presence of Fc. Fortunately, only the first six aliquots from each elution were needed for further processing. 135

Figure 4.5. Intensity Differences by Capture Element Type and Concentration. **A)** Photomicrograph of six different bead types reveals intensity differences. **B)** Bar graph of signal intensity for five bead types. Beads functionalized to F(ab')₂ are represented only once—the isomolar antibody and fluorophore values were calculated relative to these beads. This data reveals that the isomolar antibody has much larger signal intensity due to the additional numbers of dye that may be bound to Fc region. Photomicrograph in **B** created with DVC camera settings of gain 10, offset 0, and 25 ms of exposure time. Note that IgG/647 isomolar antibody beads are saturated at a pixel depth of 255. Exposure times below IgG saturation were insufficient to record signal from fragment beads. 138

Figure 4.6. Signal Intensity Generation in Different Capture Element Types. Radar plots of CEA assays with beads containing isomolar amounts of capture antibody bound to Alexa Fluor 647 as well as unlabeled capture antibody were performed and evaluated via the four different analysis methods (LP, CP, CAOI, D). **A-C** details the results of these assays for three different detection schemes, again at isomolar capture ligand concentrations, including IgG (**A**), F(ab')₂ (**B**), and Fab (**C**). **D-F** displays the same data as **A-C**, but with axis redrawn to the same scale. The most intense signal output comes from the IgG-IgG interaction. 140

Figure 4.7. Signal Distribution Generation in Different Capture Element Types. Three different detection schemes (**A**, IgG₁; **B**, Fab; **C**, F(ab')₂) yield three different patterns in beads. The top row of photomicrographs show beads with IgG₁, Fab, and F(ab')₂ capture antibody as well as an isotype control. The middle collection of surface plots reveal that IgG₁ and F(ab')₂ beads relegate most of their signal to periphery of the bead; Fab beads have signal more evenly distributed. This pattern remains the same regardless of detection antibody type. That is, capture element type determines location of antigen, and hence, location of detection antibody. The lower panel offers an alternative view of bead intensity. 144

Figure 4.8. Ideal Antibody Combinations and Analysis Methods to Improve Signal and Reduce Background. **A)** Background and noise for three different approaches reveals that signal generated with zero antigen (background, B) is consistently low for F(ab')₂ beads. The lowest B values come from the Fab-Fab interactions, which also gives the lowest signal values. Also, the isotype control beads (Ctrl.) reveals that the lowest values of N comes also from F(ab')₂ beads, followed by IgG, and Fab. **B)** IgG beads are used with three different detection methods and interpreted with the four analysis techniques described in **Section 4.2.5**. For highest signal, *IgG beads and a line-profile analysis approach is the best technique.* 146

Figure 4.9. Signal Optimization. **A)** One row cropped sections of photomicrographs analyzed with three different detecting antibodies. Again, the most intense signal came from the IgG-IgG interactions. **B)** LP intensity values from the photomicrographs in A were scaled in relevance to the most intense signal. Whole IgG antibodies were used for the remainder of the studies. (All images have been background corrected and use one second of exposure.) 148

Figure 4.10. Antigen Location in Bead. **A)** Confocal image of antigen location in beads with either Fab, IgG, or F(ab')₂ as the capture moiety. **B)** Line profiles from the three different bead types reveal differences in both intensity and distribution. As the capture antibody becomes larger (IgG) beads sequester more of their target on the exterior. Smaller capture elements (Fab) allow penetration of analyte deeper into the exterior. Data compendium in **C** was determined as penetration at one-half of maximum signal. 150

Figure 4.11. Three-Color Colocalization. **A)** All three parts of the bead-based sandwich immunoassay are linked to fluorescent tags in the following studies. The agarose bead substrate is coated with capture antibody/Alexa Fluor 647, which fluoresces

in the red. Antigen is identified by its Alexa Fluor 546 tag, an orange dye. For confocal imaging, this fluorophores corresponds to a blue lookup table. Finally, detecting antibody is identified by an Alexa Fluor 488 (green) tag. **B**) The excitation and emission spectra of the three fluorophores mentioned above reveals overlap and the need for careful optical controls to prevent unauthentic signal. (Spectra in **B** is copyright and reproduced courtesy of Invitrogen/Life Technologies, Inc.) 152

Figure 4.12. Three Color Imaging via Epifluorescent Microscope. Signal bleed and cross talk were negated by reducing camera integration time, reagent concentration, and via background subtraction. Optical settings: c.Ab. (647), gain 0, offset 0, 6 ms exposure; antigen (543) gain 5, offset -7.5, 1 sec exposure; d.Ab. (488) gain 5, offset -7.5, 1 sec exposure. Tabular results indicate signal present before next layer of immunocomplex was applied. For orange and green signal, this is the amount of “bleed” and is expressed parenthetically as a percentage of authentic signal. Note that an additional set of images were collected at lower exposure time to eliminate optical saturation in the high concentration beads..... 154

Figure 4.13. Bead Porosity Determines Function. The agarose microspheres have pores of tunable porosity. By selecting the percentage agarose in water during the synthesis, the immunoassay infrastructure may be tuned. Here, SEM images for beads of 0.5% (**A**), 2.0 (**B**), 4.0% (**C**), and 8.0% (**D**) reveal that pore size increases as percent agarose decreases. Through this electron microscopy technique, pore size estimates were gleaned through distances between adjacent agarose nanometer scale fibers. Green and pink arrows indicate representative measurements used to construct the green and pink curves in **Figure 4.14B**. (These images collected and reproduction permission granted by Dr. Jorge Wong.)..... 156

Figure 4.14. Characterization of Bead Porosity. (**A**) Permeability of a model porous structure, based on agarose, decreases exponentially as weight percent of solid phase (agarose) increases. A situation measured experimentally in (**B**). Here, three different approaches measured the diameter of pores in agarose gels, a descriptor similar to permeability. The atomic force microscopic (AFM) approach gives a tight cluster of pore sizes between 200-400 nm,²⁴⁵ while absorption-based, spectroscopy experiments (Absorbance) techniques show the exponential decay predicted by the model.²⁰⁷ Data from SEM images gathered in conjunction with this dissertation (SEM - UT) also correlate to the exponential reduction in pore size with increasing agarose concentrations predicted by model and agree nicely with the AFM published literature values..... 157

Figure 4.15. Bead Porosity via Computation Fluid Dynamics. Here, additional details including pressure and bead size was used in tandem with a penetration depth versus time study to give estimates for the 2% (wt./wt.) agarose (cross linked) used in this study. . 159

Figure 4.16. Size Features of Immunoassay Components. To illustrate the necessity to consider bead porosity in assay design, CEA²⁰⁶ (PDB ID = 1e07) (A) and IL-1 β ²⁶⁴ (PDB ID = 1t4q) (C) antigens are displayed, drawn to scale. Regardless of antigen size, IgG¹⁵⁰ (PDB ID = 1igy) recognition element remains nearly identical in size (B). (D) The larger size of CEA results from its increased molecular weight (* indicates glycosolated weight) and larger number of amino acids. (Images reprinted in accordance with the policies of the *Research Collaboratory for Structural Bioinformatics' Protein Data Base* at Brookhaven National Laboratory.²⁶⁵) 160

Figure 4.17. Analyte Size Affects Bead Behavior. (A) Three-color identification approach is used for two different size analytes. (B) Signal from the larger CEA molecules (27 nm) signal remains on the exterior. (C) IL-1 β is a smaller, globular protein (5 nm) and allows for deeper penetration of immunoassay components. (D) Regardless of bead porosity, all CEA antigen and detecting antibody remains in the thin layer on the bead exterior, unlike IL-1 β behavior (E) in which a gradual decrease in analyte is seen from exterior to interior. (Please see **Figure 4.15** for optical settings.) 162

Figure 4.18. Concentration affects bead behavior. (A) The three-color identification approach from **Figure 4.2** is retained for two concentrations of CEA detecting antibody. (B) At high concentrations, signal remains on the exterior; however, at lower concentrations (C) the distance between capture elements increases allowing deeper penetration of immunoassay components. (Please see **Figure 4.20** for optical settings.) 165

Figure 4.19. Line profiles of immunoassay components from Figure 4.18. The behavior of detecting antibody is confined to the bead exterior at higher concentrations of capture antibody (A) than the isotopic distribution seen at lower concentrations (B). (C) This accumulation of detection body on the periphery of A is in sharp contrast to the capture antibody distribution seen in the same system. (D) At lower concentrations of capture antibody, the differences in bead potency may be seen. In the 1% beads, there is an excess of capture reagent, allowing this signal to penetrate all the way to center. In contrast, the 4% beads have more active sites, effectively depleting all of the reagent before penetration to center is possible..... 166

Figure 4.20. Chip Design Considerations. Computational fluid dynamic (CFD) studies indicate that the vast majority of NBC flow when using the silicon MEMS chip is around the bead. Red arrows in **A** (xz plane), **B** (xy plane), and **E** (xz plane expanded) indicate the most flow at 0.3 mL/min passes through the openings between bead and bottom of the well. Indeed the convective flow indicated by red in **D** is in contrast to the mostly diffusive transport in the bead, shown in blue. Although no CFD work has been done modeling the stainless steel support (**C**), observations made with the NBC suggest that it behaves very differently than the etched silicon chip (**D**). 168

Figure 4.21. Optical Settings Experiment for Verification of Signal. In **A**, the same image is seen as in **Figure 4.14B** along with the optical settings needed for all three photomultiplier tubes on the confocal microscope. **B**) Here also is the same specimen imaged at the more sensitive optical settings required for the lower concentration specimen from **Figure 4.14C**. The similarity of the two images implies that the distribution differences seen in **Figure 4.14** are not due to increased gain (sensitivity) or offset of confocal optical settings as penetration depths do not increase. 170

Figure 4.22. Cross Talk Negative Control. Beads only functionalized to capture antibody imaged at the optical settings detailed in **Figure 4.14B** with all three photomultiplier tubes. That absence of signal in the green and blue channels implies that the presence of signal in the above experiments is genuine. 171

Figure 4.23. Occlusion of Nano-Channels. **A** and **B**) Agarose pore channels coated with detecting antibody. Smaller bodies, however, such as IL-1 β (35 nm) shown in **C**, allow penetration deeper into the bead interior. **D**) Larger immunocomplexes however, such as CEA (57nm) may block reagent transport in the agarose pores. 173

Figure 4.24. Reagent Usage in Sandwich Immunoassay Systems. The above comparison illustrates the fundamental differences between ELISA and the bead-based NBC for protein measurements. By using a 3D versus 2D reaction vessel (**A**) and an intricate lattice of immobilization moieties versus a planar system (**B**), the NBC allows for a much higher density of reagent capture centers and thus a high capacity for reporting the presence of analyte (**C**)..... 178

Figure D.1. Horizontal Cross Section of Compact NBC Labcard. A variety of components condense to create the integrated NBC. These include the buffer storage blister packs, fluid direction cavities, waste disposal reservoirs, and the analysis chamber. 184

Figure D.2. Complete Assembly of Working Parts. Many different components condense to create the integrated NBC (**B**), which contains the buffer storage blister packs, fluid direction cavities, waste disposal reservoirs, and the analysis chamber. The two processor types (**C**) cited above (**ii – Chapter 2, ii – Chapter 2 and 3**) include the membrane-based, cellular processing unit (upper scheme **i**), for cellular assays, while the bead-based, chemical processing unit (lower scheme **ii**), is typified by protein assays. Both must bridge nanometer scale gaps between bioligand and signaling probe (**E and F**) to create bioconjugates for analyte fluorescence labeling (**D**) within the CPU. Data contained in the samples and processed by the labcard is transcribed by a portable, self-contained analyzer (**A**)..... 185

Figure D.3. Scaling and Moore’s Law Behavior. The ability to bridge different gaps in scale (**A**) and combine the attributes of different layers results in an increasing number of analysis events on a small device footprint advances at a rate reminiscent of Moore’s Law in the microelectronics industry (**B**). 186

Figure A.1. Optimization of Excitation and Emission Optics. These experiments reveals the importance of considering and evaluating carefully all optical assemblages used in conjunction with the NBC. 188

Figure A.2. Optimization of Primary and Secondary Antibody Concentrations. A) A constant volume secondary antibody was used in tandem with increasing volumes of primary. Collected were total cell counts as well as non-specific (NS) aggregates outside of the cellular analysis parameters. This NS value was used in tandem with background (**B**) counts to give a ratio of these events versus authentic cell counts. Concentrations of reagents that minimized this parameter were needed. **B)** After 10 µg/mL was identified as the optimal quantity of primary antibody, the secondary antibody was similarly optimized. Future experiments used 10 nM secondary antibody. Two different camera exposure times were used, one and three seconds. 189

Chapter 1: Background for and Introduction to Nano-Bio-Chip Approach to Point-of-Care Diagnostics

1.1 OVERVIEW

This dissertation research focuses on developments occurring in the nanomaterial, microfluidic, and clinical communities by integrating semiconductor nanoparticle quantum dots (QDs) into miniaturized sensor systems as a new labeling and detection modality for “nano-bio-chip” (NBC) applications. These efforts have resulted in a superior fluorescent transduction signal with reduced optical requirements for multianalyte assays targeting cellular and protein-based disease biomarkers relevant to cancer diagnosis and staging as well as HIV monitoring. Implications of such QD applications include enhanced potential for miniaturization of sensor components toward development of portable, point-of-care devices which could increase access to diagnostic testing in remote or unconventional locations as well as decreased limits of detection due to QD signal strength.

This introductory chapter will serve to define the general problems addressed by the dissertation as well as to detail key terms used throughout the remainder of the document. In addition, a brief account of nanotechnology, miniaturized microfluidic hardware, and molecular diagnostic biomarkers will demonstrate the trend towards coherent and integrated assemblages. After highlighting some of the work of leaders in these fields, a summary will paint a picture of the research landscape in 2003, when this investigation was initiated. Such a précis will expose some of the fundamental shortcomings associated with previous work and orient the reader to the laboratory infrastructure used in these studies. Finally, brief synopses of the following three chapters will outline their role in making this study of nano-bio-chip systems complete.

1.1 STATEMENT OF PROBLEM

Two core deficiencies in existing biomedical infrastructure and technologies motivated this work with NBC systems. First among these unmet clinical needs, is a lack of access to diagnostic testing, and hence results, to dictate the proper course of treatment for HIV positive individuals.^{1, 2} The majority of the world's population lives in the developing world where there is little, if any, regular access to a healthcare provider, much less a well-equipped clinical laboratory. In these environments, pharmacologic therapeutic interventions may exist due to humanitarian efforts, but a lack of diagnostic equipment prevents these drugs from being appropriately dispensed, as information on HIV disease state progression to AIDS is unavailable. Lack of access to HIV appropriate prognostics, namely T lymphocyte counts, in these environments results in patients being staged with AIDS by opportunistic infections (*symptoms*), not *cell counts*. In these resource-scarce settings, rapid and cheap diagnostic and prognostic tests create the ability to identify individuals who may be best helped by the available therapeutics and work to delay the HIV to AIDS process.

Alternatively, in more affluent regions, the most prominent causes of death change to heart disease and cancer as life expectancy is increased. Here, the unmet clinical need is no longer accessibility, but rather diagnostics that identify the disease in its early stages with sensitivity and selectivity. Similar to resource-scarce settings, tests that are *inexpensive* and *rapid* remain important, but these diagnostic schemes must also meet additional requirements. First, they must monitor *many different analytes concurrently*—this so called “disease fingerprinting” allows clinicians to make much more timely and accurate diagnoses. A second requirement is *portable tests* that can be used in the doctor's office or ambulance, that is, the *point-of-care*. These decrease the time from diagnosis to therapy which has the potential to improve overall patient

outcomes. The approach to making rapid, reliable, rugged, multiplexed, portable, and inexpensive diagnostic aids, detailed in this dissertation, builds upon previous work.

1.2 BACKGROUND

Traditional approaches to testing clinical biological samples involve a well-appointed centralized laboratory, serviced by technicians and coupled to patients through various staff including nurses, aids, and phlebotomists. The physician's laboratory orders relate to the lab also through nursing and support staff. In this arrangement, laboratory diagnostic medicine is effectively three degrees of separation removed from the patient and this hierarchy introduces a number of critical junctures in which errors may be introduced and delay incurred. To simplify, a push has been made toward devices that give results at the point-of-care (POC), i.e. bedside, ambulance, or remote location, a situation advantageous to patient, provider, and nursing.³⁻⁶ The POC solution used in this work, the NBC, utilizes components from the three areas detailed below. **Figure 1.1** illustrates that the evolution of work leading to the nano-bio-chip proceeded along three main avenues. First, nanoparticle quantum dots have been better characterized, more biocompatible, and eventually commercially available. Second, biological markers of disease whether cellular, proteomic, or genetic have increased in number and relevance. Third, microfluidics and other miniaturization schemes have led to a rapid decrease in instrument size and an increase in chip-based, hand-held approaches to biological determinations.

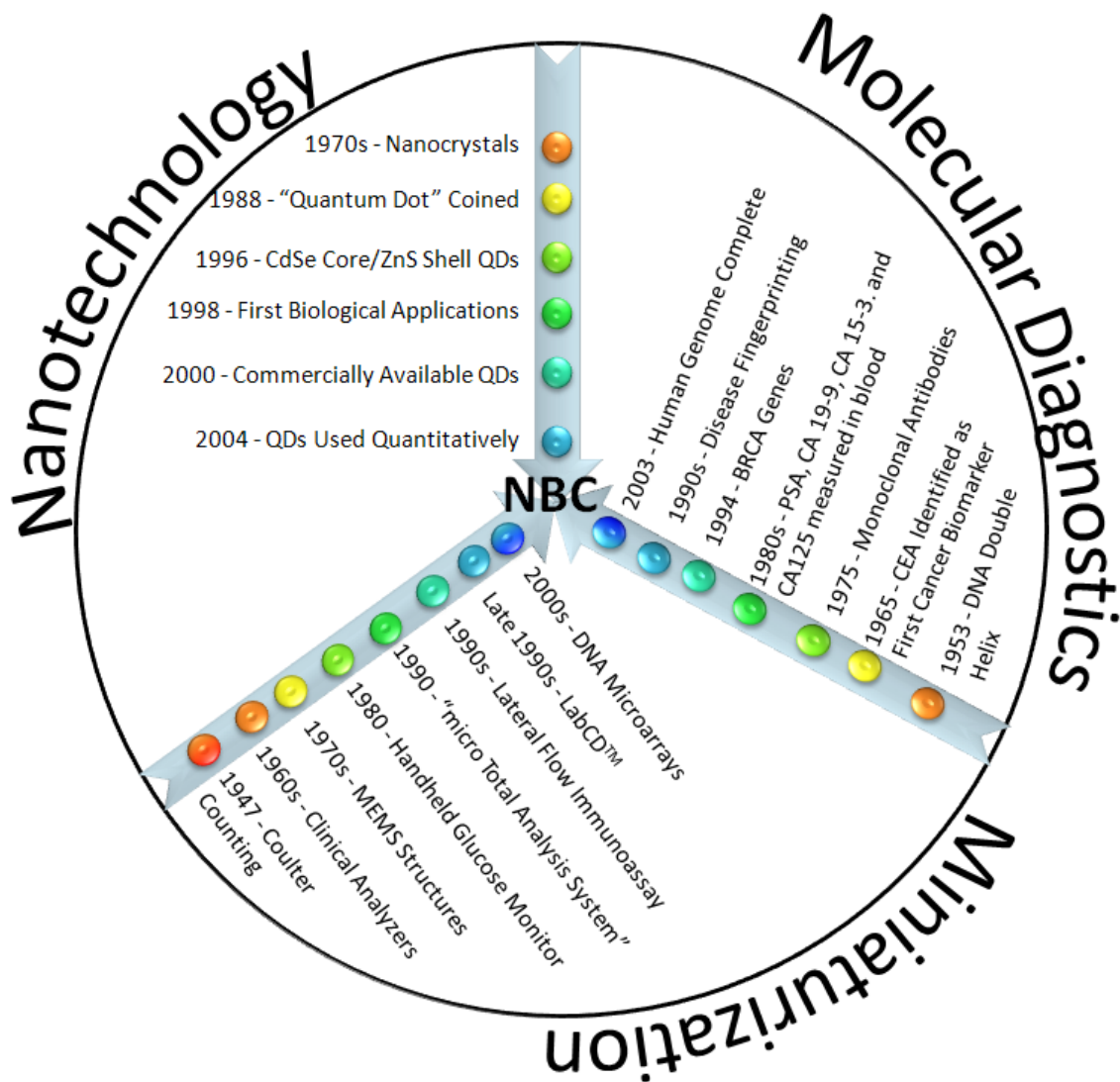


Figure 1.1. Trends Toward Coherent POC Biomedical Devices. Triumvirate advances in areas essential to development of the current NBC design: molecular diagnostic biomarkers, miniaturization of laboratory components via microfluidics, and nanoparticle quantum dots.

1.3.1 Biomarkers of Disease

Critical to the NBC are two key types of elements found in (or inspired by) nature or else synthesized in living organisms. First, is the biological recognition element. Common to nearly all approaches of disease monitoring is the presence of some type of molecule or other moiety, tasked with specifically isolating the analyte from the larger,

more complex sample. Lechtins for carbohydrates, oligos for nucleic acids, and aptamers, peptides, antibodies, and scFv fragments for proteins are all commonly used to achieve this task.⁷ Typically, this arrangement demands that each analyte be segregated by a unique recognition body and advances in dense arrays, especially genomic, has increased dramatically the density of such patterns as evidenced by such companies as Affymetrix.⁸ Emerging schema propose molecular recognition, without prior knowledge of the exact structure and identity of the target.⁹⁻¹¹

The second “bio” entity in the NBC is the malady-specific indicator, or biomarker. Beginning with protein studies at the turn of the last century, to the elucidation of DNA structure in 1953, and the advent of biomarker panels in the 1990s, clinical laboratory science has advanced substantially to increase both the number of molecular diagnostics tests, but also their impact on treatment.¹²⁻¹⁴ From CEA’s identification as the first biomarker, to later broad acceptance of proteomic PSA and genomic BRCA1 as cancer indicators, to emerging molecules for stroke, Alzheimer’s, cardiac, and pancreatic monitoring, the importance and relevance of these markers has been drastic.¹⁵ As a larger number of proteins and cell types were able to be routinely analyzed, more studies into their role in disease could be performed, which in turn increased the importance of monitoring these analytes after their implication in disease prediction or response to therapy was established.

With the commercialization of monoclonal antibodies, matched immunoassay antibody pairs, and modern instrumentation a new generation of experiments were possible to measure proteins and large numbers of cells and cell populations. By the 1980s extensive laboratory panels including complete blood counts as well as chemical, coagulation, immunology, and microbiology information were possible. Later, the next generation of the genetic revolution—completion of the human genome project in

2003—added yet another layer of complexity to the variety of components necessary to arrive at an accurate diagnosis.¹⁶ No longer were single assays acceptable to diagnosis patients, rather, the requirements for disease identification moved to a battery of analyses. Here, disease fingerprinting utilizes large information pools while companion diagnostics further defines disease subsets.^{17, 18} Ultimately, these advances in the number and use of genetic and proteomic biomarkers have begun to transform health care into personalized medicine.^{19, 20} More detailed descriptions of the proteins and cells analyzed by the NBC will be given in the introductions of the respective chapters.

1.3.2 Instrumentation Evolves via Microfluidics

Early chemical analysis was not amenable to biological systems. These classical methods isolated the analyte from the sample through some type of chemical transformation, i.e. precipitation, distillation and/or the compound of interest was titrated with a secondary reagent. A change in physical property such as color, refractive index, boiling point, etc. then determined the amount of analyte present. Near the turn of the last century, scientists moved beyond these easily monitored physical properties to more difficult characteristics including absorption or emission of radiation, conductivity, and mass-to-charge ratio. In addition, more evolved separation methods such as electrophoresis and chromatography began to supplant extraction and other less sophisticated isolation methods. As more reliable tools were engineered to use advanced physical properties for transduction, in tandem with advanced separation schemes, *instrumental analysis* was born.

Still, biological analysis was not easily performed with the vast majority of instrumental techniques for reasons of sensitivity, selectivity, and the destructive nature of sample preparation. Nevertheless, from such humble beginnings as Coulter counting and ion selective electrodes, clinical chemistry began to have a profound impact on the

way physicians treated their patients.^{21, 22} Similar to the history of the biomarkers themselves, a positive feedback loop emerged in which the importance of the disease indicators fed a need for instrumentation to study the biomarker, in turn uncovering more information about its role in disease. The 1980s saw a true coming of age of clinical instrumentation with the advent of large scale commercially available flow cytometers, hematology instruments, as well as automated benchtop immunoassay and clinical chemistry analyzers.²³ During this same time, however, researchers began to shrink these room-sized pieces of equipment into smaller spaces for ease of both patient and provider.

The first commonly accepted “lab-on-a-chip” (LOC) type study dates to Terry’s work with miniaturized gas chromatography in the late 1970s.²⁴ For the next decade, miniaturization researchers focused mainly on the electronics industry, although a few key innovations were introduced for biomedical applications. Importantly, the 1980s saw the handheld glucose meter become one of the first pieces of miniaturized diagnostic equipment to enjoy any commercial success.²⁵ As diabetics must frequently monitor their blood glucose and dose insulin accordingly, having a device for frequent home use was critical. Another huge commercial success was the home pregnancy test—a slightly more elegant piece of engineering and science that began to use biological components such as lateral flow immunoassay.²⁶ Still, these devices analyzed one biomarker per handheld unit; the next steps in evolution would seek to perform many analyses on a small device footprint.

The term micro total analysis systems (μ TAS) was coined by Manz in 1990 for systems in which chip-based analyzers incorporating on-board sample pretreatment, separation, and detection played a fundamental role.^{27, 28} While μ TAS or LOC systems perform similar tasks as their larger, benchtop counterparts, they offer several advantages including decreased volume of sample and analyte, reduced turnaround times, greater

sensitivity, reduced cost leading to disposable devices, and finally a portability leading to POC capable systems.²⁸⁻³² Key to the sample and reagent handling capabilities of μ TAS is a miniaturized circuitry of valves, channels, pumps, filters, and reservoirs to manipulate the fluidic and gas components of the system, that is, a *microfluidic* design. By definition, microfluidic structures manipulate small fluidic volumes through various analysis and sensing steps.³³ **Table 1.1** illustrates the dramatic improvements that are possible for a representative measurement. Here, the concentration of 250 molecules of sample X is listed as a function of typical volumes encountered in the laboratory bench, the microfluidic chamber, and human cells. Importantly, as the volume progressively decreases, the concentration of the same 250 molecules increases to levels amenable to measurement. Indeed, when these volumes decrease to the nL, pL, or fL regimes, concentrations increase into picomolar range—values commonly observed in the bioanalytical chemistry laboratory.

Representative Sample	V scale	Vol. (L)	Conc. (pM)
Flask	1 L	1.00E+00	4.15E-10
Graduated Cylinder	1 mL	1.00E-03	4.15E-07
Micro-Pipette	1 μ L	1.00E-06	4.15E-04
Agarose Bead	11 nL	1.00E-08	4.15E-02
WBC	1 pL	1.00E-12	4.15E+02
RBC	100 fL	1.00E-13	4.15E+03

Table 1.1. Concentration as a Function of Volume. For a sample type with 250 molecules of analyte, measurement is impossible when volumes are on the order of the benchtop. As the same number of analyte molecules are concentrated into a smaller microfluidic volume, analysis becomes much more realistic as concentrations increase.

Due to the reduced requirements of microfluidic sampling and reagent usage, costs decrease drastically and assay times cut substantially. Rapid prototyping, assembly-line compatible designs, and extremely low-cost materials lead to further reductions of costs versus instruments that require individual assembly.³⁴ Furthermore, the contributions of microfluidics to analyte isolation and concentration as well as their capacity for mixing, allotment, and fluid focusing, rapidly decrease the number of required sample-handling steps.^{33, 35} Below are some commonly used dimensionless parameters for microfluidic description as recently highlighted in a *Nature Insight*³⁶:

- Péclet number, Pe , describes the ratio of axial bulk flow to diffusion mass transport (rate of transport due to advection over rate of diffusion). Values less than unity imply a linear, diffusion-transported system while values above imply that concentration gradients may exist.
- Fourier number, τ , describes the average number of times a molecule contacts the wall of a fluid containing channel
- Bodenstein number, Pe , characterizes the back mixing within a system
- Reynolds number, Re , represents the ratio of inertial forces to viscous forces; Re characterizes the degree to which a flow is laminar or turbulent. Re less than 2,300 characterizes laminar flow, above 4,000 is turbulent with values in between considered transient.³⁷

Although not all of these descriptors are applicable to the NBC, optimization of these parameters has led to microfluidic architectures with the ability to perform separations, with detection elements designed in-stream, all on a small size scale, which make them highly compatible with next-generation analysis platforms.^{4, 5}

Microfluidics has followed a path roughly analogous to the microelectronics industry. In this arena, beginning with vacuum tubes, work to create intricate circuitry was initially extremely expensive, bulky, and inefficient. The creation of the transistor

effectively eliminated vacuum tubes, but because connections between transistors were still manually soldered, and these links were prone to failures.³⁸ In fact, the failure of even a single hand-soldered connection within the cascade could effectively paralyze the entire system; a situation analogous to the single burned out bulb on a strand of lights. To overcome this hurdle, the new paradigm of photolithography allowed transistors, as well as other resistors and capacitors, to be fabricated along with their respective connections, from single piece of substrate, earning Kilby the 2000 Nobel Prize in Physics.³⁹ While many researchers originally believed this paradigm could be neatly replicated for microfluidic structures, devices fabricated with silicon for biological applications were usually unnecessary or inappropriate.⁴⁰ Many teams discovered that the expense of silicon, even when mass fabricated, were difficult to reconcile with μ TAS systems. In addition, silicon is optically incompatible with the spectral regions usually employed for microanalytical systems. The cost, ease of fabrication, and elastomeric properties of plastics have ultimately made them the preferred underlying material for construction of POC devices. In addition, plastics such as poly-dimethylsiloxane (PDMS) are highly permeable to gases such as oxygen and carbon dioxide required for cell culture *in micro*.⁴¹

Microfluidics has yet to see a similar breakthrough piece of work as photolithography, or a “killer app” with highly profitable commercial success, although a number of critical advances and applications have demonstrated utility in a variety of experiments.^{35, 42} The scope of the field disallows any type of comprehensive review in this chapter, however a few key groups deserve mention. Whitesides’ work, beginning with fundamental studies of self-assembled monolayers,⁴³ helped define the ideal materials,³² coatings,⁴⁴ and designs needed to create microchannels and manipulate fluids, creating the potential to do a variety of chemical and biological analysis. The

identification of (PDMS) and poly(methylmethacrylate) (PMMA) as elastomeric materials for the underlying skeleton of microfluidic devices, and knowledge on handling of this material was critical to future successes.³²

Quake's work with microfluidics, leading to the formation of the Fluidigm corporation, has advanced the "large scale integration" of microfluidics, analogous to the electronics field.^{38, 45} By designing some of the first microfluidic devices with many integrated valves and other connections, this work has improved the capabilities of microfluidics for high throughput automation.³⁸ Micromechanical valves, created via multilayer soft lithography, allowed the binary positions of open and closed, but also a variety of positions in between which could be exploited as a peristaltic pump, or for mixing and sample/reagent volume allotment purposes.⁴⁵ This experimental design has been used to explore genetic⁴⁶ and protein⁴⁷ applications as well as the biophysical properties of single molecules. Quake's group was the first to successfully sequence a single DNA molecule.⁴⁸

Thus, a significant body of work created by these and other researchers, result in LOC systems that could perform biological assays on a miniaturized system. **Section 1.4** will describe some approaches that have further incorporated microfluidics with additional components of the laboratory such as signal transduction, including the few that have become compatible with clinical samples to glean meaningful information. Unfortunately, most applications are not fully freestanding and require extensive support networks of compressed gases and liquids, syringes and external pumps, as well as any necessary optics and light handling hardware. These systems are best described as "chips in a lab", rather than true labs on a chip.

1.3.3 Nanotechnology

Although nature has been creating elegantly controlled nanomaterials such as small molecules, antibodies, biomarkers, and the other life-inspired components described in **Section 1.3.1** for eons, it was not until approximately the last 20 years that the ability to design, synthesize, measure, characterize, and further manipulate materials below 100 nm has been fully realized.⁴⁹ One of the first and most popular types of nanoscale preparations are silver or gold nanoparticles.^{50, 51} These have found use in Raman scattering and surface plasmon resonance experiments, and numerous reports of nucleic acid conjugated nanoparticles appear in the literature.^{52, 53} Magnetic nanoparticles have also garnered attention as contrast agents in medical imaging experiments as well as underlying support for bio-barcoding designs.^{54, 55}

For the signaling requirements of the NBC, semiconductor nanoparticle quantum dots (QDs) have stood out as next generation fluorescent probes and one of the best examples of practical nanomaterials.^{56, 57} These inorganic compounds are synthesized from group II-VI elements through a number of synthetic routes with CdSe particles being the most common.^{58, 59} One or more passivation layers are generally coated around the fluorescent core serving to increase hydrophilicity, reduce agglomeration and increase fluorescence intensity, resulting in particles with diameters between 5-20 nm depending on the size of the original core semiconductor.⁶⁰⁻⁶⁴ **Figure 1.2A** shows the cross section of a typical commercially available QD and its onion-like structure resulting from the layers of core, clad, and coat. Attributes such as long-term photostability, high quantum yield, resistance to quenching, and narrow emission profile have made QDs a popular alternative to traditional organic fluorophores, which often suffer from photobleaching, broad bandwidth emission, and specific excitation ranges.^{65, 66} In contrast, QDs possess a broad excitation spectrum spanning the UV and near visible range, and their emission

wavelength is dependant solely on the size of the inorganic core with larger particles fluorescing closer to the IR and the smaller at shorter wavelengths (**Fig. 1.2D**).

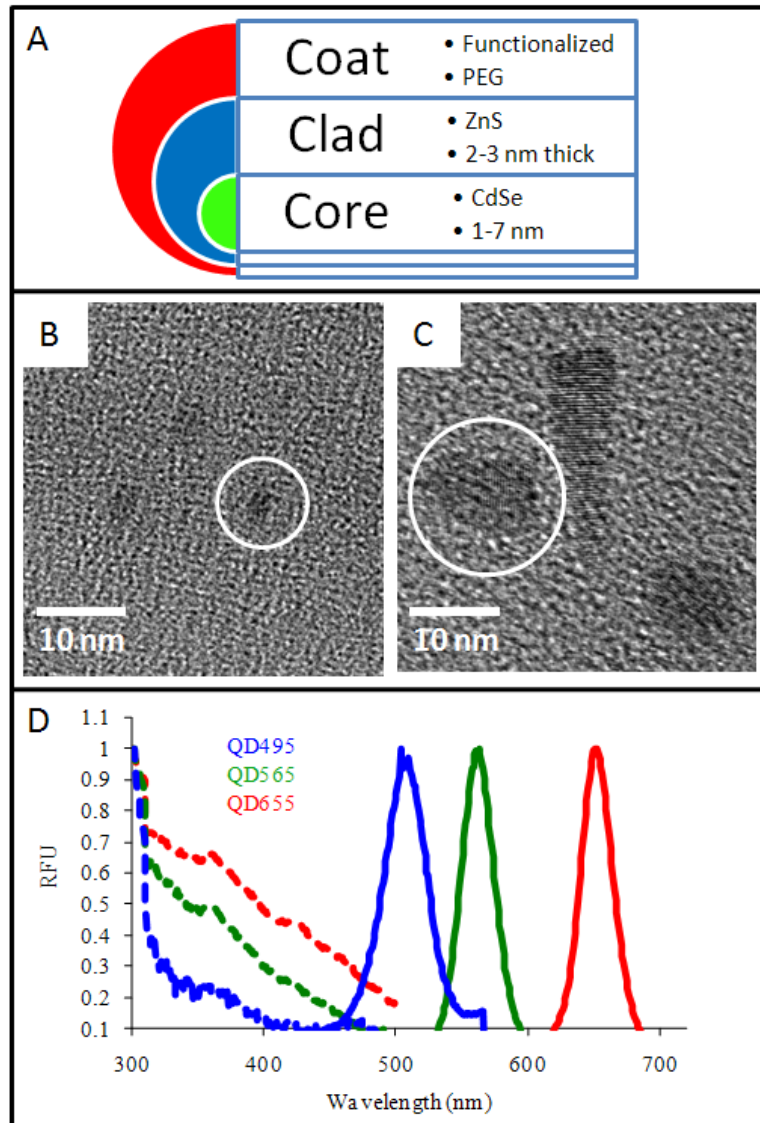


Figure 1.2. Quantum Dot Essentials.⁶⁷ **A)** Commercially available hydrophilic QDs consist of the fluorescent core semiconductor followed by a shell of passivation material designed to preserve structural integrity of the core and increase fluorescent signal and quantum yield. This is capped by an additional coat of polymer or other material to increase hydrophilicity and allow coordination of any additional chemistry. **B)** TEM images of QDs with peak emission at 495 nm show smaller nanoparticles than those in **C)** with λ_{em} of 655 nm. **D)** QDs size determines their λ_{em} with larger particles emitting more red shifted light. Nevertheless, all particles are easily excited in the UV, an ideal arrangement for multiplexed experiments. (Units in relative fluorescence units, RFU.)

Thus, QD's extremely long Stokes shift, combined with intense, narrow emission profiles and the ability to simultaneously excite a number of different size nanoparticles with characteristic emission wavelengths, have made them especially attractive for multiplexed experiments. In 2003, few designs harnessed the full capability of QDs, and those that did used them for qualitative imaging, rather than quantitative analysis. Nevertheless, these particles were gaining traction as strong candidates for signal generation in devices dedicated to a number of important diagnostic applications. *The above listed attributes of QDs, well established in 2003, yet not fully utilized in a biosensing platform, was a key motivator for their inclusion in the work detailed herein.* Parameters that needed empirical optimization include: the best method to conjugate QD to recognition elements, approaches to reduce non-specific binding and background while retaining high fluorescent signal in cellular and protein arrays, and schemes that reduce aggregation of the inherently hydrophobic QD material.

Nanoparticles with structures resembling today's definition of QDs were first described in the literature by Brus in the early 1980s.⁶⁸⁻⁷⁰ The term quantum dot was later coined in 1988 by Mark Reed of Texas Instruments because of the quantum confinement of the particles, that is, their behavior mimics many aspects of molecular and atomic systems, unlike bulk semiconductors.⁷¹ **Figure 1.3** explains this behavior graphically. Succinctly, the small size of QDs change the continuous energy levels found in bulk semiconductor material (**Fig 1.3A**), to a larger bandgap, and thus alters the distribution of energy levels found in nanoparticles to a discrete arrangement, similar to an atomic system. (**Fig. 1.3B**). Importantly, another physical definition of QDs is particles smaller than the Bohr exciton radius (**Fig. 1.3C**). The exciton is most simply defined as an excited state electron and the hypothetical, positively-charged hole particle. Coulomb forces attract electron and hole forming the short-lived exciton that disappears

upon collapse of electron from excited to ground state and subsequent release of a photon. To be considered QDs, the particles must have a diameter smaller than the distance between electron and hole.

Later research found that core/shell QDs behaved differently than their core counterparts with an increase in signal and stability all resulting from a coat of secondary semiconductor. Hines and Guyot-Sionnest found a ZnS layer to be particularly useful as its bandgap energy is higher than CdSe and thus can preserve the excited state of the CdSe core and prevent non-radiative relaxation.⁶⁴ Two breakthrough papers in 1998 published independently by Nie and Alivisatos opened the door for biological experiments—these demonstrations added an additional layer to the core/shell composite to create water soluble QDs, followed by scaffolding chemistry to attach a biological recognition element.^{72, 73} These nanoparticles have demonstrated use in such bioanalytical applications as Förster resonance energy transfer (FRET),⁷⁴ cellular imaging,⁷⁵⁻⁷⁷ immunolabeling,^{78, 79} and protein assays;^{80, 81} however it was not until 2004 that investigators, led by Mattoussi, from the Naval Research Lab published some of the first quantitative, multiplexed work with QDs.⁸²

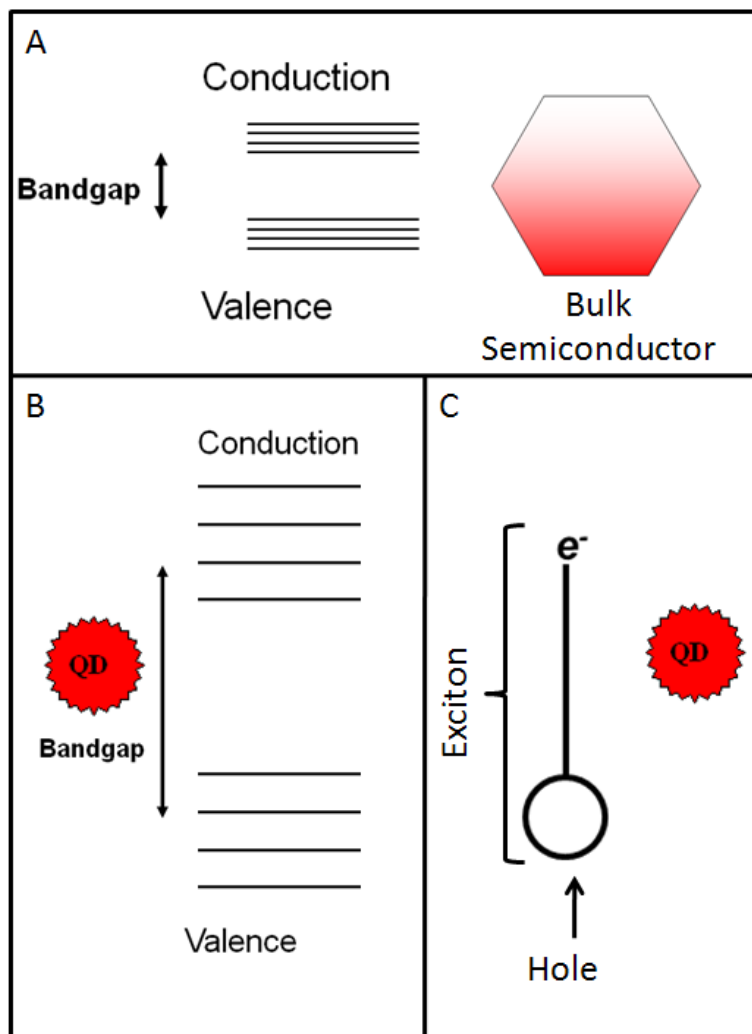


Figure 1.3. Quantum Dot Electronic Structure. **A)** Bulk semiconductor materials have a small bandgap and closely spaced, continuous energy levels both in the valence and conduction bands. **B)** As the physical dimensions of semiconductor materials are decreased, not only does the bandgap energy increase, but so does the difference between energy levels within valence and conduction bands. These increases eventually make the energy levels *discrete*, rather than *continuous*. **C)** The QDs have physical dimensions smaller than the Bohr exciton radius, creating a quantum confined situation.

A common scheme is seen in these biological QD applications. The first step in the pathway between signaling moiety and bioligand, is solubilization of the hydrophobic inorganic nanoparticle in an aqueous environment, which is usually accomplished via a

passivation layer, frequently a polymer coating, such as PEG or other charged moieties.^{60, 83, 84} As a colloidal suspension, any disorder in the monodispersity of this passivation layer creates flocculation and sedimentation of the QDs out of solution. Next, the hydrophilic QD is coupled to biological recognition moieties, such as antibodies, with all schemes emphasizing the importance of maintaining biological activity in the ligand, while simultaneously retaining the fluorescent advantages of the quantum particle.⁸⁵ Currently, conjugation strategies involve diverse reagents and methodologies, including electrostatic interactions,⁸⁶ avidin/biotin affinity,⁸⁷ and a variety of covalent techniques.^{88,89}

Of the latter, conjugation schemes abound, including 1-ethyl-3-[3-dimethylaminopropyl]carbodiimide/N-hydroxysulfosuccinimide (EDC/NHS) coupling of carboxyl coated QDs to free antibody amines,⁹⁰ creating free sulfhydryl on the biomolecule with succinimidyl 4-(N-maleimidomethyl)cyclohexanecarboxylate (SMCC) facilitating QD linkage,⁹¹ and hydrazine modified QDs with periodate oxidized antibodies.⁹² Common to all covalent conjugation schemes is a modification of both the antibody structure and of the QD surface, with an inherent risk to alter the recognition specificity of the biomolecule and fluorescence characteristics of the nanoparticle. The most appropriate method has shown to be dependent upon the specific end application and one important goal of this dissertation is to define the optimal conditions for inclusion of QDs into the NBC sensor array.

1.4 INTEGRATED SYSTEMS

Although the discovery of new biomarkers, advances in microfluidic condensation, and simpler synthetic approaches for nanoparticle bioconjugates are all valuable additions to the bioanalytical chemist's palette, the individual contributions of these unique elements pale when contrasted with the cogent elegance of rational,

integrated designs. As Ligler sagaciously observes in her recent perspective, ideal system designs are best described as Gestalt—the configuration of the whole possesses attributes unattainable by the summation of the individual parts.⁹³ Advances in design and molecular-level engineering that suggest certain systems are nearing *singularity*—complete unification of working parts for rapid, previously unattainable, advances in diagnostic relevance and access. Interestingly, this approach to systems building is in sharp contrast to many of the scientific and engineering challenges of decades past. Here, much work was on “scaling up” systems to synthesize or measure large amounts of material, while POC, microfluidic devices require *scaling down*.

Although this dissertation focuses on an optical, fluorescence-based approach to coherent medical sensors, researchers such as Corn and Van Duyne have done exemplary work with label-free techniques using the surface plasmon resonance (SPR)⁹⁴ and surface enhanced Raman spectroscopy (SERS).⁹⁵ There is also a large body of work using electrical and electrochemical signaling for biosensing.⁹⁶ In addition, a number of non-medical applications exist. Indeed, since 2001 the role of POC-type sensors as screening tools for chemical, biological, and radiological threats has increased dramatically.⁹⁷ Food, environmental, and narcotics applications expand further the contributions of integrated sensors and ever evolving advances continue to decrease assay requirements.⁹⁸ Despite the excitement of these other areas, the remainder of this treatise will focus on biomedical applications and *in vitro* diagnostics.

Sensors themed around human health, designed intelligently and rationally, *command quality* results. The easily remembered acronym COMMAND QUALS summarizes the most commonly cited attributes of coherently designed sensors and serves as wish list when designing POC diagnostic systems. All integrated approaches for use in both developed and resource-scare settings seek to create devices and assay platforms that are:

- **Cheap** - keeping costs low increases access to diagnostic testing
- **Obvious** - simple and easy user-interfaces allows use by unskilled operators
- **Miniaturized** - devices with reduced footprint are amenable to POC use
- **Multiplexed** - the ability to quantitate a number of different analytes concurrently increases the ability to effectively make diagnoses
- **Automated** - built-in sample processing, reagent handling, and data interpretation further promotes widespread access of diagnostic aides
- **Non-perishable** - rugged designs survive difficult storage, shipping, and handling as well as extreme temperatures; eliminating the so-called ‘cold-chain’ also increases access to such systems; 1 year half-lives are desirable
- **Dependable** - the design should have an extremely low rate of failure and be highly reproducible, similar to six sigma and GLP quality control designs
- **Quick** - short turnaround time (TAT) gives information to physicians quickly which is especially important in emergency room environments
- **Unobtrusive** - non-invasive diagnostic specimens and sampling procedures reduces patient testing antipathy, making regular screening events possible
- **Adaptable** – modular devices have the ability to quantitate a variety of analytes (cells, proteins, nucleic acids, small molecules, ions)
- **Limited** - small reagent and sample volumes decrease costs and minimize requirements of biohazard waste disposal and environmental impact
- **Self-contained** - reagent and power integration makes for a smaller device footprint; a closed system prevents exposure to biohazard waste

A variety of proposed systems meld nano, bio, and chip-based components into working systems with a high level of integration while featuring the above attributes. Several pioneers have performed landmark studies in the area. Whitesides' later work served to integrate advances in nanotechnology into existing systems and later proposed microfluidic structures constructed only of paper and tape.^{34, 49} Groups such as Mirkin's and Lieber's began to use nanowires,⁹⁹ precious metal nanoparticles,⁵² and nanolithographic techniques to measure diverse sample types and create a variety of assembly types.¹⁰⁰ Other designs, in which a capillary tube serves to not only direct fluid flow and serve as attachment point for biologands, but also serve as a waveguide for excitation beam and conduit for emission signal, illustrate the potential of high level integration.¹⁰¹

While the i-STAT[®] platform was the first sensor array to be microfabricated and vended commercially as a whole-blood diagnostic tool, it has had problems in establishing a dedicated manufacturing program and designing device packing in a reliable, user-friendly format.¹⁰² With a handheld analyzer costs between \$6,000 – \$10,000 and EC 8+ cartridges (Na⁺, K⁺, Cl⁻, BUN, glucose, pH, pO₂, and pCO₂) approximately \$15 apiece, this scheme remains inaccessible to the most disadvantaged regions. In addition, the i-STAT system has yet to be approved for more complex analytes such as protein biomarkers and lymphocyte discrimination.

Other assembled systems, while nearing completion, have not yet been released commercially. Work by Madou and others has resulted in the LabCD[™] which eliminates traditional valves and pumps by using centrifugal and centripetal force to perform fluid movements.¹⁰³ Similar, to audio and data compact disks, this model divides the diagnostics scheme into the disposable component (disk) and the instrument component,

the reader. As the LabCD™, is solid state, injection molding and other standard manufacturing techniques offer rapid prototyping at low cost.¹⁰⁴

Other relevant prior work for this dissertation research includes the contributions of Walt and coworkers. Walt's work with "electronic noses" in which arrays of optical fibers serve as the underlying infrastructure for biological sensing systems.¹⁰⁵ With this underlying fiber substrate in place, a variety of secondary schemes can be used including the placement of beads for analysis arrays.¹⁰⁶ Live cells can be loaded into the arrays, and their unique response monitored over time, enabling cytotoxicity screening of biologically active substances. Alternatively, individual enzymes immobilized on the fiber substrate allow detection of single molecules via enzyme-catalyzed signal amplification.¹⁰⁷

Despite this plethora of advances, the field of usable and FDA-approved miniaturized biological sensors is still in its infancy and experience many challenges, mostly because only a small part of the analysis scheme is actually 'micro' in nature.

- Upon moving from microfluidic *components* to analysis *systems* the success of microscale fluid handling may disintegrate. Actual clinical analysis via microfluid ensembles frequently require external pumps, valves, and fluid handling and these systems are best described as "chips in a lab" versus true labs on a chip.¹⁰⁸
- The pumps, valves, and other fluid manipulators with demonstrated capacity, used in conjunction with other external support structures, are frequently only validated with highly controlled fluids, not the diverse range of samples likely to be encountered in routine testing.⁹³
- Modular systems, attuned to the requirements of diverse samples types (whole blood, plasma, urine) and analyte forms (cells, ions, proteins, nucleic acids), have yet to emerge.¹⁰⁹ These LOC systems generally have one analyte (or small number of similar analyte types, i.e. ions) per chip. Improving the number of applications that may be performed on a single system is key.

- The lack of unified sample metering and processing, within the confines of the LOC structure, retards the development of deployable systems. Methods to selectively isolate plasma, specific cell types, or cell lysate from a sample are incomplete and are nearly always performed off-chip.¹¹⁰
- Refuse handling remains ill defined and the engineering of disposable LOC components is needed to prevent exposure of healthcare workers and the citizenry at large to the potentially dangerous waste of biomedical testing.¹¹¹
- Finally, very few integrated systems are sensitive to the increasingly budget-conscious nature of health care both in the developed world and in resource-scarce settings and the changes that are occurring to health budgets in the 21st century.¹¹²

Indeed, POC diagnostic devices need be cheap in *both* developed and developing reasons. Currently, nearly 90% of global healthcare expenditures are spent on approximately 10% of the population. In the United States, per capita health care costs are \$7,439 annually, while in certain African nations, this expenditure drops below ten US dollars.¹¹³ Furthermore, this rate is increasing at a rate of between 7 and 8 percent annually, a unsustainable percentage much higher than that of inflation.¹¹⁴ Even within the resource-heavy US population, a tiny subset of the population consumes the majority of healthcare resources. Five percent of the population consistently use 50 percent of the healthcare budget and the last week of life is often the most expensive.¹¹⁵ One reason this select subset takes such a large slice of the ‘healthcare pie’, is their frequent need of clinical laboratory testing. Thus, both the *lack* of resources in underdeveloped countries and the *disparity* of resources with the United States are strong motivators for the development of cost-effective POC diagnostic and prognostic schemes.

Although the fundamentals are in place to solve these daunting problems, other challenges of science, technology, and engineering linger. Proper identification of initial applications and finding flexible strategies to move the technology from the laboratory to the marketplace remain inadequate.⁴⁰ Products reaching commercialization often remain

out of the reach of end users or those most in need due to insufficiencies in cost, durability, ease of use, their need for support infrastructure, and the resistance of pertinacious clinicians and healthcare administrators to emerging technology. Ultimately solving the defects of design will require knowledge integration from diverse backgrounds and the utilization of a variety of ideas. The work below with programmable NBC systems works to fulfill some of these deficiencies.

1.5 McDEVITT GROUP INTEGRATED APPROACH—THE PROGRAMMABLE NBC

For over a decade, the McDevitt, Neikirk, Shear, and Anslyn research groups have sustained work utilizing microelectromechanical structures (MEMS) for studies of the design, fabrication, and testing of microfluidic structures with integrated fluid handling and optical detection capabilities.¹¹⁶ Inspired by the microelectronics industry that has created ever cheaper manufacturing methods for electronic components that scale and adjust to the desired application, this team has developed two highly functional NBC sensor ensemble approaches. Created with many of the same microfabrication methods popularized by the electronics industry, the first such sensor system can be described as a “chemical processing unit” and serves for the measurement and collection of soluble analytes. More recently, a second class of miniaturized sensor system, based on a membrane capture element that is integrated into a fluidics structure, emerged.¹¹⁷⁻¹¹⁹ These “cellular processing units” serve as miniaturized analysis systems that mimic flow cytometry (FC) instrumentation in their capacity to complete vital cell collection, processing, labeling, image and counting applications from complex biofluid samples such as whole blood. In both NBC types, a closed system allows these specific analytes to be immobilized from complex matrices and quantitated via a colorimetric or fluorescent signal. In **Figure 1.4A**, the rudimentary, research-grade NBC system is illustrated in profile. This research-grade system serves to optimize assays and is used in

tandem with the benchtop analysis components seen in **Figure 1.4B**. The epifluorescent microscope and peristaltic pump, both digitally controlled, form the support structure of this NBC system. More elegant condensations of these components will be subsequently described in greater detail.

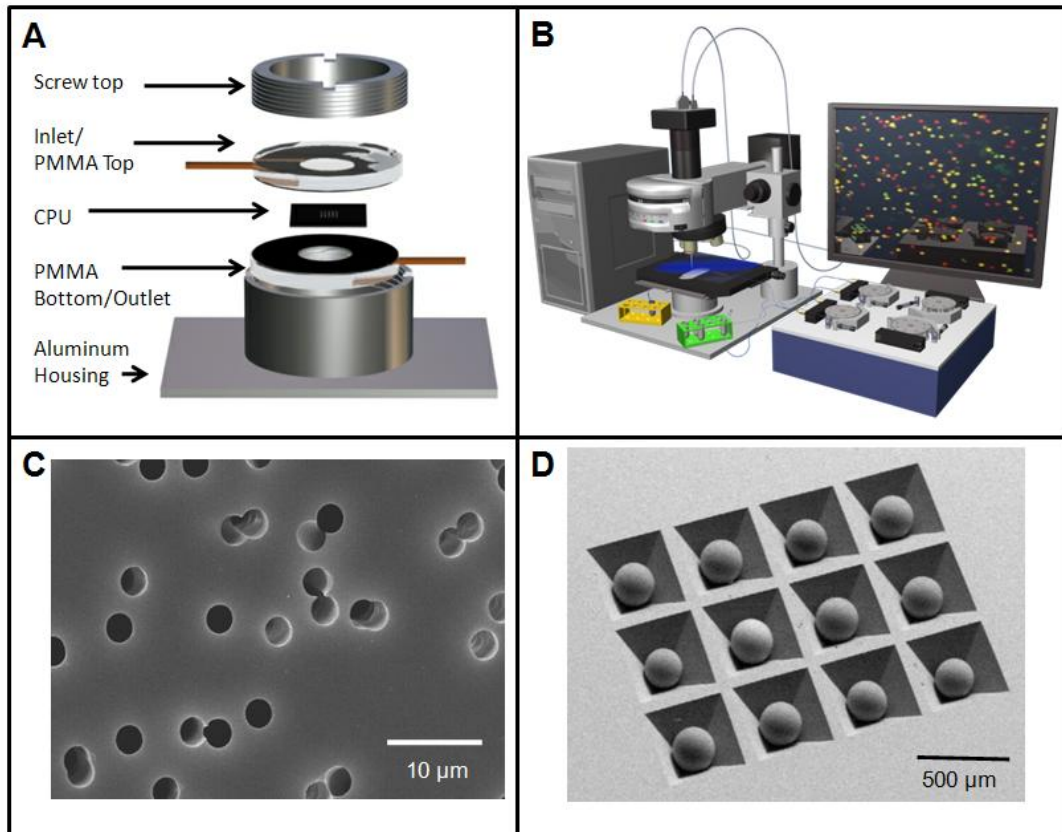


Figure 1.4. Nano-bio-chip Design. **A)** The research-grade NBC used these studies consists of an aluminum housing with a central processing unit sealed between PMMA layers designed to direct fluid flow. **B)** The benchtop support equipment used in conjunction with research-grade NBC includes a modified epifluorescent microscope with CCD digital camera as well as a peristaltic pump fluid delivery system. **C)** For membrane-based NBC experiments, a polycarbonate track-etched membrane is used. Pore diameter is determined by analyte size. **D)** In bead-based experiments, agarose microspheres form the underlying infrastructure. Any number of chemistries may be performed to make the beads selective for proteins, ions, or small molecules.

Analyte Class	Examples	Range/LOD	Gold Standard	Agreement	Sample Matrix	Ref.
Simple Cations	H ⁺ , Ca ²⁺ , Citrate	2 < pH < 12 10 ⁻⁷ M	ISE	R ² = 0.999	Serum, Buffer	116, 120
Small Molecules	Saccharides, ATP/ADP	20 mM	ELISA	N/A	Buffer	121, 122
Peptides	Tachykinin, Neurokinin	N/A	EIA	N/A	Buffer	123
Nucleic Acids	DNA-18mer	10 ⁻¹³ M	PCR	N/A	Buffer	124
Spores	Bacillus	N/A	Culture	N/A	Bioaerosols	119
Cytokines	TNF- α , IL-1 β , IL-8	1 ng/mL	ELISA	N/A	Serum, Saliva	
Cells	CD3, 4, 8, 56; Lymphs., Monos., CBC, Epithelial	50 – 15,000 cells/ μ L	Flow Cytometry	R ² = 0.98	Whole Blood	117, 125
Biomarkers	Cardiac: CRP, MPO, cTnl Cancer: CEA, CA125, Her-2/Neu	10 pg/mL CRP 0.11 pM CEA	ELISA, Benchtop Analyzers	R ² = 0.987	Serum, Plasma, Buffer	126-128
Assays Completed: CRP, Myeloperoxidase, Soluble CD40 Ligand (sCD40L), Monocyte chemoattractant protein-1 (MCP-1), Human serum albumin, Cardiac troponin I (cTnl), D-dimer, Apolipoprotein A1 (apoA1), Apolipoprotein B (apoB), Tumor necrosis factor-alpha (TNF-alpha), Interleukin-6, Interleukin-1beta, Transferrin, Amylase (with scFvs), Total human IgE, Allergen specific human IgE (~ 8 allergens), Brevetoxin (competitive), Myeloperoxidase (MPO), Aflatoxin B1 (competitive), Matrix metalloproteinase 8 (MMP8), MMP9, B-natriuretic peptide (BNP), HepB-specific IgG, p24 antigen (proof of principle)/competitive, gp125-specific human IgG, Her-2/ <i>neu</i> , Carcinoembryonic Antigen (CEA), Cancer Antigen 125 (CA125)						

Table 1.2. Assays Demonstrated on NBC Device. A wide variety of sample and analyte types have been incorporated into the McDevitt NBC analysis scheme. All of these assays were performed using a traditional molecular fluorophore or a conventional colorimetric assay. This dissertation seeks to detail analytical improvements available via QDs. (Green inset lists all assays with proof-of-principle on NBC)

Sample types amenable to the NBC include, but are not limited to, serum, plasma, saliva, whole blood, as well as environmental samples. These structures have been shown to be suitable for the identification and quantitation of C-reactive protein,¹²⁷ other cardiac risk markers,¹²⁸ pH, and physiologically relevant cations.¹²⁹ More recently

work has progressed to develop miniaturized microfluidic systems that service cellular analysis applications.¹²⁵ These membrane-based micro-systems have been shown to be suitable for the determination of lymphocytes for HIV immune function and total white blood cell counts for cardiac risk assessment.^{117, 130} **Table 1.2** illustrates with more detail the breadth and depth of the NBC approach to measuring biologically important analytes.

Although this work with NBC systems has been established for well over a decade as illustrated in **Table 1.2**, recently, a new paradigm has evolved from the initial LOC-type, “electronic taste chips”¹²⁹ to state-of-the-art, integrated NBC systems.¹³¹ The NBC ensemble employs a size-tunable nano-net within agarose microspheres or polymer membrane, and a fluorescent transduction signal arising from nanoparticles (nano) to isolate and quantify biological analytes (bio) from complex matrices within a closed, miniaturized system (chip). The modular NBC used in this work employs two central reaction unit types, each tailored to application. First, a bead-based platform consisting of individually addressable agarose beads functionalized with specific chemistry types and immobilized within a customizable, etched silicon chip has been employed for the quantitation of proteins, including cancer biomarkers (**Fig. 1.4D**). Second, membrane-based experiments (**Fig. 1.4C**), utilizing a size exclusion device, have been employed to sequester and count blood cells.

These NBCs combine the sample handling abilities and reduced sample requirements of microfluidics with the attributes of nanomaterials to quantitate both established and emerging biomarkers. This system analyzes complex samples such as blood, plasma, saliva, as well as environmental samples. An important difference between the NBC systems of the previous generation, and the current NBC design is that signal output is accomplished via semiconductor nanoparticle quantum dots (QDs). Both the bead and membrane-based approaches are part of a much larger effort within the

scientific community towards miniaturized and portable biomedical devices that offer diagnostic and prognostic information rapidly, cheaply, and robustly. **Figure 5** details some of the considerations and essential pieces of the analytical machinery needed when designing the NBC. Biomedical devices need have these characteristics to meet the demands of clinicians, practitioners, and academicians alike.

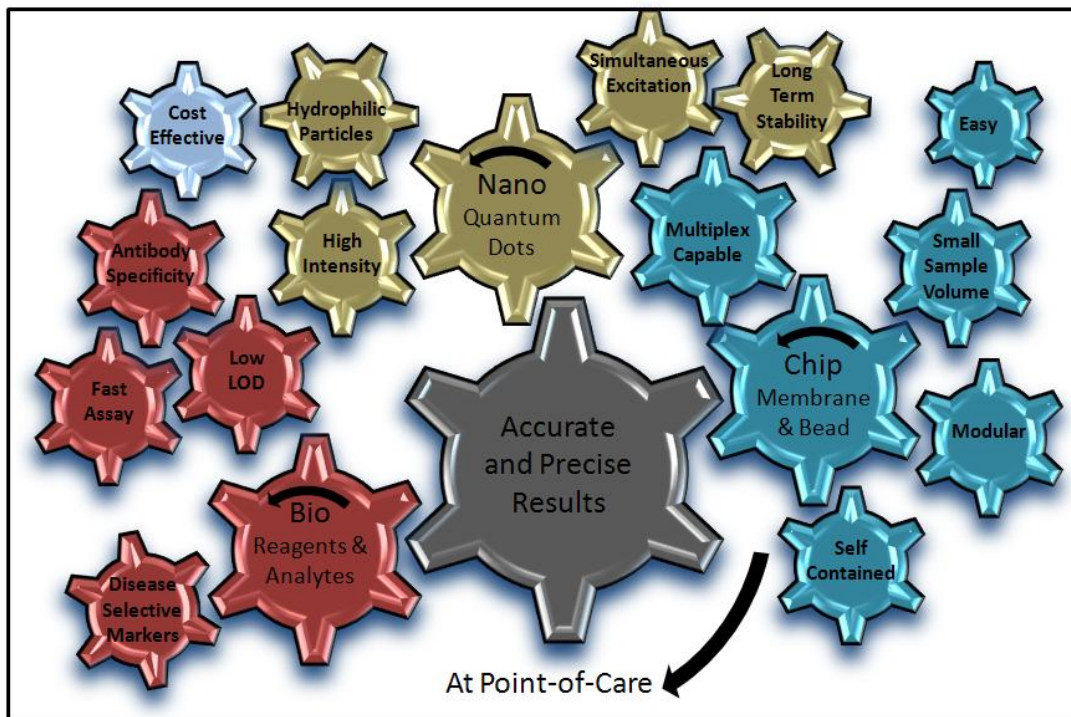


Figure 1.5. Essential Elements of the NBC for POC Assays. The nano-bio-chip contains attributes and design contributions from three key areas: biomarkers of disease and biological reagents/controls, nanometer size fluorescent tags and the nano-net formed within the agarose microspheres, and the microfluidic cartridges that focus fluid flow and contain reagents and waste. All must synchronize to achieve reliable results that meet the COMMAND QUALS descriptors.

1.6 SUMMARY AND DISSERTATION OVERVIEW

Definitive solutions for all the challenges listed in **Section 1.4** is beyond this period of study, however this dissertation will explore both membrane and bead-based uses of the NBC in tandem with QD nanoparticles for improvements to biological determinations and assay development. Although each chapter will have specific aims, the dissertation as a whole seeks answers to the following fundamental questions:

- Which QDs (size, source, passivation method) offer the most robust signal?
- What are the best conjugation methods to link QDs to recognition bodies while retaining both nanoparticle attributes and bioligand specificity?
- How can non-specific binding and aggregation of QDs be reduced/eliminated?
- Which optical components are best suited to the NBC?
- How do QDs behave relative to traditional, molecular fluorophores in term of photostability and signal intensity?
- How is the QD signal best interpreted?
- How can QDs improve the multiplexing capabilities of the NBC system?
- How can very low limits of detection be achieved with the NBC?
- Which antibodies and bead types are best suited to our assays?
- What is the best method to capture and detect proteins in small channels?

Chapter 2 details a membrane-based platform for the analysis of T lymphocytes in HIV patients, crucial as the enumeration of such CD3+CD4+ cells is required to establish the level to which the immune system has been compromised. After initial experiments for optimization of labeling efficiency and flow parameters, cells were exposed to primary antibody specific to CD3 and CD4 followed by QD-labeled secondary antibodies specific to the primary. With CD3 coded red and CD4 in green, the dually stained T lymphocytes are detected and quantitated using custom automated image

analysis algorithms, with QDs allowing for simultaneous excitation of differently colored nanoparticles resulting in a reduction in overall analyzer footprint. This effectively cut the optical requirements in half, as molecular fluorophores, such as Alexa Fluor dyes, require filters specific to each color channel. Furthermore, in a side by side comparison, cells labeled with Alexa Fluor probes displayed exponential signal decay within minutes, unlike their QD counterparts.

Chapter 3 describes how the NBC system may be used as a bead-based sensor for protein biomarker determinations in clinical samples including serum and saliva. For this study, three previously identified analytes were chosen: carcinoembryonic antigen (CEA), Her-2/*Neu* (c-erbB-2), and cancer antigen 125 (CA125), markers which have shown correlation to colon, breast, and ovarian cancers, respectively. The multiplexing capabilities of the system were explored from both an intra-bead and inter-bead standpoint. First, beads functionalized to CEA and CA125 capture antibodies were compared to beads dually loaded with both. These dual-type beads have the capability to further increase the NBC output by allowing an even greater number of analytes to be bound and quantified in our small device area. Second, in a demonstration of signal specificity, beads sensitized to CEA, Her-2/*Neu*, and CA125 were exposed to each antigen individually, followed by a cocktail of detecting antibody; the majority of signal comes from the specific interaction with non-authentic output emanating from the untargeted beads. This multiplexing approaches are critical as few cancer biomarkers have complete specificity or specificity for their respective disease.

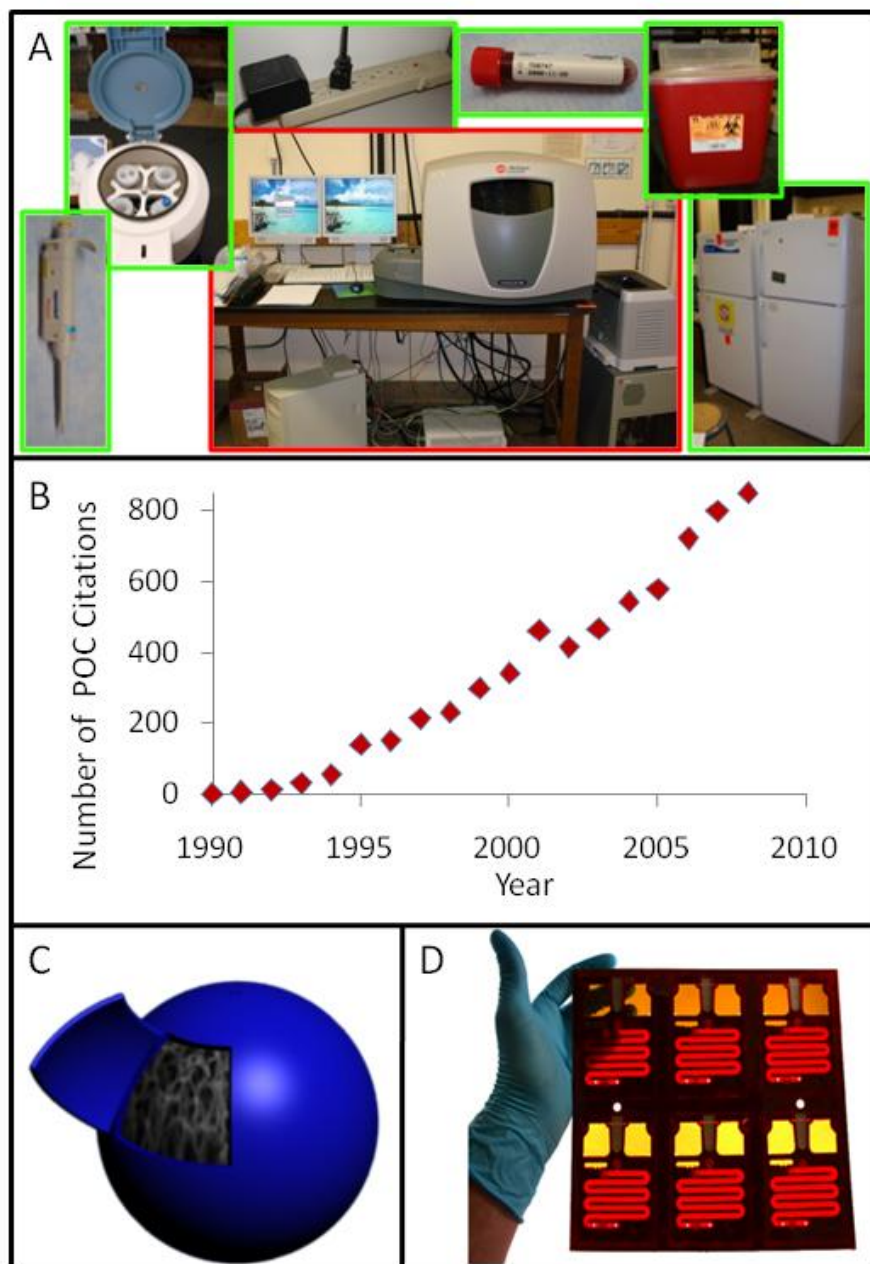


Figure 1.6. Motivation and Direction. A) Current laboratory designs include a bench-top instrument with fluid handling, electrical, waste, and refrigeration supporting instrumentation. In contrast, POC-type systems work to condense this entire lab infrastructure into a small, device with COMMAND QUALS descriptors. The strong trend toward POC systems is illustrated in B. C) This dissertation will explore the core subcomponents of the NBC system with work targeting singularity in a truly integrated POC device (D). (Fig. 1.6B constructed via the number of returns on a search for “point of care” in SciFinder Scholar[®] literature service.)

Chapter 4 employs confocal fluorescent microscopy, proteolytic digestion, and tunable agarose porosity systems to better understand the distribution of the various elements composing the immunoassay throughout the bead. By reducing both capture and detecting fluorescently tagged antibodies from whole IgG molecules to smaller Fab and F(ab')₂ fragments control of signal dissemination was explored. Additional experiments varied bead porosity via agarose percentage to optimize efficiency of immobilization and the results from such a nano-tailored system reveals the importance of size and concentration considerations in designing immunoassays.

In summary, this dissertation probes the areas of applied nanomaterials, biosensors, and clinical indicators of disease, all within the framework of experiments designed to analytically improve performance of the NBC and validate it as a diagnostic device versus established systems. Extensive characterization of QD nanoparticles as fluorescent probes yielded key information necessary for their inclusion in both cellular and protein experiments. Immunoassay development and microfluidic design as well as established analytical techniques including flow cytometry and protein assays were used as tools to understand better complex questions about protein and cellular capture and signaling as well as the ideal parameters to measure these systems within the NBC.

Chapter 2: Integration of Semiconductor Quantum Dots into NBC Systems for the Enumeration of CD4+ T Cell Counts

2.1 CHAPTER OVERVIEW

Recent humanitarian efforts have led to the widespread release of antiretroviral drugs for the treatment of the more than 33 million HIV afflicted people living in resource-scarce settings. Here, the enumeration of CD4+ T lymphocytes is required to establish the level at which the immune system has been compromised. The gold standard method used in developed countries, based on flow cytometry, though widely accepted and accurate, is precluded from widespread use in resource-scarce settings due to its high expense, high technical requirements, difficulty in operation-maintenance and the lack of portability for these sophisticated laboratory-confined systems. As part of continuing efforts to develop practical diagnostic instrumentation, the integration of semiconductor nanocrystals (quantum dots, QDs) into a portable microfluidic-based lymphocyte capture and detection device is completed. This integrated system is capable of isolating and counting selected lymphocyte sub-populations (CD3+CD4+) from whole blood samples. By combining the unique optical properties of the QDs with the sample handling capabilities and cost effectiveness of novel microfluidic systems, a practical, portable lymphocyte measurement modality that correlates nicely with flow cytometry ($R^2 = 0.97$) has been developed. This QD-based system reduces the optical requirements significantly relative to molecular fluorophores and the mini-CD4 counting device is projected to be suitable for use in both point-of-need and resource-scarce settings.

2.2 INTRODUCTION

Of the more than 33 million people infected with HIV globally, more than 85% live in developing countries with significant resource limitations.¹ While portable lateral immunoassay kits are available and can be used to diagnose patients with HIV, a missing

link remains with respect to the treatment and management of HIV patients in these developing countries. As HIV infection progresses into active AIDS, clinicians must frequently monitor the patient's CD4+ T lymphocytes to assess the degree of immunological deterioration.^{132, 133} According to Center for Disease Control and Prevention guidelines, absolute T-cell counts of 200 cells/ μ L or 14% CD3+CD4+ are reference values at which HIV is considered to become active AIDS.^{134, 135} These cellular assessments require a dual staining signaling approach to identify and differentiate between the two different CD markers of interest, and are typically obtained on flow cytometers (FC), or on double platforms involving FC and hematology analyzers.

Although such instruments are widely available in the United States and in other affluent regions, in resource-scarce settings, access becomes difficult or impossible. Frustratingly, these settings may frequently have *noblesse oblige* stockpiles of anti-retroviral drugs available, but because T lymphocyte testing remains out of reach, it is not until patients begin developing advanced symptoms of AIDS that clinicians become aware of whom to dispense the medications. **Figure 2.1** illustrates the distribution of HIV positive individuals throughout the world. Noticeably, the region with the largest percentage of positive individuals i.e. sub-Saharan Africa, is also a region without broad access to diagnostic laboratories.

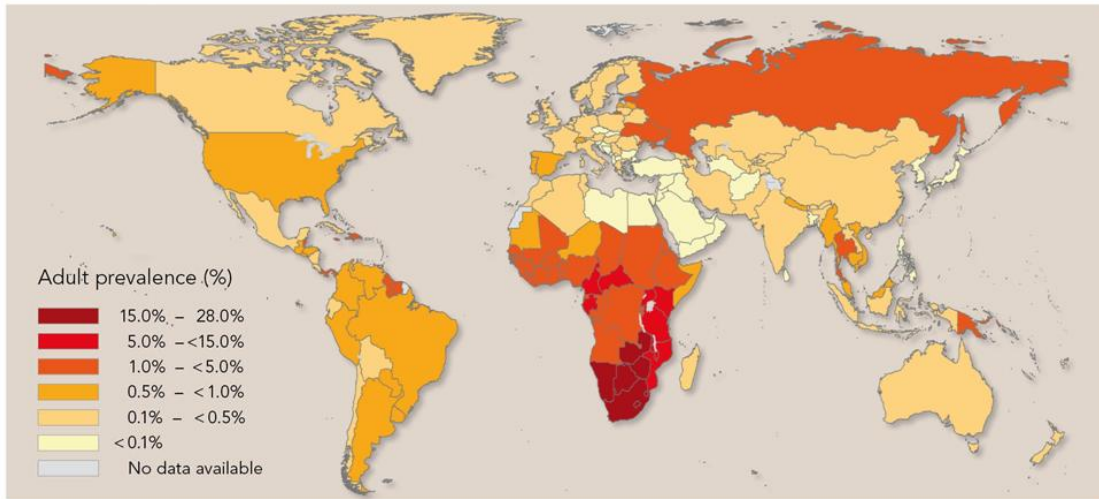


Figure 2.1. Distribution of HIV positive individuals. The highest rates of HIV infection are found in sub-Saharan Africa, a region also known for scarcity of biomedical infrastructure. In these areas, the unmet clinical need is access to diagnostic testing. (Reprinted with permission of UNAIDS. Copyright 2008.)

To fill this unmet clinical need, a number of more compact FC instruments have been developed such as Guava EasyCD4 and the PointCare instrument, however, these alternative flow methods have not been widely adopted.^{136, 137} Nonflow alternatives have also been developed based on impedance, microfluidics, or magnetic beads, yet these methods suffer from lower throughput and more labor-intensive manipulations.¹³⁸⁻¹⁴² These alternatives are also less accurate than FC and have not received endorsement from the World Health Organization^{138, 141}

In this area, the development of increasingly smaller bio-analysis devices is attractive for several factors including enhanced portability, decreased sample size, and reduced turnaround times.^{28, 31, 143, 144} Nano-bio technologies, advanced microfluidics and lab-on-a-chip sensor systems offer interesting and exciting new prospects for these humanitarian diagnostic challenges. However, despite the remarkable advances in the development of miniaturized sensing, and analytical components for use in a variety of

biomedical and clinical applications, the ability to assemble and interface individual components in order to achieve a high level of integration in complete working systems continues to pose daunting challenges for the scientific community as a whole. For example, the optical requirements present in many miniaturized systems frequently challenge their development. Fluorescence, as a common transduction analytical signal, presents unique opportunities, as well as demands, in a miniaturized assay platform. A robust excitation source, used in conjunction with ideal reagent components, to generate a strong target-specific signal and a reduced non-specific background, is crucial for the miniaturized system's ability to detect the intended target with sensitivity and accuracy. Current efforts on these challenges include advanced excitation sources such as lasers and powerful light emitting diodes (LEDs), miniaturized charge coupled devices (CCDs), as well as next generation fluorophores.

Here, QDs are an ideal fit. Their extremely long Stokes shift combined with narrow emission profiles and the ability to simultaneously excite a number of different size nanoparticles with characteristic emission wavelengths, make QDs ideal fluorophores for multiplexed experiments such as CD3+CD4+ dual labeling. This work was also literature-inspired, as QDs have previously been demonstrated to label cells for cancer biomarkers and other biologically interesting molecules.^{79, 145} In addition, experiments with lymphocytes on microscope slides labeled with QDs have demonstrated the feasibility of such labelings.¹⁴⁶ The clinical chemistry and biomedical engineering challenge is the *integration of the optical properties of QDs into a useable POC device while retaining the previously demonstrated capability of the NBC platform to count circulating cellular disease indicators.*^{118, 147}

Working to advance another generation in overall device condensation, we describe the integration of nanoparticle QDs into a LOC sensor system for the

determination of CD4⁺ T lymphocytes using unprocessed whole blood samples. These efforts synergize developments in the nanomaterials and microfluidics communities to simplify the optical requirements and engineering demands of LOC systems, and the advances in performance achieved by the NBC bring the release of diagnostic tools to resource-poor settings an additional step closer towards realization. In this chapter, efforts are devoted to creating a bridge between QD-based detection methods and the integrated membrane-based NBC systems. The efforts strive to relieve the optical requirements and reduce the overall engineering demands for both the integrated NBC sample processing modality along with the associated fluorescence-based detection system. Specifically, the photostability of QDs and the ability to excite and image two different colors concurrently with a single epifluorescent arrangement are exploited to reduce the optical pathway and thus decrease the overall analyzer size. These efforts strive to bring these evolving diagnostic tools an additional step closer to widespread use in resource-scarce settings.

2.3 MATERIALS AND METHODS

2.3.1 Reagents and Samples

Primary mouse antibody specific to CD3 from OEM (Clone 289-13801 (UCH-T1), Toms River, NJ) and rat antibody to CD4 from Genetex (Clone YNB46.1.8, San Antonio, TX) were purchased and centrifuged briefly prior to use. Goat anti-mouse secondary antibody conjugated to QD with peak fluorescence intensity at 655 nm (QD 655), goat anti-rat QD 565, and goat anti-mouse QD 565 were similarly obtained from Invitrogen (Carlsbad, CA). Also from Invitrogen were amine-PEG activated QDs, streptavidin coated QDs, biotinylated QDs, and carboxy activated QDs. Alternative sources of nanoparticles that were investigated include PlasmaChem (Berlin, Germany), and Evident Technology and their distributor eBioscience (San Diego, CA). For

comparison studies goat anti-mouse Alexa Fluor 647, goat anti-mouse Alexa Fluor 488, and goat anti-mouse FITC (Invitrogen) were also procured.

Modified Dulbecco's phosphate buffered saline (PBS) at a concentration of 0.008M sodium phosphate, 0.002M potassium phosphate, 0.14M sodium chloride, 0.01M potassium chloride, pH 7.4, from Thermo Scientific (Rockford, IL) was used as diluent for all solutions. To prevent non-specific binding, Fraction V bovine serum albumin (BSA) from Sigma Aldrich (St. Louis, MO) was added at 1% by weight. All buffers were filtered by a 0.2 μm Nalgene Supor mach V membrane. Fluorophore and antibodies at immunolabeling concentrations were again filtered immediately before injection into NBC with a 4mm 0.2 μm nylon syringe filter (Whatman).

Fixative and FC reagents were also acquired from Becton Coulter (Fullerton, CA). InSpeck™ calibration beads with a green-channel fluorescence fingerprint similar to that of FITC, and reagents for a SMCC and EDC/NHS facilitated conjugation were purchased from Invitrogen and Thermo Scientific via Pierce (Rockford, IL), respectively. Here, intact IgG molecules were subjected to dithiothreitol (DTT) treatment to cleave disulfide bonds. The SMCC-activated QD particles were then incubated with the reduced antibody fragments linking them to the nanoparticles. The conjugate was purified by size exclusion chromatography to remove unbound antibody and concentrated with 50 kD cutoff centrifuge tubes to approximately 1 μM . For Alexa Fluor labeling, monoclonal antibodies were labeled via a tetrafluorophenyl activated form of the fluorochrome. The EDC/NHS conjugation was performed as described previously.⁷⁶ For indirect linkages, biotin functionalized Protein A from Calbiochem (San Diego, CA), Sulfo-NHS-LC-Biotin (Pierce), and Zeba™ desalting columns (Pierce) were purchased and used according to manufacturer's instructions. Whole blood samples were collected from anonymous donors at the University of Texas at Austin in accordance with Institutional

Review Board procedures by standard venipuncture technique using dilute EDTA as an anticoagulant. Samples were evaluated within 24 hours of collection.

2.3.2 NBC Construction

The aluminum housing used in the first generation NBC was machined in house as was the polymethyl methacrylate (PMMA) base for second generation NBC. PMMA top and bottom layers for the first generation were also constructed at UT Austin. Stainless steel support frits were photofabricated and treated with a non-reflective coating. Vinyl adhesive layers from 3M (Minneapolis, MN) were precision-cut according to evolving computer-aided designs via AutoCAD drafting software from AutoDesk (San Rafael, CA) and served to focus fluid flow through the nucleopore track-etched membrane from Whatman/GE Healthcare (Piscataway, NJ). Stainless steel conduits were purchased from Small Parts, Inc. (Miramar, FL). Each unit was typically assembled in under five minutes. The research prototype was used in conjunction with a customized optical station.

2.3.3 Optical Station

This NBC was secured beneath an infinity corrected 10X objective and analyzed with a modified epifluorescent microscope from Olympus (Center Valley, PA) equipped with a 12 bit CCD camera from DVC Co. (Austin, TX) and high pressure mercury bulb excitation source, which was evaluated with a universal optical power meter from Melles Griot (Albuquerque, NM). Sample flow was controlled by a variable speed peristaltic pump from FIALabs (Seattle, WA) with a 500 μ L sample loop. The QD 565 images were acquired with a filter cube consisting of a 425 nm downfield excitation filter, a 475 nm long pass beam splitting dichroic mirror, and a 565 \pm 10 nm emission filter. The QD 655 images were obtained via a 420 \pm 20 nm excitation filter, a 475 nm long-pass beam splitting dichroic mirror, and a 655 \pm 10 nm emission filter. When these two

fluorophores were to be visualized concurrently, a 350 ± 25 nm excitation filter, a 475 nm long-pass beam splitting dichroic mirror, and a 520 nm long-pass emission filter were employed (please see **Appendix A**). Alexa Fluor 488 was viewed via a standard FITC filter cube: 480 ± 20 nm excitation filter, 505 nm long-pass beam splitting dichroic mirror, and a 535 ± 25 nm emission filter. Alexa Fluor 647 was viewed via a standard cytochrome-5 filter cube. Photomicrographs were captured via DVC software with adjustable gain, offset, and exposure time, and stored for later analysis.

2.3.4 Cell Immunolabeling

Aliquots of 50 μ L from a thoroughly homogeneous whole blood reservoir were briefly treated with 5 μ L Cytochex fixative from Streck (Omaha, NE) before dilution to 1 mL with 1% bovine serum albumin in phosphate buffered saline (PBS/BSA) purchased from Sigma Aldrich (St. Louis, MO) and Thermo Scientific (Waltham, MA), respectively. The prepared sample, at 500 μ L volume, was injected into the NBC with a flow rate sufficient to separate the lymphocytes from the remaining blood components. The sample was then subjected to a 500 μ L treatment of 10 μ g/mL primary antibody at a flow rate of ~ 17 μ L/min for 10 minutes. Unbound antibody was subsequently removed with PBS rinse at which point 500 μ L of 10 nM secondary antibody was introduced, incubated, and rinsed similarly to the conditions described above. Alternatively, this labeling could be performed in microcentrifuge tubes prior to delivery to the NBC; total assay time was under 30 minutes. For SEM images, the membrane was removed from the NBC and fixed with 4% glutaraldehyde followed by ultrapure water washes. This was additionally stabilized with OsO₄ and hexamethyldisilazane (HMDS).

As a reference method, flow cytometry data was collected on a Beckman Coulter (Fullerton, CA) Cytomics FC 500 flow cytometers using protocol provided by the manufacturer. Aliquots from the same blood reservoir were prepared with Immuno-

Prep™ lysing reagents (Beckman Coulter) and labeled with CD3-Alexa Fluor 488 and CD4-Alexa Fluor 647 (Invitrogen). Immuno-Trol™ and Cyto-Comp™ standards and Flow-Count™ calibration microspheres (Beckman Coulter) as well as mouse IgG negative control Alexa Fluor 647 and 488 from Serotec (Raleigh, NC) were used for negative control experiments and instrument calibration.

2.3.5 Image Analysis

Image analysis was performed with ImageJ analysis software from the National Institutes of Health (Bethesda, MD.)¹⁴⁸ Raw color photomicrographs were split into their individual RGB components as 8-bit grey-scale images to identify the different lymphocyte subsets. This technique allowed a single image collected with the long-pass filter to give information on two different color channels. Pixels were then thresholded to a value 2 standard deviations above the mean of all. The resulting image contained pixels having a value of either 0 or 255. Thresholded areas were then subjected to a ‘watershed’ filter to separate any overlapping lymphocytes and analyzed in terms of size and circularity with these regions defined as an area of interest (AOI). These AOIs were utilized to glean a variety of characteristics from the cells such as mean and maximum intensity, integrated density per pixel, standard deviation, and total count recorded from the original image. In dual staining experiments the geographic location of the red and green cells were also recorded.

To estimate the number of cells on the membrane, the following procedure was used. First, the average number of cells per 5 fields of view (FOVs) was calculated. Each image captured by the CCD had dimensions of 1292 pixels x 1030 pixels. Via a stage micrometer the image area was found to correspond to 860 μm x 690 μm. Total available membrane area is 0.74 cm² resulting in approximately 125 available FOVs. This correction factor was used to calculate the total number of cells immobilized on

membrane. Please see **Appendix B** for an example of the Java-based deconvolution macro used for lymphocyte analysis.¹⁴⁹

2.4 RESULTS

2.4.1 NBC Device

For the integrated NBC approach, it is essential that both the optical and microfluidic systems operate in a synchronized fashion to provide efficient cell capture, as well as imaging. In **Figure 2.2A** the optical arrangement of excitation, emission, and beam filtering optics inherent to an epifluorescent design is seen. Optical wavelength requirements are determined by the molecular structure, and are specific to each fluorophore. In a multi-color analysis, separate filter cubes would be necessary for each color regime. In contrast, the QD-based system utilizes a reduced optical pathway (**Fig. 2.2B**) in which a single UV excitation source and a long-pass emission filter replaces the unique optical hardware requirements of multiple organic fluorophores.

Complementary to the condensed optics, the NBC miniaturized cell capture device serves to sequester specific cells of interest from the larger whole blood matrix. The NBC used herein was constructed internally and is based on evolution from designs described previously, and illustrated in **Figure 2.2C**.^{117, 125} The stainless steel research grade NBC contains reusable parts (except membrane) for conservative materials management and is rapidly constructed. Only a loosening of the top support structure, addition of a fresh membrane, followed by sealing is needed to construct a new NBC structure. Because of its speed, this model was used for preliminary experiments in which only qualitative information was needed.

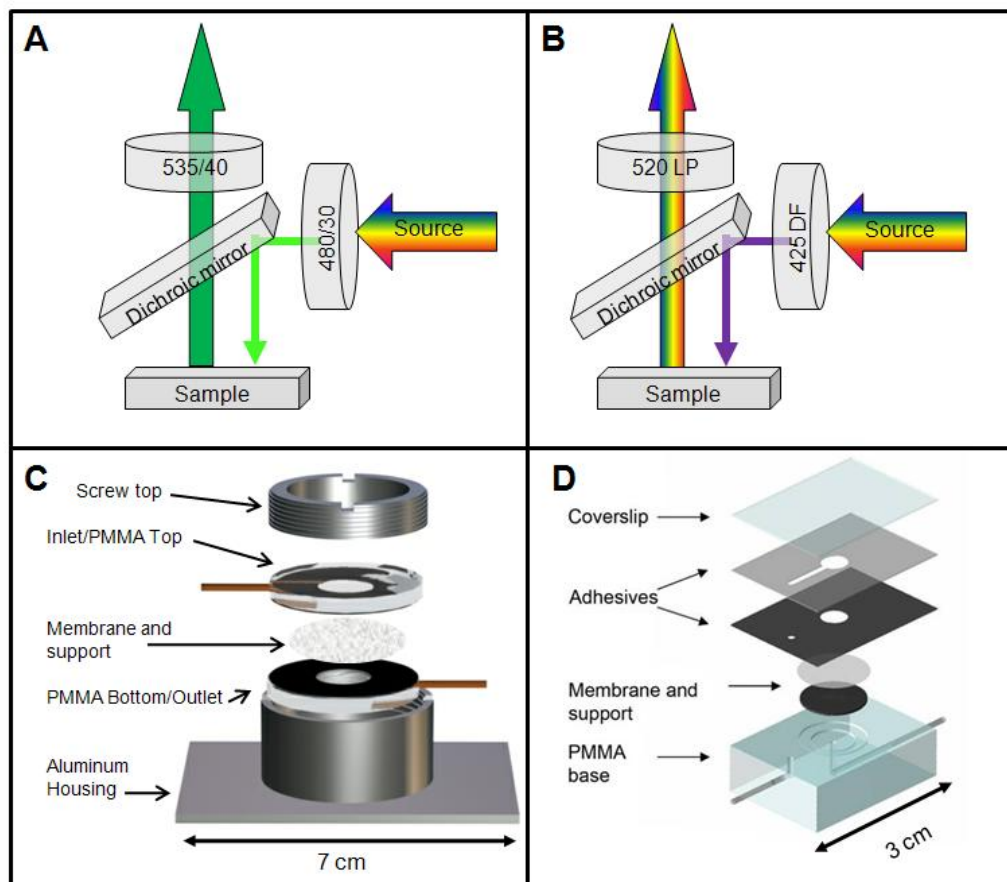


Figure 2.2. The optical and mechanical requirements of the membrane-based NBC. Typical arrangement in an epifluorescent experiment contains excitation and emission filters as well as beam splitting optics. **A)** With traditional molecular fluorophores, each dye has its own requirements, and thus, illuminating different color concurrently frequently requires multiple optical sets. Conversely, with a QD arrangement (**B**), a single UV excitation source, in tandem with a long pass emission filter allows simultaneous excitation and visualization of a number of differently colored QDs. **C)** The first generation “flow cell” NBC assembly was constructed from an aluminum housing in which PMMA support mechanisms along with plastic gasket material served to immobilize a polycarbonate membrane. This aluminum model was used for preliminary, qualitative experiments. **D)** The second-generation NBC was constructed entirely of disposable material including vinyl adhesive and precision-cut laminate layers designed for fluid flow.

Later, through evolving microfluidic structure design, this bulky stainless steel platform was replaced with a more condensed and elegant NBC ensemble (**Fig. 2.2D**).

Here, a rectangular base houses the complete assembly including the support frit which serves to maintain a level surface and provide for membrane integrity, while allowing for waste flow through. A polycarbonate track-etched membrane with pore size determined by experiment is then positioned upon the support. The clinical data presented in **Chapter 2** was collected using this second-generation, disposable NBC.

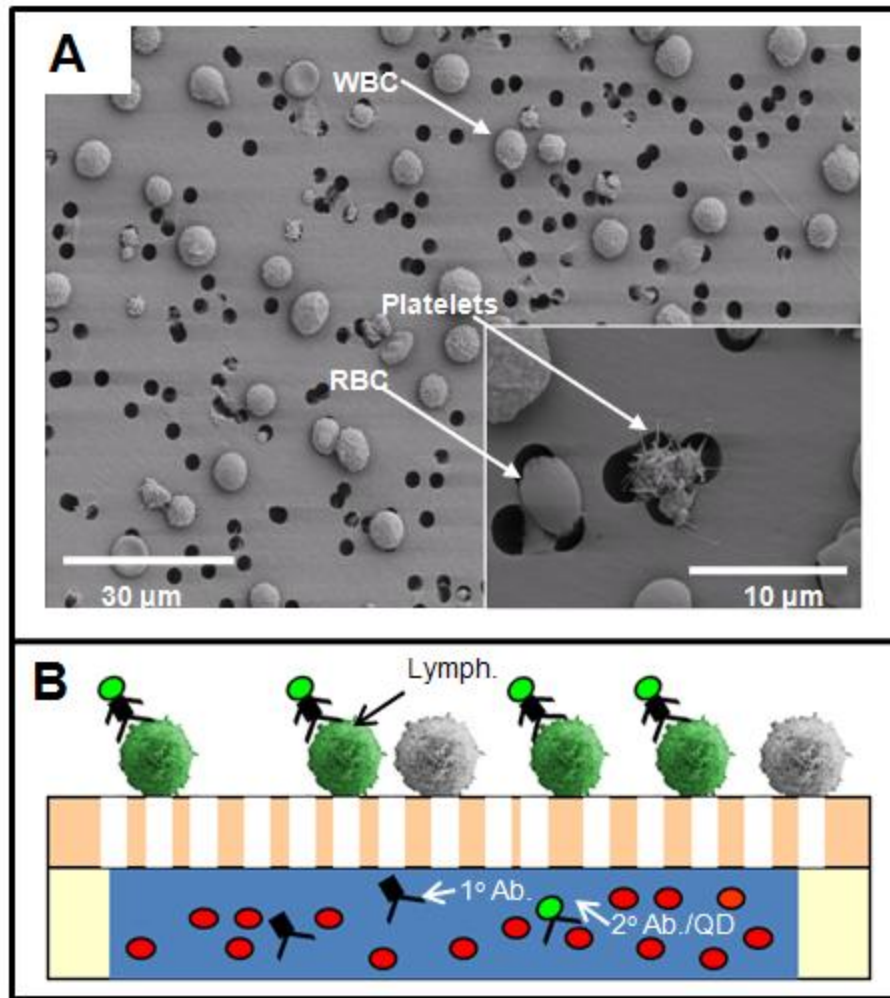


Figure 2.3. Cells immobilized and isolated by NBC. A) SEM image of whole blood sample after NBC processing indicates that the vast majority of erythrocytes and platelets are relegated to waste while leukocytes are preserved on top of membrane. B) Cartoon cross section of membrane illustrates the ability of the NBC to concurrently isolate a cellular fraction and label it by subtype.

For this lymphocyte-specific application, 3 μm diameter holes within the membrane serve a dual role of both retaining structures larger than that of the pores while allowing the sample matrix to pass through. Thus, the more rigid and structured lymphocytes are immobilized, while the remaining blood components including the more supple erythrocytes and platelets, as well as plasma, are allowed to pass, effectively isolating the cells of interest while allowing the remaining blood components and unbound antibody to be relegated to waste without lysis or additional preparatory steps (**Fig. 2.3**). After support frit and membrane are inserted, a precision-cut layer of double-sided vinyl adhesive is affixed to the top of the device effectively immobilizing the separation mechanism. The adhesive vinyl layer seals the membrane securely around the surface of the underlying support, and also fastens a cover slip to top the system. The NBC is serviced by inlet and outlet channels fitted with stainless steel tubing facilitating fluid flow including sample introduction and waste removal.

2.4.2 QD Evaluation

For initial attempts to explore QD-labeled lymphocytes, survey studies were completed using reactions in microcentrifuge tubes whereby direct conjugation schemes were employed including EDC (**Fig. 2.4**) and SMCC-facilitated (**Fig. 2.5**) coupling of antibody to nanoparticle surface. This involved a 5 min incubation of 50 μL whole blood with 5 μL of QD-antibody adduct, subsequent dilution to 1 mL total volume with buffer, and injection of 500 μL of the sample into the NBC. After a 3 min wash to ensure separation of blood components, images were captured with both a 1 and 3 sec exposure. This assay procedure was repeated with 50 μL of buffer replacing blood.

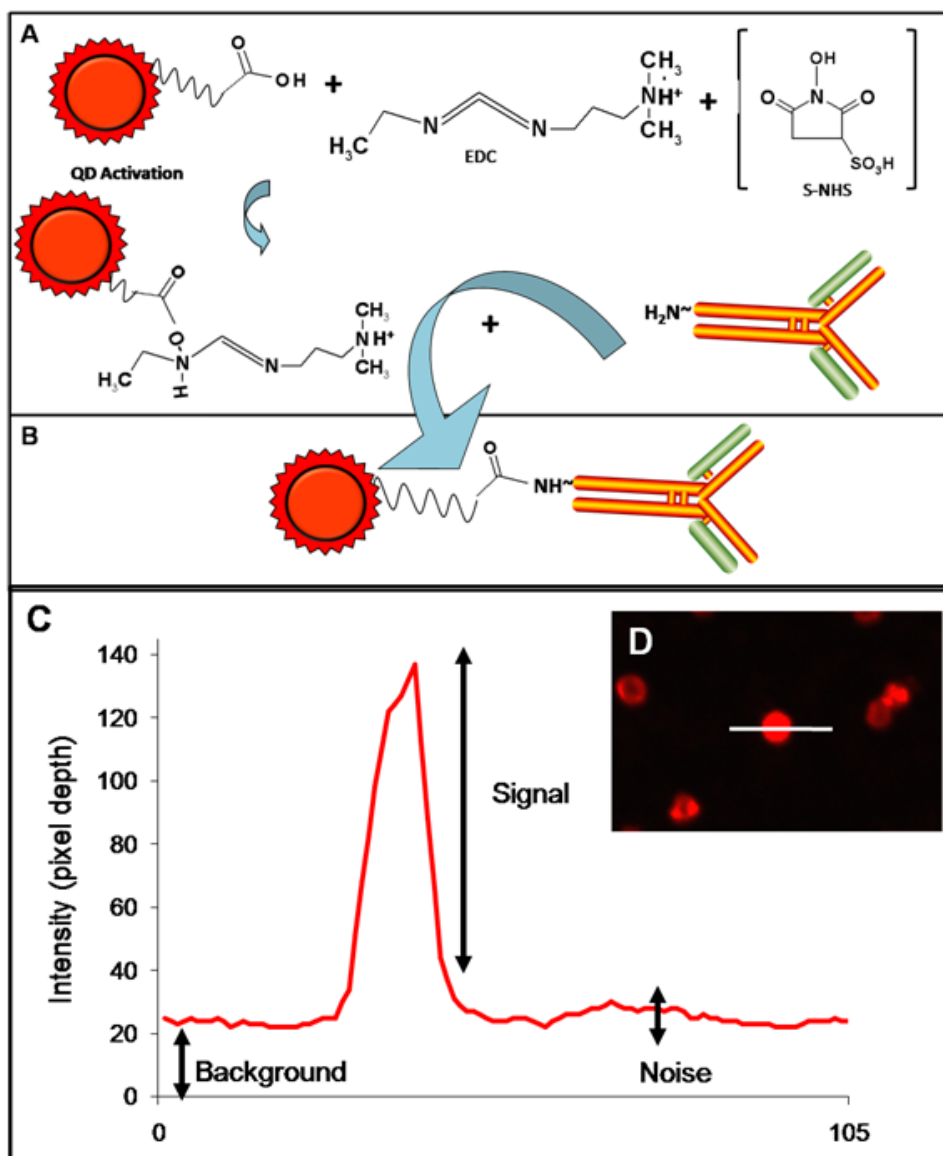


Figure 2.4. EDC Conjugation. A-B) The EDC cross linker was examined both in the presence and absence of the S-NHS stabilizer to link carboxy-coated QDs to IgG antibodies. This technique gave poor results as it non-specifically cross links amines to carboxy groups. C) The method to determination signal (S), noise (N), and background (B) is reminiscent of traditional methods in spectroscopy and are created by drawing line profiles through the fluorescently labeled cells (D). For the lymphocyte counting application in the NBC, signal to background ratio (SBR) was a particularly important descriptor as it defined an authentic cellular event. White line in D indicates line profile leading to optical cross section in C.

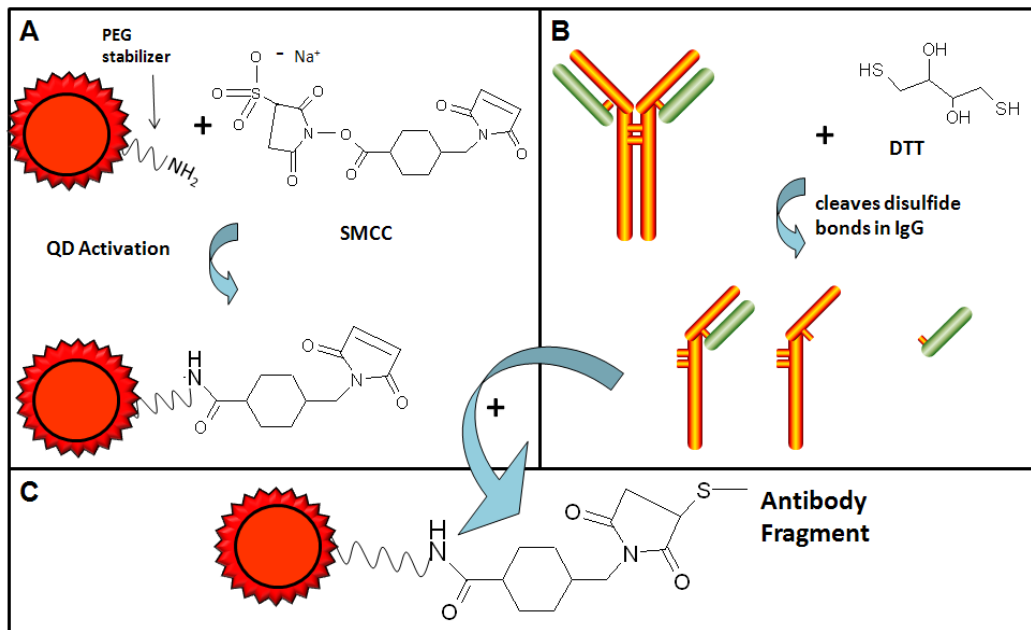


Figure 2.5. SMCC Conjugation. **A)** SMCC coats the surface of amine functionalized QDs with an active maleimide group. **B)** DTT reduces disulfide bonds effectively cleaving whole IgG into smaller fragments with a free sulfhydryl. **C)** This sulfhydryl can then reduce into the maleimide ring structure linking fragment to QD.

The resulting photomicrographs were then analyzed for particles via digital image processing in terms of size (70-500 pixels), circularity (0.6-1.0 and defined as $4\pi(\text{area}/\text{perimeter}^2)$) and intensity (2σ above mean of image). We found the 2σ discrimination point to be sufficient to identify 95% of fluorescent bodies on the membrane. The pixel size range was determined empirically and evolved from experiments with InSpeck™ 6 μm fluorescent polystyrene beads serving as a model for the lymphocytes. This range was sufficiently broad to identify particles immobilized in slightly different focal planes as well as those partially overlapping.

The cells could be further characterized by comparing the signal intensity present in the AOI to the signal of membrane surrounding the area, i.e. the background signal. Variation (RMS) in this background membrane signal was defined as noise. Signal to background (SBR) ratios could then be determined by subtracting background from signal, with the resulting value divided by background (see **Fig. 2.4C, D**). Signal to noise (SNR) ratios were calculated by taking the background corrected signal over noise. In this application, SBR served as the more relevant figure-of-merit as it was the basis for identification of the AOI as a cell; particles with an SBR above a value of 1 were considered to be an authentic event.

With these techniques, photomicrographic results of different QD-antibody conjugation methods could be qualitatively and quantitatively evaluated for labeling performance. With the SMCC conjugation, in addition to particles matching the lymphocyte qualification descriptors, additional fluorescent artifacts with irregular patterns, very large size, and extremely high intensity were seen. Especially important were the blank experiments in which only QD-antibody conjugate, in the absence of blood, was introduced into the NBC. Here, total mean membrane auto-fluorescence without blood was actually higher than in the presence of sample, 8.08 and 5.11 a.u., respectively. This problem persisted despite filtration, sonication, and further purification. Although it is possible that some of the particles in the sample-positive experiment were authentic lymphocytes, discriminating between artifacts and labeled cells using only morphological characteristics is impossible with the current software protocols. Aggregates could be misconstrued to be lymphocytes, thus contributing to the overall count of authentic cellular events.

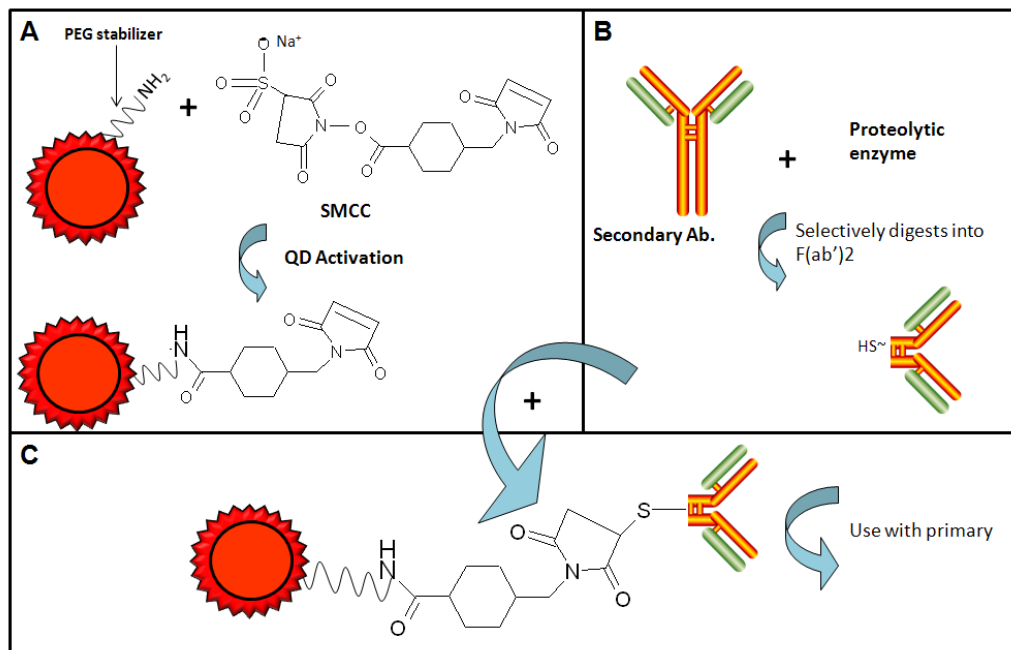


Figure 2.6 Secondary Antibody QD Linkage Conjugation. A) SMCC coats the surface of amine functionalized QDs with an active maleimide group. B) Proteolytic digestion DTT reduces disulfide bonds specifically cleaving whole IgG into F(ab')₂ fragments including a free sulfhydryl. C) This sulfhydryl can then reduce into the maleimide ring structure linking fragment to QD. This conjugate was purchased in the form of panel C from Invitrogen.

The EDC technique, though less problematic in terms of precipitation (negative control mean membrane fluorescence 3.66 a.u.), gave vague and dim labeling. This conjugate behaved well for labeling stabilized, FC blood-type products, but results were unacceptable with traditional venipuncture samples. Mean SBR ratios were near unity, and although some lymphocyte identification was possible, further optimization was not performed. This poor performance of established conjugation methods may be

attributable to the specific structure of the antibodies employed and reinforces the necessity to separately consider each application in terms of conjugation scheme.

Effective in eliminating the obtrusive precipitate and increasing signal, were commercially available QDs, thiol-linked to secondary antibodies (**Fig. 2.6**) Here, unlabeled primary antibodies specific to CD markers were applied first, followed by a 2 minute on-membrane wash; secondary QD-labeled antibody specific to primary was then applied. Clone specificity of the secondary antibodies to their respective primaries was exploited to allow simultaneous staining of two different lymphocyte populations. To find experimental conditions optimized for highest cell intensity with low membrane staining and low non-specific signal, a series of titrations were performed using varying concentrations of secondary antibody versus a constant primary and vice versa (see **Appendix B**); 10 $\mu\text{g/mL}$ primary antibody and 10 nM secondary QD conjugate were used for the remainder of the experiments. This was repeated in the absence of any blood components and a nearly complete lack of precipitate was observed. Negative and positive control mean membrane fluorescence was 2.80 and 5.28 a.u, respectively for QD 655 and 15.01 and 19.56 a.u for QD 565. SBR ratios were well above 4 for QD 565 and 10 for QD 655 (see **Figure 2.7**).

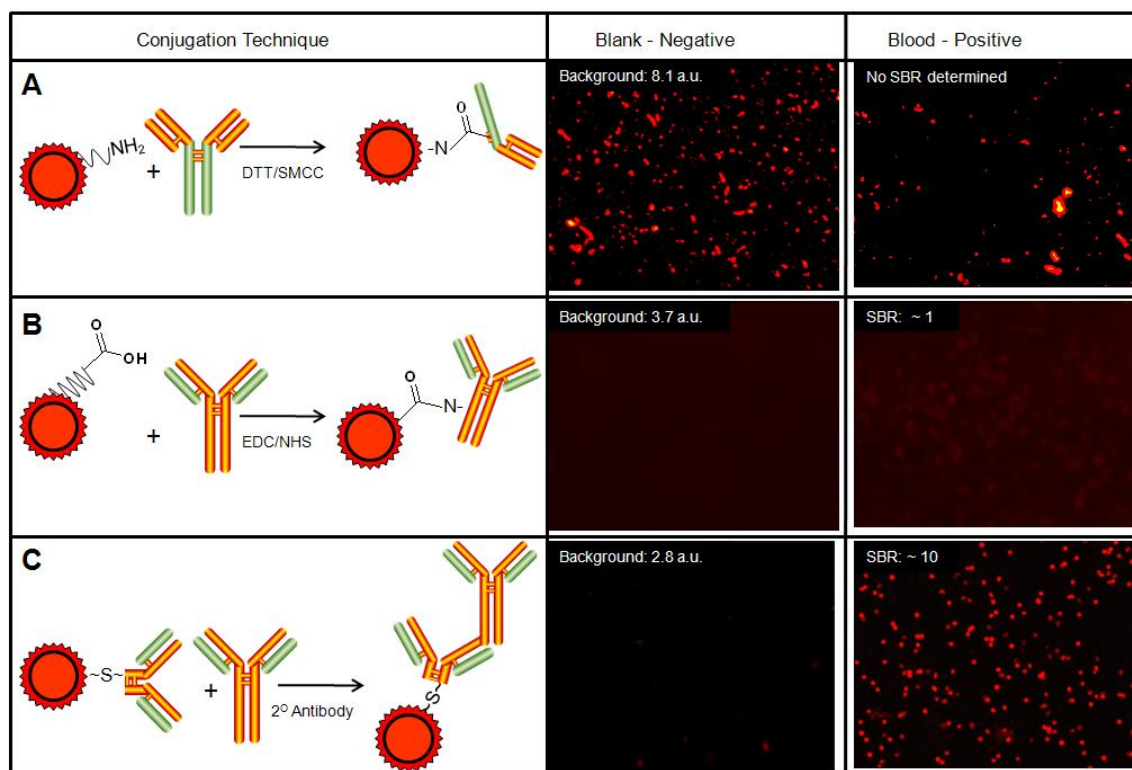


Figure 2.7. Performance Features of Three QD Linkage Strategies. A) SMCC technique non-selectively links fragmented IgG onto QD surface. This strategy consistently gave unacceptable fluorescent precipitate both in the presence and absence of blood sample. B) Although the EDC technique was more reliable at giving low backgrounds, its lack of a defined orientation and high fluorophore to antibody ratios resulted in cells with low SBR. C) The secondary antibody scheme specifically labeled cells with high specificity and little background.

2.4.3 Expanded Pathway Assessment

Later, to confirm the identified secondary antibody based system was indeed the ideal choice, a more extensive evaluation of the QD performance metrics was done. QDs have yet to completely replace molecular fluorophores partly because they are inherently hydrophobic and thus tend to flocculate out of aqueous solution. Due to their size and surface chemistry, fewer established protocols for bioligand labeling exist. Nevertheless, a number of different pathways use either novel reagents or build upon previously

demonstrated linking strategies. **Table 2.1** shows some of the most common routes and their performance in the membrane-based cellular processing unit. Here, a more in depth characterization of the different pathways was undertaken as determined by a number of descriptors. First, the length of the linkage from target to QD surface was calculated from crystallographic data.¹⁵⁰⁻¹⁵² Additional performance descriptors include antibody to fluorophore ratio, quantum yield (Φ), molar extinction coefficient (ϵ) at 350 nm, *aggregation coefficient* (\check{A}), non-specific signal (NS), and signal to background ratio (SBR). The antibody to fluorophore ratio^{153, 154}, Φ ^{155, 156}, and ϵ ^{156, 157} were determined similar to previous reports; however the \check{A} , NS, and SBR (*vide supra*) values offer fresh insight into how to characterize QDs as labeling tools in NBC-type devices. Briefly, Φ was determined by **Equation 2.1**.

$$\Phi = \frac{\Phi_R m \eta^2}{m_R \eta_R^2} \quad (2.1)$$

Where Φ_R is the quantum yield of a reference material, m is the slope of an absorbance versus integrated density linear plot across five different concentrations of samples and reference, and η is the refractive index of the medium in which the fluorophore is dissolved. For these experiments quinine in 0.1 N sulfuric acid was used as the reference material. Values for ϵ were determined by **Equation 2.2** in which a linear relationship between absorbance and concentration is determined in a 1 cm path length cell.

$$\epsilon = \frac{A}{C} \quad (2.2)$$

The antibody to fluorophore ratios were calculated by determining moles of antibody or fluorophore per volume, either through a protein assay or a spectroscopic absorbance (A_{280}) measurement.


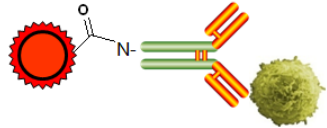

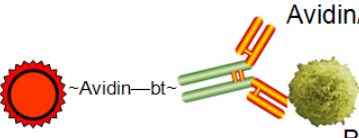
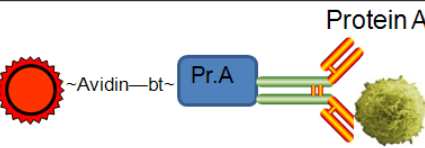
	Length (nm)	Ab./Fluor Ratio	Φ_{366} $\Delta\Phi$	$\epsilon, 350$ (million)	\checkmark	NS	SBR
A  SMCC/DTT	8	2-4	0.06 -0.03	14.2	0.90 ± 0.15	46	1.8
B  EDC	8	9+	0.06 -0.05	12.9	1.24 ± 0.18	231	1.4
C  2 ^o Antibody	16	6	0.09	15.5	0.10 ± 0.04	11	9.8
D  Avidin/Biotin	12	4	0.05	10.6	2.26 ± 0.94	95	4.9
	32	4	0.09	14.1	0.07 ± 0.02	65	0.7
E  Protein A	20	4	0.05	10.6	2.26 ± 0.94	95	n.d.

Table 2.1. Extended Evaluation of QD Conjugation Schemes. SMCC (A), EDC (B), and secondary (C) techniques were subjected to an extended evaluation in addition to an avidin/biotin linkage (D) and protein A facilitated pathway (E). Some avidin/biotin labeled cells were subjected to additional biotin amplification (Bt. Amp.) and those values separated by dashed line. These were characterized in terms of path length (as determined by crystal structure and literature reports), antibody to fluorophore ratio, quantum yield, molar extinction coefficient, background, non-specific signal, and signal to background ratio. The superior performance of the secondary antibody scheme remains apparent by its high SBR and low non-specific signal. Note $\Delta\Phi$ is change in quantum yield upon linkage to antibody and ϵ is measured at 350 nm. Other descriptors are explained further in the text of **Section 2.3.3**.

SBR was determined and evaluated as above while \checkmark was calculated by passing antibody labeled QDs over the membrane (in the absence of any blood sample) and observing aggregates. The percentage of the membrane that was covered by this aggregate was recorded and defined as \checkmark ; acceptable values are well below 1%. This method is a

straightforward way to determine passivation layer defect and addresses a critical need addressed in Nann's recent *Nature Methods* paper.¹⁵⁸ Finally, NS signal was determined by incubating raw QDs with blood and then analyzing with the NBC. Raw QDs only were then analyzed with NBC (\check{A}). The difference in number of counts between the two experiments results in an increased number of particles present with blood which is due to the non-specific interaction of QDs with cells and is reported as the value NS. This method effectively eliminates any of the biological components and is a straightforward method to determine non-specific binding. Not surprisingly, QD particles with a high negative charge, i.e. carboxy QDs, have a higher coefficient of non-specific binding.¹⁵⁹

Conjugation pathways have been discussed in detail in a number of quality reviews.^{59, 66, 160} The values for \check{A} , NS, and SBR reinforce what has been previously demonstrated—for our lymphocyte application, a secondary approach is the best fit. The proper conjugation pathway will have not only low \check{A} and low NS, but also high SBR. The secondary labeling approach remains the ideal choice for lymphocyte labeling.

All of the data in **Table 2.1** was collected with source QDs from Invitrogen. To evaluate differences between vendors, a study with CdSe/ZnS particles from Invitrogen and Evident were compared, in addition to CdTe particles from PlasmaChem. **Table 2.2** illustrates that the CdTe particles are substantially dimmer; a 50X concentration increase needs to be performed before signal can be observed. They do however, demonstrate less non-specific binding and yielded fewer problems with aggregates. The high signal intensity of the Invitrogen particles, as evidenced by their higher Φ ultimately influenced the decision towards their use. Interestingly, their greater than 50% reduction in Φ upon antibody linkage is consistent with the literature and may be due to non-radiative decay of excited states as influenced by singlet oxygen.¹⁶¹

Vendor	ϵ , 350 (million)	Macro PPT	Ab./Fluor Ratio	Φ , 366 nm $\Delta\Phi$	\AA	NS	SBR
A Invitrogen	14.2	+	9	0.06 - 0.05	1.24 \pm 0.18	231	1.36
B EvidentTech	9.2	+	6	<0.01 -0.02	0.92 \pm 0.25	36	1.27
C PlasmaChem	1.1	-	<1	<0.01 n.d.	0	0	0
D PlasmaChem (Increased Conc.)	1.1	++	<1	<0.01 -0.04	0.47 \pm 0.04	2	3.16
E Invitrogen EDC/NHS	14.2	+++	11	0.02 - 0.09	0.13 \pm 0.08	231	0.45

Table 2.2. Performance Features of QDs From Various Vendors. QDs were used in conjunction with the EDC method to label CD3+ lymphocytes in the NBC. Invitrogen (**A**, **E**) and EvidentTech (**B**) QDs are carboxy coated and consist of CdSe core and ZnS coat. PlasmaChem (**C**, **D**) QDs have a CdTe core which resulted in a much dimmer signal; however, these QDs also had much less problems in terms of aggregation and non-specificity. An additional parameter included here not in **Table 2.1** is macroscopic precipitation (macro ppt) a term used to evaluate how much of the antibody-QD conjugate is in solid form at the end of conjugation.

2.4.4 Optimization and Validation

To validate further the secondary antibody QD-based labeling scheme, whole blood samples were labeled with Alexa Fluor 488 bound directly to CD4-specific antibody from mouse. The sample was then counterstained with QD 655 secondary antibody specific to the mouse IgG. This sample was analyzed with the NBC and imaged through filters specific to the two fluorophores with >99% spectral overlap (data not shown) of the red and green signal seen, verifying this secondary antibody QD visualization methodology. Unlabeled primary antibodies were henceforth used. When secondary antibodies were incubated with blood samples devoid of primary antibody, and subsequently injected into the NBC, fluorescence signal was reduced by 86.5% relative to the positive controls, as the unbound fluorescent antibody is passed on to waste. This

background signal is attributable to membrane staining and stray, conspicuous aggregate—both easily identified and removed via image processing.

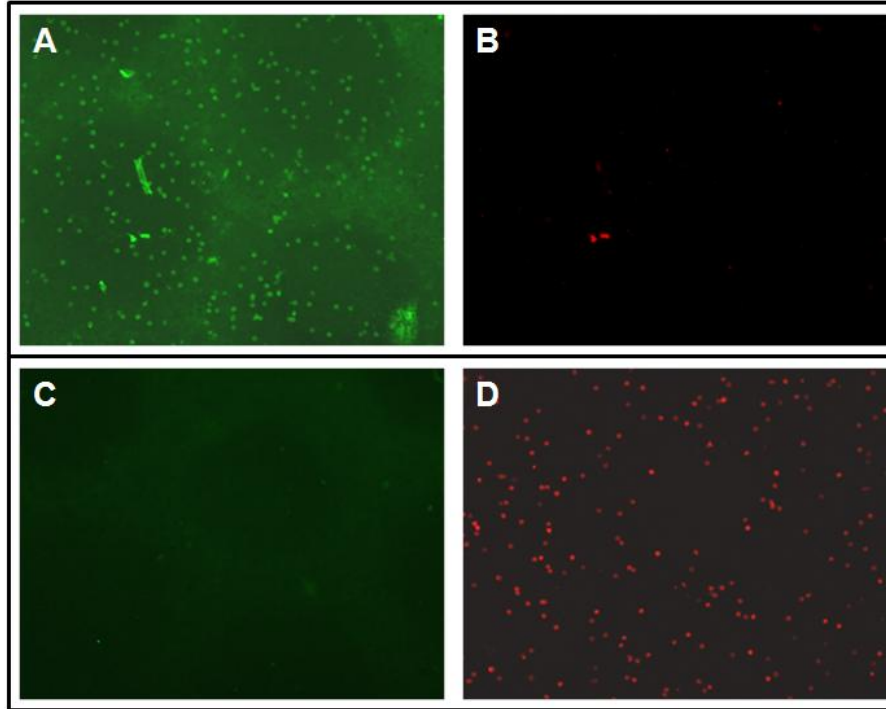


Figure 2.8. Cross Reactivity in Secondary Antibody Labeling Pathway. Panel **A** and **B** are the same sample subjected to CD4 primary antibody raised in rat and then subjected to secondary staining by both goat anti-rat (QD565) and goat anti-mouse (QD655) antibodies. The sample was then imaged with optical settings specific to either green (**A**) or red (**B**) QDs. Only the specific rat-rat interaction elicits a signal. Conversely, panels **C** and **D** employed a CD3 specific primary antibody raised in mouse and an identical secondary cocktail as employed above. Again, specific signal comes from the iso-species interaction. Images captured at three seconds exposure.

As clone specificity between the primary and secondary antibodies is of utmost importance in this dual color staining approach, any non-specific binding within the system was also investigated. Whole blood samples were first incubated with CD4 primary antibody raised in rat; washed, blocked, and incubated with QD 655 labeled secondary antibody specific to both mouse and QD 565 goat anti-rat (**Fig. 2.8A, B**). Non-

specific signal was 9.1% in such a trans-species experiment. CD3 mouse primary/QD 565 goat anti-rat and QD 655 goat anti-mouse secondary experiment was performed analogously to that described above with similar results (Fig. 2.8C, D).

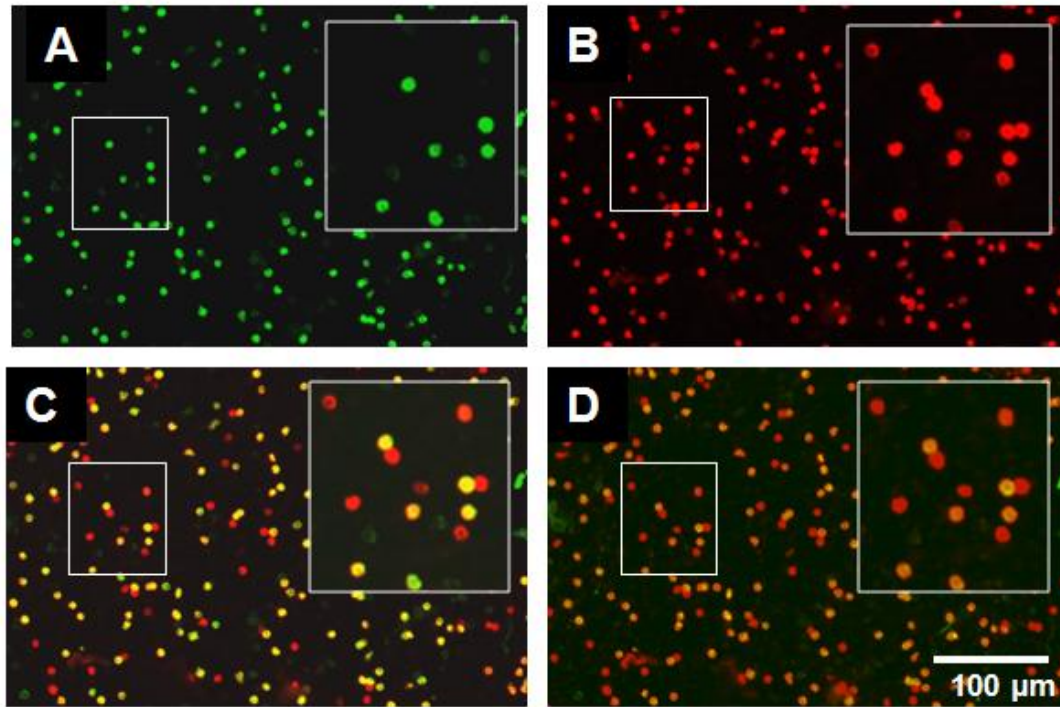


Figure 2.9. Lymphocyte subset profiling via QDs. Representative photomicrographs of whole blood labeled with CD specific antibody and QD fluorescently tagged secondary antibody taken with a 10X objective and 3 seconds of exposure time. The QD 565 labels CD4+ cells including monocytes and T lymphocytes in the green channel (A) while QD 655 stains CD3+ lymphocytes red (B), as observed through separate filter cubes specific to each fluorophore. A digital overlap of the red and green images (C) shows monocytes (CD3+CD4+, green), T lymphocytes (CD3+CD4+, yellow) resulting from signal both in red and green channels, and remaining NK and CD8+CD3+ T-killer lymphocytes (CD3+CD4+, red). An alternative approach (D) utilizes a long-pass emission filter cube (520 nm and longer) allowing a single capture event to produce a similar image to that generated by separate photomicrographs. Insets illustrate highlighted areas with 2X digital zoom; images captured with three seconds of exposure.

Thus, for the remainder of the experiments, CD4⁺ lymphocytes appear green (**Fig. 2.9A**) and CD3⁺ cells red (**Fig. 2.9B**). Upon digital overlay of these two images, the dually stained cells of interest emerge yellow (**Fig. 2.9C**). Dim green cells in the image are monocytes, as they express the CD4 surface receptor to a much lesser degree than lymphocytes. Cells remaining solely red represent CD8⁺ killer T lymphocytes. Images were also obtained with a long pass emission filter (**Fig. 2.9D**) similarly to those acquired with individual filters. Monocytes were found to have a fluorescent intensity approximately 6 times less than lymphocytes. This is consistent with their decreased expression of the CD4 epitope relative to the T cells.

2.4.5 Monocyte Discrimination

Monocytes, like CD4⁺ T lymphocytes, possess the CD4 surface marker and, as such, are a critical consideration in the membrane-based NBC analysis. The presence of monocytes can lead to artificially high CD4 counts. **Figure 2.10** details both the spatial and intensity gating strategies employed to diminish any artificial monocyte contribution to desired cell count. First, the CD4⁺ cells are divided into two categories, dim and bright, with only the bright cells subjected to further processing (**Fig. 2.10A**). Second, the presence of the CD3 marker is required to confirm the cell's authenticity as a T lymphocyte (**Fig. 2.10B**) Only cells positive for both markers are then counted (**Fig. 2.10C**). Monocytes and lymphocytes are clearly separated by the membrane-based NBC into two distinct populations with a bimodal distribution as seen in the histogram in **Figure 2.10D**. The distribution gives baseline separation between the two populations of CD4⁺ cells. Flow cytometry produces a similar distribution, but also contains a low level population of non-specifically stained cells (**Fig. 2.10E**). Monocytes in the membrane-based NBC were found to have a fluorescent intensity approximately 4 times less than

lymphocytes. This is consistent with their decreased expression of the CD4 epitope relative to the T cells.¹⁶²

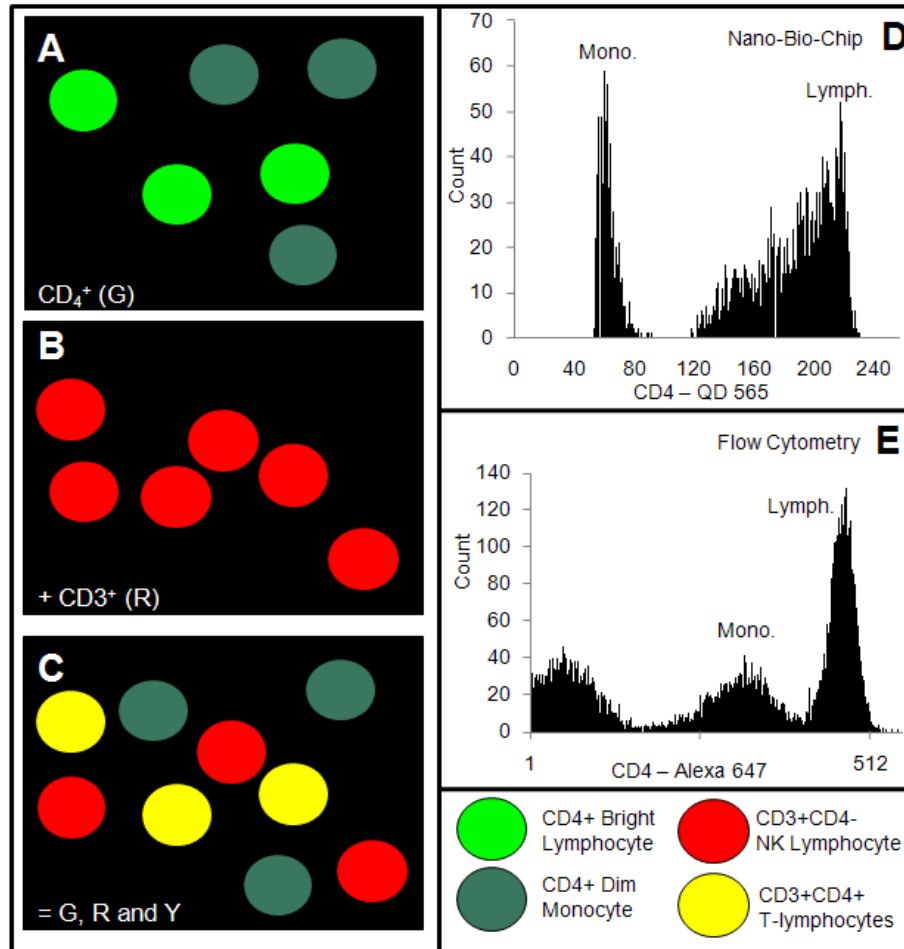


Figure 2.10. NBC Gating. Graphical depiction of cells and the spatial and intensity gating procedures used for selected lymphocyte and monocyte populations. **A)** The CD4+ cells fall into two distinct populations: CD4+ bright, lymphocytes, and CD4+ dim, monocytes as shown in the schematic. The intensity of this CD4-specific signal is an initial descriptor to remove monocytes from analysis. **B)** The CD3+ cells include T and NK lymphocytes. **C)** Overlap of the two images results in red, green, and yellow cells. Cells doubly positive for red and green, and thus yellow, are the CD4+ T lymphocytes of interest. Cells remaining green are the interfering monocytes. **D)** A green color channel 8-bit intensity histogram is shown for the CD4+ cells as analyzed by the membrane-based NBC. The cells are labeled with QD 565. **E)** A similar 10-bit histogram is shown for the populations as determined by FC. (FC histogram truncated from 1024 to ~550 to maximize plot area.)

2.4.6 Absolute Determinations

Having validated that the fluorescent particles seen on the membrane were indeed authentic lymphocytes of identifiable subsets, the ability of the membrane-based NBC system to count QD-labeled cells was next explored. Critical to this success, was a NBC design in which a near uniform distribution of sample is achieved across the entire membrane area. To evaluate whether this was indeed the case, photomicrographs in five different FOVs across the membrane were captured, with one in the center of the membrane and 4 additional locations arranged orthogonally from each other and surrounding the center image. This consistent method of defining FOVs across the membrane involves analysis areas both in the center and near the edges of the membrane and creates a broad sampling of surface area. Additional investigations have used different membrane sizes, pore sizes, and flow rates and found that with the parameters used herein, low CVs were routinely obtained, consistent with previous work.¹³⁰ Cell counting and profiling studies were done to show that a small fraction of the membrane could be used to accurately represent the total count within the entire volume. Standard deviation and mean when 5 FOVs were used result in a %CV value that was typically 5-10% (*vide infra*). These measurements serve to establish that the cell distribution is optimized across the membrane structure. No further decrease in variance was seen upon the inclusion of more than 5 FOVs.

Also critical were consistent background autofluorescence of the membrane as this served to define the SBR ratio. Autofluorescence is reduced in the red, QD 655, channel relative to the green, QD 565, channel. Fortunately, this was negated by the high QD signal to still measure high SBRs. An alternative method used image capture before introduction of sample and a resulting background subtraction.

Converting digital images into meaningful cell counts utilizes digital image processing and custom-built deconvolution coding macros. To initially optimize the

software to correctly interpret our photomicrographs, fluorescent beads with physical dimensions near lymphocytes were first used. Next, through an iterative process, such descriptors as size, circularity, and signal to background ratio were trained on nearly 1 million individual cellular events to result in cell counts that were statistically identical to those provided by flow cytometry. The difference between each FOV is less than 10% and indicates that the arrangement of cells on the membrane is random and generally free of bias. Importantly, with appreciably different blood volumes ($< 10 \mu\text{L}$ or $> 75 \mu\text{L}$) the distribution moves away from random distribution. The variance between repeated analyses of the same sample within the NBC is 5-8% compared to values nearing 25% for flow cytometry. This cell counting approach has been validated down to 50 cells/ μL and up to 600 cells/ μL which includes both the region where increased testing is recommended (200-600 cells/ μL) as well as the area considered active AIDS (< 200 cells/ μL). Cellular crowding on the membrane leads in inaccurate counting and may hamper cell counts above 600 cells/ μL as lymphocyte overlap leads to exclusion from macro analysis. Photomicrographs containing more than 20% of active pixels generally had a large number of overlapping lymphocytes. To circumvent this shortcoming, an alternative method of analysis—total membrane fluorescence—was demonstrated to extend the linear dynamic range in a spore counting applications by three orders of magnitude. This system achieved detection limits of ~ 500 *Bacillus globigii* (a commonly used simulant for *Bacillus anthracis*) spores, a value highly competitive with similar technology, but with analysis times of approximately 5 minutes.¹⁶³

To demonstrate the ability of the membrane-based NBC ensemble to count across a wide linear dynamic range of cells, increasing volumes of whole blood ranging from 5 to 100 μL were stained for CD4 cells and injected into the mini cell capture system. The resulting cell count values were plotted versus volume and yielded a linear response over

this sample volume range ($R^2 = 0.98$, **Fig. 2.11A**). The linearity of this dose response curve provides strong evidence for the analytical capabilities of the approach and suggests that the fluorescent nanoparticles and automated digital counting methodologies here defined may be used to measure lymphocyte populations under these conditions. As might be expected, at either very high or very low blood volumes, the %CV of the measurements increases. This behavior is due to overlap and clumping at the high end, and lack dissemination (reduced sample viscosity) across the entire membrane at low volumes. For the remainder of the experiments 50 μL of sample was used. **Fig. 2.11A** also demonstrates the importance of the threshold parameter in CD3 counting. For the blue “set” approach, a $S = 17$ was designated as the discriminator between background and cell surface while for the “auto” approach a floating cut-off of 2δ above the mean of all pixels. The simplicity of this data analysis approach allows digital changes to the macro to produce the most accurate results output.

To simulate the ability to perform cell counts over the range of values typically encountered in both healthy and immunocompromised individuals, a dilution study was performed in which blood volumes of 5-50 μL were diluted with 1% PBS/BSA to a total volume to 50 μL . Cells were stained for both CD3 and CD4 and doubly positive cells (yellow) from 5 FOVs were counted. This was again extrapolated via entire analysis area to give a total cell count which was divided by the 50 μL sample volume resulting in a measurement of counts per μL . Good linearity was observed across the 350 to 500 cells/ μL region where increased monitoring is recommended.¹³⁴ Lymphocyte counts below 200 cells/ μL were measured with acceptable accuracy indicating the diagnostic criterion for the separation barrier between HIV and AIDS, in addition to measurement of healthy cell count values, can be achieved with this approach ($R^2 = 0.92$, **Fig. 2.11B**).

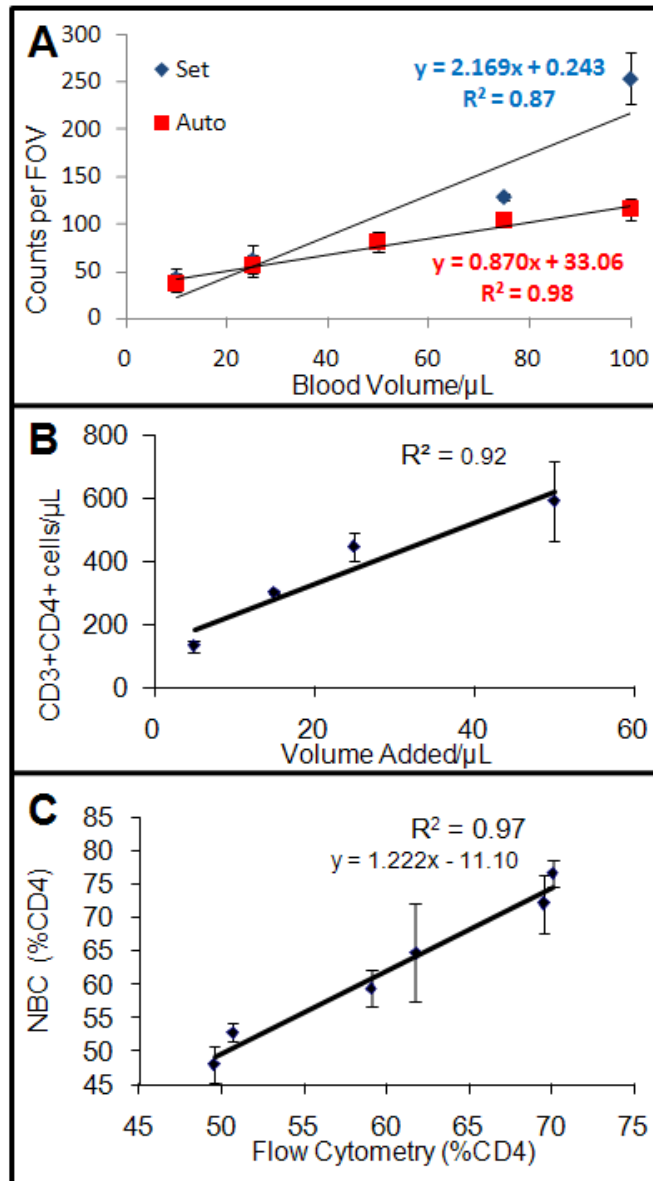


Figure 2.11. Cell Counting and NBC Validation for HIV Studies. Whole blood of varying volume was subjected to the staining process and membrane-based NBC analysis. **A)** Undiluted blood was stained for CD4+ lymphocytes and counts per field of view translated into total number of cells distributed across the entire membrane. This was interpreted by either a constant (*set*) or dynamic (*auto*) threshold value. **B)** To simulate immunocompromised samples, blood volumes were subjected to PBS/BSA dilution to a total volume of 50 μL and stained for CD3+CD4+ lymphocytes with total membrane area and dilution correction factors utilized to estimate cells per μL in the original 50 μL sample. **C)** Small pilot study comparison of the membrane-based NBC method to flow cytometry for %CD4 determinations correlates at $R^2 = 0.97$.

2.4.7 Flow Cytometry Correlation

To compare the membrane-based NBC to the gold standard of cellular determinations, flow cytometry, parallel experiments were executed to measure values of %CD4 (i.e. CD3+CD4+ cells per total CD3+ cells). Similar measurements have been completed previously using a combination of red encoded CD3, CD19 and CD56 cell surface markers to secure the entire population of lymphocytes.¹⁶⁴ For the purpose of these experiments, whole blood samples were collected from 6 different healthy donors by venipuncture, divided into 2 aliquots, and analyzed the same day as collection on both the FC and membrane-based NBC systems. Through the image analysis protocol described above, the number of cells displaying both the CD3 and CD4 receptors can be determined and compared to CD3 counts. In the membrane-based NBC, this corresponds to the total number of dually-positive yellow cells divided by total red cell counts. In FC, lymphocytes were first identified from monocytes and granulocytes via their unique side and forward scatter signature. These cells were further characterized by the number of CD4 and CD3 surface receptors present, as determined by red and green fluorescence intensity, respectively. Separation between dually positive and CD3+CD4- cells was seen and cell counts per μL derived via calibrator bead standards. The values of %CD4 could then be determined by number of cells CD3+CD4+ divided by total CD3+. Regression analysis shows correlation between the methods using a single long pass emission filter ($R^2 = 0.84$) or separate filter cubes ($R^2 = 0.97$, **Fig. 2.11C**). Differences between the two optical approaches include higher background, and thus less contrast between the membrane and cells, resulting in fewer events detected during image analysis of photomicrographs obtained with the long pass filter. This optical interference could possibly be eliminated with a dual band pass emission filter or simply a more discerning long-pass filter. Nevertheless, this degree of agreement in a small pilot study is an encouraging example of the utility of nanoparticle QDs employed in a biochip sensor.

To assess the precision of both approaches one sample was repeatedly assayed 6 different times with both flow cytometry and the NBC. Although the NBC system showed higher standard deviation, the CD4% values for individual filters, $53.28\% \pm 5.13\%$, and long pass filter $46.96\% \pm 8.83\%$, were within the statistical range of that given by flow cytometry, $51.11\% \pm 0.35\%$. Differences here may be attributed to variation in NBC construction, pipeted volume, or sample decay. Typical trial to trial variance values for flow cytometry is in the range of 5 to 8%.¹³⁴ The FC procedure takes > 60 minutes from startup to results as its' elaborate optical and fluid handling design require daily maintenance. The NBC system produced results in < 30 minutes.

2.4.8 Comparison to Molecular Fluorophores

For evaluation of QDs relative to organic fluorophores, 50 μL whole blood was labeled with mouse CD3 primary antibody and then fluorescently tagged with equimolar quantities of goat anti-mouse secondary antibody conjugated to QD 655, QD 565, Alexa Fluor 647, Alexa Fluor 488, or fluorescein isothiocyanate (FITC). A sequence of images was acquired with photomicrographs taken every 20s for 15 minutes. The AOIs, specific to each experiment, were created from the initial and most intense image, and then applied to subsequent photomicrographs recording the mean intensity of each AOI collection. This value was plotted vs. time for three of the fluorophores resulting in **Figure 2.12**. The attributes of the fluorescent nanoparticles becomes clear as the intensity ratio advantage versus their molecular counterparts (with the exception of Alexa Fluor 488) after only one minute was 1.4 and 3 for the red and green fluorophores, respectively. At fifteen minutes these ratios increase to 2.2 and 6. Power meter interrogation of the two systems, indicates an excitation intensity advantage factor in the QD system of 1.3 versus Alexa Fluor optics. The Alexa Fluor dyes used in these comparisons are provided

with a fluorophore to antibody ratio of $\sim 7:1$. Conversely, due to the large size of the quantum particles relative to the molecular dyes, this ratio drops to $\sim 0.3:1$.

This stability is particularly advantageous to our NBC system as multiple FOVs are captured and in which any loss of fluorescence would directly translate into a reduced number of lymphocytes imaged. Furthermore, additional reagents targeting other intra, or extra, cellular moieties of interest could be added after this initial analysis gleaning supplementary information from the sample while retaining the stable QD signal. The powerful Alexa Fluor 488 signal is likely due to its very large excitation spectrum and high quantum yield and a higher fluorophore to antibody ratio.

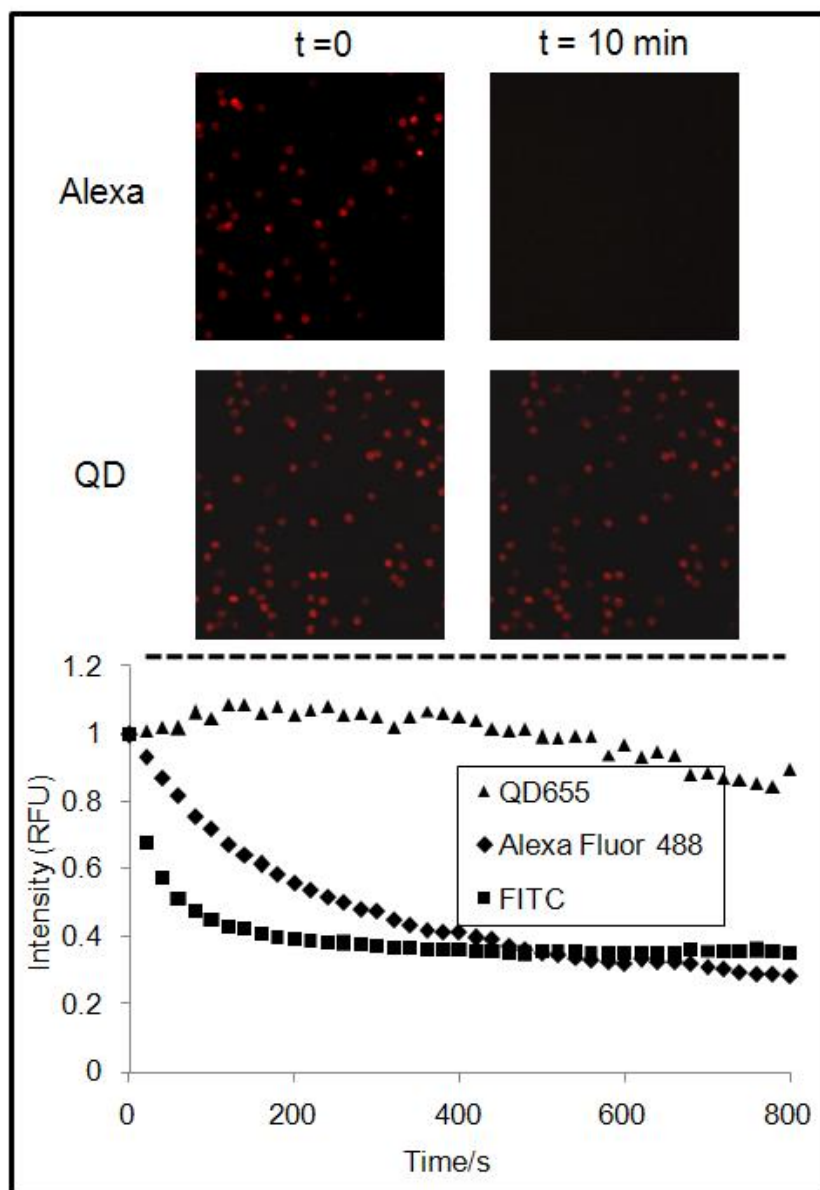


Figure 2.12. QD Photostability. CD3⁺ cells were processed with equimolar concentrations of both primary and secondary-antibody-fluorophore conjugate, which was normalized to fluorophore. This was injected into the NBC, and images captured every 20 sec for 15 min. Intensities from each fluorophore were plotted relative to their individual maximum, initial intensity. Conventional fluorophores exhibit exponential decay versus QD photostability that is critical for capturing a number of FOVs in the NBC system. This stability may also be exploited to add additional reagents for further cell analysis. Images captured at one second exposure.

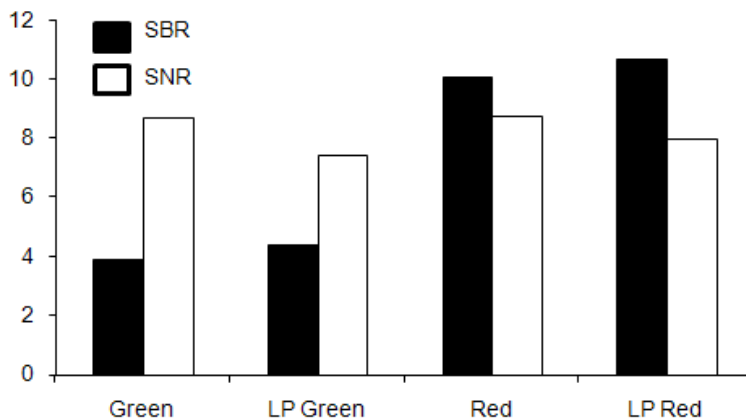


Figure 2.13. QD Filter Optical Properties. Signal to noise and signal to background ratios for individual filter cubes versus a single long pass filter for staining CD3+ cells. Individual cell intensities were evaluated relative to immediate environment in terms of membrane auto-fluorescence and variation in background signal. For this application, SBR proved critical in identifying authentic events.

2.4.9 Optical Pathway Evaluation

To evaluate the performance characteristics between individual filter cubes for red and green QDs versus a single long pass filter, images were captured under both conditions. Photomicrographs were split into their RGB components, AOIs determined as described above, and average pixel intensity in the gated regions recorded. The SNR and SBR values were calculated, the results of which may be seen in **Figure 2.13**. Amplification of SBR by 13.7% is observed with the long-pass filter for QD 565, 6.2% for QD 655. SBR values for the green channel QDs are 61.4% lower than red channel QDs. This is attributable not to decreased intensity, but rather to increased autofluorescence of the membrane. Capturing an image before sample introduction with resulting background subtraction negates this effect. The system was capable of adequately identifying cells even at SBR values approaching unity. The similarity

between the individual filter cubes and a single condensed method demonstrates the ability to develop QD-based NBC systems utilizing only a single optical pathway for reduced overall analyzer footprint.

2.5 DISCUSSION

2.5.1 Role in HIV

Despite the availability of antiretroviral therapy (ART) as treatment for declining immunity, use of ART as a tool to decrease morbidity among the more than 33 million people infected with HIV has not become widespread in resource-scarce settings. Lack of CD4 HIV immune function testing has been described as the “missing link” in the management of HIV+ patients in resource-scarce settings.¹ Problems with CD4 measurements here can be attributed to the above highlighted infrastructure requirements including a lack of skilled operators, high cost, constant power supplies, the need for refrigerated reagents, and lengthy sample preparation. Identifying those individuals most at need for ART as determined by the immunological profile remains the ultimate goal of these efforts. In order to meet that goal and push for further reductions in overall analyzer size, this chapter demonstrates the feasibility of incorporating next generation, nanometer-sized fluorophores into a microfluidic device to monitor the progression of HIV and other immunologically relevant diseases. Existing techniques, including flow cytometry and nonflow alternatives, have the drawbacks of low throughput, extensive sample preparation, and limited portability. The self-contained NBC apparatus is completely disposable reducing risk of biological contamination and allows fingerprick-sized samples to be analyzed in under an hour, with CD4 percentages obtained to a degree similar ($R^2 = 0.97$) to traditional flow cytometry without the need for erythrocyte lysis, manual counting, or internal bead standardization.

2.5.2 NBC Advantages

The analytical behavior observed by the NBC is an effective proof-of-principle demonstration of the miniaturized system with several advantages versus flow cytometry. First, the use of reagents is greatly simplified; no lysis reagents are required to remove erythrocytes and no calibration beads are required as in single platform FC. Fixation and dilution are the only a single sample preparation steps required in the NBC system. Second, the optical and fluidic standardization protocols required of FC for maintenance and calibration are largely eliminated with the NBC. In contrast to the complex and relatively delicate optics of benchtop cytometers, our NBC system needs only a single set of excitation/emission optics when operated in tandem with QD probes; a reduction in moveable subcomponents is an attribute to LOC-type devices. Third, size is drastically reduced from a FC apparatus requiring an entire benchtop to a potential hand-held device. Finally, the amount of sample required is less than half of that required for flow cytometry. Although the difference between 50 μL and 100 μL is not especially substantial, this decreased volume moves the sample size into a range highly compatible with finger-prick sized samples, a less invasive collection method. Additional studies are needed to further determine the validity of finger-prick as a venipuncture replacement.

The NBC served to effectively isolate components of interest from the greater sample matrix. Critical to our success was NBC design with optical considerations in mind. A flat and monodisperse membrane prevented uneven illumination and allowed nearly all cells in one field of view to be in focus concurrently. Cell overlap on the separation mechanism, although minimized by small sample volumes and injection flow rate, was sometimes unavoidable. However, digital imaging functions were capable of separating these AOIs based on size and location. The mean diameter of cells present in the photomicrographs when imaged with a 10X objective is 14 pixels or 8 μm . This

value correlates nicely to commonly accepted values for CD3 and CD4 lymphocyte subset size.¹⁶⁵

2.5.3 Fluorophore Considerations

Low membrane auto-fluorescence and resistance to non-specific staining from the quantum particles increased SBR and facilitated accurate cell identification. Red emitting nanoparticles had a greater propensity to stain the membrane than their green counterparts which is likely attributable to their larger size and increased attraction to the membrane. Although initial experiments using covalent coupling between cell specific antibody and QDs resulted in vague labeling and disappointing aggregation, these challenges were remedied with a secondary antibody-QD approach. **Table 2.3** further elucidates the shortcomings and attributes of the three covalent linking strategies. Although not the most direct route between biological target and fluorescent label, this method proved to be a specific and effective transduction pathway. This labeling scheme utilizing secondary antibodies provides the advantage of increasing the number of fluorophores immobilized on a single lymphocyte. With organic fluorophores, upwards of 7 molecules of dye per antibody may be achieved, but due to their larger size, this becomes impossible with QDs (5-20 nm). Allowing multiple secondary antibodies to bind to a single primary further amplifies the signal output.

<u>Technique</u>	<u>Drawbacks</u>	<u>Attributes</u>
Amine/Sulfhydryl (SMCC)	<ul style="list-style-type: none"> • may denature antibody • may bind inactive antibody fragment • 2-4 antibody per QD 	<ul style="list-style-type: none"> • fixed orientation of antibody • experimentally simple • 2-4 antibody per QD
Amine/Carbodiimide (EDC)	<ul style="list-style-type: none"> • antibody cross linkage • random antibody orientation • 15 + antibodies per QD • poor specificity 	<ul style="list-style-type: none"> • antibody cross linkage • random antibody orientation • 15 + antibodies per QD • poor specificity
Secondary Antibody	<ul style="list-style-type: none"> • sterically large • restricted by specificity of 2° • takes longer experimentally 	<ul style="list-style-type: none"> • native primary - high specificity • high SBR • low non-specific binding • secondary signal amplification

Table 2.3. Performance Features of Covalent QD Linking Techniques. A summation of the shortcomings and highlights of the EDC, SMCC, and secondary antibody conjugation methods reveals that, for this application, secondary antibodies are best suited due their lack of aggregation and intense, specific signal.

2.5.4 Quantum Dot Performance

A definitive explanation for the failure of established direct conjugation protocols in this application may be impossible; however, it may be attributable to the specific types of antibody used in the application or the generation of QD probes obtained from the vendor. As the EDC technique links non-specifically through free amines, a variety of antibody orientations is possible. This method yields high antibody to QD ratio which could potentially induce steric hindrance of active sites. Further, this EDC can potentially induce cross-linking of non-targeted amines. The SMCC method employs DTT, a strong reducing agent. While DTT may cleave the disulfide linkages along the IgG backbone, it may also break other S-S bonds, damaging tertiary structure and thus antigen specificity. This damage may go so far as to denature the protein and perhaps explains the aggregates seen. It should be noted, however, that this phenomenon is likely specific to individual antibody structure as **Chapter 3** details the use of the SMCC

method with excellent results in other non-cellular applications. Poor performance with directly bound QDs is not uncommon, and the secondary antibody method thus employed proved to be a specific and effective transduction pathway.^{76, 85} In addition, more than one secondary antibody may be bound to each primary, further increasing the number of fluorophores per lymphocyte and thus signal output. QD-avidin produces a large number of aggregates perhaps due to the size of avidin relevant to QD. The high NS from the Protein A experiment signal indicates that the protein is not specifically targeting the primary antibody and may be binding to irrelevant cell surface markers.

An accurate comparison of the performance features between biologically active QDs and molecular dyes is admittedly difficult.¹⁵⁸ Although information describing the attributes of QDs in their native state abounds in the literature,¹⁶⁶⁻¹⁶⁸ the spectroscopic data characteristic of the particles upon synthesis including molar extinction coefficient, quantum yield, FWHM, emission maximum, and average radius can radically change after passivation and further functionalization with biological ligands. Evaluation versus organic fluorophores adds the additional challenge of uncertain antibody to fluorophore ratio and differences in excitation intensity. Nevertheless, we observed photostability in the QDs superior to their molecular counterparts. In the time dependant study, in which relative intensities were calculated via each fluorophores initial intensity, Alexa Fluor 488 diminished to an intensity one half maximum in 280 s with Alexa Fluor 647 and FITC achieving this value in less than 80s (**Fig. 2.12**). Neither QD 565 nor QD 655 displayed significant intensity loss during this period.

2.5.5 Optical Gating

Analogous to the gates placed on data by flow cytometrists with parameters such as scatter and intensity, our microfluidic NBC and subsequent image processing allows individual components of a complex sample to be identified and quantified. In lieu of

lysing to isolate the fraction of interest, our system utilizes a size gate, i.e. membrane, to isolate white blood cells from the greater sample matrix. Both the size gate described above as well as a fluorescent intensity discriminator replace the scatter gate, typically related to cell morphology in FC. The intensity gate has two important applications. First is the SBR ratio, used to discriminate between authentic and non-authentic events. Secondly, the intensity gate addresses monocytes, an important consideration in these types of cell assays as the presence of such cells in samples could artificially contribute to the total CD4 count. Thus, low-level CD4 expressing monocytes are effectively ignored in the digital image leaving only green channel positive lymphocytes. Literature reference values of approximately 48,000 copies of the CD4 antigen on lymphocytes, with 3,000 – 9,000 copies on monocytes,¹⁶² corresponds nicely to the factor of 6 intensity difference between monocytes and lymphocytes in the NBC. Intensity histograms for all CD4 positive cells show baseline resolution between lymphocytes and monocytes. From these histograms, the ratio of monocytes to lymphocytes could be determined for each image and compared to the ratio determined by flow cytometry. The difference between the two methods was less than 6%. Finally, cell location on the membrane serves as a spatial gate to identify doubly positive CD3+CD4+ T lymphocytes of interest and a circularity gate in the ImageJ software rejects any debris that may be present on membrane surface.

2.5.6 Limitations and Comparison to Other Miniaturized Techniques

Although many reports have been published in which QDs are used for cellular imaging,^{30, 31} to the extent of the author's cognizance, this is the first report in which QDs are used for cellular quantitation in an enclosed, disposable device. Other methods using interference or impedance are frequently incompatible with peripheral blood samples as

they are overwhelmed by the presence of erythrocytes.^{139, 142} Manual counting methods involving magnetic beads¹⁴⁰ often fail to correlate to established methods above $R^2 < 0.90$, perhaps due to residual monocyte contamination. Other alternatives to FC using QDs are not self-contained,⁷⁷ an important consideration when dealing with HIV-positive samples. Literature reports using QDs quantitatively is limited to protein disease markers.¹⁶⁹ The membrane-based NBC correlates to FC at levels similar to non-labeling methods, based on cell affinity immobilization,^{138, 141} but also has the built-in capability for further analysis including ratios and percentages along with the capacity to exclude monocyte contamination in a rigorous way. Indeed, the membrane-based NBC can be extended to measurements of CD4/CD8 ratios, rare cell event detection,^{170, 171} panel evaluations similar to complete blood counts^{172, 173} and other advanced FC experiments.^{174, 175} As such, the membrane-based NBC serves as an interesting new approach that can service the requirements for a “personal flow cytometer” for use in both resource-scarce environments as well as in numerous research settings where the cost and complex nature of FC limits its current utility. Although only 6 samples were available for analysis with the QD-based approach (**Fig. 2.11C**), the correlation of results to FC suggests a study of greater scope be performed as well as experiments including immunocompromised individuals. To be certain, additional large-scale clinical trials including immunocompromised individuals needs to be performed before further claims may be made. Other limitations of this approach include the lack of FDA-approval and no integrated online filtration system for QD bioconjugate as the QD-secondary antibody conjugate required filtration by hand before labeling. Nevertheless, these results intimate another generation of analyzer size reduction may be realized.

2.5.7 Bridging Gaps—Towards a Condensed Analyzer

Thus, a number of different size regimes have been crossed through this use of the NBC system, **Figure 2.14**. On the cell surface, immunoreagents and QD particles with nanometer size characteristics are assembled to create a specific, intense signaling method (**2.14A**). Cells (microns, **2.14B**) then decorate a single FOV (millimeter, **2.14C**) within the NBC (centimeter, **2.14D**). The NBC shown in **2.14** is an additional generation forward-looking assay platform to be used in tandem with a similarly condensed analyzer (**2.14E**). Additional details on this unique analyzer type will be discussed in later. Regardless of whether signal is read with a benchtop microscope, or compact analyzer, these results have high potential to impact global health concerns.

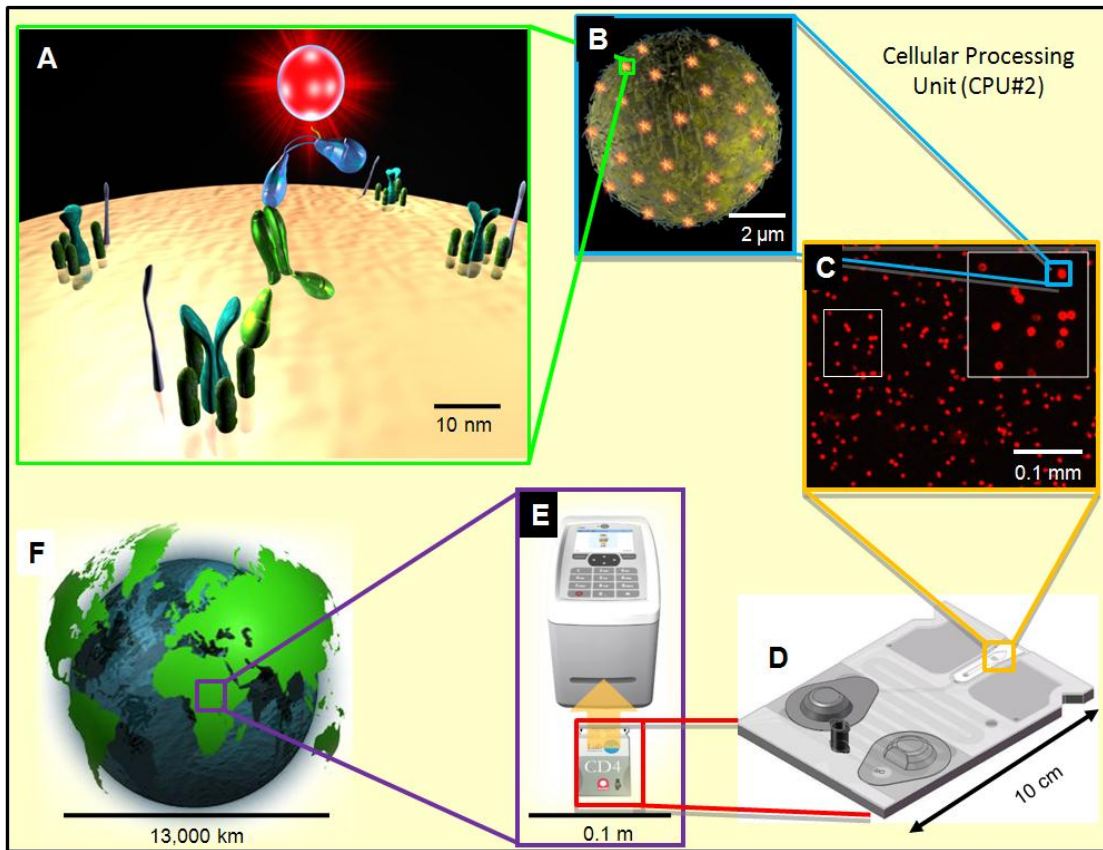


Figure 2.14. Size Regimes Involved in NBC. The NBC uses elements from many different size scales including nano (A), micro (B, C), and macro (D, E). The integration ultimately has the potential to have a global impact (F).

2.6 SUMMARY AND CONCLUSIONS

These experiments demonstrate the viability of incorporating a quantum dot detection scheme into a microfluidic analysis device for lymphocyte enumeration as a tool for monitoring HIV progression. Cell counts are obtained through interpretation of the fluorescent images with automated software and require no manual counting. The device's strong ($R^2 = 0.97$) correlation to gold standard flow cytometry is superior to bead-based systems and some other chip-based approaches. Proof-of-principle CD4% determinations, verified by traditional FC could be extended to absolute CD4 counts and CD4/CD8 ratios and other cellular analyses. Although additional trials are needed to fully assess the comparability of this cellular processing unit within the NBC system to traditional cell analysis methods, preliminary data shows strong correlation among healthy individuals. This synergy of advances in nanotechnology, materials chemistry, and microfluidics, promises to yield a final product with relaxed optical requirements, which yields diagnostic information rapidly, robustly, and reliably. Such a device would serve as a transformative tool in joining currently available anti-retroviral therapies with those individuals in need of such treatment, especially in resource-poor environments.

Chapter 3: Utilization of QD Bioconjugates in Nano-Bio-Chip Assemblages for Multiplexed Detection of Oncologic Biomarkers

3.1 CHAPTER OVERVIEW

The integration of semiconductor nanoparticle quantum dots (QDs) into a modular, microfluidic biosensor for the multiplexed quantitation of three important cancer markers, carcinoembryonic antigen (CEA), cancer antigen 125 (CA125), and Her-2/*Neu* (C-erbB-2) was completed. The functionality of the integrated sample processing, analyte capture and detection modalities was demonstrated using both serum and whole saliva specimens. Here, nano-bio-chips that employed a fluorescence transduction signal with QD-labeled detecting antibody were used in combination with antigen capture within a microporous agarose bead array supported within a microfluidics ensemble so as to complete the sandwich-type immunoassay. The utilization of QD probes in this miniaturized biosensor format resulted in signal amplification 30 times relative to that of standard molecular fluorophores, affording a reduction in observed limits of detection by nearly 2 orders of magnitude (0.021 ng/mL CEA; 0.11 pM CEA) relative to enzyme-linked immunosorbent assay (ELISA). Assay validation studies were also completed and demonstrated that measurements achieved by the nano-bio-chip system correlate to standard methods at $R^2 = 0.94$ and $R^2 = 0.95$ for saliva and serum, respectively. This integrated nano-bio-chip assay system, in tandem with next-generation fluorophores, promises to be a sensitive, multiplexed tool for important diagnostic and prognostic applications.

3.2 INTRODUCTION

Despite advances in treatment strategies, as well as molecular diagnostics, cancer remains a disease of grave lethality with more than 1.44 million new cases and

approximately 567,000 deaths estimated in 2008 in the United States.¹⁷⁶ Fundamental to the progression of healthy cells to cancerous ones is an alteration in the genomic and proteomic makeup of tissue; early detection of these changes remains key to decreasing morbidity. Protein biomarkers show promise in the treatment of cancer early in its development through screening as well as staging, metastasis evaluation, and determining response to pharmacologic intervention.^{177, 178} Occult blood tests, PAP smears, and prostate specific antigen (PSA) are established screening tools for cancer detection in asymptomatic individuals.¹⁷⁹ Breast cancer companion diagnostic tests based on Her-2/*Neu* and prognostic assays utilizing alpha-fetoprotein in testicular cancers have also been developed.^{3, 180} Additional progress has been made using protein biomarkers to monitor colon cancer response to treatment via carcinoembryonic antigen (CEA) or ovarian cancer via cancer antigen 125 (CA125).¹⁸¹ In spite of these advances, widespread use of protein biomarkers remains elusive due to methodological and technological obstacles.

Most biomarkers provide evidence for a generalized disruption of homeostasis, rather than indicate the presence of a specific disease as illustrated in **Figure 3.1**. Therefore, values outside the physiological normal range demand interpretation in conjunction with other assay results and clinical symptoms.^{182, 183} Early stage detection of cancer frequently requires the use of four or more biomarkers analyzed simultaneously to identify at-risk individuals with adequate confidence and currently used methods, based on ELISA, are not easily multiplexed.¹⁸⁴ Furthermore, in order to diagnose a cancer in its nascency, physicians recommend regular and frequent screening events—an arrangement incompatible with the high cost, lengthy turnaround times, and intrusive sampling procedures of current assay designs. In addition, most of the currently used screening methods have limits of detection (LODs) near the diagnostic decision values

that provide optimal separation between clinical categories, creating difficulties in accurately evaluating patients in early stages of neoplastic disease, when biomarker concentrations are only slightly altered.¹⁸⁵ Thus, the lack of cost effective, convenient and minimally invasive testing instrumentation, for use without sacrificing analytical and clinical accuracy, may translate into inferior clinical performance and hence poor patient outcomes.

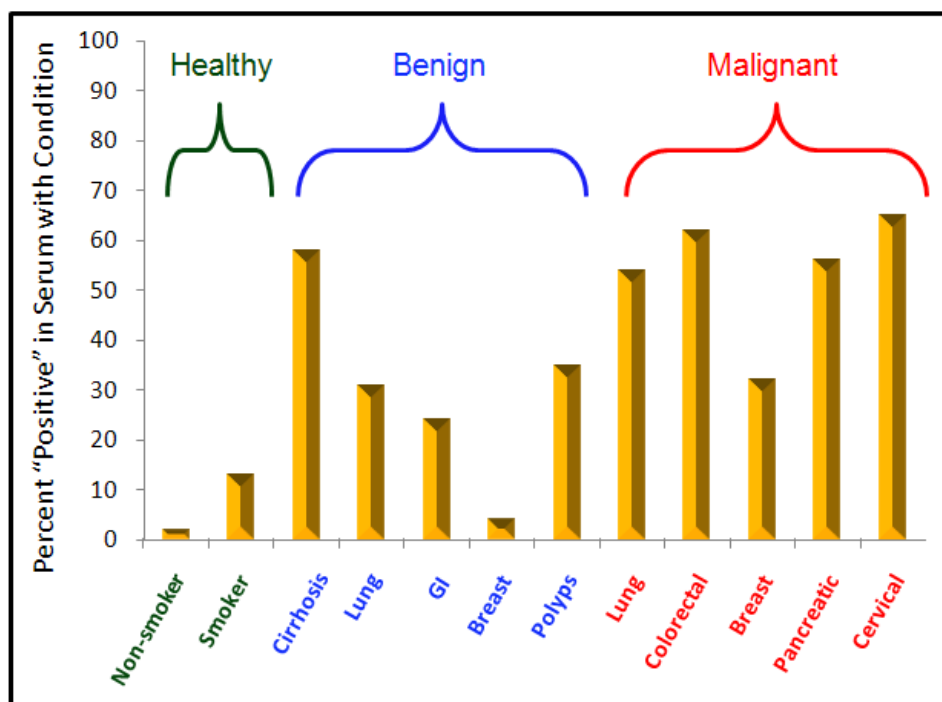


Figure 3.1. Ratios of Individuals Testing Above CEA Disease Threshold. Cancer and other disease biomarkers are rarely the proverbial “smoking gun” sought by diagnosticians. Rather, they indicate a generalized disturbance in normal body function and may present in both benign, malignant, and even asymptomatic individuals. For CEA, any number of conditions may cause an increase in serum levels. Note too, that no one condition is represented by uniform upregulation of serum CEA. (Data reproduced from Bayer Diagnostics/Siemens white paper.)

To satisfy this unmet clinical need, advanced integrated systems have become an increasingly attractive alternative to the centralized laboratory paradigm. These approaches combine a microfluidic architecture for sample and reagent handling with a biological receptor to identify the analyte followed by a reporter scheme and signal transduction and readout. These POC systems allow clinicians to have access to a wide array of diagnostic test results, information that is conventionally only available at large oncology-focused hospitals or via lengthy and expensive reference laboratories. From the perspective of cancer prevention and treatment, in which early diagnosis is key to long term survival, POC analysis devices are particularly advantageous. Their ability to offer early, routine, and frequent diagnostic events increases the ability of clinicians to identify neoplastic abnormalities. To supplement further the potential for facile screening events, an increasing number of POC methods have begun using saliva as a diagnostic medium. As dentists are the most frequent medical contact among asymptomatic individuals, the integration of oral fluids as a diagnostic medium into compact bioanalytical instruments allows a new generation of affordable, broadly accessible cancer screening.¹⁸⁶

Indeed, there is growing evidence that saliva serves as a “mirror of the body” and contains biomarkers that offer important information on both oral and systemic disease.^{187, 188} Important studies completed by Wong, Oppenheim, Malamud, Streckfus and others have resulted in critical information related to the genomic and proteomic profiles that are present in various oral secretions.^{189, 190} These profiles are critical to development of new diagnostic devices utilizing glandular secretions as well as components of the serum proteome present in these samples.^{191, 192} Whole saliva is simple to collect, store and is obtained easily in sufficient quantities for testing. For patients, the non-invasive collection method of oral fluid sampling reduces anxiety and discomfort,

thereby ameliorating testing antipathy and promoting more frequent screening events. In addition, as a constantly regenerated fluid, saliva offers a physiological snapshot with temporal resolution; work by Wong, Singh and others has made important initial contributions toward the use of saliva for POC analyses.^{193, 194}

Despite the obvious advantages offered by saliva, there are also distinct challenges associated with its use for analytical diagnostic testing. The saliva sample matrix is more variable and heterogeneous than serum, and contains high levels of mucins as well as proteolytic enzymes.¹⁹⁵ In addition, the concentrations of disease-relevant biomarkers in saliva are different from those found in serum specimens. Membrane proteins especially, may be expressed at concentrations several orders of magnitude lower than in serum, although they still reflect nicely the expression profiles of biomarkers found in blood that are of diagnostic significance.¹⁹⁶ Thus, because of the low levels of salivary biomarkers, it sometimes becomes difficult to distinguish between background and target-specific signal in these low concentration samples.

Here, the use of advanced detection methodologies, such as QDs, promises to help overcome some of the challenges inherent to using saliva in POC devices for cancer diagnostics. For the applications discussed in **Chapter 3** the high intensity and capacity for simultaneous emission are the most important attributes of QDs. In this study, the incorporation of QDs as detection elements in the NBC system is detailed for the measurement of three well-characterized cancer biomarkers: carcinoembryonic antigen (CEA), cancer antigen 125 (CA125), and Her-2/*Neu* (C-erbB-2). These NBC assay systems are explored in their capacity to serve as sensitive and specific cancer diagnostic tools for use with both serum and saliva samples. Here, the advantages of QDs relative to gold standard molecular fluorophores, are explored in an integrated, POC-compatible

device using a completely integrated system including all optics, mechanical and microfluidic elements in tandem with clinical samples.

3.3 MATERIALS AND METHODS

3.3.1 Immunoreagents

Phosphate buffered saline (PBS) at pH 7.4, used as a wash buffer as well as a diluent of the protein standards for the NBC assays, was prepared fresh daily and filtered with 0.2 μm membrane filter from Thermo Scientific (Waltham, MA). To maintain protein stability and reduce non-specific binding, bovine serum albumin (BSA) was added at 1% by weight from Sigma Aldrich (St. Louis, MO) to PBS. CEA antibody clone 057-10009 (capture) and M111147 (detecting) and CA125 M8072321 (capture) and M8072320 (detecting), were purchased from Fitzgerald (Concord, MA); Her-2/*Neu*-specific antibodies (AF1129-capture and MAB1129-detecting) were acquired from R&D Biosystems (Minneapolis, MN). An isotype (same species) control antibody was procured from Fitzgerald. Recombinant CEA, CA125, and Her-2/*Neu* antigen were obtained from Biodesign (Saco, MA), Fitzgerald, and R&D Biosystems, respectively. These were used without further purification and diluted in PBS/BSA to appropriate concentration. QDs with emission maximum at 565 nm (QD 565) and 655 nm (QD 655) were purchased from Invitrogen (Eugene, OR) as were reagents for a succinimidyl 4-(N-maleimidomethyl) cyclohexanecarboxylate (SMCC) facilitated antibody conjugation. Alexa Fluor 488 and reagents for immunolabeling were purchased from Invitrogen along with purification supplies.

3.3.2 Preparation of Beads

Agarose bead preparation was adapted from Gustavsson's method and tailored by Wong.¹⁹⁷⁻²⁰⁰ Briefly, agarose from Sigma Aldrich (St. Louis, MO) was added to 50 mL

water to the desired percentage and heated to 85°C in a water bath. A suspending solution of 10 mL Span85 also from Sigma Aldrich in 100 mL n-heptane was heated to 61°C. The agarose mixture was then introduced into the suspending solution and stirred for 1 min. As temperature dropped with vigorous stirring, the agarose gel beaded out of solution and precipitated to the bottom of the flask. Beads were then washed with a 50/50 ethanol/water mixture for hydration and size sorted by a sieve. Beads were stored at 4°C until future use. For linkage of antibodies and antibody fragments to the beads, the well established sodium cyanoborohydride technique described in Goodey and Lavigne's initial papers was used.^{116, 120, 201}

3.3.3 IgG-Fluorophore Labeling

Passivated CdSe/ZnS QDs were linked to antibody by established techniques.⁸⁵ Briefly, intact IgG molecules were subjected to dithiothreitol (DTT) treatment to cleave disulfide bonds. SMCC-activated QD particles were then incubated with the reduced antibody fragments linking them to the nanoparticles. The conjugate was purified by size exclusion chromatography to remove unbound antibody and concentrated with 50 kD cutoff centrifuge tubes to approximately 1 µM. Monoclonal detection antibodies were labeled with Alexa Fluor 488 via a tetrafluorophenyl activated form of the dye.

3.3.4 Clinical Sample Acquisition and Preparation

University of Texas Institutional Review Board approval was obtained to minimize patient risk for collection of both saliva and blood samples. Saliva was collected from 6 volunteers after stimulation of salivary glands by chewing an unflavored, sugar-free gum base for 5 minutes while expectorating into a collection tube with flow rates determined gravimetrically. The sample was protected from enzymatic digestion by addition of 1 µL 1 mM DTT and 1 mM sodium orthovanadate from MP Biomedicals (Solon, OH) per mL of sample and kept at 4 °C until analysis the same day.

Blood samples were collected via standard venipuncture at The University of Texas Health Sciences Center at San Antonio (UTHSCSA), centrifuged after clotting to remove cellular components, and stored at -20 °C until analysis. Serum analyzed with NBC at UT were drawn from a sample bank at UTHSCSA with the 24 samples selected across a range of CEA concentrations with 7 samples < 2.5 ng/mL, 10 between 2.5 and 7.5 ng/mL, and 7 > 7.5 ng/mL. In addition, 1 sample with a very high concentration (> 100 ng/mL) was used for linearity studies. Saliva samples were analyzed at dilutions of 1:20 and serum samples were analyzed undiluted unless sample volume available was less than 1 mL, in which case a 1:2 dilution was performed.

3.3.5 NBC System and Assay Conditions

As described previously, 280 µm agarose beads were prepared and covalently coupled with capture antibody via reductive amination, as were anisotropically etched silicon wafers which served to sequester the beads into unique, individually addressable wells.^{116, 120} Chip arrays with a 3x4 configuration were used for single analyte determinations allowing measurements of 9 analyte beads and 3 isotype control beads; 4x5 chip arrays were used for multiplexed analyses. The chip was immobilized between precision-cut adhesive layers designed for optimized microfluidic flow and affixed onto a polymethylmethacrylate (PMMA) base. Assays were performed at room temperature under continuous flow conditions: an initial 5 min 1% BSA/PBS blocking step to reduce non-specific binding (1.1 mL/min), antigen incubation with sample recirculation for 15 min effectively exposing sample to beads 3 times (0.2 mL/min), 2 min wash (1.1 mL/min), 5 min detecting antibody exposure (0.1 ml/min), followed by stringent washings and image acquisition.

The NBC was secured firmly beneath an infinity-corrected 4X objective and analyzed with a modified epifluorescent microscope from Olympus (Center Valley, PA)

equipped with a 12 bit CCD camera from DVC Co. (Austin, TX) and high pressure mercury bulb excitation source, which was evaluated with a universal optical power meter by Melles Griot (Albuquerque, NM). Sample flow was controlled by a variable speed peristaltic pump purchased from FIALabs (Seattle, WA). QD 565 images were acquired with a filter cube consisting of a 425 nm downfield excitation filter, a 475 nm long pass beam splitting dichroic mirror, and a 565 ± 10 nm emission filter. QD 655 images were obtained via a 420 ± 20 nm excitation filter, a 475 nm long pass beam splitting dichroic mirror, and a 655 ± 10 nm emission filter. Alexa Fluor 488 was viewed via a standard FITC filter cube: 480 ± 20 nm excitation filter, 505 nm long pass beam splitting dichroic mirror, and a 535 ± 25 nm emission filter.²⁰² Photomicrographs were captured via DVC software with adjustable gain, offset, and exposure time.

3.3.6 LOD and Assay Range

The LOD for the NBC assays were established as follows. First, assay dilution buffer in the absence of antigen was processed to establish the mean signal intensity on the analyte-specific beads for the zero-analyte condition. The standard deviation of the zero-analyte signal from bead to bead was recorded. The assay was then repeated with increasing concentrations of protein standard added in each experiment. The LOD was defined as the lowest concentration of antigen yielding an average bead signal three standard deviations above the mean value recorded for the zero analyte.

The linear dynamic range of the assay was defined by its LOD at the low end of the protein standard concentrations, and by limit of linearity, or the concentration producing a near saturation signal in the CCD camera, at the high end. The mean signal intensities of the analyte-specific beads from each run were then plotted against the analyte concentration to establish the dose-response curve for the given assay. The linear

portion of the dose-response curve established the quantitation range (also known as useful range) of the assay.

3.3.7 System Precision

Both intra-assay and inter-assay precision of our bead-based studies were determined. Intra-assay precision, in the context of system parameters, was derived from the degree of agreement in the signals obtained from at least three redundant beads within the array used in an assay run. Inter-assay precision was determined after evaluating the agreement between repeated measurements of an unknown sample. Repeatability of each assay was evaluated with a standard curve, testing the sample six times and then interpolating the value of the unknown from the standard curve for each assay run. Results from each run were compared and precision was reported as percent coefficient of variation (%CV).

3.3.8 System Linearity

A series of assays using one high volume, high concentration sample gave critical information on the ability of the NBC system to determine accurately sample concentration over several dilution factors, as well as the linearity of system response across a range of analyte intensities. This high concentration sample was diluted with increasing amounts of buffer, with a fixed total volume, until the signal produced by the diluted sample approached that of buffer only. Signal could then be plotted versus dilution factor and concentration determined for each dilution via calibration curve.

3.3.9 Immunodepletion

A depletion experiment, resulting in sample consisting of the remaining saliva matrix, verified the specificity of the CEA signal in saliva. To remove specifically CEA from saliva samples, agarose beads coated with three different types of monoclonal

antibody specific to CEA were mixed and incubated with the sample for one hour with moderate shaking as appropriate for a viscous solution. The sample centrifugation removed beads with the resulting supernatant decanted for analysis.

3.3.10 Method Comparison Studies

Saliva samples were analyzed for CEA both with NBC and with ELISA from BioQuant (San Diego, CA). CEA antigen standards used in the NBC were analyzed on the ELISA plate in addition to the manufacturer's provided standards, at identical concentrations for comparison purposes. ELISA was performed according to manufacturer's instructions on the same day as NBC saliva determinations and spectrophotometric color change was determined with a Molecular Devices SpectraMax Plus spectrophotometer (Sunnyvale, CA).

Method comparison studies for the serum tests were conducted in collaboration with UTHSCSA and the University Hospital, the primary in-patient facility for the University Health System of Bexar County, Texas. The Clinical Chemistry Laboratory retained serum samples submitted for routine testing that would normally be discarded after testing was completed. Marker values from these samples had been determined using conventional clinical laboratory FDA-approved technology, a Siemens Centaur (Deerfield, IL).

The patient identifiers were removed from the sample tubes and new identification numbers were assigned. Each sample was split into two aliquots and frozen at -20°C for future testing. One aliquot from each sample was shipped on dry ice to UT and the second aliquot was kept in the University Hospital Clinical Chemistry Laboratory. Testing by both methods was performed on the same day to minimize bias resulting from storage age differences between the specimens at the time of testing and to eliminate potential difference due to stability problems. Therefore, the serum marker

values using gold-standard testing could be compared with values obtained using the NBC system

3.3.11 Data Interpretation

Photomicrographs were saved as 12-bit colorized TIFF files and analyzed via ImageJ software from the National Institutes of Health (NIH, Bethesda, MD) with bead fluorescence signal intensity correlating to the concentration of analyte in the sample. Deconvolution macros were written using JAVA that converted the image to a grayscale 8-bit image with areas of interest (AOIs) drawn corresponding to individual beads. These AOIS serve as a rough boundary in which the bead resides. Four different methods were then be used to describe the information contained within the AOI. The line profile (LP) method scanned the AOI one row of pixels at a time—the highest pixel value from each successive line profile was then averaged to calculate a mean signal. The circular AOI (CAOI) method begins analysis in the geographic center of the region and expands outwards until it finds a circular region of pixels having the highest intensity. All pixels inside this circle are then averaged to give a measurement of intensity. The integrated density (D) technique takes the same circular region of pixels having the highest intensity uncovered in the CAOI method, and expands the analysis region 2 or more pixels on either side of the maxima. All pixels in this region are then averaged to yield an intensity measurement. Finally, the circular profile (CP) scheme simply averages the circular region identified in the CAOI and takes the mean pixel values. All four of these parameters may then be reported with their respective standard deviations and coefficients of variation.

3.4 RESULTS AND DISCUSSION

In previous work, the NBC assay platform was successfully employed in a number of analytical applications targeting detection of analytes in complex fluids, such

as serum and saliva.^{128, 203, 204} These assays utilized molecular fluorophores conjugated to analyte-specific antibodies as detection elements for the LOC sensors. The advanced performance characteristics of the LOC were attributed to the inherent properties of the porous structure and three-dimensional nature of the agarose bead sensor as well as the stringent washes associated with the microfluidic LOC design. The main objective of this study was to characterize the analytical improvements of cancer antigen NBC assays employing QDs as a detection moiety.

The QD-based platform includes all fundamental components of sandwich immunoassay, with the inclusion of agarose beads as solid phase support. Different clones of monoclonal antibody, specific to the protein of interest, serve as capture and detection bodies. **Figure 3.2** more clearly illustrates the differences between the NBC (**Fig. 3.2B**) systems and conventional ELISA (**Fig. 3.2A**) and its additional requirements of enzyme and conjugate. The other fundamental distinction between the two designs is the 3-dimensional design of the bead arrays versus ELISA's 2-D, planar plastic substrate. The sponge-like capacity of the NBC to sequester large amounts of analyte from samples is exploited—a sample pre-concentration method similar to dynamic headspace sampling.²⁰⁵ Also in contrast here are differences between QD-based and Alexa Fluor labeled detecting antibody. Due to size differences, the QD nanoparticle (**Fig. 3.2C**) can be linked to larger number of antibodies relative to its molecular counterpart. The effect this has on signal intensity is explained in greater detail in **Section 3.4.2**

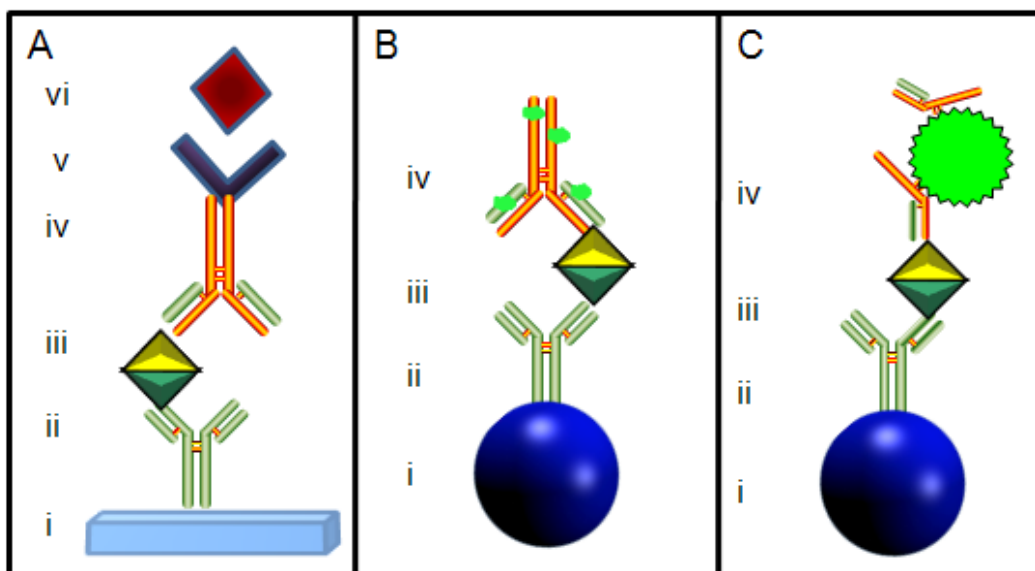


Figure 3.2. Formats of Sandwich Immunoassay. The fundamental components of sandwich immunoassay are retained across all three types of assay designs including underlying assay support (i), capture antibody (ii), antigen or biomarker (iii), and detecting antibody (iv). **A)** ELISA designs expand further this transduction pathway and include an enzyme (v) and substrate (vi) to affect a color change for a later absorbance measurement. **B)** The NBC system changes planar substrate in A, for the sponge-like agarose solid-phase support. The transduction pathway is also truncated to fluorophore tagged detecting antibody. **C)** The QD-based NBC design is typified by a larger fluorochrome and thus a detecting antibody to fluorophore ratio that inverts relative to **B**.

Each bead is individually addressable by location of well within the silicon chip and bead specificity determined by type of antibody covalently bound to the agarose support (**Fig. 3.3A**). The agarose bead supports are layered within the NBC between precision-cut layers of laminate adhesive designed for reagent delivery (**Fig. 1.4A**). These fluids are delivered through the top inlet of the flow cell apparatus, allowed to pass through and around the sensitized beads with nonreactive components passed on to waste through the lower port. Fluorophore conjugated detection antibody completes the immunocomplex and yields signal output digitally recorded by CCD camera. The intensity of fluorescence signal, embedded in a digital photomicrograph, relates directly

the amount of detecting antibody immobilized on the bead completing the sandwich immunoassay and thus, amount of antigen originally present in the sample (**Fig. 3.3B**).

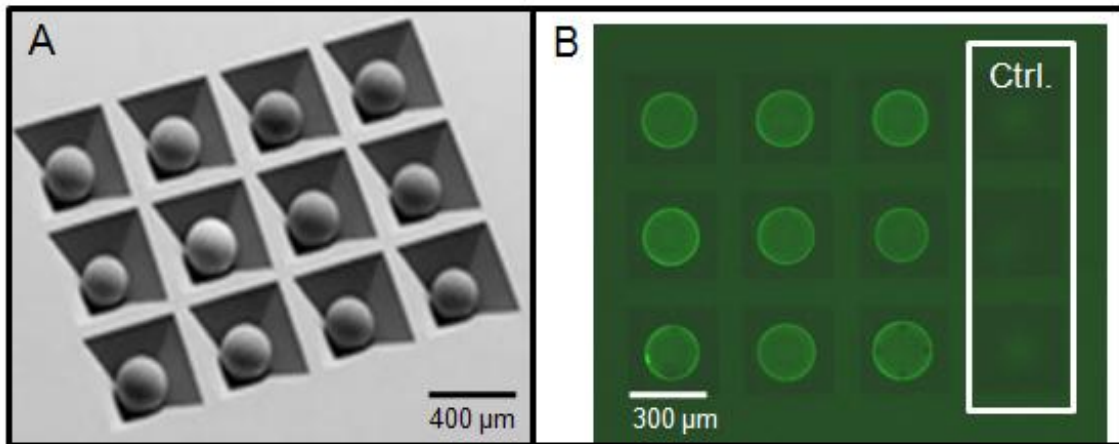


Figure 3.3. Bead-based NBC. **A)** SEM photomicrograph of beads in anisotropically etched silicon chip. **B)** Fluorescent image of beads after immunoassay including negative controls with DVC camera settings of ‘gain’ 10, ‘offset’ 0, and 1 sec. exposure.

3.4.1 QD Integration into NBC

Several steps are required to make optimal use of QDs in POC cancer diagnostic systems. For life science applications, stabilized nanoparticles are linked to a recognition element, i.e. antibody, through a variety of covalent and non-covalent strategies with all techniques emphasizing the importance of retaining QD optical properties and hydrophilicity as well as recognition moiety specificity.⁸⁵ The first challenge was identification of the optimal source of the QD labels for bead-based assays. Using a microtiter plate and spectrofluorimeter with $\lambda_{\text{ex}} = 400 \text{ nm}$, a 1 nM solution of Invitrogen (Life Technologies) nanoparticles ($\lambda_{\text{em}} = 655 \text{ nm}$) yielded fluorescence signal of 691.1 a.u., and a 1 nM solution of Evident Technologies nanoparticles ($\lambda_{\text{ex}} = 625 \text{ nm}$) signaled at 7.8 a.u., an amplification of nearly two orders of magnitude for the former. Thus, the remainder of these experiments utilized Invitrogen QDs.

Characterization of QDs in the transduction pathway of the bead-based sensors employed such figures of merit as background, signal, and non-specific signal (noise). Importantly, the definition of S, B, and N changes from that used in **Chapter 2**. Beads were analyzed with the line profiling method described in **Section 3.3.10**, which presents four possible methods to interpret the images. To determine which method delivered the most efficacious signal, **Figure 3.4** was constructed indicating that the LP method gives the steepest dose response curves and the most sensitive signal. In typical 3 x 4 arrangements, 9 bead replicates with a concentration of 3.0 mg/mL capture antibody reported specific signal and 3 beads with an isotype antibody served as controls (**Fig. 3.3B**). With a 4X objective, the macro resulted in the averaging of 104 successive line scans across each 280 μm bead or a resolution of 2.69 $\mu\text{m}/\text{pixel}$. The mean of the 9 beads was defined as *signal* (S), with the non-specific signal emanating from 3 isotype beads termed *noise* (N); *background* (B) was defined as output from biomarker-specific beads in the absence of antigen (zero calibrator).

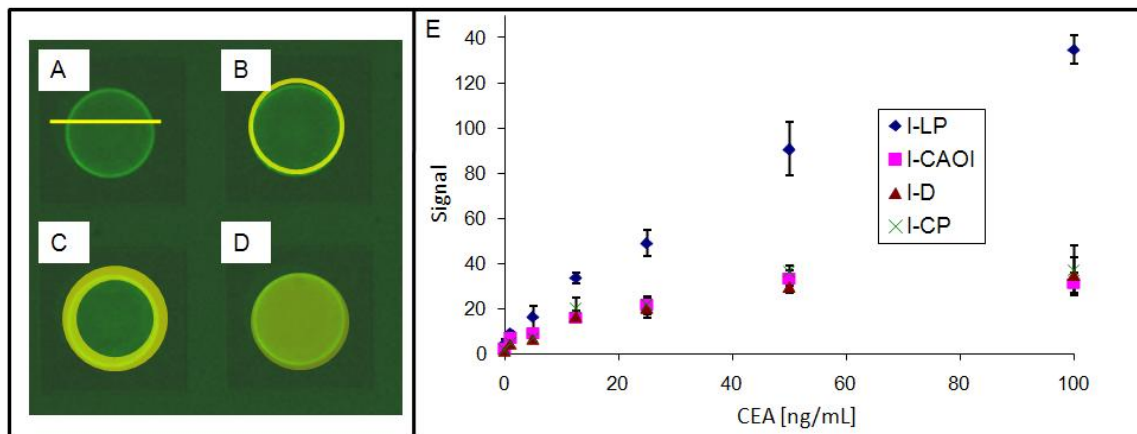


Figure 3.4. Analysis Methods Used in the Bead-based NBC. A graphic representation of the analysis methods described in **Section 3.3.10**: (A) Line profile (LP), (B) circular profile (CP), (C) integrated density or doughnut (D), (D) circular area of interest (CAOI). E) Dose response curves of the three different methods of analysis indicates that the LP approaches consistently yields the highest signal and most sensitive response.

With the proper source of nanoparticles indentified, naked QDs (unbound to antibodies), were examined for non-specific binding without any antigen present and yielded a S/N ratio of 1.05. When 100 ng/mL of CEA antigen was included and experiment repeated with bare QD particles, S/N was 0.70. These ratios, in addition to low signal output ($S < 2$), for these two experiments indicates that the minimal background and noise later observed should be attributed to non-specific biological interactions between antibody moieties, and not to aberrant binding of nanoparticle to immobilized antigen or bead scaffold. Next, this investigation explored the most appropriate method to prepare QD-antibody bioconjugates for quantitative biological analyses.

In **Chapter 2**, excellent labeling was achieved in the NBC via a secondary antibody strategy in which QD was thiol bound to secondary F(ab')₂ which was then linked to primary antibody on the cell surface (**Fig. 2.6**).¹³¹ This scheme was found to be incompatible with the bead-based assays, as the secondary antibody binds to the capture as well as detecting molecules. Other groups report using the avidin/biotin pathway for labeling biological analytes with QDs.^{81, 87} Although a pathway using biotinylated detecting antibody and avidin coated QDs successfully reported mid-level antigen values at S values above 60, it unfortunately resulted in non-specific noise and yielded S/N values of 0.82. This use of avidin/biotin is compounded by the sponge-like agarose solid phase support and its net of nano-scale tubules. The poor response observed for this application is due to inadequate passivation of the QD surface, electrostatic attraction of avidin to agarose, and the inability to remove the relatively large unbound QD-avidin-biotin-antibody immunocomplex from the bead's (2% agarose by weight) nano-net pores. For the CEA assay, this structure consists of QD (~15 nm) bound to avidin (12nm),¹⁵¹ biotinylated detecting antibody (10nm),¹⁵⁰ as well as antigen (27 nm),²⁰⁶ and capture

antibody (10nm), for a total immunocomplex length of 74 nm and molecular weight 550 kD. This size is on the order of the 100 to 300 nm pore diameters typical of 2% agarose gels making these conditions consistent with the clogging of bead apertures or QD probe trapped non-specifically in substrate interior.²⁰⁷

To engineer probes more compatible with the agarose environment, the protein capture elements were tailored to a size roughly half the QD diameter, or 7.5 nm. This decreased steric crowding within the bead, while retaining the analyte recognition portion of the antibody, by reduction of whole antibody via DTT, effectively cleaving the disulfide IgG backbone and exposing free sulfhydryls (**Fig. 2.5**). Preparation of the QD component of the bioconjugate proceeded via SMCC activation of PEG-carboxy coated nanoparticles.⁹¹ The active groups on cleaved IgGs then reduced onto activated QDs yielding an intense, specific transduction bioconjugate that was stable up to six months from preparation.

To verify specificity of the QD-antibody bioconjugate and determine B, an antigen free sample, consisting only of PBS buffer, was introduced followed by detecting antibody conjugate. After washing steps, B and N values below 1 resulted (**Fig. 3.5A**). Upon inclusion of CEA antigen in buffer, exposure of sample to CEA sensitized beads, followed by QD-CEA detecting antibody bioconjugate, a signal on the CEA sensitized beads developed proportional to amount of antigen introduced (**Fig. 3.5B, 3.5C**). For example, at 10 ng/mL, $S = 65.23$ and $S/N = 17.17$. Importantly, S values drop by 97.4% when a Her-2/Neu detecting antibody replaces the QD-CEA bioconjugate, demonstrating specificity of reporter probe. Values for N were 3.1% of S at mid level antigen concentrations, further authenticating the specificity of the immunoassay and remains consistently low across the range of antigen concentrations used in these experiments.

Results of background and isotype-controlled experiments for Her-2/Neu and CA125 antigen were similar to those of CEA with N less than 10% of S, and B values below 2.

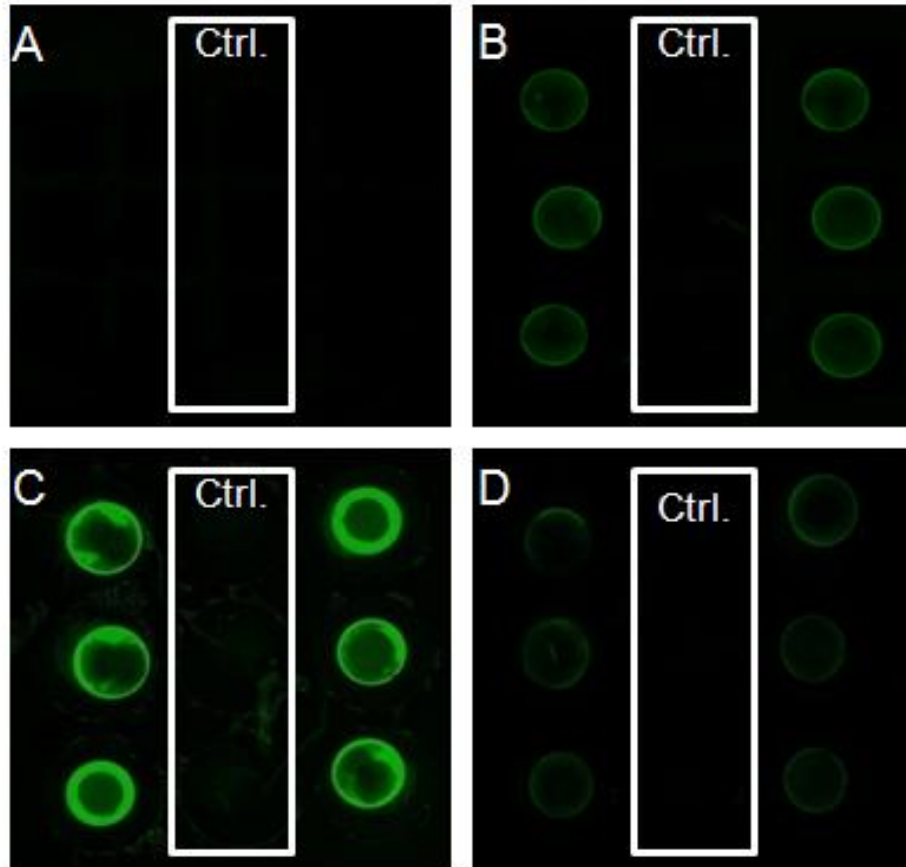


Figure 3.5. Photomicrographs Show Intensity Differences Between Samples. A) Zero-calibrator, negative control, consisting of buffer only gives little signal, while 50 ng/mL (B) and 100 ng/mL (C) show increasing fluorescent output. Fluorescent signal intensity advantage with QDs (C) versus molecular Alexa Fluor dye (D) is greater than 30 fold at identical antigen concentration. An additional row of negative control beads with similarly negative output on the photomicrograph right side was digitally cropped. All images procured at DVC camera settings ‘gain’ 10, ‘offset’ 0, with one sec. exposure.

3.4.2 The QD Advantages Relative to Molecular Fluorochromes

Having defined optimal modes for protein detection within the NBC system and having demonstrated a proof-of-principle application of QDs as the detection modality

for the NBC assays, the next objective was to compare their performance to traditional fluorophores. Such comparisons have challenges including the maintenance of similar excitation energies and antibody/fluorophore ratios.¹⁵⁸ For comparison purposes, isomolar concentrations of recombinant CEA (100 ng/mL) were analyzed under identical experimental conditions except for fluorophore on the detecting antibody. Through titration studies similar to **Appendix B**, 3.7 nM of the QD element of the detection body (0.47 $\mu\text{g/mL}$ of antibody) was determined to be optimal for labeling efficiency while keeping background signal to a minimum. As inherently hydrophobic materials, the tendency of QDs to aggregate at high concentration can be a challenge for use. Detecting antibody bioconjugates at 3.7 nM in PBS/BSA, in tandem with 0.2 μm nylon filtration of antibody-QD conjugate immediately prior to introduction into the NBC eliminated flocculation. These conditions were used for the below described comparisons.

Before exploring the capabilities of QDs relative to standard organic dyes, an initial study examined the attributes of three established fluorophores: fluorescein isothiocyanate (FITC), Alexa Fluor 488, and Alexa Fluor 647. The stability and intensity of isomolar concentrations of these three dyes were examined under constant excitation at λ_{ex} of 490 nm for FITC and Alexa Fluor 488 and 650 nm for Alexa Fluor 647. Signal intensity decreased to one half of initial maximum within 80 seconds for FITC and Alexa Fluor 650 and 280 seconds for Alexa Fluor 488. Furthermore, the initial values of S/N before significant photobleaching were recorded at 21.8, 8.0, and 4.2 for Alexa Fluor 488, Alexa Fluor 647, and FITC, respectively. These observations of Alexa Fluor 488 robustness are confirmed secondarily.²⁰⁸ Thus, to make the most stringent evaluation between nano-based and molecular systems, Alexa Fluor 488 was chosen for further direct comparisons.

To characterize the exact amount of both antibody and fluorophore in the AF488 and QD bioconjugate stock, quantitative absorption spectroscopy was employed. First, calibration curves using the monoclonal detecting antibody were constructed via a Bradford assay. These curves, in tandem with values for the fluorophore labeled bioconjugate, gave amount of IgG in the two detecting antibody preparations. Specifically, 5.9×10^{-6} M IgG was present in the AF488 conjugate and 7.6×10^{-7} M antibody was found for the QD case. To calculate amount of fluorophore, absorbance measurements were used with the extinction coefficients provided by fluorophore manufacturers; concentrations of 3.7×10^{-7} M QD and 2.5×10^{-5} M AF were measured. Since both bioconjugates were extensively purified with size exclusion chromatography, the fluorophore and IgG concentrations determined here reflected the amount of labeled detecting antibody.

To complete the studies exploring the intrinsic signaling capabilities of the QDs, a series of conditions were explored as follows. First, isomolar concentrations of fluorophore in the bioconjugate were prepared (3.7 nM) and used to label 100 ng/mL of CEA antigen, and images for both QD (**Fig. 3.5C**) and Alexa Fluor 488(**Fig. 3.5D**) recorded. Due to the larger size of the quantum dot (~15 nm with passivation layer) relative to the molecular Alexa Fluor dye, a greater number of antibodies may be bound to its surface (Immunoschematics in **Fig. 3.2B and 3.2C**). This specific batch of QD-antibody conjugate had an antibody to fluorophore ratio of 2:1. Conversely, more than one Alexa Fluor labeling molecule may be bound to each antibody and this ratio becomes inverted; approximately four Alexa Fluor elements attach to each whole IgG antibody. This necessitated an additional assay at isomolar concentration (0.47 μ g/mL) of antibody in the Alexa Fluor 488 bioconjugate.

Comparison of S values for the three photomicrographs (1 QD-based and 2 Alexa Fluor-based) indicates a values 33.5 times higher for QD versus Alexa Fluor 488 at isomolar fluorophore concentration and 6.5 for the isomolar antibody experiment. Similar to QD, Alexa Fluor 488 yielded N values less than 10% of S. Interrogation of the excitation optics with power meter at 400 and 480 nm, corresponding to the QD and Alexa Fluor optics, respectively, indicated a QD illumination strength advantage of 1.3. Thus, even when the relative concentrations of the labels are tracked carefully alongside the excitation powers, there is a significant enhancement of QDs relative to Alexa Fluor 488, one of the most robust commercially available fluorochromes. In addition to whole IgG for Alexa Fluor 488 labeling, Alexa Fluor 488 bioconjugates consisting of Fab and F(ab')₂ antibody fragments were also explored. These values were lower by a factor of 1.5 relative to whole IgG. An extended treatment of these results will be reported in **Chapter 4**. Regardless, the QD system was an order of magnitude more intense than Alexa Fluor 488—this substantial signal increase aids in detection of ultra-low concentrations of analyte as described below.

3.4.3 Analytical Performance of NBC Assays

After validating the QD immunoassays, the next objective was further characterization of their utility by determining the assay analytical performance, especially versus ELISA systems, the gold standard protein detection method since 1971.²⁰⁹ The first descriptor explored was assay time, which minimized four separate assay events: sample introduction, sample wash, detection bioconjugate incubation, and bioconjugate wash. On the NBC system, sample and bioconjugate incubation times were empirically determined by systemically reducing them from 30 minutes until the 5.0 ng/mL calibrator dropped below S/N of 10. Times of 5 minutes for sample flow and 15 minutes for bioconjugate were optimal and further reductions resulted in unacceptable

reductions in LOD. For washing, 1 minute of 1.1 mL/min PBS/BSA rinse eliminates the vast majority of unbound immunocomplex. For very low backgrounds, however, a two-stage final washing scheme was critical, which used the stringent 1.1 mL/min flush, followed by a 5 minute, 0.2 mL/min, gentle cleanse cycle. This slower rate allowed both diffusion and convection to remove unbound bioconjugate deep within bead infrastructure. The assay outline detailed above results in a total analysis time of 27 minutes, versus the 4 – 24 hours needed for conventional ELISA.²⁰⁹ Assays based on ELISA require the NBC steps described above, and also include substrate and color change (stop) steps. Furthermore, ELISA methods require a lab-based infrastructure including spectrophotometer, incubator, as well as manual liquid handling steps. Additional analytical parameters, such as assay range, linearity, precision, limit of detection were determined as follows.

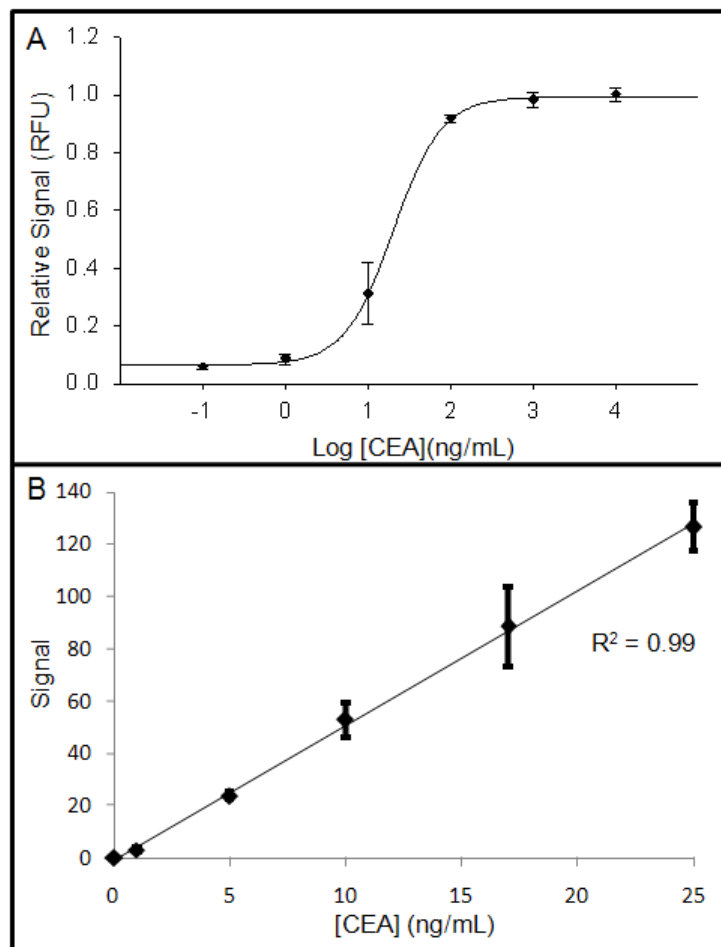


Figure 3.6. CEA Dose Response Curves. Curves were constructed by adding recombinant antigen to buffer followed by analysis with the NBC. **A)** Logarithmic figure spanning six orders of magnitude concentration of CEA with sharpest response overlapping physiologically relevant range from 0.1 to 100 ng/mL. Signal is relative to the maximum intensity produced by highest concentration calibration point and expressed as relative fluorescence units (RFU). **B)** Linear and sensitive dose response over region of typical sample concentration.

Calibration curves for all three analytes were constructed across a range of concentrations using recombinant antigen in buffer as well as a negative control, zero calibrator point. To determine the linear dynamic range, increasing concentrations of analyte across six orders of magnitude—from the limit of detection to the saturation point of the assay—give differing intensities as detailed in **Figure 3.6A** for CEA. Here, it was

critical that the linear dynamic range of the NBC assay overlap with the physiologically relevant range of analyte in biological samples. Commonly accepted disease diagnostic decision thresholds for the three analytes in serum are 2.5 ng/mL for CEA (5 ng/mL for smokers), 15 ng/mL Her-2/Neu, and 35 U/mL CA125.^{210, 211} The three analytes on the NBC system gave linear dose responses across the range of 0 – 100 ng/mL CEA, 0 – 60 ng/mL Her-2/Neu, and 0 – 400 U/mL CA125. Although all had acceptable performance, CEA was the focus for the remainder of the quantitative studies and later optimized to give the very sensitive dose curve seen in **Figure 3.6B**. Calibration data above 25 ng/mL was unnecessary for routine analysis, especially upon sample dilution. Importantly, the sensitivity of the NBC for any of the analytes attenuate easily in order to have a wider linear dynamic range by decreasing either capture or detection antibody concentrations (*vide infra*). Best-fit line regression analysis for the two methods gives $S = 5.144 [\text{CEA}] + 11.86$ ($R^2 = 0.99$) with the NBC approach, and $S = 0.0562 [\text{CEA}] + 0.2071$ ($R^2 = 0.98$) for ELISA at 0 – 50 ng/mL, where S, signal, is QD fluorescent intensity as described above in the NBC or absorbance at 450 nm (substrate λ_{max}) in ELISA. When S is standardized relative to the highest calibrator, and NBC and ELISA data plotted on the same axis, sensitivity, as determined by the slope of a best-fit line, is 1.9 times larger with the NBC versus ELISA.

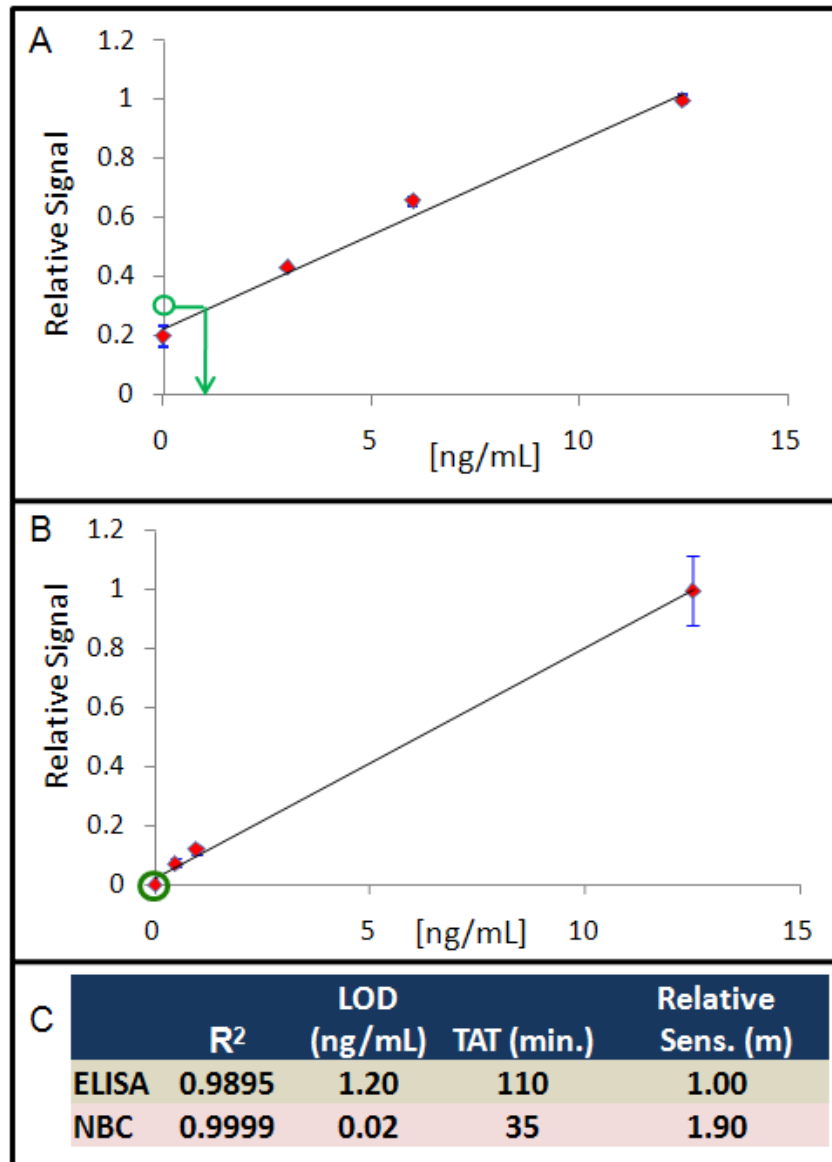


Figure 3.7. Limits of Detection via CEA Dose Response Curves. Both ELISA and NBC methods allow calculation of a LOD and are compared here by maximizing their 12.5 ng/mL signal intensity to unity and scaling the others relative to the most intense point. **A)** ELISA data is indicated by the red points while 3σ above the background (zero calibrator) is indicated by the green circle. The point is then graphically translated via the best fit line, to a point on the ordinate for LOD determination. **B)** This is repeated with NBC data to give the results in **C)** that indicates the enhanced performance of the NBC relative to conventional enzyme-based assays.

As mentioned above, low LODs are critical when analyzing saliva for biomarkers as analytes may be in lower concentrations than serum. The NBC system obtained excellent LOD values by having both a powerful transduction signal, as well as low background. Increasing the amount of fluorophore can increase the intensity of signal output, but may also increase background and non-specific signal. The use of QDs allows for a high signal output at relatively low concentrations of detection element to maintain the low background signals critical for excellent LOD measurements. The LOD for CEA, defined at 3σ above background, was 0.021 ng/mL in the NBC, 2.61 ng/mL when Alexa Fluor 488 signaling method replaced the QD-based system, and 1.20 ng/mL in ELISA; see **Figure 3.7**. The limit of linearity as calculated as 10 standard deviations above the signal of the background was 0.10 ng/mL CEA. This value was the LOD observed for more typical calibration curves as well. Similarly, low LODs were seen with Her-2/Neu with results of 0.27, 3.70, and 1.50 ng/mL for NBC, NBC-Alexa Fluor 488, and ELISA, respectively. For CEA, a glycosylated protein with a molecular weight of 180 kD, the LOD corresponds to 0.11 pM.²¹² Although improved performance with molecular Alexa Fluor fluorophores results after that system's optimization, these experiments were performed at the concentrations optimized for the QD platform allowing for a direct comparison between the two methods. Importantly, this order of magnitude improvement in LODs via QD detection compensates for the order of magnitude decrease in concentration of some biomarkers in saliva and also demonstrates the efficacy of the NBC for detecting trace amounts of biomarkers in diluted samples.²¹³ Thus, the enhanced signaling capabilities afforded with the QDs in the NBC system allow for salivary diagnostics to be completed more readily using the QD detection modality.

Reproducibility of the system was evaluated both from an intra-assay and inter-assay approach. As each analysis contains nine analyte beads, every assay results in a

mean concentration with standard deviation. The RSD values are <10%, with lower values found at decreasing concentrations of analyte. Even illumination within the excitation path, uniformity of NBC optical layers, and monodispersity of the reagent flow fields across beads within the silicon chip affects this value. Bead to bead variations are partly due to fluid dynamics for the setup used in these experiments, but do not appear to be due to inherent differences in bead composition or disparity in amount of capture antibody present on the beads. Computational fluid dynamic experiments, to homogenize the flow conditions across all bead local environments, are ongoing.

To evaluate precision between assays, one serum sample (mean value 8.60 ng/mL) was examined 6 times—these analyses had a %CV of 6.5; variances for ELISA approach 40% depending upon analyte concentration.²¹⁴ An additional study of linearity and precision utilized a single high volume, high concentration serum sample analyzed unadulterated and at five dilutions down to 1:32. Background corrected intensities were converted to concentration by calibration curve, and multiplied by dilution factors resulting in the corrected concentration. Fluorescence signal as a function of dilution factor was also linear at $R^2 = 0.99$.

3.4.4 Analytical Performance of NBC for Clinical Samples

The NBC analytical performance was evaluated in the context of CEA determinations for both saliva and serum samples. The NBC approach was compared to standard methods in the context of correlation studies. For the initial stages of these clinical proof-of-principle studies, signal generated by saliva was compared to recombinant CEA antigen. **Figure 3.8A** displays rows of beads from larger photomicrographs of recombinant CEA antigen (**Fig. 3.8Ai**, 50 ng/mL), 1:4 dilutions of saliva (**Fig. 3.8Aii**), saliva (1:4, **Fig. 3.8Aiii**) spiked with recombinant antigen (to 50 ng/mL), and saliva (1:4, **Fig. 3.8Aiv**) depleted of CEA by immunoaffinity

chromatography. The presence of signal in saliva, increase upon spiking with antigen, but most importantly, 94.84% (**Fig. 3.8B**) reduction in signal when CEA was exclusively removed from the sample, gives strong credence to the validity of this saliva-based assay on the NBC and the authenticity of CEA-specific signal. Indeed, saliva signal changes from near saturation of 8-bit camera (S values approaching 255) with the authentic sample, to values near PBS buffer blank for depleted samples.

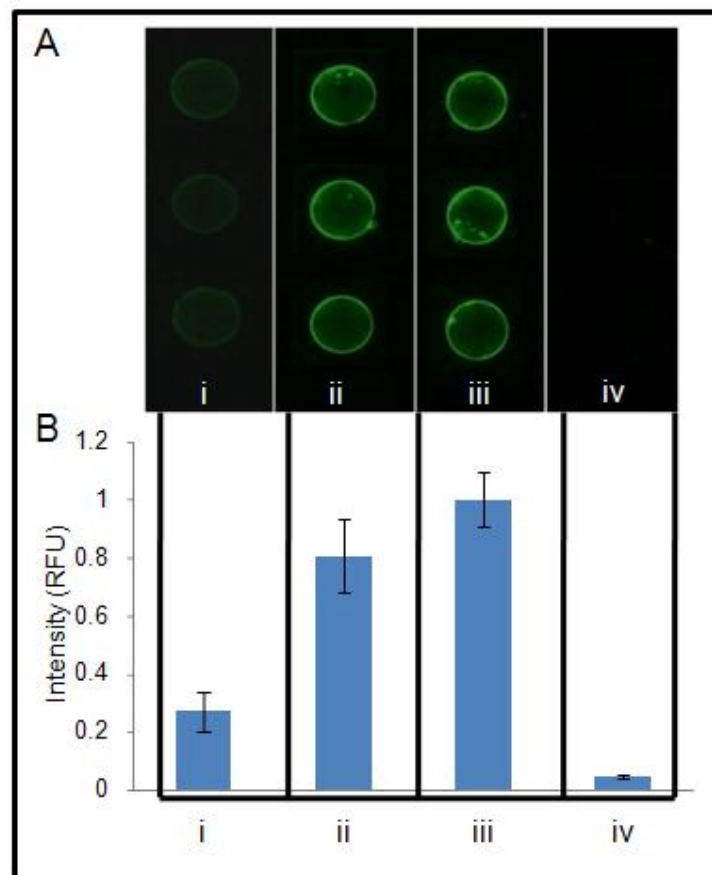


Figure 3.8. Validation of authentic CEA signal in saliva. A) Assay results of **i**) recombinant antigen at one half calibration curve maximum (50 ng/mL), **ii**) saliva at 1:4 dilution, **iii**) saliva sample spiked with recombinant antigen, **iv**) CEA depleted saliva. One row from each image was digitally sliced to create montage above. B) Results after digital image processing indicates the specific nature of CEA signal. (All images have been background corrected and use one second of exposure.)

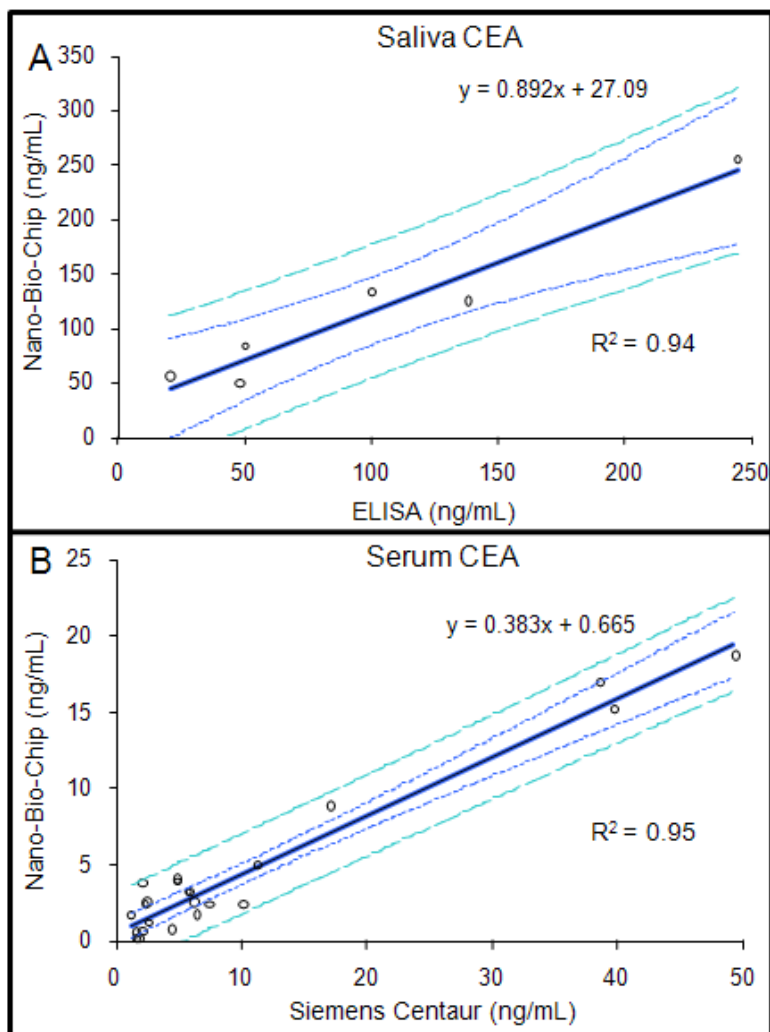


Figure 3.9. Analytical Validation of NBC System via Clinical Samples. Saliva (n = 6) (A) and serum (n = 24) (B) samples correlate well with measurements achieved on reference methods. Saliva samples were validated versus ELISA; serum samples via a Siemens Centaur clinical chemistry analyzer. In addition to best fit line (solid), the 95% confidence interval (short dash) and 95% prediction interval (long dash) are presented.

For a correlation study, stimulated whole saliva was collected from apparently healthy subjects and these specimens analyzed with the NBC and concurrently with ELISA. Shown in **Figure 3.9A** is the correlation graph between the two methods. Here

a strong correlation is noted with R^2 value of 0.94. The relatively high concentration (> 50 ng/mL) of analyte present in saliva is consistent with previous reports and is reasonable, as CEA is a known epithelial protein.^{215, 216} In serum, the NBC platform correlates nicely also with an automated clinical analyzer (Siemens Centaur) and yields R^2 value of 0.95 for 24 samples (**Fig. 3.9B**). Although the serum results correlated, they did not agree. This may be due to differences in standards as the NBC reports results approximately double that of Siemens Centaur. Unfortunately, it was not possible to analyze the onboard standards used in the Siemens instrument on the NBC. To ascertain whether matrix interferences were responsible for this discrepancy, standard additions allowed concentration calculations in addition to the calibration curve method for a single sample. The standard additions experiment resulted in an approximately 2-fold higher concentration value than the single point calibration curve determination, which corresponds to the twice-high concentrations found by the Siemens instrument. These systematic differences may also be due to variations in the values for standards and/or changes in the specimen concentrations that resulted from the differences in sample handling at the two sites. Nevertheless, these proof-of-principle pilot studies yielded strong correlation results for both serum and saliva analysis using the new NBC relative to established laboratory-based methods.

3.4.5 Multiplexing Capabilities

As stated above, the use of numerous cancer biomarkers increases both the sensitivity and specificity of cancer assays; the capacity of the NBC for use in multiplexed tests is demonstrated.¹⁸⁴ First, dose response curves for Her-2/Neu, and CA125 were prepared and tailored to match the physiologically relevant range of concentrations. The analytical response of these assays and LOD calculations are presented in **Figure 3.10**.

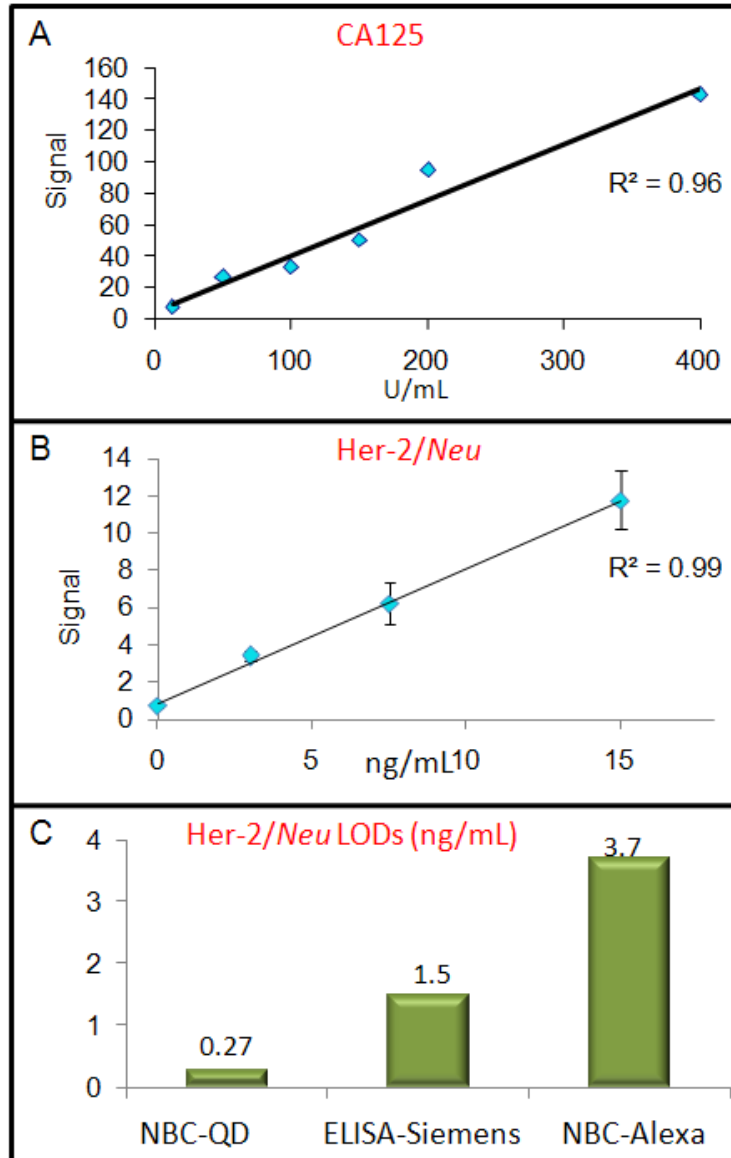


Figure 3.10. Expansion of NBC to Additional Analytes. Dose response curves for CA125 (A) and Her-2/Neu (B) show linear response across the physiologically relevant range. C) Her-2/Neu detection limits calculated for three different detection methods. The NBC-QD approaches yields values five times lower than ELISA methodology, and nearly 14 times lower than NBC-Alexa Fluor 488. This order of magnitude is similar to the intensity advantage seen in Section 3.4.2.

Next, beads in redundancies of three and sensitized to either CEA, Her-2/Neu, and CA125, were arranged in a 4 x 5 chip along with isotype control beads. One-row portions of the resulting photomicrographs appear in **Figure 3.11A**. All beads produced signal upon introduction of all three antigens, in buffer, at concentrations near the dose curve maximum, as well as a 9.2 nM cocktail of all detecting antibodies (). When only Her-2/Neu antigen and the detecting antibody cocktail was introduced, signal from the specific interaction between immobilized Her-2/Neu antigen and Her-2/Neu detection bioconjugate was 20.2 with a small amount of signal cross talk emanating from the CEA ($S = 0.03$) and CA125 non-specific beads ($S = 0.97$) (**Fig. 3.11Aii**). This assay was repeated for CA125 (**Fig. 3.11Aiii**) and CEA (**Fig. 3.11Aiv**) analytes and the strong, specific signal normalized to a value of unity (**Fig. 3.11B**). Signal from non-specific beads was less than 5% of the most intense, specific signal for all three experiments. Importantly, no signal increase occurred when using the detection cocktail, versus individual detecting antibodies.

In addition, an analogous series of assays in which all three antigens at values near the dose curve maximum, i.e. 25 ng/mL for CEA were introduced concurrently, followed by sequential interrogation by a single detection antibody (3.7 nM) resulted in non-specific interactions that were less than 5% of the specific signal. This data demonstrates the utility of the NBC sensor as a highly specific, multiplexed tool for analysis of complex fluids and reinforces the capability of use in diagnostic profiles.

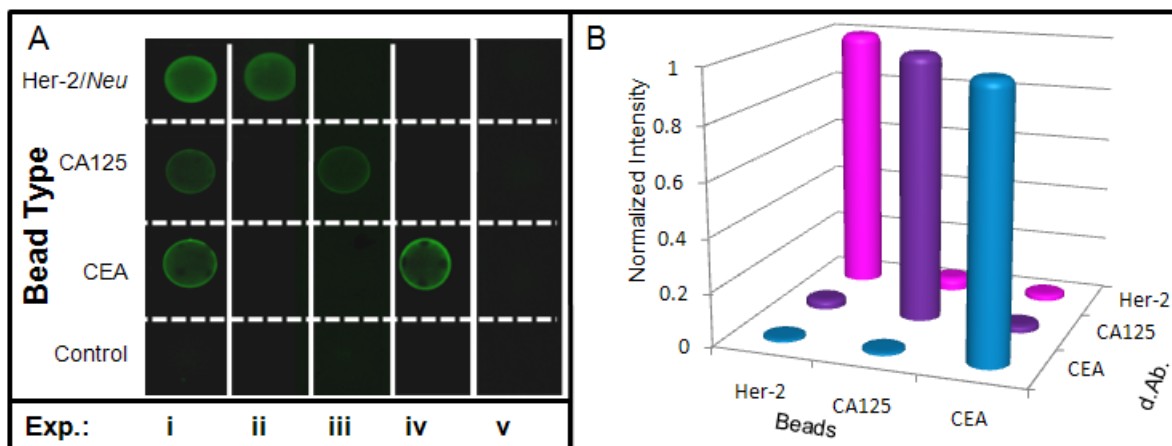


Figure 3.11. The NBC Multiplexes via the Spatial Arrangement of Beads. **A)** In these experiments, cross-reactivity was evaluated. **(i)** All three antigens, at concentrations near calibration curve maximum, were incubated concurrently followed by a cocktail of all three detecting antibodies. **(ii)** Beads were exposed to only Her-2/Neu antigen, and again, the detecting antibody cocktail. Similarly, assays specific to CA125 **(iii)** and CEA **(iv)** were performed, as well as a zero antigen, negative control **(v)**. **B)** Non-authentic output emanating from untargeted beads plotted as a percentage of specific signal intensity shows strong specificity across all three analytes. Non-specific signal (noise) was less than five percent of the intense, specific signal. (All images have been background corrected and use one second of exposure.)

To demonstrate the capacity of the NBC system to perform a multiplexed assay within a single bead, beads functionalized with 1.0 mg/mL CEA or 1.0 mg/mL CA125 specific capture antibodies (or both antibodies at 1.0 mg/mL) were arrayed on a single chip along with beads conjugated to isotype control antibody. Both antigens and a cocktail of relevant fluorescently labeled detection antibodies at (1:100 dilution or 3.7 nM) were introduced into the NBC. Here, detecting antibody specific to CEA and bound to QD 565 fluoresces green, and CA125 antibody labeled with QD 655, emits red shifted signal. These experiments revealed the specificity of bead-based reactions on beads loaded with single-type antibodies, as well as the capacity of the dual function beads (loaded with both types of antibody) to capture and detect both antigens.

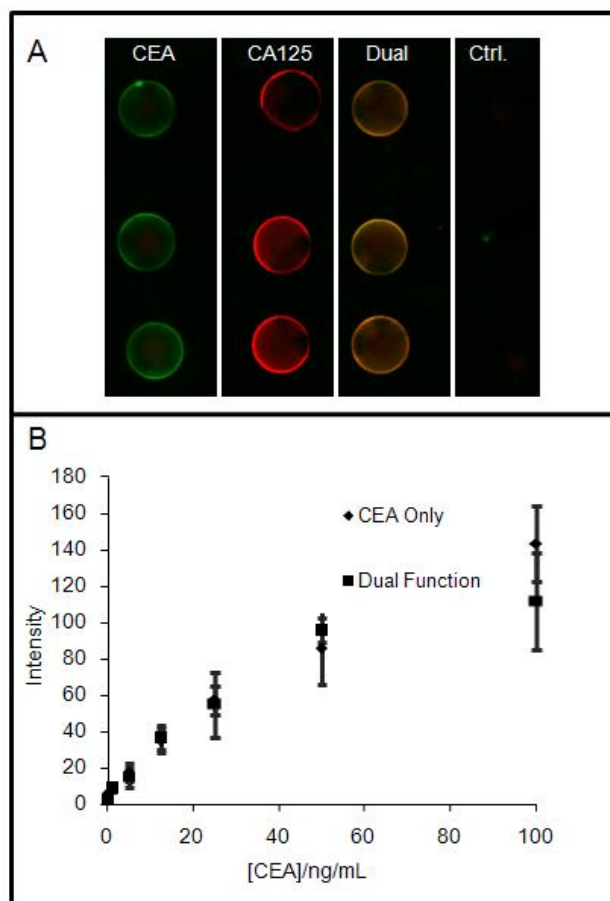


Figure 3.12. Intra-bead Multiplexing. **A)** Multi-analyte capabilities of the NBC include intra-bead duplexing in which dually functionalized beads measure two analytes concurrently. Beads sensitized to CEA, CA125, and both biomarkers are used simultaneously on a single chip and demonstrate independent assay behavior. **B)** Across the physiologically relevant range of concentrations, no statistical difference is seen in fluorescent signal output between sole CEA and dual CEA/CA125 beads. (All images have been background corrected and use one second of exposure.)

As expected, the CA125 sensitized beads fluoresced red, while the CEA sensitized beads fluoresced green (**Fig. 3.12A**). The dual-function beads, which fluoresced orange after this assay, demonstrate efficient detection of both captured analytes and later, their respective detecting antibody. For assays at concentrations near the dose curve maximum (25 ng/mL CEA and 300 U/mL CA125), the S/N values for the dual function and singly selective CA 125 beads are not significantly different at $1.59 \pm$

0.25 and 1.79 ± 0.30 , respectively. Similarly, S/N values for single and doubly selective CEA beads are 130 ± 12 and 104 ± 22 . Differences between the two assays systems are due to non-specific binding of detecting antibody.

This bead type increases NBC throughput by quantifying a larger number of analytes in the same small device footprint. Furthermore, the CEA-specific signal response achieved by both CEA-sensitized and dual-function beads are statistically identical across the physiologically interesting region (**Fig. 3.12B**). Here, little to no reduction of signal is seen in the dual-function beads versus their singly selective counterparts either at higher (100 ng/mL) analyte or lower concentrations (1 ng/mL), again demonstrating that these bead types may be efficiently used in this system to increase throughput. When CA125 antigen dose response is performed (0 - 400 U/mL), dual function beads and single function beads behave identically regardless of CEA antigen presence, similar to **Fig. 3.12B** (data not shown). This is the first demonstration of multianalyte detection on a single bead with this NBC system type. The additional element of multiplexed capacity demonstrated here via multiple colors on individual beads, allow an increased number of independent assay systems to achieve robust measurements in the same miniaturized space. In addition, as UV light easily excites different color QDs (corresponding to unique analytes), this novel multiplexing scheme, in tandem with a dual bandpass emission filter and color CCD detector, would not increase analyzer optical requirements, a design critical for POC systems.

Table 3.1 expounds further the performance descriptors of the NBC versus ELISA as well as other clinical chemistry analyzers for the CEA assay. Modern pathology laboratory analyzers yield utilize a chemiluminescent pathway with results in approximately an hour. An important feature not detailed in **Table 3.1** is analyzer size. None of the methods other than the NBC is amenable to POC analyses.

Instrument	Manufacturer	Method	LOL (ng/mL)	LOD (ng/mL)	Inter-assay CV	Intra-assay CV	Time (Minutes)
NBC	UT	Fluorescence Immunoassay	100	0.02	<10%	6.5%	27
ELISA	BioQuant	ELISA	50	1.2	10%	< 40%	120
Vitros Eci	Ortho	Electrochemiluminescence	100	0.5	10%	10%	60
IMMULITE	Siemens	Chemiluminescence	550	0.2	< 10%	< 10%	> 60
Elecsys	BMC	Electrochemiluminescence	25,000	100	4.6%	8.5%	Unknown

Table 3.1. Performance features of CEA analysis methods. Comparisons between the NBC, ELISA, and bench-top hospital laboratory analyzers reveals superiority of NBC. Detailed here are coefficient of variation (CV) both within a single experimental run and between assays. The LOD listed here was defined previously while limited of linearity (LOL) is defined classically as the concentration at which a best-fit curve deviates at greater than 10%.^{217, 218}

3.5 CONCLUSION

The construction and validation of a microfluidic biosensor incorporating the intensity and fluorescence attributes of semiconductor nanoparticle QDs is completed. Although some reports have recently demonstrated quantitative immunoassay of cancer biomarkers such as CEA with QDs via both avidin and SMCC facilitated bond formation, very few studies have utilized QDs to measure human specimens versus gold standard methods.⁸¹ These prior studies rely on QDs in tandem with a chaperon structure such as a latex bead.¹⁶⁹ To the extent of the author's cognizance, this is the first report in which QDs provide quantitative cancer biomarker information using blood and/or salivary clinical samples.

The NBC system has several advantages over conventional approaches. First, the QD-facilitated transduction signal yields output values >30 times that of conventional

fluorophores without enzymes or any secondary signaling amplification reagents. This feature allows the device to produce sensitive, linear response curves across the physiological relevant range of CEA, Her-2/*Neu*, and CA125. Second, this high signal output, combined with effective QD conjugation methods and efficient analyte processing within bead-populated MEMS structures, affords very low LOD values for these essential cancer antigens. In this study, we achieve LOD values of 0.02 ng/mL (or 0.11 pM) for CEA, values competitive with the most sensitive CEA assays reported to date.²¹⁹ The LOD for Her-2/*Neu*, 0.27 ng/mL, is lower than commercially available ELISA kits (2.5 ng/mL) and benchtop analyzers (0.5 ng/mL). These values translate into low-level detection of the analyte in saliva for minimally invasive screening procedures. Third, turnaround time (<30 min) is substantially shorter than methods based upon ELISA technology and is quite amenable to analyses at the POC. Finally, preliminary studies combining all three biomarkers onto a single chip reveal low cross-talk and high analyte specificity using real biological samples. The NBC also demonstrates the capacity to increase throughput via multianalyte beads. Such multiplexing capacity is critical in designing cancer sensors that are both selective and specific. As mentioned by QD pioneer Shuming Nie in a recent review, the potential for “nanotyping”, or multiplexed profiling of disease fingerprints via QDs, is an exciting application of this class of fluorophores that is closer to realization upon completion of this study.⁸⁵ Flexible, modular, and multiplexed analysis platforms are essential tools in better understanding the relationship between a dynamic proteome and clinical symptoms and disease outcomes.

The NBC system was validated as a tool for the detection of CEA in both saliva and serum clinical samples and correlated to reference methods, $R^2 = 0.94$ and $R^2 = 0.95$, respectively. The inclusion of saliva and other glandular secretions opens the possibility

for a new testing prototype to emerge. This area was previously relatively unexplored due to the low levels of analyte present, but due to the efficient capture of agarose beads and high signaling capabilities of QDs, new advances in saliva-based diagnostics may now be envisioned. The demonstration of the NBC's ability to obtain low LODs, in conjugation with its verified compatibility with oral fluids, suggests that it would be an ideal tool for use in screening individuals for cancer by detecting biomarkers in saliva. This work is consistent with other literature reports describing methods to quantify tumor markers in saliva as screening cancer tools,^{194,220} but is among the first to validate QDs as quantitative and sensitive reporters in the context of clinical sample analysis.²²¹ The integrated, disposable NBC described herein is highly compatible with the prototype analyzer described previously that combines optics, battery power, optics, and image analysis into a compact tool.¹³¹ Such an arrangement is among the most integrated use of applied nanomaterials reported to date and expands further the utility of our compact NBC analyzer.²²¹

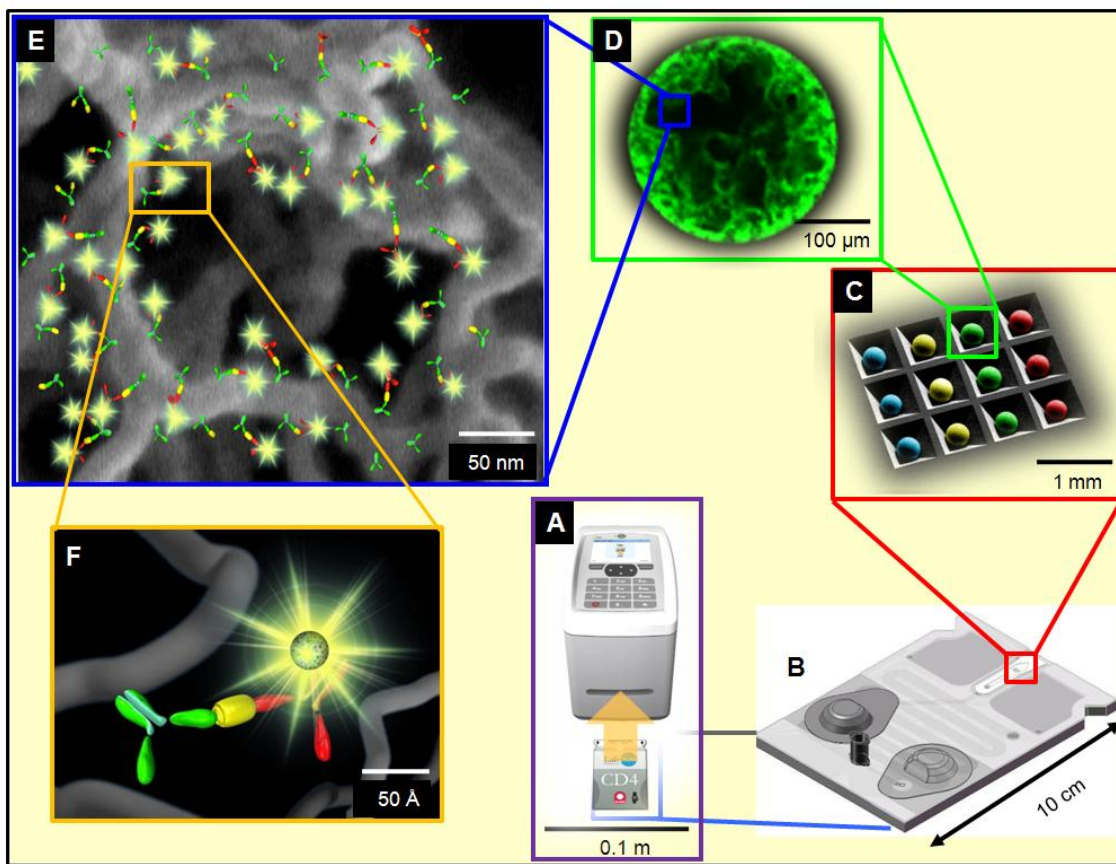


Figure 3.13. Molecular Level Programming of NBC Assay components. The integrated NBC cartridge (**B**) is read with a compact, self-contained analyzer (**A**). This labcard still contains the fundamental agarose bead micro-reactors (**C**) as the research grade NBC (**Fig. 1.4A**) only in tandem with more elegant microfluidic condensations. It is this agarose core (**D**) that contains the nano-net serving as support for immunocomplexes. **E**) Close-up of a single sandwich immunocomplex within the bead gives molecular-level insight not attainable in the typical representations such as those in **Figure 3.2**.²²²

In addition to hosting ultra-sensitive assays, the miniaturized NBC assay platform, offers a multi-analyte testing capacity, whereby results for multiple targets come from single experimental runs. Future work will incorporate additional biomarkers onto the platform as well as arrays designed to meet specific diagnostic needs as in a ‘well-woman’ themed chip similar to the cardiac chips previously reported.²²³ Such a system

would have markers indicative of female-specific cancers integrated onto a single wafer used in tandem with current well-woman type exams, again at the POC. A further application for these ultra-low detection limits includes screening patients for reoccurring cancers post-surgical tumor removal.²²⁴ For example, PSA levels in patients post-prostatectomy do not drop to zero, rather they decrease 2-4 orders of magnitude lower than patients who enjoy a healthy prostate—values in the femtomolar regime are reported.^{224, 225} The PSA analyte also shows promise in detecting breast cancer in women.²²⁶ Conventional ELISA cannot screen these patients with ultra-low amount of circulating PSA for the subtle changes in levels that may indicate a resurgence or presence of cancer. This work with NBC systems is potentially appropriate in this area. In addition, other applications including oligonucleotide quantitation, gene expression work, and biomarker discovery could all potentially benefit from these advances in NBC performance.^{227, 228} Future work toward decreased fluid handling techniques and next generation optics that behave in a cohesive fashion with the QD signaling moieties, will continue to reduce overall analyzer size leading to even more elegant and functional POC designs.

Chapter 4: Molecular Level Programming of NBC Sensor Components for a Universal Approach to Assay Building

4.1 CHAPTER OVERVIEW AND GOALS

The work presented in **Chapter 4** draws more analytical comparisons between the NBC and typical ELISA measurements that those presented in **Chapter 3**. The three elements identical in both systems: capture antibody, antigen, and detecting antibody are examined and their impact on immunocomplex and assay development is elucidated. The unique features of the bead's three-dimensional reaction coordinates are not fully understood relative to the extensive characterization of the ELISA system.^{209, 229} Here, another generation of study on the 3D bead matrix and internal reagent transport, including location of all three immunocomplex contributors, helps to solidify insight into those factors that contribute to the high performance assay characteristics typical of the NBC. **Figure 4.1** illustrates that diffusion, convection, and kinetics are all important contributors to reagent transport in the NBC and experiments in this chapter strive to gain both a mechanistic understanding of these phenomenon as well as to exploit this knowledge in context of exploring enhanced immunoassay performance characteristics. Improved molecular-level perspectives on the space-filling geometries typical of the agarose bead will hopefully lead to a superior appreciation for the variables necessary to consider upon construction of a new assay system or optimization/attenuation/variation of a current analysis format.

As detailed in **Figure 3.2C** and **Figure 4.1D-F**, at the core of the bead-based NBC is an immunoassay sandwich attached to the NBC scaffolding infrastructure (agarose strands). In this chapter, the *concentration* and *size* of fundamental experimental building blocks within the NBC will be tailored to optimize assay performance: capture antibody, detecting antibody, and agarose filament. Previous studies using the NBC take the general format of addressing a unique challenge. Assay

conditions are usually manipulated to solve a specific problem, that is, to optimize an assay or series of assays for an individual application. The studies in **Chapter 4** work to develop a *universal approach* to assay building.

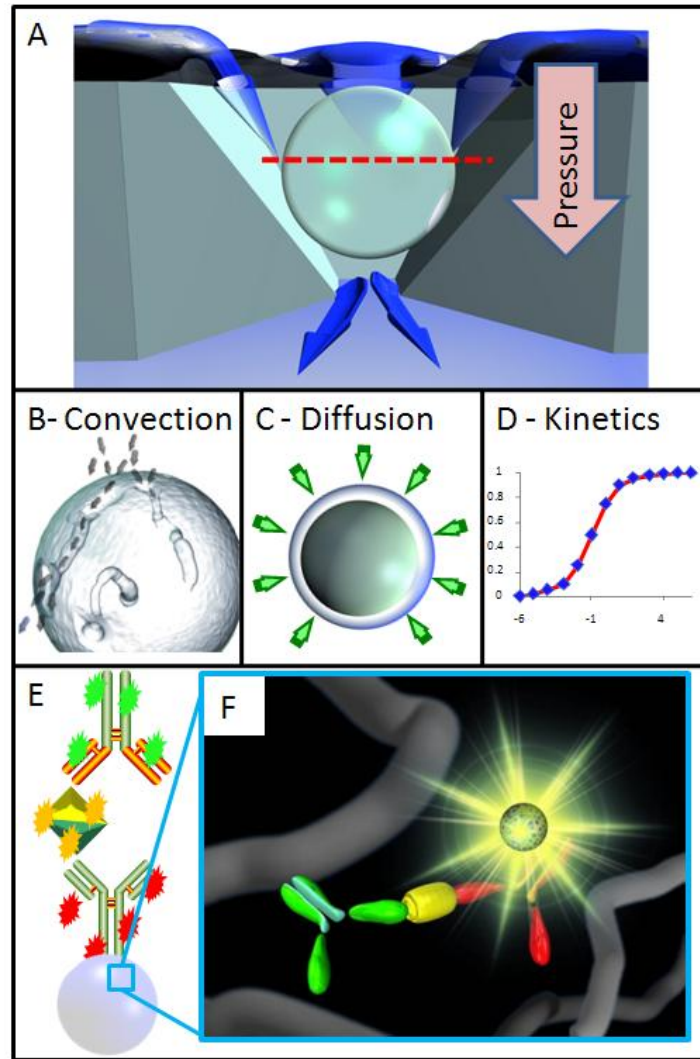


Figure 4.1. Contributors to assay performance in NBC. In **A** the location of an agarose microsphere in the MEMS structure is considered from the xz optical plane. Reagent transport into the bead structure is affected by active transport (flow) of material (**B**), diffusion of reactants into the sponge-like bead center (**C**), and the kinetic rate constants of interaction between non-covalently linked antigen and antibody (K_{on} and K_{off} , **D**). In this chapter, work is performed to move beyond a 2D conception (**E**), to an improved 3D appreciation of the agarose bead environment (**F**). Red line in **A** indicates the plane used for fluorescent confocal imaging studies.

4.2 INTRODUCTION

Two dimensional surface areas as the underlying support structures for immunoassays have been the norm for many decades now.²³⁰ Microtiter plates in a variety of formats and from many different material types are common with the 96-well “ELISA plate” from poly-vinylchloride (PVC) being one of the most common. Coating techniques have remained relatively unchanged since the 1970s and still suffer from many of the same challenges that exists during that era. First, in both commercially available ELISA kits as well as in laboratory-prepared systems, the capture antibody elements is non-covalently linked to the plate surfaces via passive absorption. This coating process takes advantage of the hydrophobic interactions between nonpolar protein structures and the plastic microtiter plate matrix.²⁰⁹ As interactions between polymer and protein are dependent on size, charge, and polarity of the two systems, each antibody has a unique affinity for substrate as well as binding constants. To allow contact between the hydrophobic protein core and well plate, and thus encourage more robust interactions between antibody and plastic, mild denaturation of antibody via pH is common. Alternatively, many researchers use the avidin/biotin pathway to link capture antibody to ELISA surfaces—this technique also may interfere with recognition kinetics of antigen and antibody. Second, systemic control of antibody orientation is largely absent in the ELISA design. **Figure 4.2** illustrates a few of the myriad scenarios possible with this non-specific approach to assay building in ELISA. Not only may the reactive site be directed away from reaction area, but layering or steric overcrowding can prevent antigen from linking to antibody due to an inordinately high concentration of antibody during the coating step.²³¹ Third, due to the non-covalent method of ligand attachment, antibody may leach off during wash steps. Finally, the extent of antibody coating is highly dependent upon the diffusion coefficient of bioligand, the ratio of surface area

being coated to the volume of reagent solution, as well as the time and temperature of the coating step.²⁰⁹

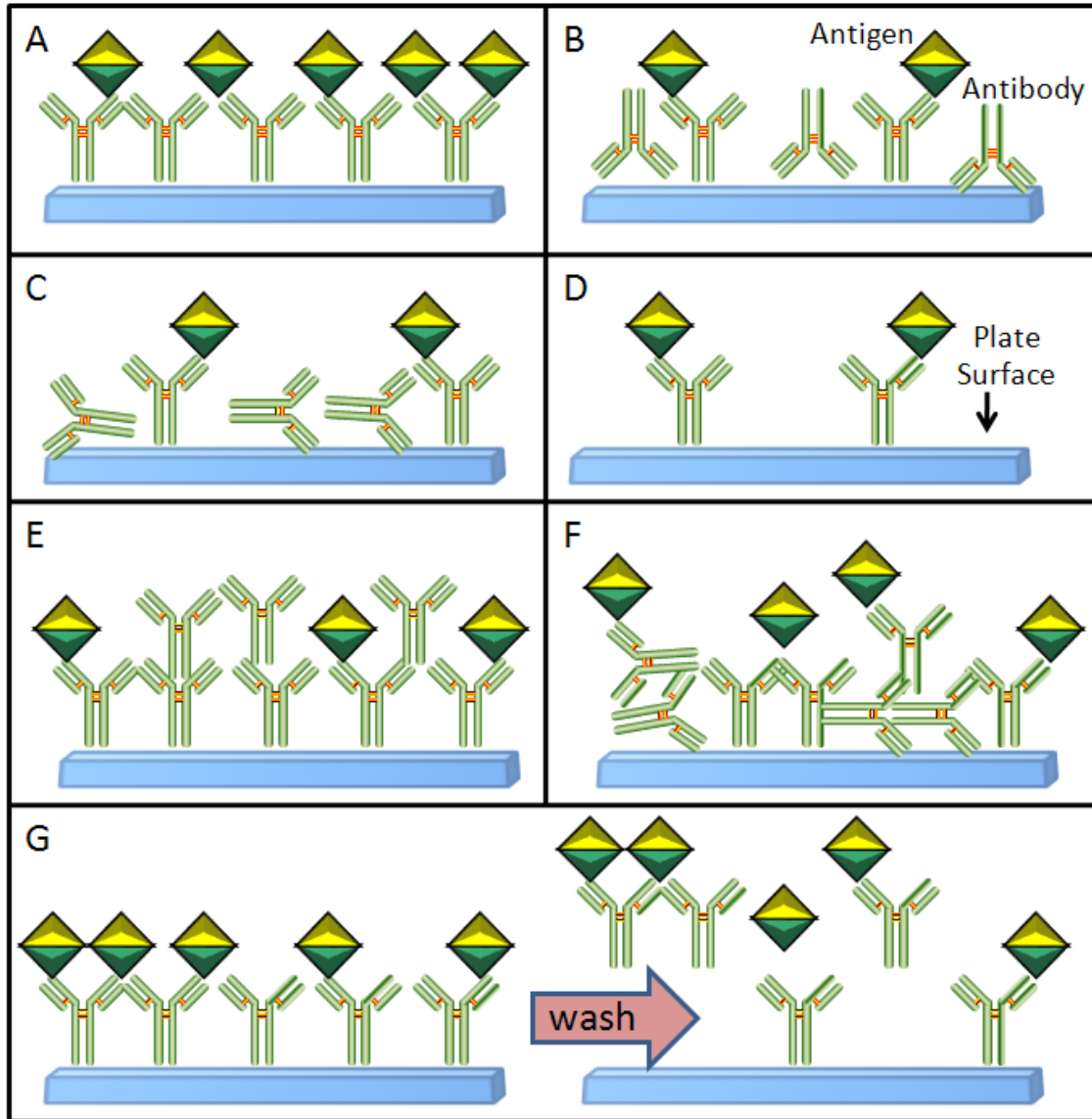


Figure 4.2. Inconsistent ELISA Capture Antibody Design. A) In optimal coating environments, capture antibody is evenly distributed across the surface of a microtiter plate. However, any number of alternative schemes can result in less than ideal antigen capture including IgG linkage through active site (B), orthogonal antibody orientation (C), insufficient antibody coating (D), antibody stacking (E), and antibody layering (F). In addition, non-covalently linked antibody may disassociate from plate surface upon washing, effectively rinsing away analyte and later decreasing signal (G).

Thus, due the above listed reasons, ELISA systems are rarely capable of ultra-low detection limits, even when used in conjunction with enzyme-amplification steps. Because of these failures in monolayer assembly, some studies estimate that the percent of capture antibodies that remain active and capable of binding antigen is below 10%.²³² This poor performance is in contrast to superior detection capabilities of the NBC both with molecular fluorophores and with QD probes (recall **Fig. 3.10** and **Table 3.1**). There are many reasons for the strength of the NBC assays, notably the highly effective washing that results from chip design, the high signal of the QD reporter, but also important here is the *avidity* with which the capture antibodies bind there target. For the purposes of this discussion, avidity is defined as a highly effective, multivalent mode of analyte capture and immobilization. The agarose beads, and their “nano-network” of fibrous, reactive strands, epitomize an analyte capture modality with high avidity. The reader is referred to **Figure 3.13E** for a deeper appreciation of the nanoscale lattice of immobilization elements, typical of the agarose bead. Methods to improve this capture efficiency and control reagent distribution is an important goal of this chapter.

First, some previous studies quickly bear mention. Former McDevitt Group member, Marc Rodriguez found that using the overnight capture antibody immobilization protocol, this reagent completely penetrated the agarose microsphere.²³³ However, for investigations using the C-reactive protein (CRP) analyte, neither the antigen, nor the detecting antibody made significant penetration into the bead core. Rather, these reagents remained on the periphery to a depth of ~20 μm for the homogenous agarose and was attributed to the size of the entire 460 kD immunocomplex. Jorge Wong, also in the McDevitt group, studied similar bead types, but with a labeled *antigen* in lieu of traditional fluorescence detecting antibody.¹⁹⁹ In this work, sample recirculation over beads resulted in a slow, radial penetration of antigen into the core of the capture

antibody coated beads over a 45-minute time course. From this progression, rates of diffusion were calculated and this work demonstrated how increased penetration could be achieved via active transport.

Both Wong and Rodriguez used confocal microscopy to optically cross section the beads, which allows a much more detailed description of the agarose substrate versus epifluorescent images. From these studies, an absence of fluorescence implied a lack of reaction participant. That is, if no green signal is present on the bead interior, then no green fluorescence labeled protein was present on the interior of the bead. Other work in the field, however, cast doubt over the exact phenomenon surrounding this ring-like effect. Yan and Lee suggested that self-quenching of signal was possible, especially at higher concentrations of fluorophore, effectively causing signal emitted by dyes near the center of the bead to be reabsorbed by fluorophores closer to the periphery.²³⁴ As this energy transfer is proportional to the Forster distance according to $1/r^6$, a small increase in concentration has the potential to dramatically impact fluorescence emission reabsorption. Other work by Kress and Bradley suggested that the lack of signal on bead interior is a result of poor illumination, that is, the incident radiation necessary to excite fluorophores on the bead interior is unable to penetrate the center either due to concentration effects or bead composition.^{235, 236} Although this other work was sometimes done using bead types other than agarose, its repercussions on NBC research was important to consider. This work implies that the dearth of signal on bead interior may not be the result of a lack of labeled probe, and hence reagent.

Fortunately, Mehnaaz Ali's dissertation offered important clarification in this area.²³⁷ Here, beads were coated with molecular beacons using biotin/avidin affinity; this reagent was demonstrated to penetrate completely into the center of the bead. Incubation of these beads with the molecular beacon target sequence gave fluorescence near the

periphery with both epifluorescent and confocal imaging techniques. Next, the beads were microtomed and imaged epifluorescently—fluorescent signal remained on the outer bead area confirming that a *physical* absence of analyte was responsible for signal decrease, not internal optical effects and interferences.

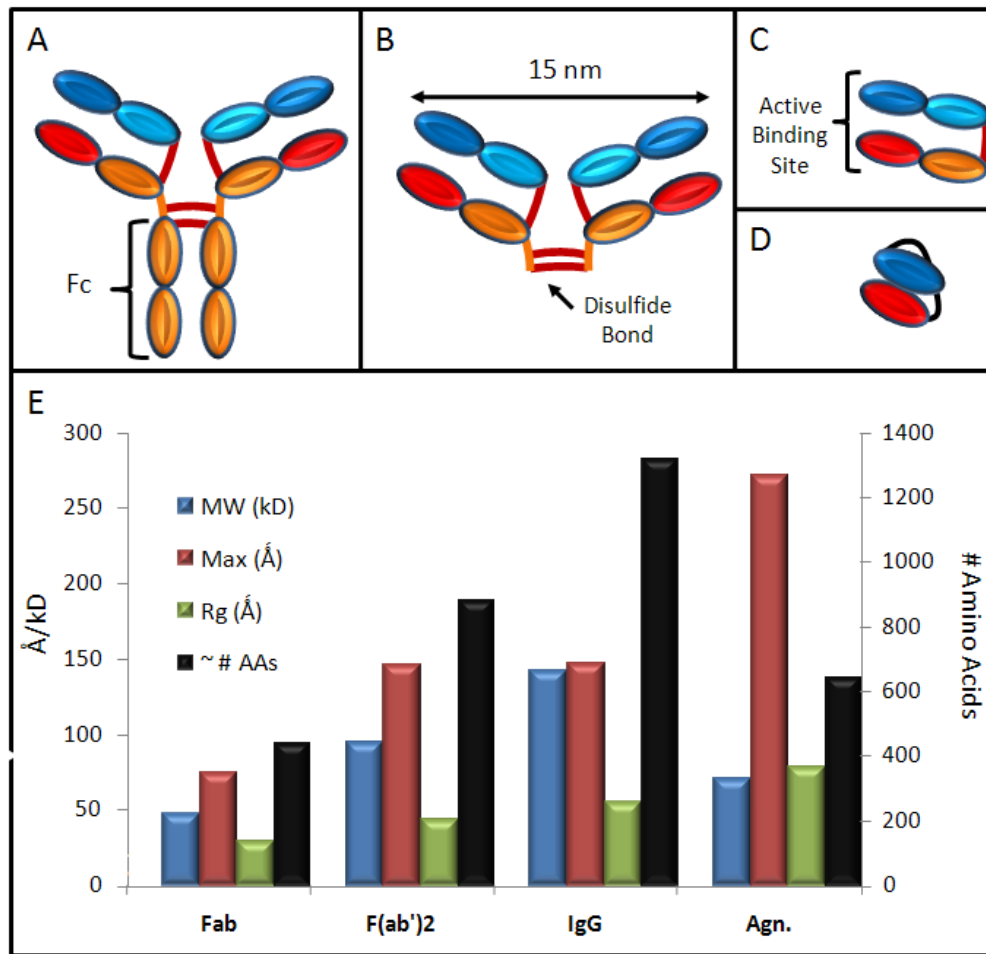


Figure 4.3. Size Considerations of Bead-based NBC Recognition Elements. Both the capture and detection bodies in sandwich immunoassay are typically whole IgG fragments (A).^{150, 238} A variety of proteolytic digestion schemes can be used to render this whole antibody into smaller F(ab')₂ (B) or Fab (C) fragments. Alternatively, scFV (single chain variable fragment, D) chains, using recombinant pathways, consist of only the heavy and light antibody target recognition chains. (E) Comparison of the molecular weight, maximum distance, radius of gyration (all left axis), as well as total number of amino acids in the protein (right axis) for different size recognition bodies as well as the CEA antigen.²⁰⁶

With this validation of confocal microscopy as an analysis tool in mind, **Chapter 4** works to understand better the fundamental components of the bead-based NBC. An initial parameter optimized in this system was the size of the capture and detection antibody via fragmentation. The use of Fab and F(ab')₂ antibody fragments has established attributes including the elimination of Fc based nonspecific binding, reduced steric hindrance with retention of active sites, decreased immunogenicity with potential for reduced immunoreactivity.²³⁸⁻²⁴¹ **Figure 4.3** offers a comparison of the size and structural differences between these various fragments. Currently, scFv fragments are the subject of intense investigation and reduced IgGs have been used in therapeutics delivery, blots, immunohistochemistry, and well as for NMR/crystal structure determinations in lieu of the larger whole fragment.^{242, 243} In an application similar to the NBC, Song and Fan demonstrated that the use of F(ab')₂ fragments as capture elements gave lower limits of detection and better correlation to reference method in a planar, sandwich immunoassay for cancer biomarkers than did whole IgG.²⁴⁴ This prior work, in addition to the capability and even necessity for antibody fragments demonstrated in **Chapters 2** and **3** is the impetus for this work with reduced recognition elements. This hypothesis, that smaller antibody fragments will allow for higher densities of antibody and thus increase analyte sequestration will be detailed in **Section 4.4.1**.

An additional focus of **Chapter 4** is an examination of the influence *antigen size* has on distribution of signal in sandwich immunoassay via the agarose beads in NBCs. Nearly any multiplexed assay with a sizeable number of analytes will contain antigens of various molecular weights, radius of gyration (R_g), and thus maximum diameter. Previous work has considered all antigens to behave identically in the NBC. Work detailed in **Section 4.4.3** will illustrate the inaccuracy of this presumption and offer guidelines for designing effective assays that consider the analytes' size and shape.

Finally, this chapter will examine the effects of agarose bead porosity has on immunoassay performance, and reagent penetration will be used to estimate bead pore sizes. Previous work using either atomic force microscopy (AFM) or advanced absorbance measurements have given a wide range of estimates for pore size in planar agarose and are highly dependent upon the method of preparation and cooling.^{207, 245} Despite this, some general trends may be discerned. Mainly, pore size decreases as agarose porosity increases and pore size is on the order of 100s of nanometers. Although excellent SEM images are detailed in **Section 4.3.3**, it is imprudent to use only this invasive sample preparation and analysis method exclusively to glean quantitative information about pore size.

Thus, **Chapter 4** will work to answer the following fundamental questions about the bead-based NBC:

- How do Fab and (Fab')₂ fragments behave relative to whole IgG?
- How does capture antibody size affect signal intensity and location?
- How does detecting antibody size affect signal intensity and location?
- How does antigen size affect signal intensity and location?
- How does bead porosity affect reagent transport?
- What more may be learned about our bead behavior in terms of diffusion, sterics, and distribution of fundamental assay building blocks?

The results will offer refined understanding of methods to develop immunoassays for ultra-low limits of detection as well as other valuable performance characteristics. Most sandwich systems explored previously have been done on a planar surface. Little information is known about protein capture and reagent distribution within 3D, pressure driven, microfluidic flow chambers. This study will allow for a more comprehensive

comparison between standard commercial ELISA assay kits and the NBC scheme under development here.

4.3 MATERIALS AND METHODS

4.3.1 Preparation of Components for CEA Assay

Similar to the work in **Chapter 3**, detecting and capture antibody pairs specific to CEA were purchased from Fitzgerald (Concord, MA) as was recombinant CEA antigen. Detecting antibody was labeled with Alexa Fluor 488, capture antibody with Alexa Fluor 647 and antigen was tagged with Alexa Fluor 546. Labeling was performed by adding a 500 μ L of protein at \sim 1 mg/mL to powdered fluorophore followed by incubation with stirring for 1 hour. All dye molecules have a tetrafluorophenyl moiety bound which forms an excellent leaving group allowing for linkage of dye to free amine on protein. Unbound fluorophore was separated from labeled protein using size exclusion chromatography.

4.3.2 Ficin Fragmentation of Whole IgG₁ Molecules

All antibodies used for this digestion were mouse IgG₁ molecules. Both labeled and unlabeled capture antibodies were subjected to proteolytic digestion while, due to the necessity of signal, only Alexa Fluor 488 bound detecting antibody was subjected to this further processing step. Both Fab and F(ab')₂ fragments were prepared via ficin, a well characterized digestion agent.^{240, 246} Reagents needed for this cleavage were purchased from Pierce (Rockford, IL) and included: immobilized ficin on 6% agarose beads in storage buffer (>1.8 mg ficin/mL resin), cysteine hydrochloride, pH 6 digestion buffer (10x), pH 8 Protein A binding buffer with EDTA, pH 6 elution buffer, and AffinityPakTM Protein A columns with Protein A immobilized onto 6% crosslinked agarose of 2.5 mL volume with a binding capacity of 6-8 mg of mouse IgG.

A detailed protocol for digestion of IgG₁ molecules is available via Pierce product #44880. Briefly, working digestion buffer was prepared from the 10x concentrate and cysteine HCl added to a final concentration of 0.011 M for F(ab')₂ digestion and 0.11 M for Fab preparations. Ficin columns were equilibrated with working digestion buffer and then sample (500 μL, ~ 1mg/mL) containing IgG₁ was introduced and allowed to enter column bed. Upon sample permeation of gel, the column was sealed and stored at 37°C for 4 hours for Fab experiments and overnight for F(ab')₂. The sample was eluted by addition of 4 mL portion of Protein A binding buffer and column washed and regenerated for additional use. The sample containing aliquot was then loaded onto a Protein A column, allowed to enter gel, followed by addition binding buffer. Fractions of 1 mL were collected and saved for later characterization by protein assays using A₂₈₀ or Bradford's method (A₅₉₅).^{154, 247} Alternatively, A₄₉₄ or A₆₅₀ could be used on the Alexa Fluor labeled fragments. Aliquots identified as containing fragments of interest were then pooled and purified using a 10,000 MW cutoff concentration microcentrifuge tube from Sartorius (Aubagne, France.) The IgG binding buffer was then used to wash the Protein A column followed by elution buffer, pH 3 0.1 M citric acid, and 10 mL water. Both the Protein A and ficin columns were stored at 4°C for later use.

4.3.3 Preparation of Beads

Agarose bead preparation was adapted from Gustavsson's method and tailored by Wong.¹⁹⁷⁻²⁰⁰ Briefly, agarose from Sigma Aldrich (St. Louis, MO) was added to 50 mL water to the desired percentage and heated to 85°C in a water bath. A suspending solution of 10 mL Span85 also from Sigma Aldrich in 100 mL n-heptane was heated to 61°C. After introduction of the agarose mixture into the suspending solution stirring proceeded for 1 min. As temperature dropped with vigorous stirring, the agarose gel beaded out of solution and precipitated to the bottom of the flask. Beads used for the

antibody fragment studies were subjected to a cross linking procedure, while those of tuned porosities remained uncross-linked. Beads could then be washed with a 50/50 ethanol/water mixture for hydration and size sorted by a sieve. Beads were stored at 4°C until future use. For linkage of antibodies and antibody fragments to the beads the sodium cyanoborohydride technique described in **Chapter 3** was again used—all reactions were allowed to proceed overnight with precocious agitation.²⁰¹

4.3.4 Microscopy Design

Beads were loaded into a silicon chip using dissection tweezers and sealed into the NBC. For preliminary experiments, the same epifluorescent microscopy design was employed as in **Chapter 3** and detailed in **Section 3.3.5**. Using the adjustable gain, offset, and exposure time of the CCD camera, settings were found to image beads with little or no saturation of pixel intensity. These images were saved as 12-bit TIFF files. Upon completion of the immunoassay sequence in the research-grade NBC, in tandem with the epifluorescent design, the NBC housing could be detached from peristaltic tubing and transported to an advanced imaging facility. Here, the NBC was positioned upside down and immobilized on two plastic supports to facilitate the inverted design of the confocal microscope.

Confocal images were taken with a Leica CTR microscope with a TCS SP2 acousto-optical beam splitter (AOBS) with a 10x objective of 0.3 numerical aperture. Optimal settings for gain and offset on the Leica instrument were determined by using a quantitative look up table and pixel saturation values. Bead medial sections were determined by scanning in the z direction until width of slice is maximized, indicating the bead's medial plane was in focal plane. Initial settings used simultaneous scanning of all color channels to determine rapidly both the best physical location and optical settings.

For data collection, channels were collected sequentially to minimize cross talk and eight images were averaged into a single scan to increase resolution and decrease pixelation.

4.3.5 Image Analysis

Photomicrographs were saved as 12-bit colorized TIFF files and analyzed via ImageJ software from the NIH (Bethesda, MD) with bead fluorescence signal intensity correlating to the concentration of analyte in the sample. Deconvolution macros, written using Java, converted the image to a grayscale 8-bit image with areas of interest (AOIs) drawn corresponding to individual beads. These AOIS serve as a rough boundary in which the bead resides. Four different methods described the information contained within the AOI. The line profile (LP) method scanned the AOI one row of pixels at a time—the highest pixel value from each successive line profile was then averaged to calculate a mean signal. The circular AOI (CAOI) method begins analysis in the geographic center of the region and expands outwards until it finds a circular region of pixels having the highest intensity. All pixels inside this circle are then averaged to give a measurement of intensity. The integrated density (D) technique takes the same circular region of pixels having the highest intensity uncovered in the CAOI method, and expands the analysis region 2 or more pixels on either side of the maxima. All pixels in this region are then averaged to yield an intensity measurement. Finally, the circular profile (CP) scheme simply averages the circular region identified in the CAOI and takes the mean pixel values. All four of these parameters may then be reported with their respective standard deviations and coefficients of variation. Additional data analysis of colocalization was performed using ImageJ supplemental code JACoP available at the ImageJ website.²⁴⁸

4.4 RESULTS AND DISCUSSION

4.4.1 Effect of Antibody Size on Assay Performance

Although a number of novel recognition elements have recently been proposed including aptamers, peptides, and surface-imprinted or molecular imprinted polymers, monoclonal antibodies have been the gold-standard for protein antigen immobilization for over 40 years.²⁴⁹ While the variety of antibodies has increased dramatically, the fundamental techniques for their production in hybridoma has largely remained the same.²³⁸ Thus, the antibodies used for these experiments were mouse IgG₁ bioligands. Unlike IgG (human IgG), mouse IgG₁ is resistant to digestion by pepsin (for F(ab')₂ production) and papain (to create Fab fragments). This inactivity is attributed to the lack of N-linked glycosylation and absence of a leucine-234 residue in mouse IgG₁, a highly conserved feature of human IgG and the active pepsin cleavage site.^{240, 250} This feature, as well as the resulting secondary, tertiary, and quaternary effects on protein structure in the mouse IgG₁ gamma chain, results in a restricted hinge region and resistance to pepsin cleavage. Furthermore, pepsin digestion requires a proton rich pH, an environment that can induce non-specific bond destruction or otherwise denature sensitive antibodies.²³⁸

A number of alternatives exist to pepsin and papain, for mouse IgG₁, the digestase ficin is an interesting option. Ficin, a thiol protease, can facilitate a diverse range of reactions that involve the interconversion of carboxylic acids, esters or amides.²⁴⁶ It is obtained from *Ficus carica* and purified from fig latex. The final product has a molecular weight of 25,000 with an extinction coefficient of 21 units at 280 nm for a 1% (wt./wt.) solution.^{251, 252} It is activated by weak reducing agents including cysteine, sulfide, sulfite and cyanide; EDTA, *N*-bromosuccinimide, acridine dyes and cysteine are enhancers of ficin. Inhibitors include sulfhydryl blocking agents such as *N*-ethyl maleimide and iodoacetamide, heavy metal ions, mercuric chloride and carbonyls.²⁵³ To determine the

optimal digestion pathway, a study of five mouse IgG₁ monoclonal antibodies with pepsin, bromelain, ficin and elastase determined which generated the high yields of stable, active F(ab')₂ fragments. Results indicated that ficin digestion produced high yields of F(ab')₂ fragments. In addition the antigen-binding activity, immunoreactivity, affinity constants of ficin-generated F(ab')₂ fragments remained similar to unadulterated IgG₁ as determined by cell binding experiments using radiolabeled fragments.²⁴⁰ For the characterization of assay performance described below, the CEA assay outlined in **Chapter 3** is elucidated in greater detail.

4.4.1.1 Characterization of Immobilization Elements

Ficin digests of CEA antibody 057-10009 (capture) and M111147 (detecting) were prepared. A fraction of the capture elements were visualized fluorescently using Alexa Fluor 647, while all detecting moieties were tagged with Alexa Fluor 488. Experiments with unlabeled capture elements were also done to determine the effect of labeling on antibody efficiency; both labeled and unlabeled whole mouse IgG₁ were subjected to Fab or F(ab')₂ digestion procedures described in **Section 4.3.2**. The resulting 1 mL aliquots from Protein A column eluate were characterized by three well-known methods as shown in **Figure 4.4**. Fractions 2-6 consistently contained the fragments on interest.

This is seen most clearly in **Figure 4.4A** in which the Alexa Fluor-tagged F(ab')₂ fragments elute early in the chromatograph, followed by a subsequent change in pH and ionic strength allowing for release of the Fc and undigested molecules retained on the Protein A column. Measurements observed with A₂₈₀ absorption (**Fig. 4.4B**) were not as clearly resolved as A₆₅₀. These experiments measure UV absorption by aromatic structures within the protein and as the starting concentration was 1 mg/mL, the concentration individual fractions was <0.1 mg/mL, a value near the low end of the

performance range of A_{280} and the available spectrophotometer. Bradford assays with Coomassie reagent (**Fig. 4.4C**) indicates presence of fragmented protein in the initial eluate fractions, while later fractions show signal undistinguishable from background. The relatively poor performance of A_{280} and Bradford assay in this range is attributed to not only low levels of protein in the samples, but also the changing solvent environment inherent to gradient elution and the presence of non-specific and background signal.

Some absorption at 280 nm can also occur due to components in the proprietary buffer, in addition to phenylalanine, tyrosine, and tryptophan residues in the protein. Furthermore, Bradford experiments are somewhat non-specific in detecting the presence or absence of arginine, lysine, or histidine in the protein—the presence of other amine compounds can increase signal. An additional inherent challenge comes from the gradient elution method used here. The background of the initial pH 8.25 binding buffer is $A_{595} = 0.30$ in the Bradford assay, a value that changes to $A_{595} = 0.37$ in the pH 6.02 elution buffer. Fortunately, the labeled capture and detecting antibody fragments were discerned visually; only the unlabeled capture antibody control experiments absolutely demanded the use of these spectroscopic methods. These experiments were not concerned with producing detailed reports of the Fc and undigested fractions. Regardless of the characterization method, fractions 2-6 for each digestion were identified as containing product and thus pooled, and later concentrated, to prepare the antibody digest required for later conjugation to bead (capture element).

Dose response curves using the A_{280} method for protein and A_{650} for Alexa 647 were used to calculate concentrations in the final pooled and concentrated retentate (**Table 4.1**). The distribution in final concentrations may be due to a number of factors including the efficiency with which 10K molecular weight centrifugal concentration tubes retain protein and interference of dye molecules with protein absorbance.

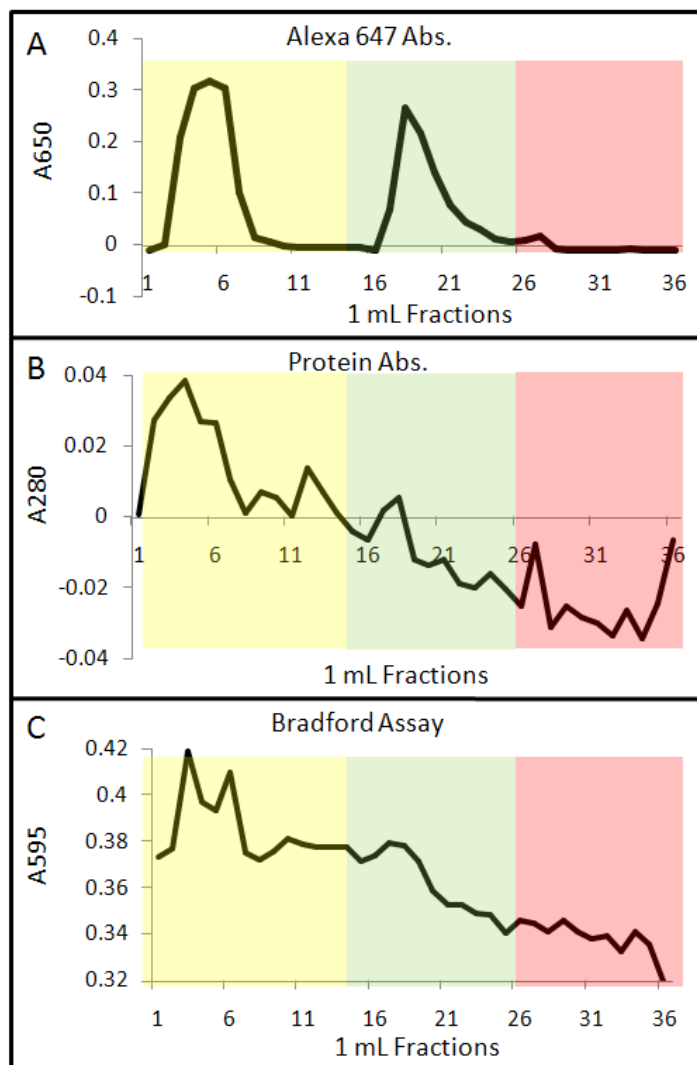


Figure 4.4. Characterization of Antibody Fragments. These figures arise from the Fab fragment preparation from Alexa Fluor 647-coated IgG capture antibody. After proteolytic fragmentation, antibody digests were purified using a Protein A affinity chromatography column with agarose solid phase support, in tandem with gradient elution. Yellow highlighted sections indicate pH 8.25 binding buffer, sections in green employ pH 6.02 elution buffer, and pink areas are pH 3.00 0.1 citric acid. **A)** Absorbance values at 647 nm indicate that the antibody fragments elute in basic buffer while Fc regions are not released from Protein A beads until change to acidic liquid phase. **B)** Absorbance at 280 nm shows similar signal increases from Fab fragments and poorly defined increase for Fc pieces. **C)** Similarly, the Coomassie reagent and 595 nm absorption indicates the presence of Fab fragments and vague presence of Fc. Fortunately, only the first six aliquots from each elution were needed for further processing.

Sample	Fab/647	Fab/Un	F(ab') ₂ /647	F(ab') ₂ /Un	IgG/647	IgG/Un
[Protein] (mg/mL)	0.494	0.689	0.154	0.092	0.883	5.2 [¥]
[AF 647] (M)	4.61 E-06	N/A	2.54 E-06	N/A	9.27 E-05	N/A

Table 4.1. CEA Capture Antibody and Antibody Fragment Characterization. Absorption at 650 nm and 280 nm was used to calculate the amount of protein and Alexa Fluor 647 fluorophore in various fractions of digested immobilization elements. The '647' indicates fluorophore labeled product while 'Un' implies unlabeled antibody. (¥ - concentration provided by manufacturer)

More importantly, it was necessary to use whole IgG to create the standard curve as prepared standards of Fab or F(ab')₂ fragments of this clone were not commercially available. Differences in amount of fluorophore may be attributed to differences in binding efficiency. Nevertheless, this method of characterizing the prepared fragments gives adequate accuracy.

4.4.1.2 Preparation of Bead Micro-reactors

As described in **Section 4.3.3**, agarose beads were linked to capture antibody. Here, it was critical to coat the bead surface and interior with an equimolar amount across all different recognition types. Upon analyzing the data **Table 4.1**, it was decided to react beads with 0.042 mg/mL of antibody. This concentration was necessitated by the low volume and low concentration of the F(ab')₂ bioconjugate. Although this is lower than the amounts used in other experiments and described in **Chapter 3**, this amount proved to be sufficient for these purposes and post-binding studies suggested that approximately 70% of this protein covalently linked to bead. Unfortunately, as illustrated in **Figure 4.5**, isomolar amounts of protein did not correspond to identical fluorescent signaling. Here, the IgG/647 beads were brighter than their Fab and F(ab')₂ by more than two orders of magnitude because they retained the dye containing Fc region in addition to the analyte

recognition epitope . At exposure times short enough to prevent IgG pixel saturation, the Fab and F(ab')₂ beads were not visible. Furthermore, when these beads were observed with a green channel filter cube (even at 0.5 s of exposure), strong, green-channel signal bleed (S = 23.5) was seen from the intense IgG/647 beads. When assays were performed with these beads, it was difficult to discriminate between aberrant signal from red channel cross talk, from authentic signal from detecting antibody. To construct a more comparable system, new batches of agarose beads were prepared with isomolar amounts of fluorophore, specifically 7.0×10^{-7} M Alexa Fluor 647. Thus, two sets of beads were prepared, one with isomolar fluorophore concentration and an additional set with isomolar amount of capture antibody.

For the remainder of fragmentation work, beads with 7.0×10^{-7} M Alexa Fluor 647 were used regardless of IgG, Fab, or F(ab') fragment status. These beads yielded statistically identical fluorescent output and have antibody concentration of 0.0066 mg/mL, 0.075 mg/mL, and 0.042 mg/mL respectively. To achieve equivalent fluorescent signal for Fab and F(ab')₂ systems, a 1.8 decrease in Fab concentration to 0.024 mg/mL of capture antibody was needed. This corresponds closely to the 2X size difference between the two systems. Similarly, the IgG scheme needs a factor 6.4 reduction to give beads with 0.0067 mg/mL of capture antibody, again compensating for the larger volume of antibody (and thus bound fluorophore) present in the Fc portion of the IgG system.

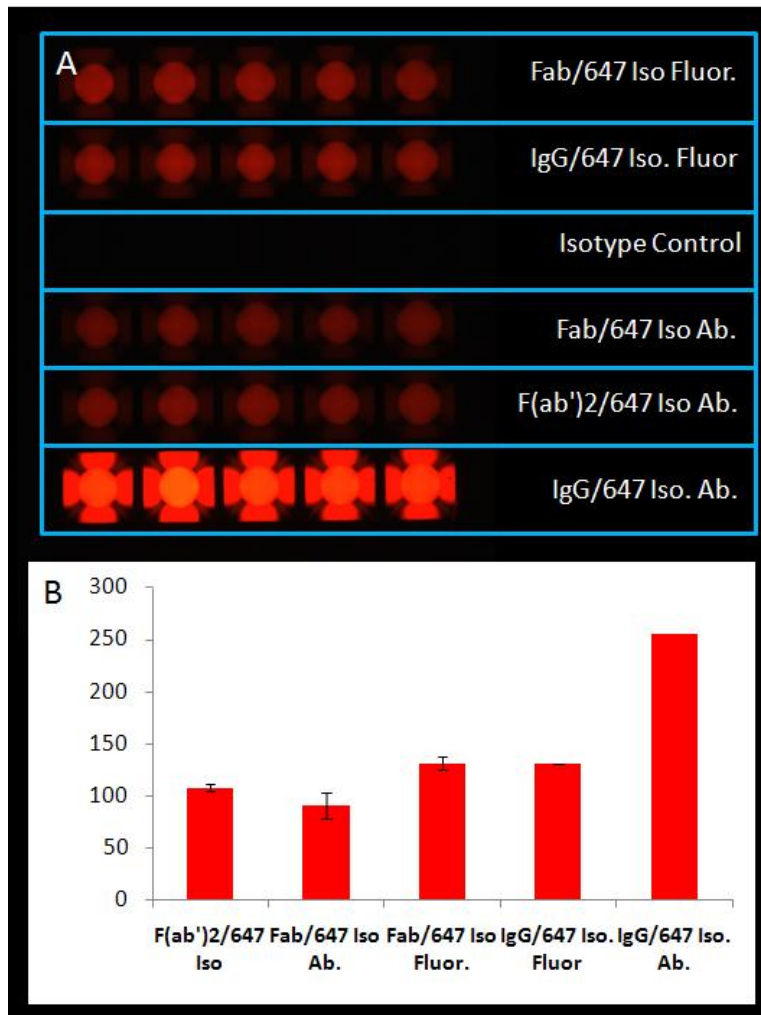


Figure 4.5. Intensity Differences by Capture Element Type and Concentration. **A)** Photomicrograph of six different bead types reveals intensity differences. **B)** Bar graph of signal intensity for five bead types. Beads functionalized to F(ab')₂ are represented only once—the isomolar antibody and fluorophore values were calculated relative to these beads. This data reveals that the isomolar antibody has much larger signal intensity due to the additional numbers of dye that may be bound to Fc region. Photomicrograph in **B** created with DVC camera settings of gain 10, offset 0, and 25 ms of exposure time. Note that IgG/647 isomolar antibody beads are saturated at a pixel depth of 255. Exposure times below IgG saturation were insufficient to record signal from fragment beads.

4.4.1.3 Fragment-Based Immunoassays—Signal Intensity

With comparable beads containing a CEA-specific, fluorochrome-labeled detecting antibody prepared, a quantitative comparison of immunoassay performance was the next goal. In addition to the three bead subsets described above, additional controls were needed. First, as the presence of the Alexa Fluor transduction method has interference potential, especially with antibody specificity, similarly digested, but unlabeled antibody fragments were also linked to beads at a concentration of 0.042 mg/mL. Second, beads with 0.042 mg/mL of a CA125 isotype control antibody were prepared. A 5 x 7 silicon chip to assay the following 7 beads types was required: Fab/647, IgG₁/647, F(ab')₂/647, CA125 isotype control, Fab/Unlabeled, IgG₁/Unlabeled, and F(ab')₂/Unlabeled.

Third, all seven bead types were assayed both in the presence (100 ng/mL) and absence of antigen (negative control) with assay conditions similar to those described previously. Completing the immunoassay, were three different detecting antibody types, again, Fab, IgG₁, and F(ab')₂. It was necessary to design experiments that exposed the beads to identical detection conditions, yet all three detecting bodies had different concentrations, and ratio of fluorophore to antibody, similar to the conundrum described for the capturing antibody. A 1:1000 dilution factor for Alexa Fluor 488 labeled IgG₁ detecting antibody was determined empirically to deliver S/N > 20 in the 3 mg/mL beads used for assays in **Chapter 3** at 100 ng/mL antigen. The 1 cm path length absorbance values at 494 nm for Fab, IgG, and F(ab')₂ portions were 0.2274, 1.504, and 0.3388; proportional calculations determined that dilutions of 6.61:1000 and 4.44:1000 were needed for Fab and F(ab')₂, respectively. The results of these six experiments are detailed in **Figure 4.6**.

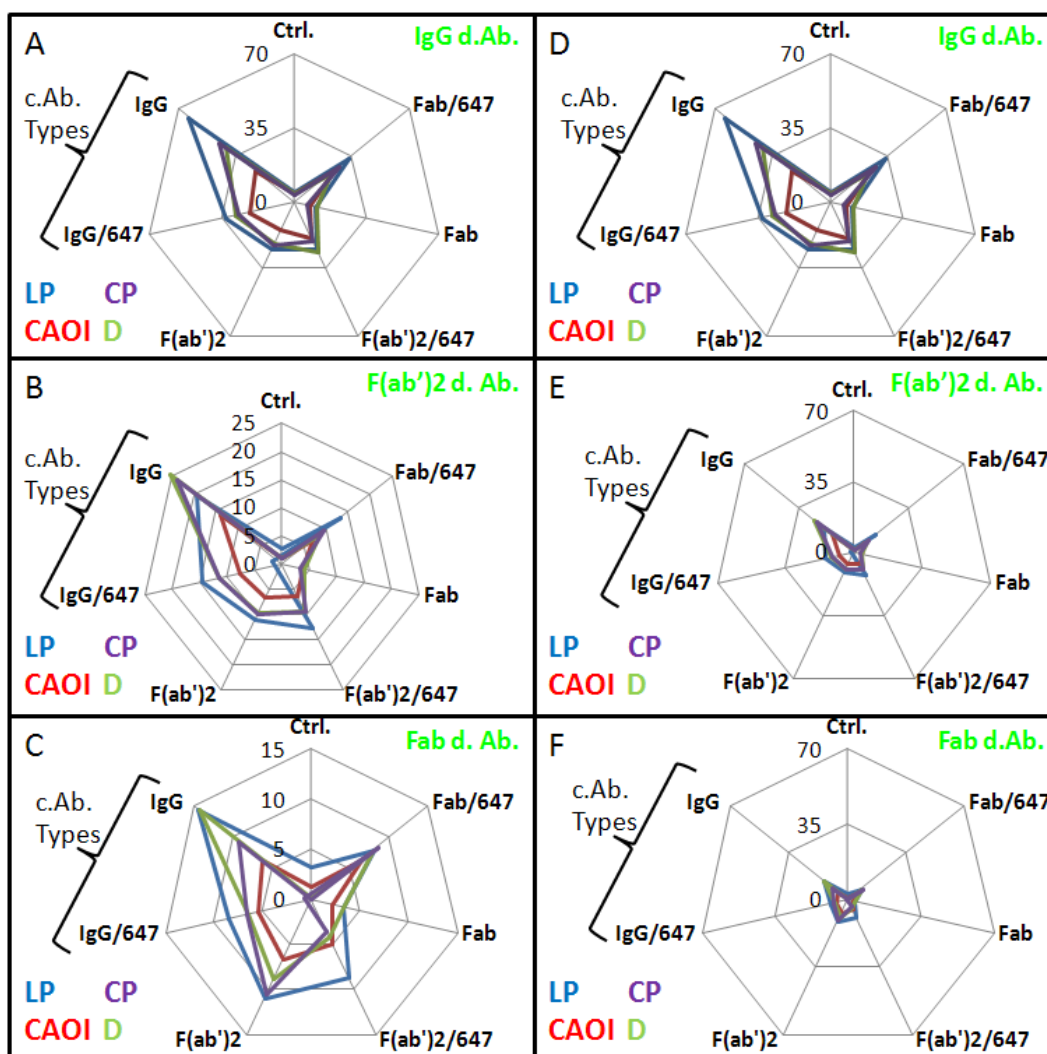


Figure 4.6. Signal Intensity Generation in Different Capture Element Types. Radar plots of CEA assays with beads containing isomolar amounts of capture antibody bound to Alexa Fluor 647 as well as unlabeled capture antibody were performed and evaluated via the four different analysis methods (LP, CP, CAOI, D). **A-C** details the results of these assays for three different detection schemes, again at isomolar capture ligand concentrations, including IgG (**A**), F(ab')2 (**B**), and Fab (**C**). **D-F** displays the same data as **A-C**, but with axis redrawn to the same scale. The most intense signal output comes from the IgG-IgG interaction.

The data acquisition displayed in **Figure 4.5** was created by collecting images both before and after detecting antibody incubation, which provided for processing into a

background-corrected digital photomicrograph. Such an image could be prepared for both the positive (100 ng/mL) and negative (0 ng/mL) experiments—it is this difference that is displayed graphically in **Figure 4.6** through the four different methods of signal interpretation described in **Section 4.3.5**. Panels **A-C** scale relative to the most intense signal in each experiment. Here, some observations on signaling trends are apparent. First, the LP analysis scheme typically yields the highest pixel depth, a trend observed previously in **Chapter 3**. Specifically, the LP method produces signal enhancement by factors of 1.8, 1.5, and 1.4 versus the CAOI, D, and CP analysis methods, respectively. Second, Alexa Fluor 647 tagged beads yield less signal relative to their unlabeled controls (with the exception of Fab), for IgG₁ beads, signal reduction happened by a factor of 1.7 to 2.8. As labeled capture antibody may have fluorophore in the binding pocket, this decreases analyte capture efficiency—the binding of fluorescent molecules to active sites on the antibody, reducing its ability to bind antigen, explains this phenomenon. Third, capture antibody *fragments* decrease signal relative to their whole IgG counterparts. Fourth, signal intensity of the different detecting antibodies is quite different and increases in strength according to size, i.e. IgG₁ signal is most intense followed by F(ab')₂ (62% reduction) and Fab (77% reduction). These results suggest that using a whole IgG₁ recognition element for both capture and detecting antibody yields the highest signal intensity

The underperformance of antibody fragments to capture analyte and higher intensity of whole IgG₁ as a reporter group may be explained by a deeper examination of these proteins' structure. The four amino acids containing a terminal amine—arginine, lysine, glutamine, and asparagine—are the basis for both dye immobilization and linkage

	IgG		F(ab') ₂		Fab		scFv	
Lys	86	6.65%	46	5.29%	23	5.29%	12	4.26%
Arg	38	2.94%	34	3.91%	17	3.91%	6	2.13%
Glu	52	4.02%	30	3.45%	15	3.45%	15	5.32%
Asp	56	4.33%	32	3.68%	16	3.68%	7	2.48%
Total	1294		880		435		282	

Table 4.2. Terminal-amine Containing Amino Acids in Recognition Elements. The major amino acids through which both fluorophore conjugation and immobilization onto agarose substrate are completed include lysine (Lys), arginine (Arg), glutamine (Glu), and asparagine (Asp). As recognition element size decreases, the percentage of amine-containing amino acids tasked with facilitating a bond increases.

to agarose substrate in the NBC system. To demonstrate the effect decreasing size has on these residues, protein database sequence details are listed in **Table 4.2**.^{150, 254, 255} These values explain in a more quantitative fashion the results seen in **Figure 4.6**. As the size of capture body decreases, so does the number of amino acids capable of performing secondary chemistry. In the third case on page **138**, a reference to **Table 4.2** is helpful to understand why capture antibody fragments underperforms whole IgG. Both fragments and whole IgG link to the agarose substrate through the roughly four amine-containing amino acids. For larger bodies, IgG₁, this is only 1.3% of the total available, but for F(ab')₂ and Fab this number increases to 2.4% and 4.2%, respectively. Thus, there is a greater chance that fragments are linked through an active site amino acid than for the larger IgG₁. For the fourth case explored on page **138**, the decreased signal by fragments as detecting antibody, it may be seen that Fab and F(ab')₂ bodies have 31% and 61% as many amine amino acids as does the whole IgG. Therefore, upon fragmentation, the Fc

region and its wealth of labeled amino acids is lost while retaining the same analyte recognition moiety.

4.4.1.4 Characterization of Immunoassay Signal Distribution

Although the results above make clear that smaller signaling probes cannot give more intense *signal*, the following work is designed to characterize whether smaller antibody fragments may be useful at detecting antigen immobilized on the bead's interior, and thus change *signal distribution*. **Figure 4.7** contains panels of photomicrographs reduced from the larger 5 x 7 array and highlighting beads with unlabeled, equimolar concentrations of Fab, F(ab')₂, and whole IgG₁ CEA capture antibody, as well as isotype control. From these studies, it is clear that, the most important variable determining location of green fluorescent detection signal is not detecting antibody, but rather *capture* antibody and its spatial arrangement inside the porous bead. While detecting antibody fragment affects output signal intensity (as illustrated above and confirmed below), it does not affect location. **Panel 4.7Aii** illustrates succinctly the spatial affects of detecting antibody size. When 125 pixels long line profiles cross each bead, the most intense pixel indicates location of highest signal. For Fab, this occurs at pixel 48, or approximately 15 pixels away from center. For F(ab')₂, peak intensity is at pixel 87 (25 pixels from center) and IgG₁ maximum is at pixel 14, or 49 pixels from center. This reproducible result indicates that detecting antibody penetrates deeper into the center of the bead when the capture antibody is reduced in size. Indeed, the F(ab')₂ and IgG₁ beads show the ring-like signal pattern typical of data seen in **Chapter 3**. It was curious that reductions in size of detecting antibody did not promote further increases in penetration depth. Again, this only served to decrease signal. This data provides evidence that little antigen is immobilized in the center of the bead without later detection output. Smaller detection antibodies would be

able to penetrate deeper and report signal, but as no such change occurred upon reduction to smaller antibody, it is tentatively postulated that all antigen is signaled.

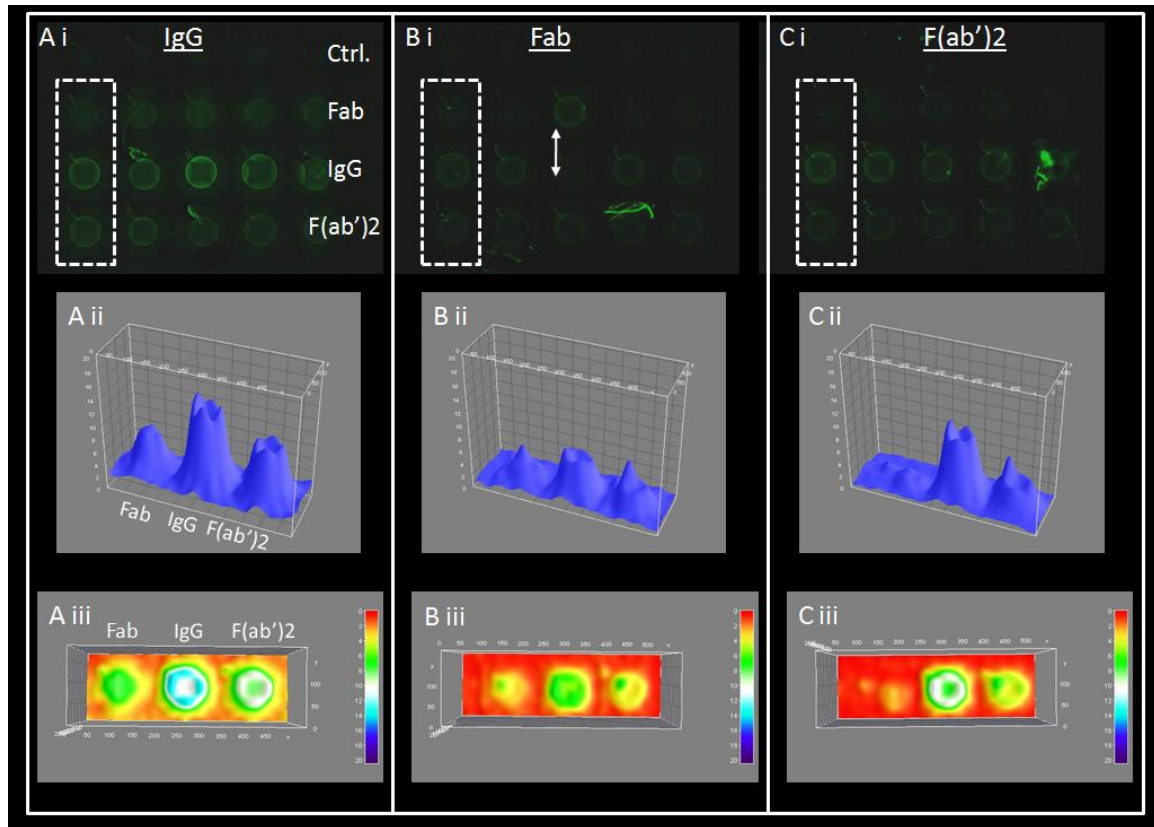


Figure 4.7. Signal Distribution Generation in Different Capture Element Types. Three different detection schemes (A, IgG₁; B, Fab; C, F(ab')₂) yield three different patterns in beads. The top row of photomicrographs show beads with IgG₁, Fab, and F(ab')₂ capture antibody as well as an isotype control. The middle collection of surface plots reveal that IgG₁ and F(ab')₂ beads relegate most of their signal to periphery of the bead; Fab beads have signal more evenly distributed. This pattern remains the same regardless of detection antibody type. That is, capture element type determines location of antigen, and hence, location of detection antibody. The lower panel offers an alternative view of bead intensity.

4.4.1.5 Further Systemic Characterization

Having studied signal intensity and distribution, the next goal was further optimization as well as interpretation of the non-specific signal (noise) and background present in the immunoassay platform. Background (B) and noise (N) were determined similarly to the methods described previously in **Section 3.4.1**. Briefly, B arises from the zero antigen calibration point and is caused by non-specific biological and chemical interactions between agarose support and detecting antibody. Noise, defined as signal from isotype control beads, is an additional descriptor of detecting antibody misbehavior. In **Figure 4.8A**, the results of both B and N are detailed. Importantly, these values increase relative to those values of **Chapter 3**, explained as follows.

Due to the lower concentration (0.042 mg/mL) of capture antibody necessary for this fragmentation work versus work in **Chapter 3** (up to 6.0 mg/mL) overall signal values are lower. This requires the use of longer exposure times even up to 3 seconds. Even though background-corrected images were used, i.e. subtraction of image before detecting antibody from image after incubation and wash, B values increase. More importantly though, is the change from a QD-based system in **Chapter 3** to this work focusing on smaller molecular fluorophores. Interactions between Fab capture and Fab detecting bodies gives the lowest values for B (B = 2.6); this interaction also gives the lowest values of S (*vide infra*). Noise in **Figure 4.8A** is indicated by the column marked 'Ctrl.' abbreviating the isotype control beads. The lowest value of N comes from F(ab')₂ detecting antibody (N = 3.0). Characterization of the changes that occur in immunoassay upon the inclusion of antibody fragments as detecting and capture elements is the focus of this study, therefore no further optimizations to reduce B or N were undertaken.

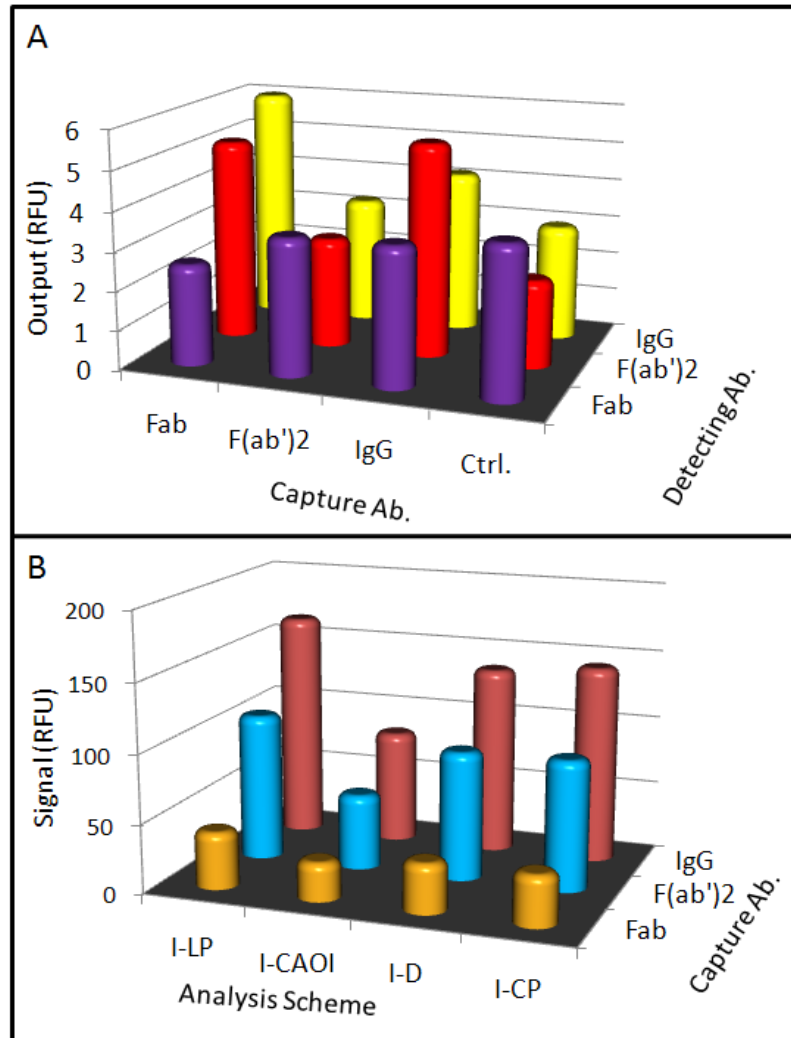


Figure 4.8. Ideal Antibody Combinations and Analysis Methods to Improve Signal and Reduce Background. **A)** Background and noise for three different approaches reveals that signal generated with zero antigen (background, **B**) is consistently low for F(ab')₂ beads. The lowest **B** values come from the Fab-Fab interactions, which also gives the lowest signal values. Also, the isotype control beads (Ctrl.) reveals that the lowest values of **N** comes also from F(ab')₂ beads, followed by IgG, and Fab. **B)** IgG beads are used with three different detection methods and interpreted with the four analysis techniques described in **Section 4.2.5**. For highest signal, *IgG beads and a line-profile analysis approach is the best technique.*

In **Figure 4.8B** the results of assays using three different unlabeled capture antibody bead types followed by 100 ng/mL CEA antigen, and whole IgG₁ detecting antibody indicates differences between the four methods of deconvolution as well as

inherent differences in capture efficiency. First, IgG₁ beads consistently generate the most intense signal, regardless of analysis approach. Versus F(ab')₂ beads, IgG₁ signal is greater by a factor of 1.54, 1.50, 1.46, and 1.52 for the LP, CAOI, D, and CP analysis method detailed in **Section 4.3.5**. When this identical comparison is relative to Fab beads, the amplification ratios rise to 4.00, 2.96, 3.80, and 3.92. The increased values of F(ab')₂ beads relative to Fab is approximately 2.5 for LP, D, and CP methods and 2.0 for CAOI, values appropriate considering the F(ab')₂ fragment's 2X increase in size versus Fab.

Comparison of the results for the different analysis methods again indicates that the LP method yields the most intense signal, followed by CP, D, and CAOI. The LP analysis technique produces output values nearly twice as high as CAOI. This observation is attributed the LP method's selection of only the most intense pixels across successive line profiles; the CAOI approach averages both the dim and bright pixels into a single value. For a 280 μm bead, the LP method takes 104 successive line scans (156 pixels wide) and effectively identifies the 104 most intense pixels out of the entire bead. The average of these 104 pixels is reported as S for the bead. Conversely, the CAOI approach takes those same 104 pixels and dilutes them with the other 76301 pixels in the entire AOI, drastically dampening their contribution to signal transduction. The D and CP approach, although analyzing fewer pixels than CAOI, are still influenced by the averaging effect of dim pixels.

Having identified the most appropriate capture and detection bioligands as well as analysis approach, a final comparison and representation of data is presented in **Figure 4.9**. Here, 50 ng/mL CEA antigen and 11 μM detecting antibody were used. These experiments again demonstrate that the IgG-IgG analyte capture and detection pathways results in the highest signal, nearly double the next nearest neighbor, F(ab')₂ capture, IgG

detection. Although Fab-Fab has low background (*vide supra*), this advantage is tempered by the poor signal output seen below.

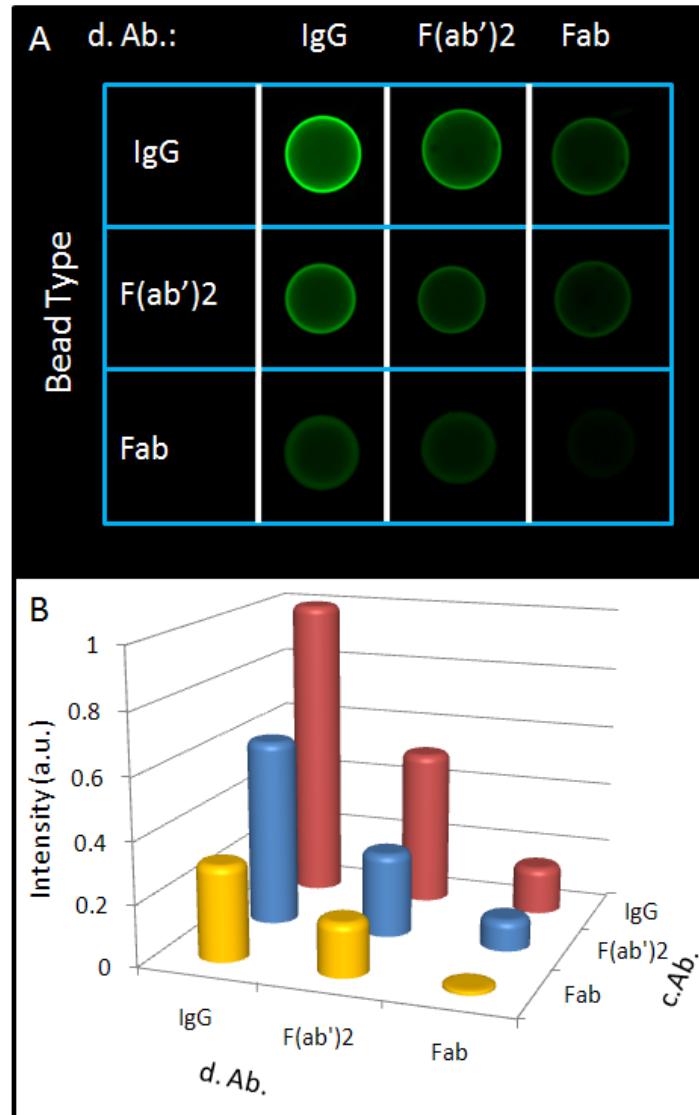


Figure 4.9. Signal Optimization. **A)** One row cropped sections of photomicrographs analyzed with three different detecting antibodies. Again, the most intense signal came from the IgG-IgG interactions. **B)** LP intensity values from the photomicrographs in A were scaled in relevance to the most intense signal. Whole IgG antibodies were used for the remainder of the studies. (All images have been background corrected and use one second of exposure.)

4.3.1.6 Effect of Capture Antibody Size on Antigen Location.

To understand better the molecular level location of all immunoassay components, fluorescently labeled CEA *antigen* was next integrated into the NBC. Initially, Alexa Fluor 350 labeled this protein, but after extensive efforts to increase the loading level on CEA it was found incompatible due to its low fluorescent intensity and low quantum yield. This blue fluorophore would have been preferable as its spectral signature is substantially different from the Alexa Fluor 488 on detecting antibody and Alexa Fluor 647 on capture antibody (see **Section 4.4.2**). While the fluorophore appeared in epifluorescent microscope images, it was invisible in the confocal arrangement and the inherent thin optical slices. To remedy this, Alexa Fluor 546, a more robust, orange fluorochrome was employed.

Figure 4.10 illustrates the differences in antigen distribution between the three different bead types: Fab, IgG, and F(ab')₂. In **Figure 4.10A**, a grayscale look up table was used in tandem with the Alexa Fluor 546 dye system and confocal microscope. Initial observations on signal intensity correlate well with the epifluorescent arrangements seen above. The S/N ratios of 11.7, 16.9, and 20.1 result from the Fab, F(ab')₂, and IgG beads, respectively; amplification factors are similar to those seen above. More interestingly, is the different behavior in bead *penetration*. Note the narrow distribution of antigen in the IgG bead—the almost near uniform arrangement of signal on the periphery. This is in contrast to the less monodisperse signal dissemination of signal in the smaller fragment beads. To characterize quantitatively these observations, 136 pixel (393 μm) line profiles were drawn across each bead (**Fig. 4.10B**). Penetration depth could then be calculated using the half-max approach as follows: The highest intensity value was identified by spatial pixel location. This intensity value was then

divided by two and the spatial pixel value that corresponded to that intensity was identified. The pixel difference between maximum and half maximum was calculated and converted into values of micrometers and listed in **Figure 4.10C**. Antigen penetrates 1.5 times deeper into the bead interior via Fab beads relative to whole IgG, an observation attributed to decreased pore occlusion, explored further in **Section 4.4.3**.

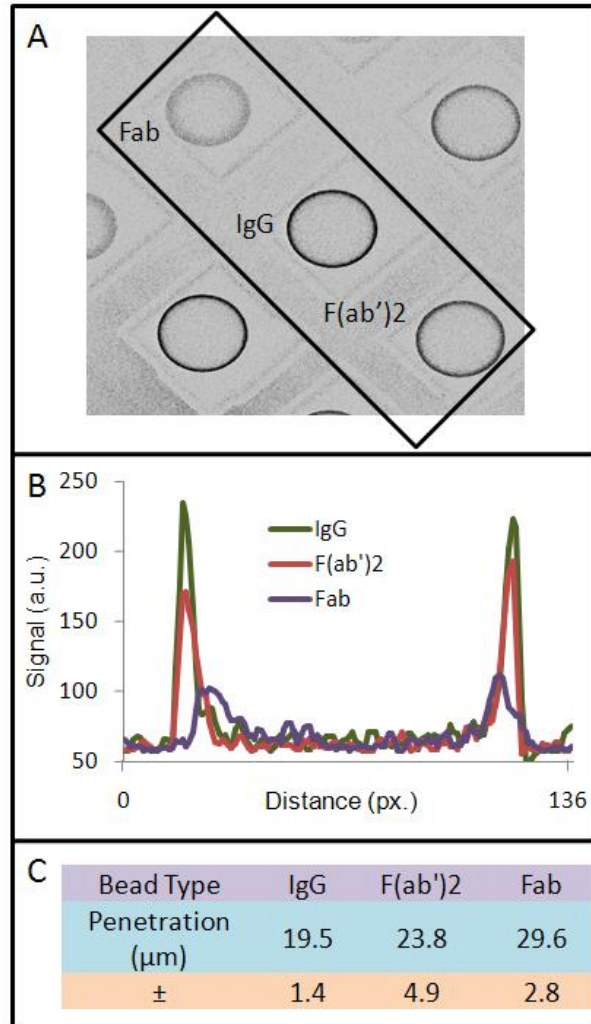


Figure 4.10. Antigen Location in Bead. **A)** Confocal image of antigen location in beads with either Fab, IgG, or F(ab')₂ as the capture moiety. **B)** Line profiles from the three different bead types reveal differences in both intensity and distribution. As the capture antibody becomes larger (IgG) beads sequester more of their target on the exterior. Smaller capture elements (Fab) allow penetration of analyte deeper into the exterior. Data compendium in **C** was determined as penetration at one-half of maximum signal.

4.4.2 Multiple Color Channel Colocalization

Figure 4.10 introduces labeled antigen as a third fluorescence body into this analysis and several challenges arise in attempting any type of colocalization, much less three-color experiments. Colocalization implies the presence of two or more reporter molecules in the same location in three-dimensional space. Key to understanding these experiments is a realization of the limitations of optical microscopy and the wavelength-dependant resolving power. Fortunately, these bead-based confocal images do not demand the kinds of cellular level resolution typical of colocalization experiments.²⁵⁶ Also, the location specificity of the signal is due to specificity of the conjugated biological moiety. Non-specific binding of a labeled antigen or antibody could imply untrue colocalization. Further, the various fragments may not have an even distribution of dye. For example, whole IgG has one third fewer amine sites for fluorochrome binding than does F(ab')₂, but both have nearly identical analyte recognition epitope. Additional challenges inherent to the microscopy arrangement include retaining excitation strengths across all three labels and minimizing chromatic aberration.

Imaging considerations also arise from the use of the fluorescent probes. First, all dyes have different quantum yields as well as characteristic excitation and emission profiles. Second, and more importantly, these dyes are not spectrally resolved either from an emission or excitation standpoint. This leads to the possibility of the signaling scheme experiencing fluorescence resonance energy transfer (FRET) decreases whereby emission from one dye may be reabsorbed by another molecule, effectively reducing signal out. Furthermore, the dye emission profiles experience overlap. For example, both Alexa Fluor 488 and Alexa Fluor 546 emit light at 575 nm and determining which molecule type (and thus corresponding bioligand) is responsible for the signal is only possible with careful controls. Third, the Bayer filters of color CCD cameras are prone to cross color channel effects, especially at higher fluorescent signals. In these situations,

improper loading levels or inappropriate camera settings such as exposure time or gain, can result in saturation of the specific CCD elements and bleed into other channels. The fluorophore and thus color choices used for the three part labeling are detailed in **Figure 4.11** and illustrate the spectral challenges in such an arrangement.

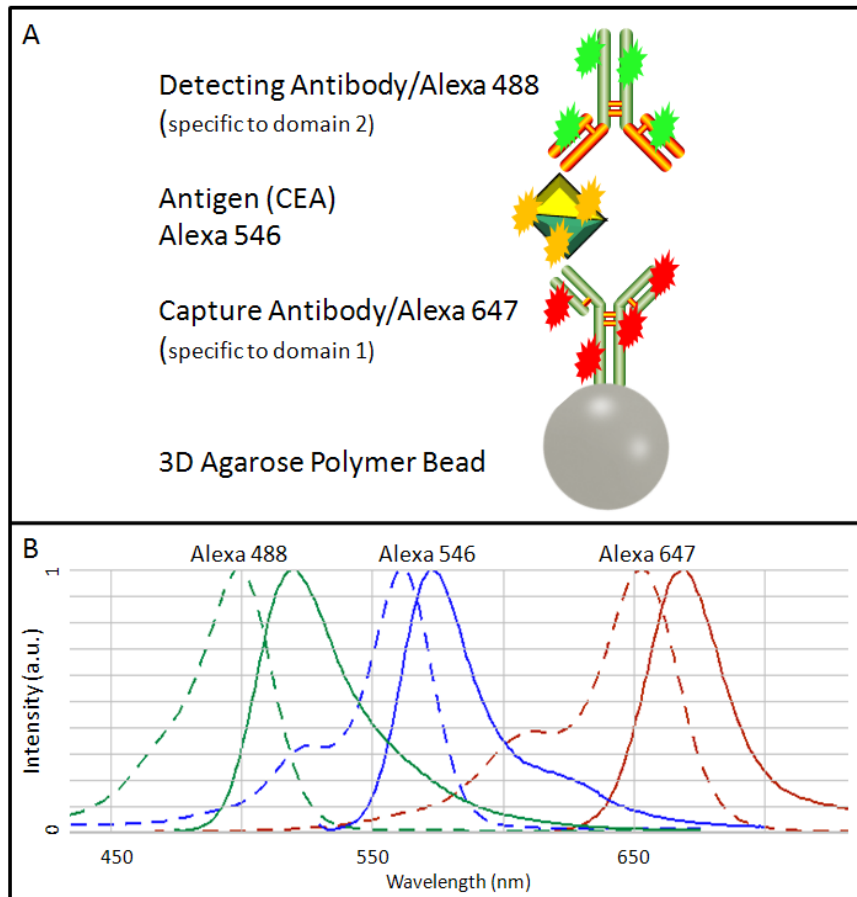


Figure 4.11. Three-Color Colocalization. **A)** All three parts of the bead-based sandwich immunoassay are linked to fluorescent tags in the following studies. The agarose bead substrate is coated with capture antibody/Alexa Fluor 647, which fluoresces in the red. Antigen is identified by its Alexa Fluor 546 tag, an orange dye. For confocal imaging, this fluorophores corresponds to a blue lookup table. Finally, detecting antibody is identified by an Alexa Fluor 488 (green) tag. **B)** The excitation and emission spectra of the three fluorophores mentioned above reveals overlap and the need for careful optical controls to prevent unauthentic signal. (Spectra in **B** is copyright and reproduced courtesy of Invitrogen/Life Technologies, Inc.)

Given the potential for cross talk limitations, it is important that careful study of control cases are completed to establish the limits of these studies. The most problematic case was high intensity red signal from the capture antibody crossing into those pixels dedicated to green channel light collection. Three approaches were used to reduce or eliminate the interference potential. The most easily controlled variable in these experiments was the exposure time of the CCD camera. The DVC software allows integration times of 0.09 ms up to many seconds of exposure time to be collected. Response curves could be collected that show the signal intensity as a function of exposure time (data not shown). 250 ms of exposure time was ideal at eliminating red bleed into the green channel. Second, was the amount of capture antibody on the bead. **Figure 4.12** illustrates the differences between a high and low amount of capture antibody and **Section 4.3.3** will give more results of these differences. Finally, a background correction procedure, in which images were collected before and after a new experimental parameter, allowed only the specific fluorescence signal increase to be evaluated. For example, after bead loading into flow chamber, image collection with the red (Alexa 647) and orange (Alexa 543) filter cubes revealed the amount of specific signal in red channel and bleed in orange. After introduction of Alexa 543 labeled antigen, another image was recorded. The difference between these two Alexa 543 images was specific fluorescence from antigen. As confocal images were taken after the entire immunoassay was completed, an alternative approach to controlling bleed was taken. Here, careful sequential scanning was performed. Although the optical design allows for the simultaneous collection of all three fluorescent images, the excitation laser lines at 488 nm, 543 nm, and 633 nm were increased in order to only excite one fluorophore at any given time. Despite only one exciter being on, all three PMTs were simultaneous active with their settings tuned to ignore non-specific signal.

	High [c.Ab.]	Low [c.Ab.]	High [c.Ab.]	Low [c.Ab.]
d.Ab.			8.3	0.7 (1.2%)
Agn.			16	0.25 (0.53%)
c.Ab.			28	2.67

Figure 4.12. Three Color Imaging via Epifluorescent Microscope. Signal bleed and cross talk were negated by reducing camera integration time, reagent concentration, and via background subtraction. Optical settings: c.Ab. (647), gain 0, offset 0, 6 ms exposure; antigen (543) gain 5, offset -7.5, 1 sec exposure; d.Ab. (488) gain 5, offset -7.5, 1 sec exposure. Tabular results indicate signal present before next layer of immunocomplex was applied. For orange and green signal, this is the amount of “bleed” and is expressed parenthetically as a percentage of authentic signal. Note that an additional set of images were collected at lower exposure time to eliminate optical saturation in the high concentration beads.

4.4.3 Effect of Agarose Porosity on Assay Performance

Having ascertained which bioligands give optimal signal as well as the preferred method to interpret photomicrographs, the next goal in understanding molecular level behavior of the NBC was a more detailed characterization of the agarose nano-net. Although previous studies in this group made casual relationships between agarose porosity and assay behavior, this work took a systemic approach. A number of factors including the heterogeneous nature of the nano and microfibers and difficulty maintaining adequate bead hydration compounds accurate characterization of the agarose beads. Furthermore, literature reports describing agarose is typically on slabs of agarose gel and not the bead structures used in the NBC. Nevertheless, valuable information on the structure of the beads and pore sizes within the beads may be interpreted from work

by Pernodet²⁴⁵ and Liu²⁰⁷ in which estimates of pore size in the 2% agarose gels used in **Chapter 3** range between 100 and 400 nm.

4.4.3.1 Agarose Permeability

Typically, agarose gels are likened to other types of chromatography; models describing agarose use the notion of particles diffusing through a porous media, i.e. packed column. Descriptors of agarose include the weight percent, fiber radius, permeability, and pore size. Depending on the synthetic approach and rate of cooling the gel from liquid to solid phase, the weight percent of agarose most typically has the greatest influence on downstream analytical descriptors, and thus performance, of beads. **Figure 4.10** more clearly illustrates differences between beads of different weight percentages. As the weight percent increases, there is more solid phase in the gel and less void volume—a situation modeled by Darcy’s permeability.²⁵⁷ Although commonly used in geology and petroleum engineering, this term has recently found to be appropriate for use in describing agarose and measures the ability of a pressure driven fluid to flow through porous media.²⁵⁸ Using the method of Clague and coworkers, later refined by Deen’s group, the Darcy permeability of agarose can be calculated using the estimates of agarose fiber radius provided by Berk.²⁵⁸⁻²⁶⁰ More explicitly, **Equation (4.1)** relates the Darcy permeability (κ) to the volume fraction of agarose (Φ) and radius of randomly oriented neutral fibers (r).

$$\kappa = [(\frac{1}{2})\sqrt{(\pi/\Phi)-1}][.71407e^{(-0.51854\Phi)}][r^2] \quad (4.1)$$

This estimated r value, as presented by Pluen and Berk, is 3.3 ± 0.4 nm by Ogsten’s method and 4.0 ± 0.5 via Brinkman’s approach; a value of 3.5 nm was used for the calculations presented below in **Figure 4.14**.²⁶⁰⁻²⁶²

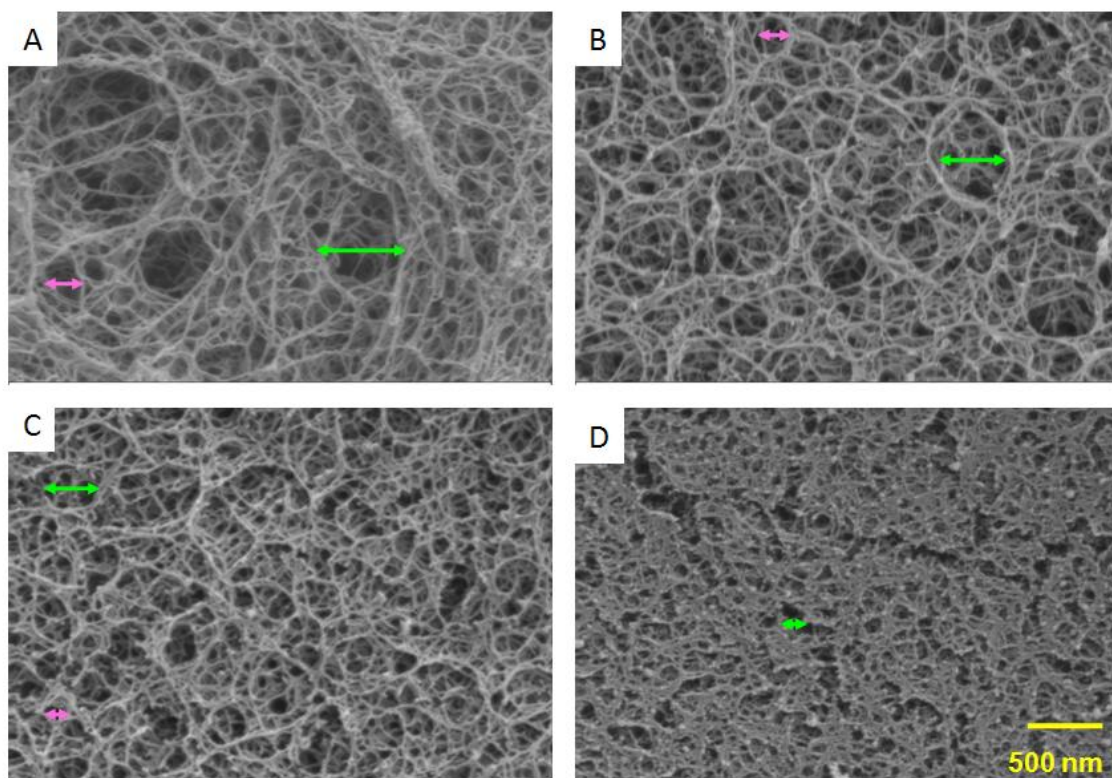


Figure 4.13. Bead Porosity Determines Function. The agarose microspheres have pores of tunable porosity. By selecting the percentage agarose in water during the synthesis, the immunoassay infrastructure may be tuned. Here, SEM images for beads of 0.5% (A), 2.0 (B), 4.0% (C), and 8.0% (D) reveal that pore size increases as percent agarose decreases. Through this electron microscopy technique, pore size estimates were gleaned through distances between adjacent agarose nanometer scale fibers. Green and pink arrows indicate representative measurements used to construct the green and pink curves in **Figure 4.14B**. (These images collected and reproduction permission granted by Dr. Jorge Wong.)

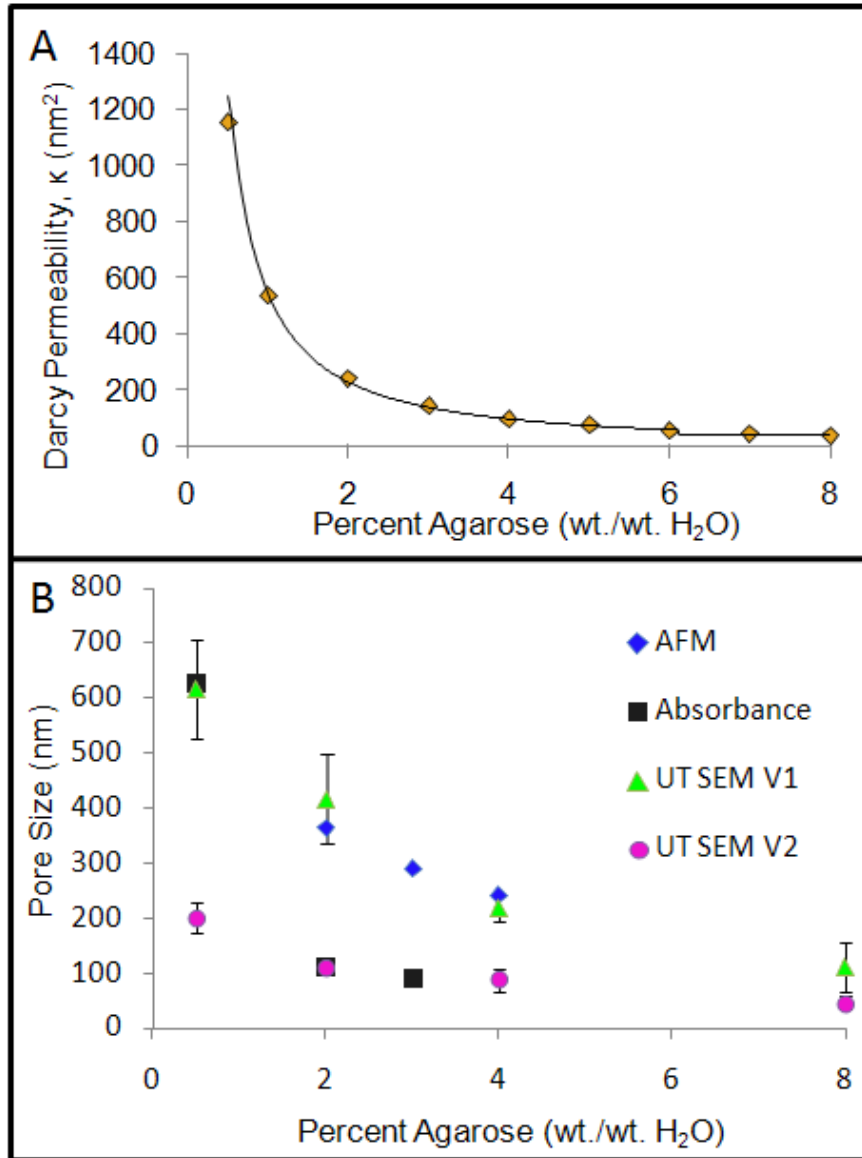


Figure 4.14. Characterization of Bead Porosity. (A) Permeability of a model porous structure, based on agarose, decreases exponentially as weight percent of solid phase (agarose) increases. A situation measured experimentally in (B). Here, three different approaches measured the diameter of pores in agarose gels, a descriptor similar to permeability. The atomic force microscopic (AFM) approach gives a tight cluster of pore sizes between 200-400 nm,²⁴⁵ while absorption-based, spectroscopy experiments (Absorbance) techniques show the exponential decay predicted by the model.²⁰⁷ Data from SEM images gathered in conjunction with this dissertation (SEM - UT) also correlate to the exponential reduction in pore size with increasing agarose concentrations predicted by model and agree nicely with the AFM published literature values.

The SEM images presented in **Figure 4.13** were taken at 100,000 X magnification and specific regions of interest cropped and tiled. Various pore sizes were measured by creating lines with width sufficient to bridge the gaps between the two adjacent agarose fibers nearest the surface of the bead. This was repeated again at for a smaller grouping of pores. The microscope's built-in scaling tool converted average pixel widths into nanometers by (4.87 nm/pixel). Values for the upper grouping of 616 ± 91 , 415 ± 80 , 218 ± 25 , and 109 ± 45 nm were obtained for the 0.5, 2, 4, and 8% (wt./wt.) agarose gels, respectively. The smaller cluster is illustrated graphically. While this method is potentially subjective and may not be representative of the hydrated, atmospheric pressurized beads, it does approximate nicely published literature values. This data is displayed graphically in **Figure 4.14B** and correlates well with the experimental model of permeability. Although the analytical descriptors between **Figures 4.14A** and **4.14B** are different, their underlying function—to detail the porosity of the substance—is identical. Important here is the exponential decline in porous nature of both the model ($y = 742.6e^{-0.41x}$) and the experimental data sets ($y = 645.4e^{-0.23x}$) at higher concentrations of agarose.

More detailed model sets should include information on capillary forces within the bead. Further, permeability changes rapidly in response to pressure by **Equation 4.2**.

$$Q = \frac{-\kappa * A * \Delta P}{\mu * L} \quad (4.2)$$

Here, Q is amount of flow (volume/time), A is cross sectional area ($62,000 \mu\text{m}^2$ for the NBC agarose beads), ΔP is pressure drop (determined by flow rate in NBC manifold), μ is viscosity of fluid, and L is length of flow path ($280 \mu\text{m}$ in NBC-type beads). Intuitively, an increase in κ or external pressure (flow rate, ΔP) leads to a greater amount of fluid flowing through the bead. Flow rate was one of the additional parameters included in a computational fluid dynamics study prepared from the data in Jorge Wong's

dissertation.¹⁹⁹ As stated in the introduction, this study monitored the increasing amount of fluorescently labeled antigen that penetrates a bead. From this **Figure 4.15** was prepared that gave estimates for the pore sizes in these 2% agarose beads.²⁶³ The estimates gleaned from this study, bead pore size of roughly 140 nm again corresponds nicely to the estimates presented in **Figure 4.14**. These different approaches to measuring pore sizes give two rough classes of pore sizes—between 100 and 200 nm and between 250 and 600 nm. In actuality, *both* of these are likely true. The SEM images above show that an extremely wide range of pore sizes are present. Even though the SEM preparation method effectively shrinks the agarose, that there are a wide range of pore sizes, likely remains in the hydrated polymer used in NBC assays. The impact this has on immunoassays performance is detailed below in a case study

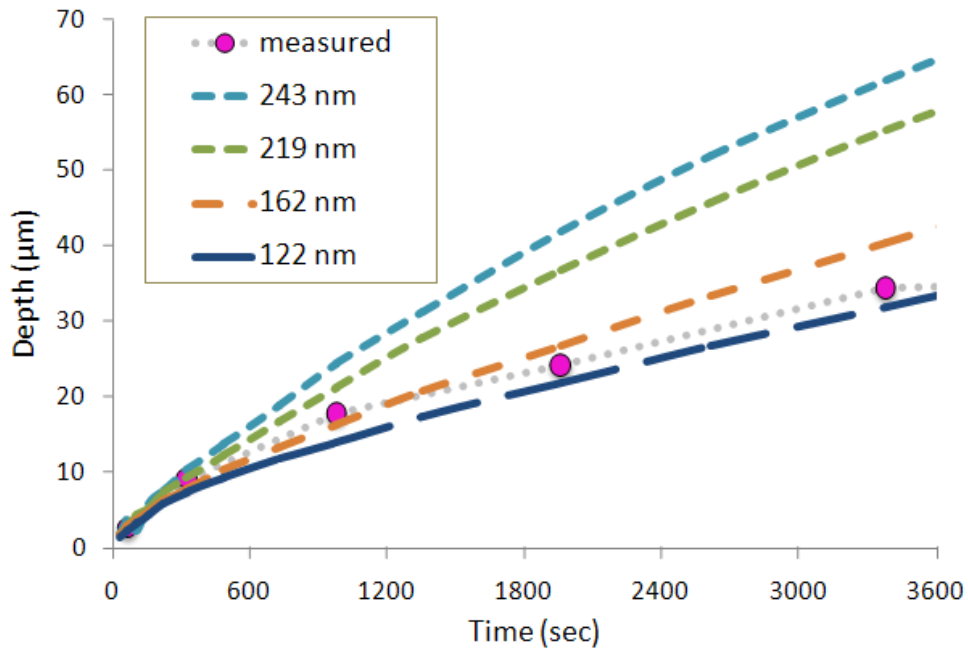


Figure 4.15. Bead Porosity via Computation Fluid Dynamics. Here, additional details including pressure and bead size was used in tandem with a penetration depth versus time study to give estimates for the 2% (wt./wt.) agarose (cross linked) used in this study.

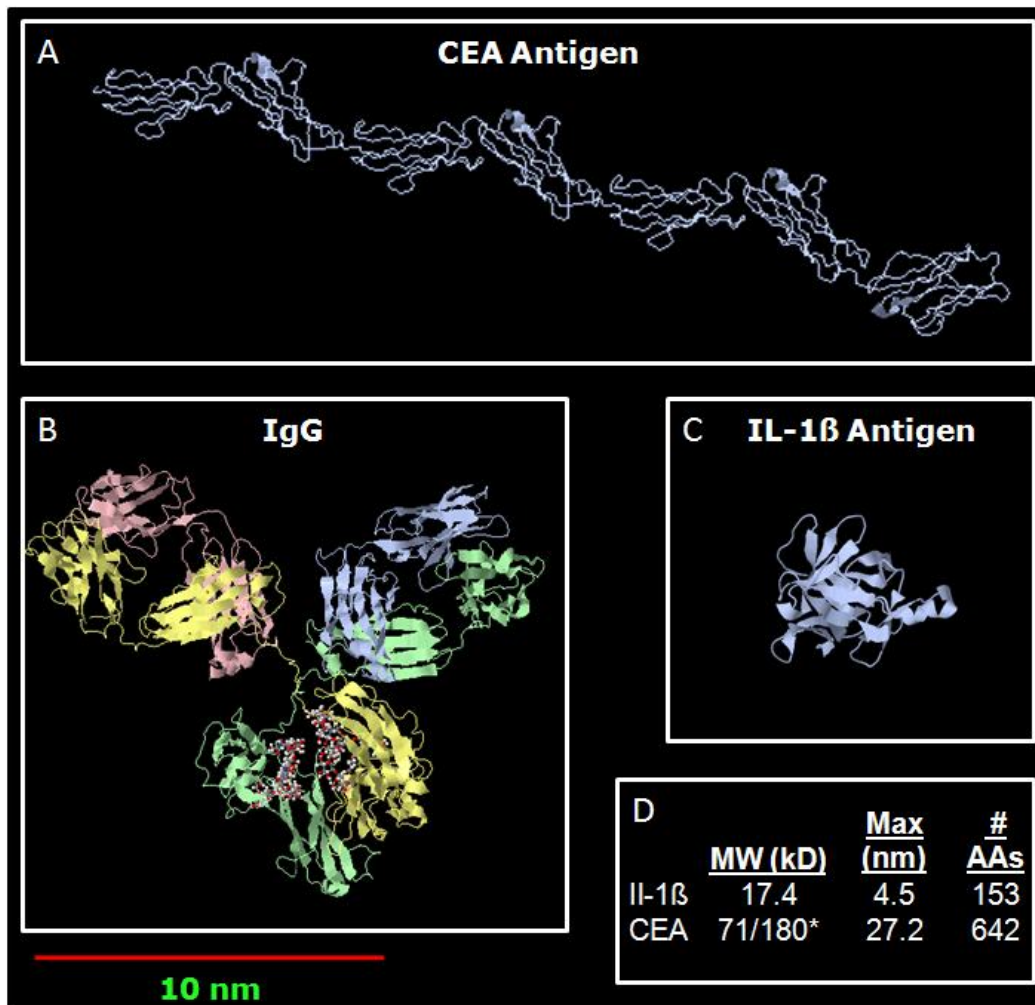


Figure 4.16. Size Features of Immunoassay Components. To illustrate the necessity to consider bead porosity in assay design, CEA²⁰⁶ (PDB ID = 1e07) (A) and IL 1- β ²⁶⁴ (PDB ID = 1t4q) (C) antigens are displayed, drawn to scale. Regardless of antigen size, IgG¹⁵⁰ (PDB ID = 1igy) recognition element remains nearly identical in size (B). D) The larger size of CEA results from its increased molecular weight (* indicates glycosolated weight) and larger number of amino acids. (Images reprinted in accordance with the policies of the *Research Collaboratory for Structural Bioinformatics' Protein Data Base* at Brookhaven National Laboratory.²⁶⁵)

4.4.3.2 Effects of Agarose Permeability and Antigen Size on Immunoassay

In **Figure 4.16**, a space-filling model of the IgG molecule is shown in addition to two representative biomarkers—CEA, and interleukin-1beta (IL-1 β). For all work in **Section 4.3.3**, fluorescently labeled, whole IgG molecules are used for both the capture and detection bodies; this design is the most commonly followed in previous NBC reports and verified by work in **Section 4.4.1**.^{127, 130} Although there is a large size difference between the two antigens presented here (22.7 nm in size or 162.6 kD), both immunoassays employ the same IgG structure basis for capture and detection. By designing identical assay systems, the effect of antigen size and agarose porosity can be elucidated.

Beads were prepared with 0.5 mg/mL capture antibody. After overnight incubation and subsequent protein assays, it was found that the CEA beads were coated with 0.29 mg/mL of antibody and IL-1 β beads were coated with 0.22 mg/mL. Differences between the two include variance in the absolute number of beads transferred from stock vial to reaction vial, as well as reactivity of the dye. This was performed for beads of 0.5%, 1%, 2%, and 4%. Importantly, these beads were not cross-linked according to Wong's, typical, previous method.¹⁹⁹ Rather than joining free hydroxyl groups together via divinyl sulfone to create agarose helices, these beads were used after initial glyoxal activation. As a result, the 0.5% beads were highly incompatible with the MEMS-based NBC—an observation that correlates to the exponential change in behavior seen at low concentrations in **Figure 4.14**. More specifically, their propensity to deform under pressure or fluid flow in the silicon chip as well as their resistance to handling by micro-manipulators under the bead-loading, dissection microscope, precluded their use in further studies. Fortunately, the 1.0%, 2.0%, and 4.0% beads maintained a sufficiently solid texture and form to allow their inclusion into the NBC.

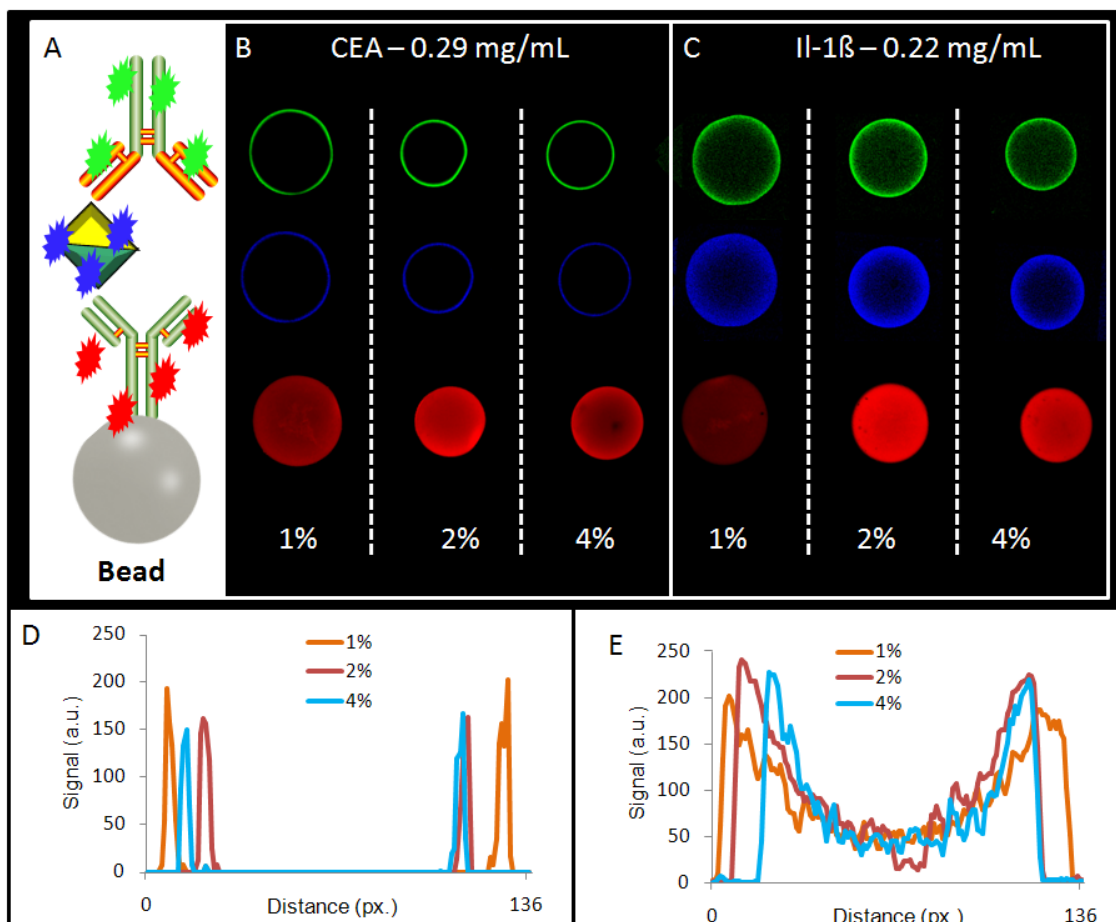


Figure 4.17. Analyte Size Affects Bead Behavior. (A) Three-color identification approach is used for two different size analytes. (B) Signal from the larger CEA molecules (27 nm) signal remains on the exterior. (C) IL-1 β is a smaller, globular protein (5 nm) and allows for deeper penetration of immunoassay components. (D) Regardless of bead porosity, all CEA antigen and detecting antibody remains in the thin layer on the bead exterior, unlike IL-1 β behavior (E) in which a gradual decrease in analyte is seen from exterior to interior. (Please see **Figure 4.15** for optical settings.)

A wealth of information may be gleaned from **Figure 4.17**, in which penetration of capture antibody, antigen, and detecting antibody is monitored via red, blue, and green

fluorescence signal. These confocal images capture the medial slice of the agarose bead and show differences between the two assay systems. Key observations include the following: First, both systems have capture antibody coated throughout the entire bead substrate, a function of the overnight incubation of capture element and the bold, even tenacious, nature of plate rocker shaking. Next, similar to **Figure 4.10C**, antigen penetration depth was determined by pixel width at half maximum. In the CEA system, penetration depths of $10.1 \mu\text{m} \pm 2.0$, $10.1 \mu\text{m} \pm 2.0$, and $8.5 \mu\text{m} \pm 0.2$, were observed for 1%, 2%, and 4% agarose, respectively. The IL-1 β beads exhibited antigen immobilization much deeper into the bead. Penetration measurements indicate depths of $78.0 \mu\text{m} \pm 6.7$, $57.1 \mu\text{m} \pm 5.5$, and $41.9 \mu\text{m} \pm 1.7$ are achieved for 1%, 2%, and 4% agarose, respectively. Here, the extent to which IL-1 β molecules enter the bead matrix is substantially higher than the degree to which CEA antigen ingresses. The CEA antigen has a maximum dimension approximately 5 times that of IL-1 β antigen, and penetration depths approximately 5 times less, depending on bead substrate type. Note that penetration depth increases with lower bead agarose percentage. That is, less agarose implies larger pores, which allows antigen to suffuse deeper into the bead—this fortifies further the observations made in **Figures 4.13** and **4.14** regarding bead porosity as a function of percent agarose. Finally, it is noted that all the green signal (detecting antibody) present in both the CEA and IL-1 β systems are confined to regions overlapping with blue signal (antigen).

Two important inferences may be drawn from this observation. First, nearly complete detection of antigen bound on the bead, in both the CEA and IL-1 β assay systems, is achieved. To determine analytically what percent of captured antigen is not later signaled by a detecting antibody, the technique of Bolte and Cordelières reported percentage overlap.²⁴⁸ In the CEA experiments, the amount of blue signal in green was

99.5% and the amount of green signal in blue is 97.9%. Thus, less than 0.5% of all antigen that is immobilized on the bead is not later transduced as signal. Furthermore, only 2.1% of green signal is present on the bead non-specifically. The Pearson correlation between these two populations of pixels indicated a strong relationship at 0.949. The intensity coefficient quotient (maximum = 0.5) was also high at 0.493. For the IL-1 β assay, percent blue in green is 95.9%; Pearson value is 0.887 and ICQ = 0.448. This lower degree of correlation is attributed to the larger number of pixels included in the analysis, i.e. more diffuse signal pattern. Regardless, these experiments reveal the reliability of the assay parameters in detecting a very high percentage of captured analyte while preventing non-specific immobilization of the reconnaissance beacon.

4.4.3.3 Antibody Concentration Effects on Immunoassay

For the assay above, signal cross talk in epifluorescent imaging was compensated for by the correction methods described in **Section 4.4.2**. This was designed to reduce the high fluorescent signal from the Alexa Fluor 647 capture antibody, which can introduce spectral bleeding and other interferences in the epifluorescent microscopy design. To overcome these challenges, beads with capture antibody concentration of 0.0096 mg/mL were prepared in addition to the 0.29 mg/mL beads. This concentration was inspired by the reduced loading levels discovered through optimization studies of antibody fragments. In **Figure 4.18**, the differences in signal distribution between the high and low capture antibody concentration beads illustrates the striking impact this factor has. Again, information from all three sandwich immunoassay components may be gleaned. First, capture antibody does not penetrate completely into the bead interior for the 2% and 4% low concentration beads, despite these beads' preparation identically to the high concentration population. Because the 2% and 4% beads have more agarose—and thus more reactive sites—than 1% beads, they are capable of depleting

completely the reserve of labeled capture antibody present in the conjugation reaction vial. This does not appear to be an effect of antibody size, but rather concentration.

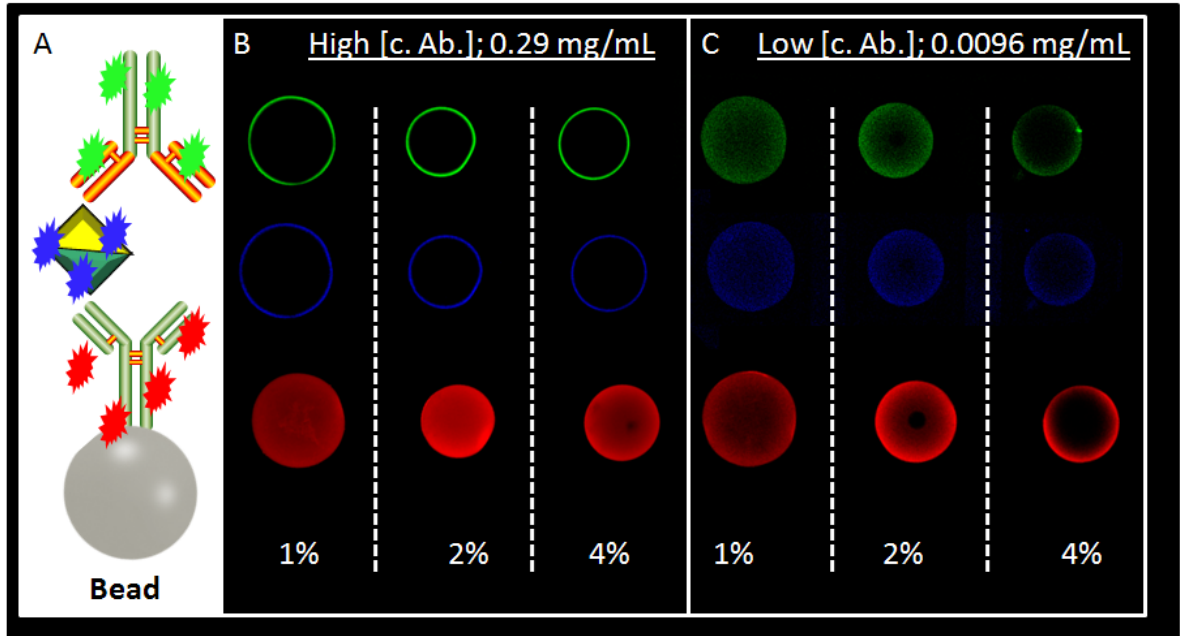


Figure 4.18. Concentration affects bead behavior. (A) The three-color identification approach from **Figure 4.2** is retained for two concentrations of CEA detecting antibody. (B) At high concentrations, signal remains on the exterior; however, at lower concentrations (C) the distance between capture elements increases allowing deeper penetration of immunoassay components. (Please see **Figure 4.20** for optical settings.)

In addition to capture antibody distribution, substantial differences are seen in the antigen and detecting antibody apportionment between high and low concentration detecting antibody beads. A drastic increase in both antigen and detecting antibody penetration is seen in the lower concentration beads. Versus the approximately 10 μm penetration depths seen in the 0.29 mg/mL beads (*vide supra*), the 0.0096 mg/mL beads have penetration depths of 52.0 μm , 43.4 μm , and 20.2 μm for 1%, 2%, and 4% percent agarose, respectively (**Fig. 4.19**). Two factors influence the trend towards less antigen penetration at higher concentrations of agarose in beads with little capture antibody. First

is a lack of capture antibody to immobilize target in the interior. Secondly, at higher concentrations of capture antibody, the immunocomplex occludes the agarose nano-channels, a hypothesis below confirmed.

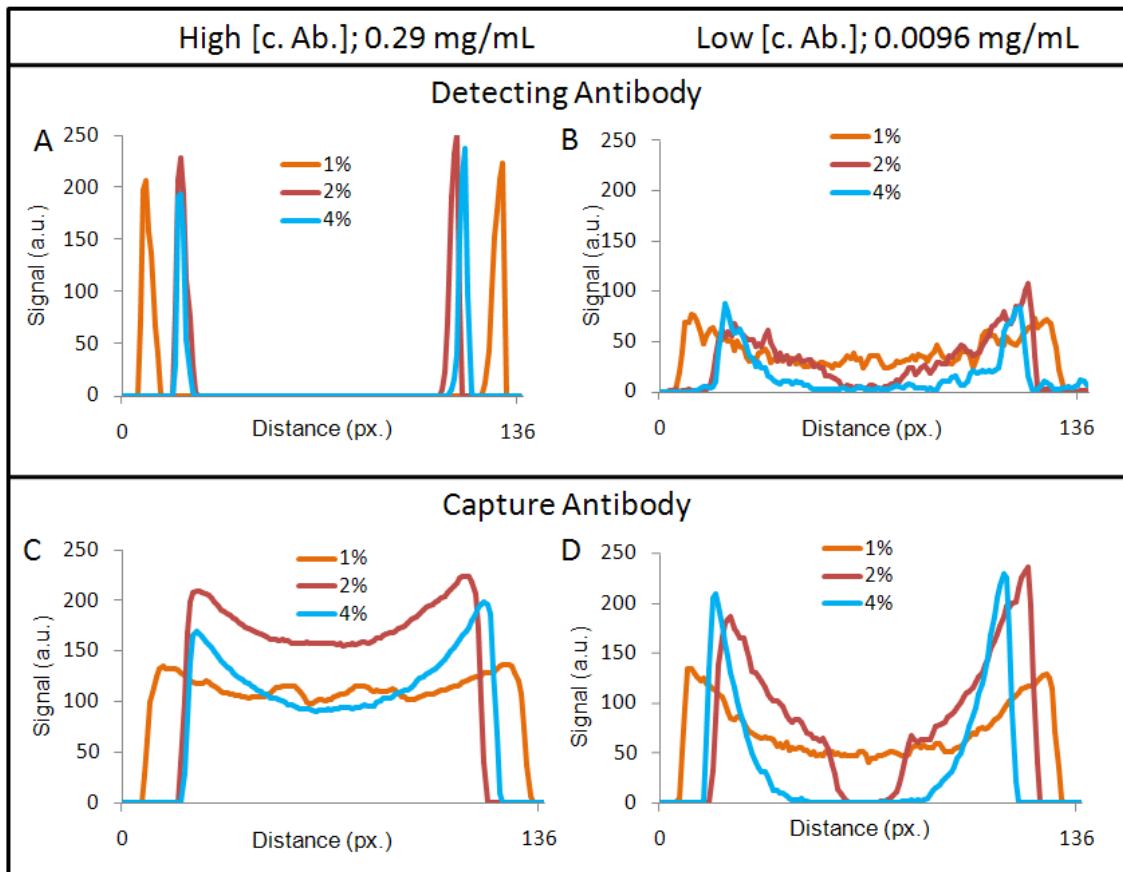


Figure 4.19. Line profiles of immunoassay components from Figure 4.18. The behavior of detecting antibody is confined to the bead exterior at higher concentrations of capture antibody (**A**) than the isotropic distribution seen at lower concentrations (**B**). (**C**) This accumulation of detection body on the periphery of **A** is in sharp contrast to the capture antibody distribution seen in the same system. (**D**) At lower concentrations of capture antibody, the differences in bead potency may be seen. In the 1% beads, there is an excess of capture reagent, allowing this signal to penetrate all the way to center. In contrast, the 4% beads have more active sites, effectively depleting all of the reagent before penetration to center is possible.

4.4.3.4 Importance of Pressure Driven Flow

Also important to consider here is fluid flow within the NBC system. **Figure 4.20** illustrates flow paths typical for a 2% agarose bead within the silicon chip used in for these experiments. The first two panels show the plan (xy) view and an elevation (xz plane). Here, red arrows indicate the areas of highest flow. Note the absence of arrows, and thus flow, through the bead interior—observations consistently with **Figure 4.18** and **4.19**. Indeed, **Figure 4.20C** indicates that nearly all of the active, pressure driven flow is above and around the bead with the blue bead itself, influenced by Fick's law of diffusion. Smaller, more diffusive analytes such as ions and small molecules have a greater propensity to diffuse into the bead with diffusion coefficients (D) $\sim 10^{-5}$ cm²/s; larger proteins have D values of 10^{-7} cm²/s and below. The diffusion limited nature of the bead interior explains the observations made in **Section 3.4.3** in which a quick flow rate of 1.1 mL/min for 1 minute was insufficient to remove enough unbound fluorescence to achieve the low backgrounds necessary for ultra-low detection limits even though this is effectively greater than 8,000 bead volumes of rinse material. A 5 minute 0.2 mL/min gentle cleanse cycle was also needed to allow material deep within the bead adequate time to diffuse to bead surface where it was removed by pressure driven flow.

Additional work used a photofabricated stainless steel support structure to support the beads in lieu of the silicon MEMS structure indicates that the 'round object in a square hole' approach has benefits. **Figure 4.20C** illustrates the higher reflectivity of this material versus the nitride-coated silicon chip (**Fig. 4.20D**) as well as the round apertures versus square. A complete understanding of the performance features of the two systems in side-by-side analysis could not be completed in the time constraints of this dissertation. However, support structures that do not allow any flow diversion around the bead consistently causes bead deformation and bead extrusion through the opening. In addition, beads with low agarose percentages or beads not highly cross

linked frequently passed through the openings at flow levels above 0.5 mL/min. Nevertheless, improved signal was sometimes observed as a greater amount of analyte was forced through the bead reactor by this method. Ongoing work by other members of the McDevitt research community are exploring the effects of changing the physical dimensions of the chip support structure to determine the exact optimal geometry.

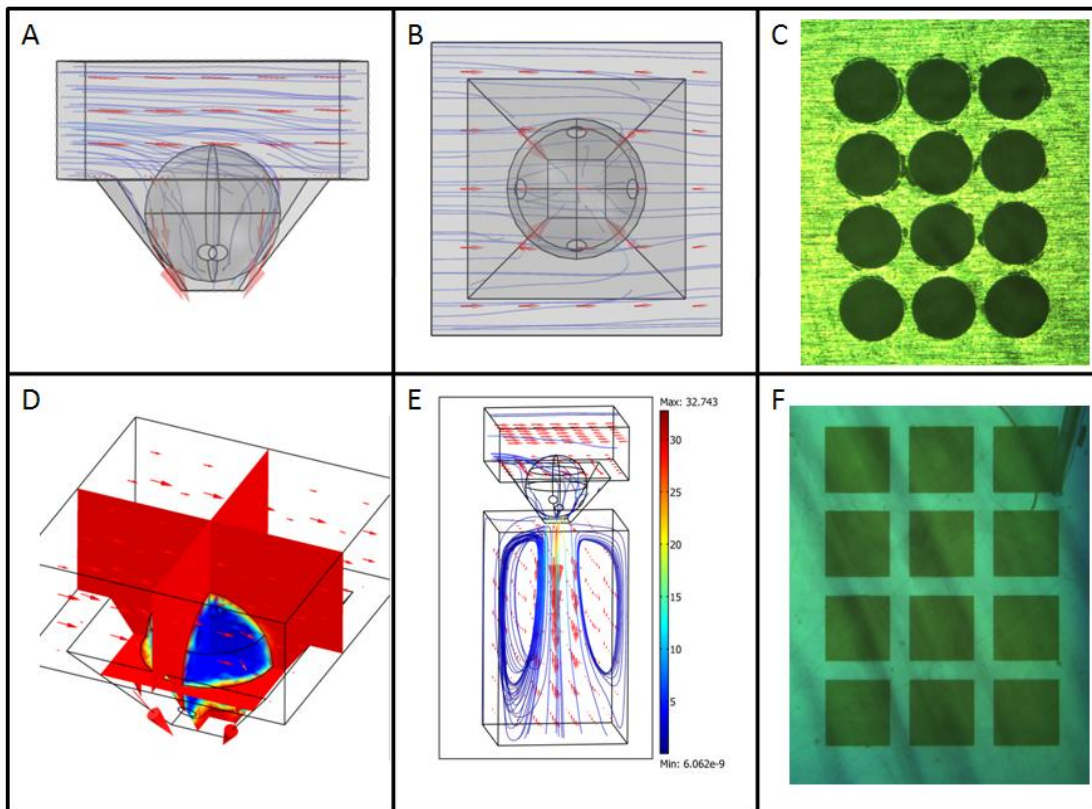


Figure 4.20. Chip Design Considerations. Computational fluid dynamic (CFD) studies indicate that the vast majority of NBC flow when using the silicon MEMS chip is around the bead. Red arrows in **A** (xz plane), **B** (xy plane), and **E** (xz plane expanded) indicate the most flow at 0.3 mL/min passes through the openings between bead and bottom of the well. Indeed the convective flow indicated by red in **D** is in contrast to the mostly diffusive transport in the bead, shown in blue. Although no CFD work has been done modeling the stainless steel support (**C**), observations made with the NBC suggest that it behaves very differently than the etched silicon chip (**D**).

4.4.3.5 Confocal Colocalization Imaging Controls

The attentive reader will note the red fluorescent intensity in **Figure 4.18B** has intensity similar to **Figure 4.18C**, despite being nearly 30 times more dilute. This is a result of the two images being captured under dissimilar optical settings on the Leica confocal microscope. Quality image capture of these less fluorescent samples required more sensitive optical settings. To confirm that the periphery-isolated patterning signal seen in the high concentration beads was a function of fluorochrome presence and not due to inadequate sensitivity of the photomultiplier tube detector, a series of images were captured at identical optical settings as the low concentration beads and presented in **Figure 4.21**. Importantly, the *intensity* of this fluorescent signal increases, but the *distribution* does not. It may therefore be concluded that the exterior-focused antigen and detecting antibody signal seen on the high concentration CEA beads is a true representation of the bioanalyte location and is not a photomicrographic optical artifact.

To determine whether the blue and green channel signal seen in the 0.0096 mg/mL capture antibody beads was a function of spectral bleed in the confocal microscope, the beads were analyzed prior to introduction of antigen and detecting antibody at the optical settings described in **Figure 4.21**. The results of that experiment appear in **Figure 4.22** indicating that the blue and green signal reported is indeed suggestive of the presence of the antigen and capture antibody and are not artifacts in the photomicrograph.

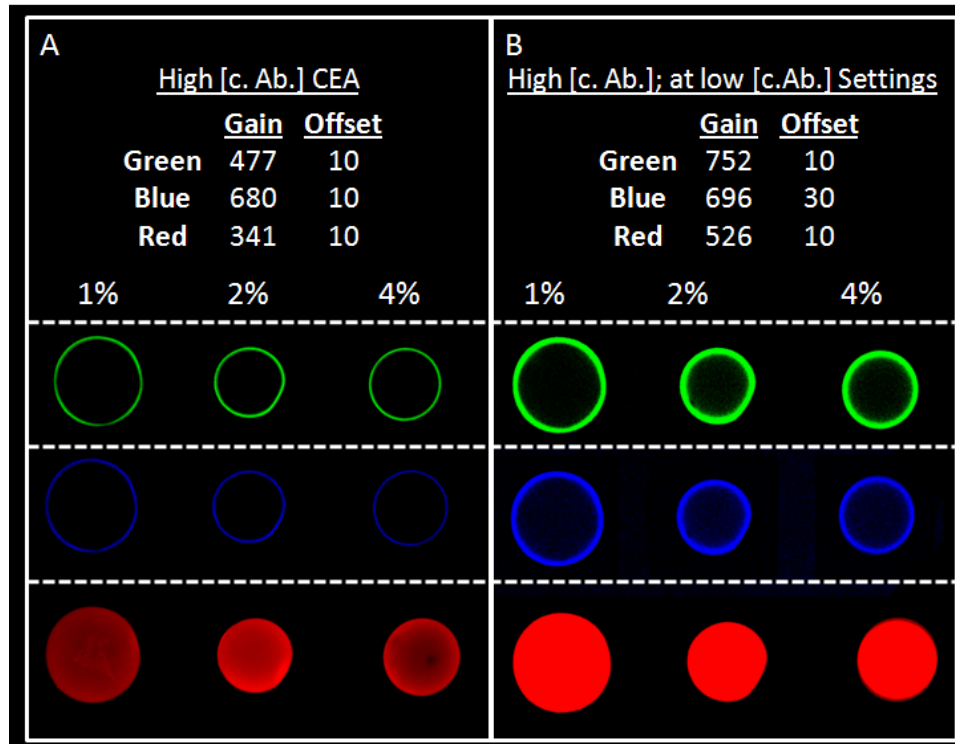


Figure 4.21. Optical Settings Experiment for Verification of Signal. In A, the same image is seen as in **Figure 4.14B** along with the optical settings needed for all three photomultiplier tubes on the confocal microscope. **B)** Here also is the same specimen imaged at the more sensitive optical settings required for the lower concentration specimen from **Figure 4.14C**. The similarity of the two images implies that the distribution differences seen in **Figure 4.14** are not due to increased gain (sensitivity) or offset of confocal optical settings as penetration depths do not increase.

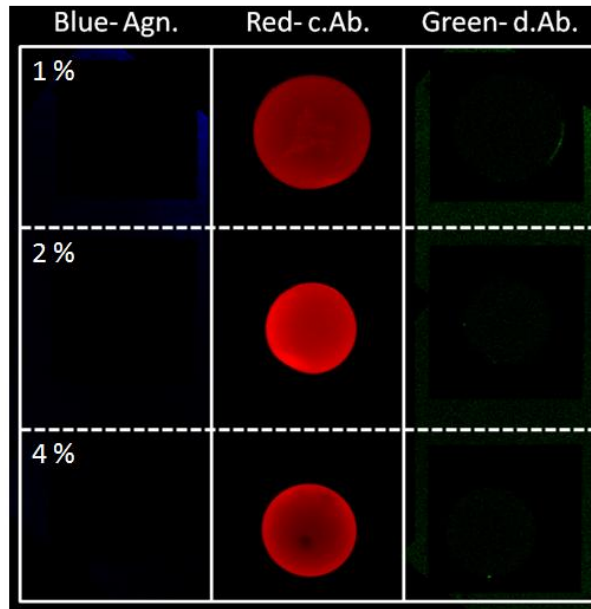


Figure 4.22. Cross Talk Negative Control. Beads only functionalized to capture antibody imaged at the optical settings detailed in **Figure 4.14B** with all three photomultiplier tubes. That absence of signal in the green and blue channels implies that the presence of signal in the above experiments is genuine.

4.4.3.5 Occlusion of Agarose Nanochannels

Being assured that the observed signal was indeed a valid representation of the presence of immunocomplex, a further disambiguation of fluorescence patterns was in order. Particularly interesting was the sharp difference between the low and high concentrations of capture antibody and the 0.0096 mg/mL beads' ability to allow analyte penetration and detection throughout more of the bead. As **Table 4.3** indicates, for the high concentration beads, only the outer shell (~ 40%) of the bead exterior is ever exposed to the entire assay sequence, with the remainder being effectively a void volume. This prevents maximum usage of the bead substrate and may be partially responsible for the plateau effect observed in high-level samples, e.g. **Figure 3.6A**. Unfortunately, using only the dimensions of pore size is inadequate to explain the behavior observed.

As **Figure 4.14B** illustrates, the pore dimensions for agarose given by all three methods indicate that the 57 nm CEA immunocomplex (15 nm capture antibody + 27 nm antigen + 15 nm detecting antibody) should pass easily through all but the most stringent of pores. Nevertheless, immunocomplex penetration is restricted to only the outermost regions of the bead and no difference was seen between 1%, 2%, and 4% beads. **Equation 4.3** helps to explain further these observations.

$$d = \sqrt[3]{\left(\frac{4/3 \pi r_b^3}{(*N_A / \mathcal{Y} * Mw)} \right)} \quad (4.3)$$

Here, d is the distance between capture antibody elements and is a function of the bead size as give by radius (r_b , nm), amount of capture antibody conjugated to beads (j , g/mL), Avagadro's number (N_A), molecular weight of the capture antibody (Mw , g/mol), and finally the number of beads per volume (\mathcal{Y} , counts/mL). For these experiments, \mathcal{Y} was determined by Kepler's conjecture as summarized in **Equation 4.4** where V_t is total volume of sample, p.e. is packing efficiency, and V_b is the volume of 1 bead.^{266, 267} For these experiments, it was found that 21,740 beads were estimated to be in 500 μ L of sample.

$$\mathcal{Y} = \frac{V_t * p.e.}{V_b} \quad (4.4)$$

Using this value, and 280 μ m beads and 155 kD IgG molecules, **(4.3)** can be decreased to the more manageable presentation in **Equation 4.5**, where the constant J condenses typical conditions of 280 μ m beads and IgG capture/dection bodies into 64.3 $\text{nm}^3 * \text{g/mL}$.

$$d = \sqrt[3]{\left(\frac{J}{j} \right)} \quad (4.5)$$

With **(4.5)** and values of j determined by protein assay before and after reductive amination of capture antibody with beads, **Table 4.3** was constructed to explain the relegation of signal to exterior in the high concentration beads. At 0.29 mg/mL of

capture antibody, the distance between each recognition element is < 83 nm, a value large enough to allow one complete CEA immunocomplex to pass. However, in the likely scenario that the bead chamber is lined with capture antibody, an 83 nm passage would be easily clogged with reagent material (**Fig. 4.22**). Two immunocomplexes have a total diameter of 114 nm—much larger than the distances between antibodies. When the concentration of capture antibody is reduced in **Table 4.3B**, the distance between antibodies increases nearly three times to 237.5 nm. This distance would theoretically allow deeper penetration of immunocomplex into the bead, an observation confirmed experimentally in **Figures 4.18** and **4.19**. It may be further surmised that the pore size in all three beads is at least greater than the 114 nm length of two immunocomplexes.

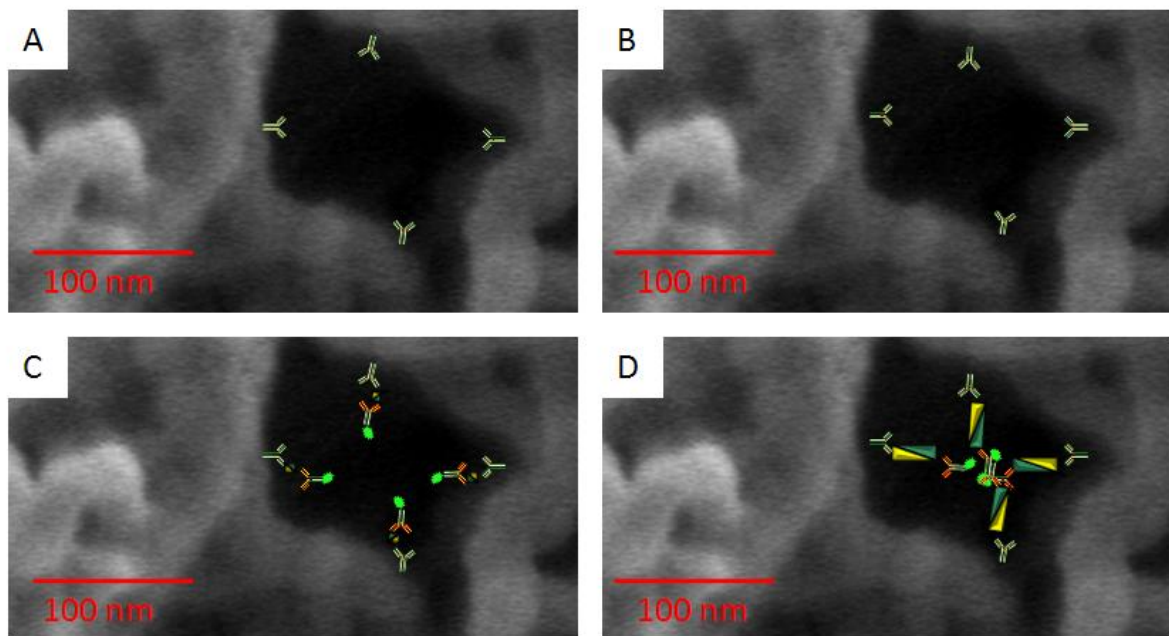


Figure 4.23. Occlusion of Nano-Channels. **A** and **B**) Agarose pore channels coated with detecting antibody. Smaller bodies, however, such as IL-1 β (35 nm) shown in **C**, allow penetration deeper into the bead interior. **D**) Larger immunocomplexes however, such as CEA (57nm) may block reagent transport in the agarose pores.

The hypothesis that the capture antibody is primarily responsible for occlusion of bead passageways is confirmed once again in **Figure 4.10**. Here, the variable changes from concentration of capture antibody, to its size. At the concentrations used in for these experiments (0.09 mg/mL), the distance between antibodies is 113 nm, just below the passage distance of the 114 nm CEA immunocomplex dimer. As with the three color experiments, all antigen is relegated to the exterior, with the important exception of the Fab capture fragments. Here, by reducing capture antibody by half, to 7.5 nm (recall **Fig. 4.3**), a critical distance barrier is passed, allowing antigen to penetrate deeper into the bead. The concentration of capture antibody needed to achieve this critical distance is expressed in **Equation 4.6**.

$$j = \frac{J}{(d_{\text{Immuno}})^3} \quad (4.6)$$

A						
High [c. Ab.]; 0.2901 mg/mL						
	Distance c.Ab. (nm)	Pore Size [§]	Pore Size [¶]	Pore Size ^{UT}	% Void	Epi. Signal
1%	82.9	408*	600	500*	60.3	77.0
2%	80.6	364	200	415	59.6	89.5
4%	78.7	243	<100	218	67.1	70.6
B						
Low [c. Ab.]; 0.0096 mg/mL						
	Distance c.Ab. (nm)	Pore Size [§]	Pore Size [¶]	Pore Size ^{UT}	% Void	Epi. Signal
1%	237.5	408*	600	500*	0.0	2.4
2%	237.5	364	200	415	0.1	4.9
4%	237.5	243	<100	218	9.6	4.7

Table 4.3. Detecting Antibody Concentration Differences Affect Signal. At higher concentrations of capture antibody (A) ~60% of the bead is unused for sandwich immunoassay. No reagents besides capture antibody can penetrate into the bead center. This remains true regardless of bead porosity. (B) At a lower concentration, the distance between antibodies is increased allowing for more of the entire immunocomplex to penetrate. Here, void volumes are reduced to zero; however, note the decreased epifluorescent signal intensity. The * indicates the values is an estimate based on the trend fitting. Data in § comes from Pernodet²⁴⁵ and ¶ is sourced to Narayanan.²⁰⁷

Importantly, in **Equation 4.6**, d_{immuno} is the size of the total immunocomplex. Thus, for the IL-1 β assay system, with whole IgG capture and detecting antibodies, the critical concentration of 1.50 mg/mL capture antibody begins occlusion. The experiments presented in **Chapter 4** are well below this value and, indeed, show no resistance to reagent transfer. It bears mentioning that the epifluorescent signal for the non-occluded bead is markedly lower than the higher concentration beads. The epifluorescent signal for the low concentration 2% beads are approximately 18 times lower than the 0.2901 mg/mL beads. Therefore, in assays seeking low limits of detection, the higher concentration beads may be more appropriate as these beads concentrate further the

analyte into a small region as they do not use entire bead volume. Unfortunately, this same phenomenon may also decrease the linear dynamic range.

4.4 SUMMARY AND CONCLUSION

A study of molecular-level modeling with experimental verification is completed and the questions addressed in **Section 4.1** may now be revisited.

- ✓ The optimal reagents for Alexa Fluor-based immunoassays in the agarose bead microreactors are identified to be whole IgG molecules for both capture and detection. This is in contrast to the observations with QDs.
- ✓ A substantial decrease in bead signaling capacity is observed for fragments of IgG₁. This observation is attributed to a higher likelihood that the fragment is coordinated to either bead or fluorophore through an amine group in the antigen-binding site. Additionally, enzymatic cleavage may induce non-specific reductions or denaturations in antibody structure.
- ✓ The use of Fab fragments for capture allow antigen and detecting antibody to permeate deeper into the bead, no increase in overall assay performance is observed.
- ✓ Larger antigens are restricted to the bead exterior at isomolar concentration of capture antibody. A direct dependence on size versus penetration into bead is observed.
- ✓ Increasing weight percent agarose, increases the number of available functional groups in agarose lattice, but also decreases pore size.

The observation here that whole antibodies are superior seems to be in conflict with the conclusions of Chapter 2 and 3 where antibody fragments gave best signal. Such a conclusion need take into account the size effects of the reporter probe. The larger QD size necessitated smaller fragments to be tailored to the agarose architecture. Any loss of immunoreactivity was compensated for by high QD fluorescent output for low limit analyte detection. In contrast, whole antibodies need to be used for molecular experiments because the Fc regions contains a large number of the molecular

fluorophores. Interestingly, both the IgG/Alexa and fragment/QD signaling bodies have sizes between 15-20 nm.

Three-color colocalization experiments reveal that nearly complete detection of immobilized antigen is achieved with the NBC system. Values of 99.5% detection typified the CEA assay. In addition, the distribution of immunoassay components throughout the bead was found to be highly dependent on two key variables—the concentration of capture antibody and the size of the antigen target. Decreasing either the antigen size or concentration of capture antibody allows a more monodisperse orientation of complex throughout the bead. High concentrations and large antigen types give the ring structures commonly observed in both confocal and epifluorescent designs. The derivation of a succinct equation to calculate the critical concentration of capture antibody to allow reagents complete access to bead interior may aid future researchers in designing experiments with optimal distribution of assay components. Although montages of bead types have been used to expand the linear dynamic range of assays, the improved understanding of the molecular conditions affecting signal output presented here, may allow for even further increases in dynamic range, e.g. bead set #1 optimal for fg/mL range, bead set #2 optimal in pg/mL, and bead set #3 measures ng/m. In addition, a variety of bead types are useful whenever a polymorphic analyte is being targeted. For example, the CRP molecule is an inflammation marker studied previously by other McDevitt group members.¹²⁶ At ng/mL levels the analyte behaves as a pentamer, however, as concentration falls into the pg/mL range, or in the absence of Ca^{2+} , however, mostly monomers are observed.¹²⁷ Having two bead types, one with smaller pores for the monomer, and one with large pores for the pentamer, all arrayed on a single chip would be very useful for extending the linear dynamic range of this immunoassay, beyond previous NBC experiments, and exponentially more than ELISA-based methods.

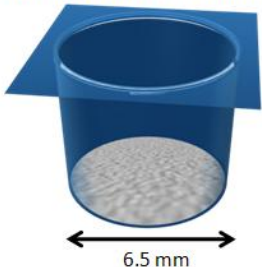
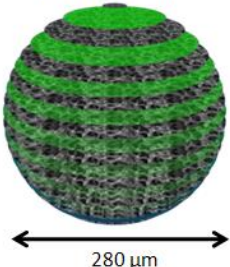
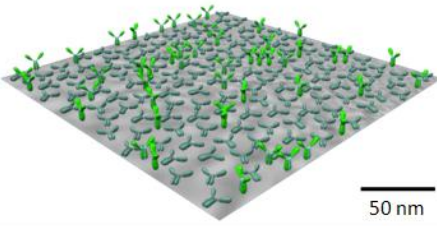
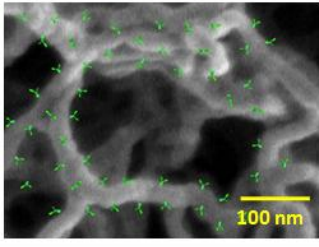
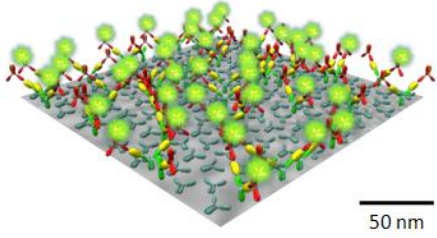
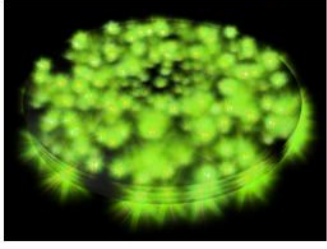
Reaction Vessel: Anchor point for reaction; serves as cuvette, light path, and as fluid handling structure	Ai ELISA: Microtiter Plate Well 	Aii NBC: Bead 
Immobilization Capacity: controls the amount of analyte that may be processed by the reaction vessel; directly proportional to amount of capture antibody	Bi ELISA: c.Ab. Monolayer 	Bii NBC: Nano-net of c.Ab. 
Signaling Ability: describes method of analyte reporting	Ci ELISA: Limited to 2D 	Cii NBC: 3D Capacity 

Figure 4.24. Reagent Usage in Sandwich Immunoassay Systems. The above comparison illustrates the fundamental differences between ELISA and the bead-based NBC for protein measurements. By using a 3D versus 2D reaction vessel (**A**) and an intricate lattice of immobilization moieties versus a planar system (**B**), the NBC allows for a much higher density of reagent capture centers and thus a high capacity for reporting the presence of analyte (**C**).

Chapter 4 offers additional insight on comparison of the bead-based NBC to ELISA systems. In **Figure 4.24**, the differences are illustrated in a space-filling model. First of notice is the size difference. A typical microtiter well has a diameter of 6.5 mm and a depth of 1 cm and comfortably contains a volume of 310 μL . Some calculations allow for a *best case* estimate of the number of antibodies in this well. For the monolayer

area of 1.33 cm^2 and IgG area of $1.5 \times 10^{-11} \text{ cm}^2$, approximately 9×10^{11} antibodies may be arranged in this space. This value is an order of magnitude lower than the 9×10^{10} copies of IgG antibody present in a agarose bead with an average uptake of 1 mg/mL protein out of reaction solution. However, when volumes are considered (330 uL well versus 0.011 uL bead), the density of antibodies is $2.9/\mu\text{m}^3$ for ELISA model and $8.2 \times 10^3/\mu\text{m}^3$ for the agarose system, nearly a 3,000 fold improvement in capture element density. More importantly perhaps than this density, is that in the arrangement typical in NBC, this density contributes to the high avidity effects seen in the bead-based unit.

Intuitively, the three-dimensional network of capture elements seen in **Figure 4.24Bii** is highly efficient at not only capturing, but also *retaining* immobilized analyte in the reaction vessel. In a monolayer, any antigen that becomes disassociated from the antibody has eight next-nearest neighbors on which to rebind. In the bead, however, this number doubles to 16. This doubling implies that the K_{off} rate is effectively negated and that a high amount of bound antigen is retained for a later signaling, an observation confirmed by other literature reports.^{268, 269} While it is true that this nano-net has the potential to increase non-specific absorption of fluorescent detecting antibody and increase assay background, the wash conditions (flow and time) described above effectively use both convection and diffusion to eliminate unbound detecting antibody. In addition, automated or manual sieving processes can select for smaller bead sizes in which the diffusion-limited behavior is reduced or eliminated.

Device Characteristic	Test Tube	ELISA	Bead	WBC
Length, d	10 cm	6.5 mm	280 μm	10 μm
Volume	10 mL	300 μL	11 nL	1 pL
# molecules at 1 μM	6×10^{21}	2×10^{14}	7×10^9	6×10^5
Diffusion Time (t_d)	9 years	14 days	37 minutes	2.9 seconds
# volumes in microtiter plate space (95 cm^2)	3	96	1.2×10^9	9.5×10^{11}
Theoretical Maximum Information Density	3 tests in 95 cm^2 space every 9 years	4.76×10^{-3} per min cm^2	3.24×10^7 per min cm^2	3.3×10^{11} per sec cm^2

Table 4.4. Size Dependent Diffusion Time and Information Density. The important effect size of reaction vessel has on system performance is illustrated above for a number of diffusion-limited hypothetical systems with dimensions and volumes listed above. Note that the ability to perform an increasingly larger number of assays in a shorter amount of time in a smaller amount of space. (t_d calculated by $t_d = (d^2/2D)$ where D is diffusion coefficient; for this example hemoglobin's value of $1.75 \times 10^{-7} \text{ cm}^2/\text{s}$ was used.²⁷⁰) Please see Manz reference for additional insight.³⁶

Table 4.4 gives one additional example of NBC assay performance versus ELISA to illustrate diffusion-limited differences. Here, characteristic descriptors for the two methods are shown in comparison to two hypothetical devices, one larger and one smaller. The theoretical maximum information density is nearly 10^{10} times larger for the bead based reactor as opposed to an ELISA plate. Although, the ability to do a large number of assays on a small device array has not been completely exploited in the NBC, the efficiency with which this system captures analytes, as well as the high percentage of antigen captured that is later signaled, suggests that this approach to immunoassay building will continue to be explored by researchers seeking quality building blocks for POC biomedical analysis devices.

Dénouement: Conclusions, Outlook, and Future-Leaning Perspective

As this work has studied improved methods to measure medically important analytes, it is now appropriate to revisit the specific questions proposed in **Section 1.6**.

- ✓ Quantum dots from CdSe with a ZnS coat, peak emission at 655 nm and coated with a PEG based polymer, consistently gave the most intense, hydrophilic signal.
- ✓ Conjugation methods linking QDs to monoclonal antibodies are specific to the application. For cellular immunolabeling, a 2^o antibody approach was most effective while cellular labeling used direct covalent linkage of nanoparticle to antibody. In both cases, antibody fragments complimented the steric size considerations of both the agarose bead and QD.
- ✓ Non-specific binding and aggregation are reduced by careful selection of conjugation method and QD surface coating. Avoid charged QDs to reduce non-specific interactions. Filtration of bioconjugate via 0.2 μm nylon filter immediately before labeling was key to minimizing aggregation.
- ✓ Narrow emission filters (FWHM = 10-15 nm) are best suited for QDs; excitation at and below 425 nm is ideal.
- ✓ The QDs are photostable up to 15 minutes of continuous excitation and give 30 times more signal versus Alexa Fluor 488, which exhibits exponential signal decay in the time domain.
- ✓ Successive line profile across the bead-based QD fluorescent signal yields the most sensitive response curves. The SBR for cellular applications need be well above unity. Background corrected images drastically improved signal quality.
- ✓ The QD systems allows a single optical pathway to be used in multicolor channel, multiplexed experiments. Demonstration of both inter-bead and intra-bead multiplexing is complete.
- ✓ Limits of detection 60 times lower than ELISA methodology are achieved by using both an intense QD reporter as well as a fastidious approach to washing upon immunoassay completion—essential for low backgrounds.

- ✓ Whole IgG monoclonal antibodies in tandem with 2% agarose beads are the most appropriate building blocks in assay building with molecular fluorophores.
- ✓ Recirculation of sample improves analyte capture 3-4 times, very important for low-level determinations. The size of analyte and the concentration of capture antibody have important influence on reagent distribution and must be considered.

The results of these questions may prove valuable to future researchers seeking to make improvements to this NBC assay design, but also to a broad class of life scientists seeking to integrate the attributes of hydrophobic nanoparticles into bioassay systems. This work serves to engineer separate working parts with nano-level (nL, nm, ng) control of individual components with the potential for powerful new measurement devices. By carefully considering and defining the nanotechnological (QD), biological (antibody), and microfluidic (chip) components of the sensor, important advances in robust sensing have been made. The processes necessary for highly efficient analyte capture and transduction in a microfluidic system is completed.

As POC solutions become more commonplace and accepted in clinical settings, more applications may be envisioned. Just as no diabetic could envision making regular trips to an outpatient hospital for glucose levels, so too may a number of assays currently confined to the laboratory be liberated. Already, levels of electrolytes, blood gases, and cardiac markers are being measured at the POC, in spite of being limited by the resistance of some in the medical community to this new testing paradigm. It should be understood that the goal of these handheld systems is to compliment other established methods, and not to reinvent those currently optimized. Clearly, additional standardization studies are needed to give evidence to those in the practicing medical community of the validity of POC systems. This work is the first to validate QD nanoparticles as reporter probes for these classes of analytes in a chip-based microfluidic ensemble.^{131, 221} Future work will focus on bring these advances to patients in need.

The majority of work presented here, employs the programmable, research-grade nano-bio-chip detailed in **Figure 1.4A**. This assembly is ideally suited for empirical studies designed to determine the optimal design conditions of various reagent and reagent systems. The modular, aluminum housing is convenient for initial studies determining such parameters as: labeling pathways between QD and bioligand, ideal antibody clones, QD vendor and emission maximum, flow rates and incubation times, and agarose porosity. The screw-top aluminum housing allowed for quick exchange of fresh membranes for lymphocyte assays, and easy loading of fresh beads in between protein-based assays. Unfortunately, the research grade NBC is not compatible with measuring samples in a clinic. For truly integrated assays designs, an exploration of integrated systems was called for. Medical clinicians and their support staff require a simple and reliable analysis scheme with the COMMAND QUALS characteristics mentioned in **Section 1.4**.

The integrated labcard currently being optimized by research collaborators in this group, contains all elements required for a complete assay, integrated into a credit card-sized device. Liquid reagents are stored in blister packs while fluorescently tagged biorecognition moieties are stored in solid form. Channels designed for mixing and fluid flow are built into this architecture. These cards are built inexpensively from common materials including vinyl adhesive and assembled using conventional layering methods. The fluidic evolving design utilizes conventional computer animated drafting (CAD) software for simplicity and universality. All cards are built in parallel, with 6-8 typically made from each page of laminate/vinyl adhesive design. **Figure D.1A** illustrates the stratum of microfluidic pieces that combine to form the compact labcard in **Figure D.1B**.

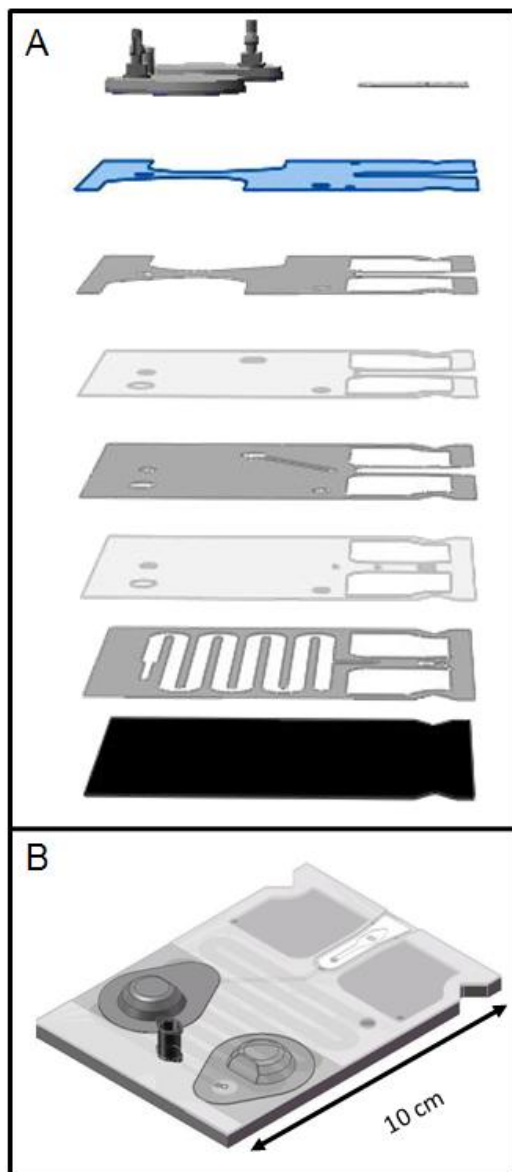


Figure D.1. Horizontal Cross Section of Compact NBC Labcard. A variety of components condense to create the integrated NBC. These include the buffer storage blister packs, fluid direction cavities, waste disposal reservoirs, and the analysis chamber.

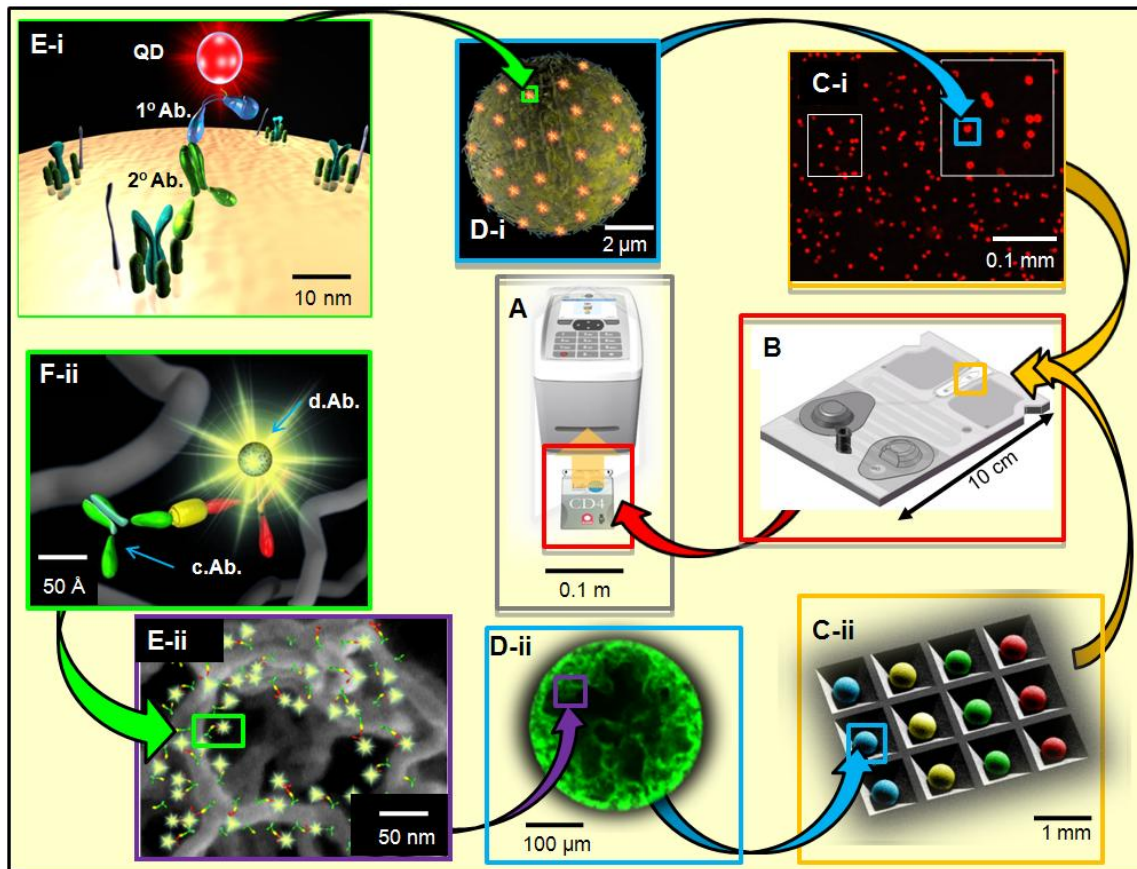


Figure D.2. Complete Assembly of Working Parts. Many different components condense to create the integrated NBC (**B**), which contains the buffer storage blister packs, fluid direction cavities, waste disposal reservoirs, and the analysis chamber. The two processor types (**C**) cited above (**ii – Chapter 2, ii – Chapter 2 and 3**) include the membrane-based, cellular processing unit (upper scheme **i**), for cellular assays, while the bead-based, chemical processing unit (lower scheme **ii**), is typified by protein assays. Both must bridge nanometer scale gaps between bioligand and signaling probe (**E** and **F**) to create bioconjugates for analyte fluorescence labeling (**D**) within the CPU. Data contained in the samples and processed by the labcard is transcribed by a portable, self-contained analyzer (**A**).

One of the most important features of the POC solution detailed in this dissertation is its capability for analysis of both cellular and circulating disease markers. The modular and *sui generis* approach detailed in **Figure D.2** is in sharp contrast to the “one assay, one chip” approach typically seen in the literature. **Chapter 2** detailed the

upper lymphocyte pathway of **Figure D.2**, while the lower scheme for proteins via agarose beads is described in **Chapter 3** and **4**. Importantly, both types of analyses are easily integrated into the compact NBC labcard and interpreted by the standalone analyzer (**Fig. D.2A**).²²³

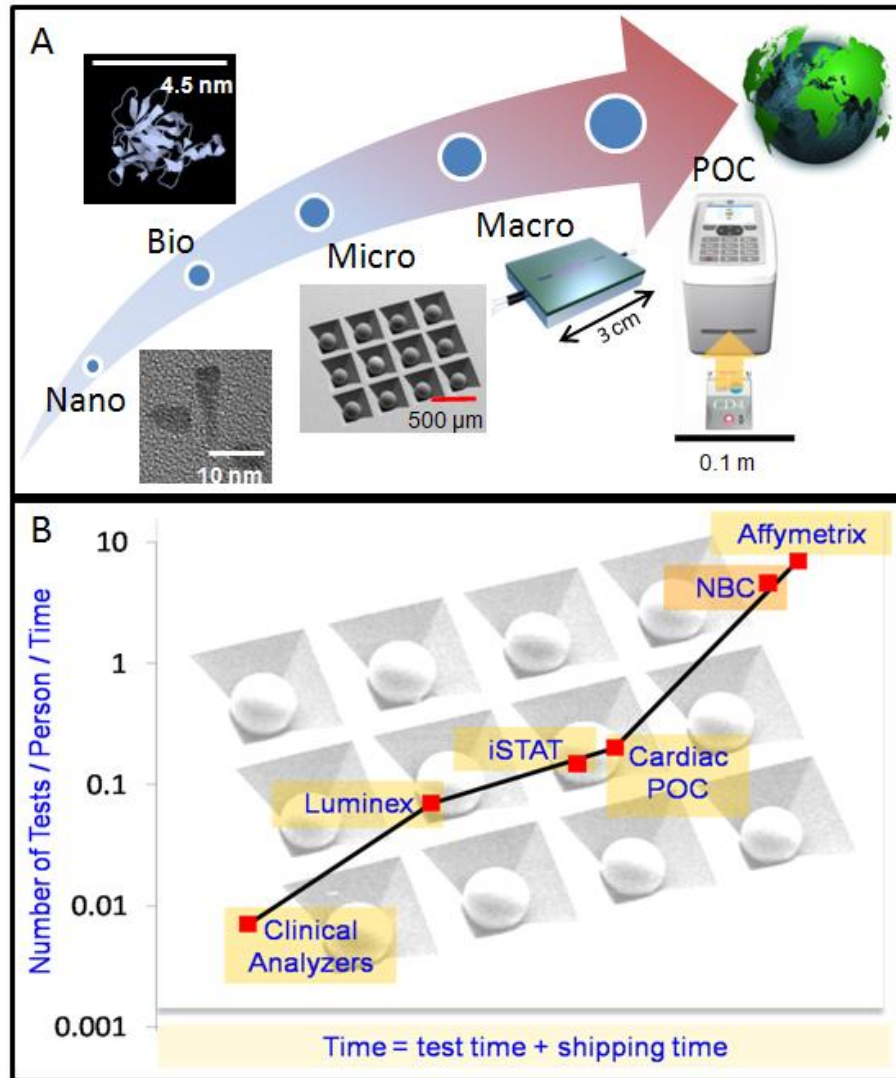


Figure D.3. Scaling and Moore's Law Behavior. The ability to bridge different gaps in scale (**A**) and combine the attributes of different layers results in an increasing number of analysis events on a small device footprint advances at a rate reminiscent of Moore's Law in the microelectronics industry (**B**).

This analyzer is currently under final revisions by a University of Texas commercialization partner and contains battery power supplies, signal capture and processing elements, readout display, memory for patient histories, and wireless communication features. Each card is designed to be used for one patient samples. After sample collection and introduction into the compact NBC, the labcard is inserted into the analyzer, similarly to a compact disk into a CD player. Through manipulations of the fluidic cartridges, reagents are dispersed through the labcard according to design. The integrated NBC is one of many contributions leading to behavior similar to Moore's Law in the electronics industry. Here, the time needed to analyze a number of analytes on a single patient has decreased exponentially. **Figure D.3** illustrates in a general way, some of the major players in this space. Owing to the theme of POC-type assay systems, time here is defined as time to perform the assay plus the shipping, or transport, time involved with the test.

In conclusion, important advances are made in increasing the fidelity of the nano-bio-chip POC sensor system of the McDevitt research community. The inclusion of quantum dots made important increases in signaling capacity and limits of detection and allows a reduction in optical components typical of POC designs. Although the field of POC systems is in its awkward adolescent phase, it remains of field of unlimited promise.⁴⁰ The genomic, proteomic, and nanotechnological advances of the past decade can only intimate where the ultimate future of biomedical devices may lie. A continued movement toward singularity in medical diagnostic, imaging, and other analysis devices remains likely for the foreseeable future.

Appendix A: Optical Optimization—Emission and Excitation Filters

Some of the initial experiments optimized the configuration of the Olympus BX2 optical filter cubes. Below is a representative example of such a systemic evaluation for the cellular NBC. Two filter sets were used to examine one sample immobilized on a 3 μm . The signal and background were captured as explained in **Section 2.4.2**. Although the signal remained nearly constant, the background was *highly* dependent on the emission optics. Although both emission filters had peak transmittance at 560 nm, the one with a 40 nm bandwidth substantially increased the amount of background fluorescence relative to the filter with a 20 nm bandwidth. Henceforth, filters with a 20 nm bandwidth were used for all bead and membrane-based assays in the NBC. This optimization was performed for each assay—the best results found are those listed in Materials and Methods for the respective experiments.

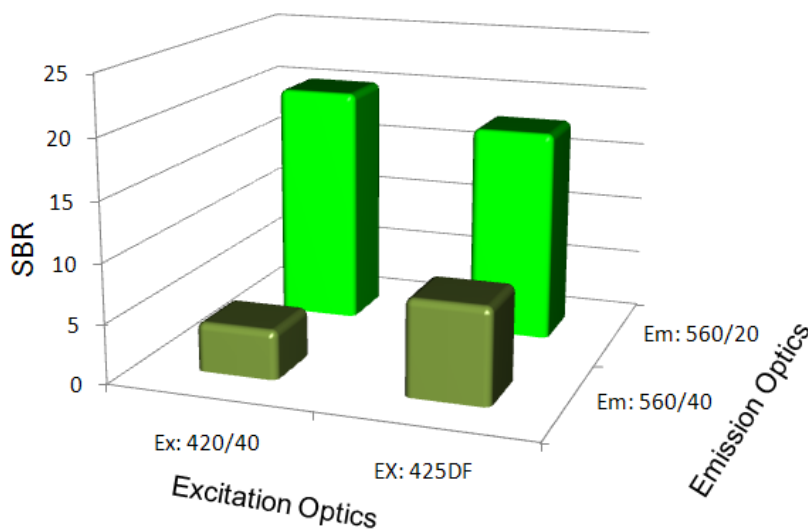


Figure A.1. Optimization of Excitation and Emission Optics. These experiments reveals the importance of considering and evaluating carefully all optical assemblages used in conjunction with the NBC.

Appendix B: Reagent Optimization—Primary and Secondary Antibody Titration Experiments

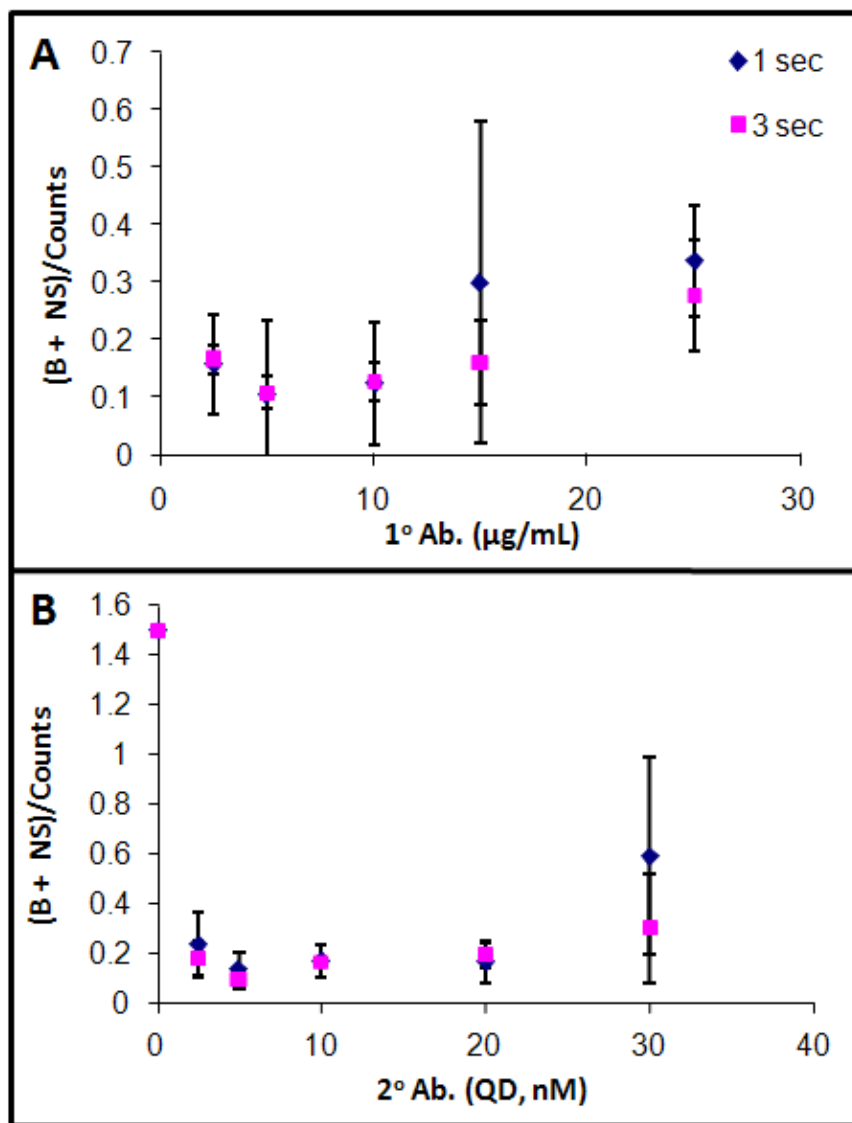


Figure A.2. Optimization of Primary and Secondary Antibody Concentrations. A) A constant volume secondary antibody was used in tandem with increasing volumes of primary. Collected were total cell counts as well as non-specific (NS) aggregates outside of the cellular analysis parameters. This NS value was used in tandem with background (B) counts to give a ratio of these events versus authentic cell counts. Concentrations of reagents that minimized this parameter were needed. B) After 10 µg/mL was identified as the optimal quantity of primary antibody, the secondary antibody was similarly optimized. Future experiments used 10 nM secondary antibody. Two different camera exposure times were used, one and three seconds.

Appendix C: Sample Cellular Analysis Method via Java and ImageJ

```
// analysis of 100906
W1=newArray(2000);
H1=newArray(2000);
Xcoord=newArray(2000);
Ycoord=newArray(2000);

for (k=1;k<2;k++){
for (j=1;j<4;j=++2){
for (i=1;i<6;i++) {

//CPL
open("C:\\Data\\Jesse\\2006\\100906\\"+k+"\\lp "+j+"-"+i+".tif");
run("RGB Split");
close();
close();
run("FFT Filter", "filter_large=40 filter_small=3 suppress=none tolerance=5
autoscale saturate");

//run("Threshold...");
run("Clear Results");
run("Measure");
m=getResult("Mean",0);s=getResult("StdDev",0);
mr=round(m);sr=round(s);twos=mr+2*sr;
setThreshold(twos, 255);
run("Threshold", "thresholded remaining black");
run("Find Edges");
run("Invert");
run("Fill Holes");
run("Watershed");
run("Clear Results");
run("Analyze Particles...", "minimum=70 maximum=500 bins=10 show=Masks
display exclude clear");
initcountsr=nResults;totalcountsr=0;
for (t=0; t<nResults; t++) {

    W1[t]=getResult("Width", t);
    H1[t]=getResult("Height", t);
    circularity = getResult('Circ.', t);
    Xcoord[t]=getResult ("BX", t);
    Ycoord[t]=getResult ("BY", t);
```

```

        if (circularity>0.68) {
            totalcountsr=totalcountsr+1;
            run("Specify...", "width="+W1[t]+"          height="+H1[t]+"
x="+Xcoord[t]+" y="+Ycoord[t]+" oval");
            roiManager("Add");
        }
    }
}

```

```

roiManager("Save", "C:\\Data\\Jesse\\2006\\100906\\"+k+"\\lp redCD3 ROIs
"+j+"-"+i+".zip");
newImage("Filter", "8-bit Black", 1300, 1030, 1);
run("ROI Manager...");
roiManager("Draw");
setAutoThreshold();
//run("Threshold...");
setThreshold(128, 255);
run("Threshold", "thresholded remaining black");
run("Analyze Particles...", "minimum=70 maximum=500 bins=10 show=Masks
display exclude clear");
selectWindow("ROI Manager");
selectWindow("Filter");close();
rename("Mask of Filter lp redCD3 "+j+"-"+i+"");
open("C:\\Data\\Jesse\\2006\\100906\\"+k+"\\lp "+j+"-"+i+".tif");
roiManager("Open", "C:\\Data\\Jesse\\2006\\100906\\"+k+"\\lp redCD3 ROIs
"+j+"-"+i+".zip");
roiManager("Draw");
roiManager("Measure");
saveAs("Measurements", "C:\\Data\\Jesse\\2006\\100906\\"+k+"\\ Resultsredlp
"+j+"-"+i+".tif");
close();
selectWindow("ROI Manager");
run ("Close");
open("C:\\Data\\Jesse\\2006\\100906\\"+k+"\\lp "+j+"-"+i+".tif");
run("RGB Split");
close();
run("FFT Filter", "filter_large=40 filter_small=3 suppress=none tolerance=5
autoscale saturate");

//run("Threshold...");
run("Clear Results");
run("Measure");
m=getResult("Mean",0);s=getResult("StdDev",0);
mr=round(m);sr=round(s);twos=mr+sr;

```

```

setThreshold(twos, 255);
run("Threshold", "thresholded remaining black");
run("Clear Results");
run("Analyze Particles...", "minimum=70 maximum=500 bins=10 show=Masks
display exclude clear");
initcountsg=nResults;totalcountsg=0;
for (t=0; t<nResults; t++) {
    W1[t]=getResult("Width", t);
    H1[t]=getResult("Height", t);
    circularity = getResult('Circ.', t);
Xcoord[t]=getResult ("BX", t);
Ycoord[t]=getResult ("BY", t);

        if (circularity>0.68) {
            totalcountsg=totalcountsg+1;
            run("Specify...", "width="+W1[t]+"          height="+H1[t]+"
x="+Xcoord[t]+" y="+Ycoord[t]+" oval");
            roiManager("Add");
        }
    }
roiManager("Save", "C:\\Data\\Jesse\\2006\\100906\\"+k+"\\lp greenCD4 ROIs
"+j+"-"+i+".zip");
newImage("Filter", "8-bit Black", 1300, 1030, 1);
run("ROI Manager...");
roiManager("Draw");
setAutoThreshold();
//run("Threshold...");
setThreshold(128, 255);
run("Threshold", "thresholded remaining black");
run("Analyze Particles...", "minimum=70 maximum=700 bins=10 show=Masks
display exclude clear");

selectWindow("ROI Manager");
run ("Close");
selectWindow("Filter");close();
rename("Mask of Filter lp greenCD4 "+j+"-"+i+"");
open("C:\\Data\\Jesse\\2006\\100906\\"+k+"\\lp "+j+"-"+i+".tif");
roiManager("Open", "C:\\Data\\Jesse\\2006\\100906\\"+k+"\\lp greenCD4 ROIs
"+j+"-"+i+".zip");
roiManager("Draw");
roiManager("Measure");
saveAs("Measurements", "C:\\Data\\Jesse\\2006\\100906\\"+k+"\\ Resultsgreenlp
ls wo math "+j+"-"+i+".tif");
close();

```

```

run("Clear Results");
run("Image Calculator...", "image1=[Mask of Filter lp redCD3 "+j+"-"+i+"]
operation=AND image2=[Mask of Filter lp greenCD4 "+j+"-"+i+"] create");
run("Analyze Particles...", "minimum=30 maximum=700 bins=10 show=Masks
display exclude clear");
percentage=nResults/totalcountsr*100;
print (" "+k+" "+j+"-"+i+".tif"+" "+initcountsr+" "+totalcountsr+"
"+initcountsg+" "+totalcountsg+" "+nResults+" "+percentage);
close();close();
close();
selectWindow("ROI Manager");
run ("Close");
close();close();
close();
close();
}
}
}
selectWindow("Log");
run("Text...", "path='C:\\Data\\Jesse\\2006\\100906\\"+k+"\\Log of lp CD3CD4
green 1s "+j+"-"+i+" .txt'");

```


Appendix D: Reprint Permissions

Bailey, Revelle <revelle.bailey@lifetech.com> Thu, Mar 5, 2009 at 11:17 AM
To: Jesse Jokerst <jokerst@gmail.com>

Hello Jesse,

This request is approved for one-time use as described below. Please keep this email for your records. Good luck on your dissertation. Thank you, Revelle

From: Jesse Jokerst [mailto:jokerst@gmail.com]
Sent: Thursday, March 05, 2009 8:51 AM
To: Bailey, Revelle
Subject: Reprint Permission

Dear Dr. Anderson,

I write to request permission to use an image from Invitrogen's website. Specifically, I would like to reproduce the output of concurrent visualization of Alexa Fluor 488, 546, and 647 from [Invitrogen's Spectral Viewer](#) in my doctoral dissertation. Only the spectra will be used via a 'print screen' and full credit and copyright will be given to Invitrogen. This dissertation will be published in accordance with protocols established by The University of Texas.

Sincerely,

- Jesse Jokerst

--

Jesse Jokerst
McDevitt Labs
The University of Texas
1 University Station A5300
Austin, TX 78712
Lab: 512-232-7113
Fax: 512-232-7052
www.tastechip.com

Jesse Jokerst <jokerst@gmail.com>
To: publicationpermissions@unaids.org

Mon, Jan 19, 2009 at 10:42 AM

Dear Sir or Madam,

I write to request permission to use an image from UNAIDS' 2008 Report on the Global Aids Epidemic. Specifically, I would like to reproduce the image "[A Global View of HIV Infection](#)" in my doctoral dissertation. Only the map and the relevant adult prevalence legend would be used and full

credit will be given to UNAIDS. This dissertation will be published in accordance with protocols established by The University of Texas.

Sincerely,

- Jesse Jokerst

--

Jesse Jokerst
McDevitt Labs
The University of Texas
1 University Station A5300
Austin, TX 78712
Lab: 512-232-7113
Fax: 512-232-7052
www.tastechip.com

publicationpermissions <publicationpermissions@unaids.org>
To: Jesse Jokerst <jokerst@gmail.com>

Thu, Jan 29, 2009 at 9:49 AM

Dear Jesse Jokerst,

Yes you have our permission to use the image in your doctoral dissertation.

Best wishes

Mahesh Mahalingam

References

1. Cohen, J., Monitoring treatment: At what cost? *Science* **2004**, *304* (5679), 1936-1936.
2. Abayomi, E. A.; Landis, R. C., Flow cytometry as the spearhead for delivering sustainable and versatile laboratory services to HIV-burdened health care systems of the developing world: a Caribbean model. *Cytometry B Clin Cytom* **2008**, *74 Suppl 1*, S80-9.
3. Soper, S. A.; Brown, K.; Ellington, A.; Frazier, B.; Garcia-Manero, G.; Gau, V.; Gutman, S. I.; Hayes, D. F.; Korte, B.; Landers, J. L.; Larson, D.; Ligler, F.; Majumdar, A.; Mascini, M.; Nolte, D.; Rosenzweig, Z.; Wang, J.; Wilson, D., Point-of-care biosensor systems for cancer diagnostics/prognostics. *Biosens. Bioelectron.* **2006**, *21* (10), 1932-1942.
4. Myers, F. B.; Lee, L. P., Innovations in optical microfluidic technologies for point-of-care diagnostics. *Lab on a Chip* **2008**, *8* (12), 2015-2031.
5. Sorger, P. K., Microfluidics closes in on point-of-care assays. *Nat. Biotechnol.* **2008**, *26* (12), 1345-1346.
6. Imperato, P. J., The potential of diagnostics for improving community health in less developed countries. *J. Community Health* **1985**, *10* (4), 201-6.
7. Chambers, J. P.; Arulanandam, B. P.; Matta, L. L.; Weis, A.; Valdes, J. J., Biosensor recognition elements. *Curr. Issues Mol. Biol.* **2008**, *10* (1 and 2), 1-12.
8. Abramowitz, S., Commercialization of DNA arrays - Affymetrix a case study. *Handb. Biosens. Biochips* **2007**, *2*, 1273-1280.
9. Fukui, S.; Feizi, T.; Galustian, C.; Lawson, A. M.; Chai, W., Oligosaccharide microarrays for high-throughput detection and specificity assignments of carbohydrate-protein interactions. *Nat. Biotechnol.* **2002**, *20* (10), 1011-1017.
10. Kulagina, N. V.; Lassman, M. E.; Ligler, F. S.; Taitt, C. R., Antimicrobial Peptides for Detection of Bacteria in Biosensor Assays. *Anal. Chem.* **2005**, *77* (19), 6504-6508.
11. Qavi, A. J.; Washburn, A. L.; Byeon, J.-Y.; Bailey, R. C., Label-free technologies for quantitative multiparameter biological analysis. *Anal Bioanal Chem*, No pp yet given.
12. Kotlarz, V. R., Tracing our roots: a professional identity emerges: 1928 to 1945. *Clinical laboratory science journal of the American Society for Medical Technology* **1998**, *11* (5), 275-9.
13. Watson, J. D.; Crick, F. H. C., A structure for deoxyribose nucleic acid. 1953. *Nature* **2003**, *421* (6921), 397-8; discussion 396.
14. Delwiche Frances, A., Mapping the literature of clinical laboratory science. *J Med Libr Assoc* **2003**, *91* (3), 303-10.

15. Bast, R. C., Jr.; Lilja, H.; Urban, N.; Rimm, D. L.; Fritsche, H.; Gray, J.; Veltri, R.; Klee, G.; Allen, A.; Kim, N.; Gutman, S.; Rubin, M. A.; Hruszkewycz, A., Translational crossroads for biomarkers. *Clin Cancer Res* **2005**, *11* (17), 6103-8.
16. Consortium, I. H. G. S., Finishing the euchromatic sequence of the human genome. *Nature* **2004**, *431* (7011), 931-45.
17. Granger, C. B.; Van Eyk, J. E.; Mockrin, S. C.; Anderson, N. L.; on behalf of the Working Group, M., National Heart, Lung, and Blood Institute Clinical Proteomics Working Group Report. *Circulation* **2004**, *109* (14), 1697-1703.
18. Papadopoulos, N.; Kinzler, K. W.; Vogelstein, B., The role of companion diagnostics in the development and use of mutation-targeted cancer therapies. *Nat. Biotechnol.* **2006**, *24* (8), 985-995.
19. Willard, H. F.; Ginsburg, G. S.; Editors, *Genomic and Personalized Medicine; Volume 1*. 2009; p 619 pp.
20. Willard, H. F.; Ginsburg, G. S.; Editors, *Genomic and Personalized Medicine; Volume 2*. 2009; p 1478 pp.
21. Lines, R. W., Particle counting by Coulter counter. *Anal. Proc. (London)* **1981**, *18* (12), 514-19.
22. Kotlarz, V. R., Tracing our roots: the rocky road toward recognition of clinical laboratory science's professional status (1962-1977). *Clinical laboratory science journal of the American Society for Medical Technology* **2000**, *13* (2), 166-71.
23. Kotlarz, V. R., Tracing our roots: new opportunities and new challenges in clinical laboratory science (1977-1992). *Clinical laboratory science journal of the American Society for Medical Technology* **2001**, *14* (1), 13-8.
24. Terry, S. C.; Jerman, J. H.; Angell, J. B., A gas chromatographic air analyzer fabricated on a silicon wafer. *IEEE Trans. Electron Devices* **1979**, *ED-26* (12), 1880-6.
25. FDA A Brief History of Self-Monitoring of Blood Glucose with Glucose Meters. <http://www.fda.gov/Diabetes/glucose.html#16> (accessed January 9, 2009).
26. Vaitukaitis Judith, L., Development of the home pregnancy test. *Ann. N. Y. Acad. Sci.* **2004**, *1038*, 220-2.
27. Manz, A.; Graber, N.; Widmer, H. M., Miniaturized total chemical analysis systems: a novel concept for chemical sensing. *Sensors and Actuators, B: Chemical* **1990**, *B1*, 244-8.
28. Reyes, D. R.; Iossifidis, D.; Auroux, P. A.; Manz, A., Micro total analysis systems. 1. Introduction, theory, and technology. *Anal. Chem.* **2002**, *74* (12), 2623-2636.
29. Van Den Berg, A.; Lammerink, T. S. J., Micro total analysis systems: microfluidic aspects, integration concept and applications. *Top. Curr. Chem.* **1998**, *194* (Microsystem Technology in Chemistry and Life Science), 21-49.

30. Auroux, P. A.; Iossifidis, D.; Reyes, D. R.; Manz, A., Micro total analysis systems. 2. Analytical standard operations and applications. *Anal. Chem.* **2002**, *74* (12), 2637-2652.
31. Tudos, A. J.; Besselink, G. A. J.; Schasfoort, R. B. M., Trends in miniaturized total analysis systems for point-of-care testing in clinical chemistry. *Lab Chip* **2001**, *1* (2), 83-95.
32. Duffy, D. C.; McDonald, J. C.; Schueller, O. J. A.; Whitesides, G. M., Rapid Prototyping of Microfluidic Systems in Poly(dimethylsiloxane). *Analytical Chemistry* **1998**, *70*, 4974-4984.
33. Gomez, F. A.; Editor, *Biological Applications of Microfluidics*. 2008; p 517 pp.
34. Martinez, A. W.; Phillips, S. T.; Whitesides, G. M., Three-dimensional microfluidic devices fabricated in layered paper and tape. *Proc. Natl. Acad. Sci. U. S. A., Early Ed.* **2008**, (Dec. 8 2008), 1-6, 6 pp.
35. Hansen, C.; Quake, S. R., Microfluidics in structural biology: smaller, faster... better. *Curr. Opin. Struct. Biol.* **2003**, *13* (5), 538-544.
36. Janasek, D.; Franzke, J.; Manz, A., Scaling and the design of miniaturized chemical-analysis systems. *Nature* **2006**, *442* (7101), 374-80.
37. Nesbitt, B.; Editor, *Guide to European Valves: For Control, Isolation and Safety; Second Edition*. 2001; p No pp given.
38. Thorsen, T.; Maerkl Sebastian, J.; Quake Stephen, R., Microfluidic large-scale integration. *Science (New York, N.Y.)* **2002**, *298* (5593), 580-4.
39. Kilby, J. S. C., Turning potential into realities: the invention of the integrated circuit. *ChemPhysChem* **2001**, *2* (8/9), 482-489.
40. Whitesides, G. M., The origins and the future of microfluidics. *Nature* **2006**, *442* (7101), 368-73.
41. Lam, E. W.; Cooksey, G. A.; Finlayson, B. A.; Folch, A., Microfluidic circuits with tunable flow resistances. *Appl. Phys. Lett.* **2006**, *89* (16), 164105/1-164105/3.
42. Verpoorte, E.; De Rooij, N. F., Microfluidics meets MEMS. *Proceedings of the Ieee* **2003**, *91* (6), 930-953.
43. Holmesfarley, S. R.; Whitesides, G. M., Reactivity of Carboxylic-Acid and Ester Groups in the Functionalized Interfacial Region of Polyethylene Carboxylic-Acid (Pe-Co2h) and Its Derivatives - Differentiation of the Functional-Groups into Shallow and Deep Subsets Based on a Comparison of Contact-Angle and Atr-Ir Measurements. *Langmuir* **1987**, *3* (1), 62-76.
44. Ostuni, E.; Chapman, R. G.; Holmlin, R. E.; Takayama, S.; Whitesides, G. M., A survey of structure-property relationships of surfaces that resist the adsorption of protein. *Langmuir* **2001**, *17* (18), 5605-5620.

45. Melin, J.; Quake, S. R., Microfluidic large-scale integration: the evolution of design rules for biological automation. *Annu. Rev. Biophys. Biomol. Struct.* **2007**, *36*, 213-231.
46. Hong, J. W.; Studer, V.; Hang, G.; Anderson, W. F.; Quake, S. R., A nanoliter-scale nucleic acid processor with parallel architecture. *Nat. Biotechnol.* **2004**, *22* (4), 435-439.
47. Hansen, C. L.; Classen, S.; Berger, J. M.; Quake, S. R., A Microfluidic Device for Kinetic Optimization of Protein Crystallization and In Situ Structure Determination. *J. Am. Chem. Soc.* **2006**, *128* (10), 3142-3143.
48. Braslavsky, I.; Hebert, B.; Kartalov, E.; Quake, S. R., Sequence information can be obtained from single DNA molecules. *Proc. Natl. Acad. Sci. U. S. A.* **2003**, *100* (7), 3960-3964.
49. Whitesides, G. M., Nanoscience, nanotechnology, and chemistry. *Small* **2005**, *1* (2), 172-179.
50. Jain, P. K.; Huang, X.; El-Sayed, I. H.; El-Sayed, M. A., Noble Metals on the Nanoscale: Optical and Photothermal Properties and Some Applications in Imaging, Sensing, Biology, and Medicine. *Acc. Chem. Res.* **2008**, *41* (12), 1578-1586.
51. Mirkin, C. A.; Letsinger, R. L.; Mucic, R. C.; Storhoff, J. J., A DNA-based method for rationally assembling nanoparticles into macroscopic materials. *Nature* **1996**, *382* (6592), 607-9.
52. Cao, Y. C.; Jin, R.; Mirkin, C. A., Nanoparticles with Raman spectroscopic fingerprints for DNA and RNA detection. *Science* **2002**, *297* (5586), 1536-1540.
53. Hurst, S. J.; Han, M. S.; Lytton-Jean, A. K. R.; Mirkin, C. A., Screening the Sequence Selectivity of DNA-Binding Molecules Using a Gold Nanoparticle-Based Colorimetric Approach. *Anal. Chem.* **2007**, *79* (18), 7201-7205.
54. Azzazy, H. M. E.; Mansour, M. M. H.; Kazmierczak, S. C., Nanodiagnostics: a new frontier for clinical laboratory medicine. *Clin. Chem.* **2006**, *52* (7), 1238-1246.
55. Cheon, J.; Lee, J.-H., Synergistically Integrated Nanoparticles as Multimodal Probes for Nanobiotechnology. *Acc. Chem. Res.* **2008**, *41* (12), 1630-1640.
56. Jovin, T. M., Quantum dots finally come of age. *Nat. Biotech.* **2003**, *21* (1), 32-33.
57. Parak, W. J.; Manna, L.; Nann, T., Fundamental principles of quantum dots. *Nanotechnology* **2008**, *1*, 73-96.
58. Murray, C. B.; Norris, D. J.; Bawendi, M. G., Synthesis and characterization of nearly monodisperse CdE (E = sulfur, selenium, tellurium) semiconductor nanocrystallites. *J. Am. Chem. Soc.* **1993**, *115* (19), 8706-15.
59. Murray, C. B.; Kagan, C. R.; Bawendi, M. G., Synthesis and characterization of monodisperse nanocrystals and close-packed nanocrystal assemblies. *Ann. Rev. Mater. Sci.* **2000**, *30*, 545-610.

60. Liu, W.; Choi, H. S.; Zimmer, J. P.; Tanaka, E.; Frangioni, J. V.; Bawendi, M., Compact Cysteine-Coated CdSe(ZnCdS) Quantum Dots for in Vivo Applications. *J. Am. Chem. Soc.* **2007**, *129* (47), 14530-14531.
61. Hines, M. A.; Guyot-Sionnest, P., Synthesis and Characterization of Strongly Luminescing ZnS-Capped CdSe Nanocrystals. *Journal of Physical Chemistry* **1996**, *100* (2), 468-71.
62. Skaff, H.; Sill, K.; Emrick, T., Quantum Dots Tailored with Poly(para-phenylene vinylene). *J. Am. Chem. Soc.* **2004**, *126* (36), 11322-11325.
63. Potapova, I.; Mruk, R.; Prehl, S.; Zentel, R.; Basche, T.; Mews, A., Semiconductor Nanocrystals with Multifunctional Polymer Ligands. *J. Am. Chem. Soc.* **2003**, *125* (2), 320-321.
64. Hines, M. A.; Guyot-Sionnest, P., Synthesis and Characterization of Strongly Luminescing ZnS-Capped CdSe Nanocrystals. *J. P. Chem.* **1996**, *100* (2), 468-71.
65. Chan, W. C. W.; Maxwell, D. J.; Gao, X.; Bailey, R. E.; Han, M.; Nie, S., Luminescent quantum dots for multiplexed biological detection and imaging. *Curr. Opin. Biotechnol.* **2002**, *13* (1), 40-46.
66. Parak, W. J.; Gerion, D.; Pellegrino, T.; Zanchet, D.; Micheel, C.; Williams, S. C.; Boudreau, R.; Le Gros, M. A.; Larabell, C. A.; Alivisatos, A. P., Biological applications of colloidal nanocrystals. *Nanotechnology* **2003**, *14* (7), R15-R27.
67. The author thanks Dr. Dwight Romanovicz for assistance with collection of TEM photomicrographs.
68. Brus, L. E., A simple model for the ionization potential, electron affinity, and aqueous redox potentials of small semiconductor crystallites. *J. Chem. Phys.* **1983**, *79* (11), 5566-71.
69. Rossetti, R.; Nakahara, S.; Brus, L. E., Quantum size effects in the redox potentials, resonance Raman spectra, and electronic spectra of cadmium sulfide crystallites in aqueous solution. *J. Chem. Phys.* **1983**, *79* (2), 1086-8.
70. Rossetti, R.; Ellison, J. L.; Gibson, J. M.; Brus, L. E., Size effects in the excited electronic states of small colloidal cadmium sulfide crystallites. *J. Chem. Phys.* **1984**, *80* (9), 4464-9.
71. Reed, M. A.; Randall, J. N.; Aggarwal, R. J.; Matyi, R. J.; Moore, T. M.; Wetsel, A. E., Observation of discrete electronic states in a zero-dimensional semiconductor nanostructure. *Phys. Rev. Lett.* **1988**, *60* (6), 535-7.
72. Chan, W. C. W.; Nie, S. M., Quantum dot bioconjugates for ultrasensitive nonisotopic detection. *Science* **1998**, *281* (5385), 2016-2018.
73. Bruchez, M.; Moronne, M.; Gin, P.; Weiss, S.; Alivisatos, A. P., Semiconductor nanocrystals as fluorescent biological labels. *Science* **1998**, *281* (5385), 2013-2016.

74. Medintz, I. L.; Mattoussi, H.; Goldman, E. R.; Clapp, A. R.; Mauro, J. M., A prototype quantum dot FRET-based nanoscale biosensor. *PMSE Preprints* **2003**, *89*, 205-206.
75. Liu, W.; Howarth, M.; Greytak, A. B.; Zheng, Y.; Nocera, D. G.; Ting, A. Y.; Bawendi, M. G., Compact Biocompatible Quantum Dots Functionalized for Cellular Imaging. *J. Am. Chem. Soc.* **2008**, *130* (4), 1274-1284.
76. Alivisatos, A. P.; Gu, W.; Larabell, C., Quantum dots as cellular probes. *Annu. Rev. Biomed. Eng.* **2005**, *7*, 55-76.
77. Bocsi, J.; Mittag, A.; Varga, V. S.; Molnar, B.; Tulassay, Z.; Sack, U.; Lenz, D.; Tarnok, A., Automated four color CD4/CD8 analysis of leukocytes by scanning fluorescence microscopy using quantum dots. *Proc. SPIE* **2006**, *6096* (Colloidal Quantum Dots for Biomedical Applications), 60960Z/1-60960Z/11.
78. Sukhanova, A.; Devy, J.; Venteo, L.; Kaplan, H.; Artemyev, M.; Oleinikov, V.; Klinov, D.; Pluot, M.; Cohen, J. H. M.; Nabiev, I., Biocompatible fluorescent nanocrystals for immunolabeling of membrane proteins and cells. *Anal. Biochem.* **2004**, *324* (1), 60-67.
79. Xiao, Y.; Gao, X.; Gannot, G.; Emmert-Buck, M. R.; Srivastava, S.; Wagner, P. D.; Amos, M. D.; Barker, P. E., Quantitation of HER2 and telomerase biomarkers in solid tumors with IgY antibodies and nanocrystal detection. *Int. J. Cancer* **2008**, *122* (10), 2178-2186.
80. Medintz, I. L.; Goldman, E. R.; Clapp, A. R.; Mattoussi, H., FRET-based quantum dot protein nanosensors. *PMSE Preprints* **2005**, *93*, 5-6.
81. Zajac, A.; Song, D.; Qian, W.; Zhukov, T., Protein microarrays and quantum dot probes for early cancer detection. *Colloids Surf. B.* **2007**, *58* (2), 309-314.
82. Goldman, E. R.; Clapp, A. R.; Anderson, G. P.; Uyeda, H. T.; Mauro, J. M.; Medintz, I. L.; Mattoussi, H., Multiplexed Toxin Analysis Using Four Colors of Quantum Dot Fluororeagents. *Analytical Chemistry* **2004**, *76* (3), 684-688.
83. Hu, F.; Ran, Y.; Zhou, Z.; Gao, M., Preparation of bioconjugates of CdTe nanocrystals for cancer marker detection. *Nanotechnology* **2006**, *17* (12), 2972-2977.
84. Kairdolf, B. A.; Mancini, M. C.; Smith, A. M.; Nie, S., Minimizing Nonspecific Cellular Binding of Quantum Dots with Hydroxyl-Derivatized Surface Coatings. *Anal. Chem.* **2008**, *80* (8), 3029-3034.
85. Xing, Y.; Chaudry, Q.; Shen, C.; Kong, K. Y.; Zhau, H. E.; Chung, L. W.; Petros, J. A.; O'Regan, R. M.; Yezhelyev, M. V.; Simons, J. W.; Wang, M. D.; Nie, S., Bioconjugated quantum dots for multiplexed and quantitative immunohistochemistry. *Nat. Protoc.* **2007**, *2* (5), 1152-1165.
86. Clapp, A. R.; Goldman, E. R.; Mattoussi, H., Capping of CdSe-ZnS quantum dots with DHLA and subsequent conjugation with proteins. *Nat. Protoc.* **2006**, *1* (3), 1258-1267.

87. Goldman, E. R.; Balighian, E. D.; Mattoussi, H.; Kuno, M. K.; Mauro, J. M.; Tran, P. T.; Anderson, G. P., Avidin: A Natural Bridge for Quantum Dot-Antibody Conjugates. *J. Am. Chem. Soc.* **2002**, *124* (22), 6378-6382.
88. Goldman, E. R.; Uyeda, H. T.; Hayhurst, A.; Mattoussi, H., Luminescent biocompatible quantum dots. A tool for immunosorbent assay design. *Methods Mol. Biol.* **2007**, *374* (Quantum Dots), 207-227.
89. Medintz, I. L.; Uyeda, H. T.; Goldman, E. R.; Mattoussi, H., Quantum dot bioconjugates for imaging, labelling and sensing. *Nat. Mater.* **2005**, *4* (6), 435-446.
90. Hua, X.-F.; Liu, T.-C.; Cao, Y.-C.; Liu, B.; Wang, H.-Q.; Wang, J.-H.; Huang, Z.-L.; Zhao, Y.-D., Characterization of the coupling of quantum dots and immunoglobulin antibodies. *Anal. Bioanal. Chem.* **2006**, *386* (6), 1665-1671.
91. Pathak, S.; Davidson, M. C.; Silva, G. A., Characterization of the Functional Binding Properties of Antibody Conjugated Quantum Dots. *Nano Lett* **2007**, *7* (7), 1839-1845.
92. Song, E.-Q.; Wang, G.-P.; Xie, H.-Y.; Zhang, Z.-L.; Hu, J.; Peng, J.; Wu, D.-C.; Shi, Y.-B.; Pang, D.-W., Visual recognition and efficient isolation of apoptotic cells with fluorescent-magnetic-biotargeting multifunctional nanospheres. *Clin. Chem.* **2007**, *53* (12), 2177-2185.
93. Ligler, F. S., Perspective on optical biosensors and integrated sensor systems. *Anal. Chem.* **2009**, *81* (2), 519-26.
94. Wark, A. W.; Lee, H. J.; Corn, R. M., Advanced methods for SPR imaging biosensing. *Handb. Surf. Plasmon Reson.* **2008**, 246-274.
95. Stiles, P. L.; Dieringer, J. A.; Shah, N. C.; Van Duyne, R. P., Surface-enhanced Raman spectroscopy. *Annu. Rev. Anal. Chem.* **2008**, *1*, 601-626.
96. Wang, J., Electrochemical biosensors: Towards point-of-care cancer diagnostics. *Biosens. Bioelectron.* **2006**, *21* (10), 1887-1892.
97. Smith, R. G.; D'Souza, N.; Nicklin, S., A review of biosensors and biologically-inspired systems for explosives detection. *Analyst (Cambridge, U. K.)* **2008**, *133* (5), 571-584.
98. Floriano, P. N.; Editor, *Microchip-Based Assay Systems: Methods and Applications. [In: Methods Mol. Biol. (Totowa, NJ, U. S.), 2007; 385]*. 2007; p 229 pp.
99. Wang, W. U.; Chen, C.; Lin, K. H.; Fang, Y.; Lieber, C. M., Label-free detection of small-molecule-protein interactions by using nanowire nanosensors. *Proc. Natl. Acad. Sci. U. S. A.* **2005**, *102* (9), 3208-3212.
100. Lim, J.-H.; Mirkin, C. A., Electrostatically driven dip-pen nanolithography of conducting polymers. *Adv. Mater. (Weinheim, Ger.)* **2002**, *14* (20), 1474-1477.
101. Psaltis, D.; Quake, S. R.; Yang, C., Developing optofluidic technology through the fusion of microfluidics and optics. *Nature* **2006**, *442* (7101), 381-386.

102. Davis, G., Microfabricated sensors and the commercial development of the i-STAT point-of-care system. *Chem. Anal. (N. Y.)* **1998**, *148* (Commercial Biosensors), 47-76.
103. Madou, M.; Zoval, J.; Jia, G.; Kido, H.; Kim, J.; Kim, N., Lab on a CD. *Annu. Rev. Biomed. Eng.* **2006**, *8*, 601-628.
104. Kido, H.; Zoval, J.; Madou, M., Applications of centrifugal microfluidics in biology. *Biol. Appl. Microfluid.* **2008**, 305-330.
105. Walt, D. R., Fiber optic imaging sensors. *Acc. Chem. Res.* **1998**, *31* (5), 267-278.
106. Walt, D. R., MOLECULAR BIOLOGY: Bead-based Fiber-Optic Arrays. *Science* **2000**, *287* (5452), 451-452.
107. Walt, D. R., Fiber optic array biosensors. *Biotechniques* **2006**, *41* (5), 529, 531, 533, 535.
108. Hambling, D., Nanotechnology Goes to War. *The Guardian* March 5, 2009.
109. Yager, P.; Edwards, T.; Fu, E.; Helton, K.; Nelson, K.; Tam, M. R.; Weigl, B. H., Microfluidic diagnostic technologies for global public health. *Nature* **2006**, *442* (7101), 412-418.
110. Toner, M.; Irimia, D., Blood-on-a-chip. *Annu. Rev. Biomed. Eng.* **2005**, *7*, 77-103, 3 plates.
111. Nathavitharana, R.; Coronel, J.; Moore David, A. J., Solar disinfection of MODS mycobacterial cultures in resource-poor settings. *PLoS ONE* **2007**, *2* (10), e1100.
112. Cortese, D.; Smoldt, R., A health system by design. The future of healthcare must be about competition for patients based on value. *Mod. Healthc.* **2007**, *37* (38), 38.
113. "National Health Expenditures, Forecast summary and selected tables", Office of the Actuary in the Centers for Medicare & Medicaid Services, 2008. Accessed March 25, 2009.
114. Ginsburg Paul, B.; Strunk Bradley, C.; Banker Michelle, I.; Cookson John, P., Tracking health care costs: continued stability but at high rates in 2005. *Health affairs (Project Hope)* **2006**, *25* (6), w486-95.
115. Berk, M. L.; Monheit, A. C., The concentration of health care expenditures, revisited. *Health affairs (Project Hope)* **2001**, *20* (2), 9-18.
116. Lavigne, J. J.; Savoy, S.; Clevenger, M. B.; Ritchie, J. E.; McDoniel, B.; Yoo, S. J.; Anslyn, E. V.; McDevitt, J. T.; Shear, J. B.; Neikirk, D., Solution-based analysis of multiple analytes by a sensor array: Toward the development of an "electronic tongue". *J. Am. Chem. Soc.* **1998**, *120* (25), 6429-6430.
117. Rodriguez, W. R.; Christodoulides, N.; Floriano, P. N.; Graham, S.; Mohanty, S.; Dixon, M.; Hsiang, M.; Peter, T.; Zavahir, S.; Thior, I.; Romanovicz, D.; Bernard, B.; Goodey, A. P.; Walker, B. D.; McDevitt, J. T., A microchip CD4 counting method for HIV monitoring in resource-poor settings. *Plos Medicine* **2005**, *2* (7), 663-672.

118. Christodoulides, N.; Floriano, P. N.; Acosta, S. A.; Michael-Ballard, K.; Weigum, S. E.; Dharshan, P.; Romanovicz, D.; McDevitt, J. T., Towards the development of a Lab on a Chip dual function white blood cell and C-reactive protein analysis method for the assessment of inflammation and cardiac risk. *Clin. Chem.* **2005**, *51* (12), 2391-2395.
119. Floriano, P. N.; Christodoulides, N.; Romanovicz, D. K.; Bernard, B.; Simmons, G. W.; Cavell, M.; McDevitt, J. T., Membrane-based on-line optical analysis system for rapid detection of bacteria and spores. *Biosens. Bioelectron.* **2005**, *20* (10), 2079-2088.
120. Goodey, A.; Lavigne, J. J.; Savoy, S. M.; Rodriguez, M. D.; Curey, T.; Tsao, A.; Simmons, G.; Wright, J.; Yoo, S.-J.; Sohn, Y.; Anslyn, E. V.; Shear, J. B.; Neikirk, D. P.; McDevitt, J. T., Development of Multianalyte Sensor Arrays Composed of Chemically Derivatized Polymeric Microspheres Localized in Micromachined Cavities. *J. Am. Chem. Soc.* **2001**, *123*, 2559-2570.
121. McCleskey, S. C.; Floriano, P. N.; Wiskur, S. L.; Anslyn, E. V.; McDevitt, J. T., Citrate and calcium determination in flavored vodkas using artificial neural networks. *Tetrahedron* **2003**, *59* (50), 10089-10092.
122. McCleskey, S. C.; Griffin, M. J.; Schneider, S. E.; McDevitt, J. T.; Anslyn, E. V., Differential receptors create patterns diagnostic for ATP and GTP. *J. Am. Chem. Soc.* **2003**, *125* (5), 1114-1115.
123. Wright, A. T.; Edwards, N. Y.; Anslyn, E. V.; McDevitt, J. T., The discriminatory power of differential receptor arrays is improved by prescreening - a demonstration in the analysis of tachykinins and similar peptides. *Angew. Chem., Int. Ed.* **2007**, *46* (43), 8212-8215.
124. Ali, M. F.; Kirby, R.; Goodey, A. P.; Rodriguez, M. D.; Ellington, A. D.; Neikirk, D. P.; McDevitt, J. T., DNA hybridization and discrimination of single-nucleotide mismatches using chip-based microbead arrays. *Analytical Chemistry* **2003**, *75* (Anal. Chem.), 4732-4739.
125. Weigum, S. E.; Floriano, P. N.; Christodoulides, N.; McDevitt, J. T., Cell-based sensor for analysis of EGFR biomarker expression in oral cancer. *Lab Chip* **2007**, *7* (8), 995-1003.
126. Christodoulides, N.; Floriano, P. N.; Miller, C. S.; Ebersole, J. L.; Mohanty, S.; Dharshan, P.; Griffin, M.; Lennart, A.; Ballard, K. L. M.; King, C. P., Jr.; Langub, M. C.; Kryscio, R. J.; Thomas, M. V.; McDevitt, J. T., Lab-on-a-chip methods of point-of-care measurements of salivary biomarkers of periodontitis. *Ann. N. Y. Acad. Sci.* **2007**, *1098* (Oral-Based Diagnostics), 411-428.
127. Christodoulides, N.; Mohanty, S.; Miller, C. S.; Langub, M. C.; Floriano, P. N.; Dharshan, P.; Ali, M. F.; Bernard, B.; Romanovicz, D.; Anslyn, E.; Fox, P. C.; McDevitt, J. T., Application of microchip assay system for the measurement of C-reactive protein in human saliva. *Lab Chip* **2005**, *5* (3), 261-269.

128. Christodoulides, N.; Tran, M.; Floriano, P. N.; Rodriguez, M.; Goodey, A.; Ali, M.; Neikirk, D.; McDevitt, J. T., A microchip-based multianalyte assay system for the assessment of cardiac risk. *Analytical Chemistry* **2002**, *74* (13), 3030-3036.
129. Goodey, A.; Lavigne, J. J.; Savoy, S. M.; Rodriguez, M. D.; Curey, T.; Tsao, A.; Simmons, G.; Wright, J.; Yoo, S. J.; Sohn, Y.; Anslyn, E. V.; Shear, J. B.; Neikirk, D. P.; McDevitt, J. T., Development of multianalyte sensor arrays composed of chemically derivatized polymeric microspheres localized in micromachined cavities. *J. Am. Chem. Soc.* **2001**, *123* (11), 2559-2570.
130. Christodoulides, N.; Floriano, P. N.; Acosta, S. A.; Ballard, K. L.; Weigum, S. E.; Mohanty, S.; Dharshan, P.; Romanovicz, D.; McDevitt, J. T., Toward the development of a lab-on-a-chip dual-function leukocyte and C-reactive protein analysis method for the assessment of inflammation and cardiac risk. *Clin Chem* **2005**, *51* (12), 2391-5.
131. Jokerst, J. V.; Floriano, P. N.; Christodoulides, N.; Simmons, G. W.; McDevitt, J. T., Integration of semiconductor quantum dots into nano-bio-chip systems for enumeration of CD4+ T cell counts at the point-of-need. *Lab Chip* **2008**, *8* (12), 2079-90.
132. O'Brien, W. A.; Hartigan, P. M.; Daar, E. S.; Simberkoff, M. S.; Hamilton, J. D., Changes in plasma HIV RNA levels and CD4(+) lymphocyte counts predict both response to antiretroviral therapy and therapeutic failure. *Ann. Intern. Med* **1997**, *126* (12), 939-945.
133. Yarchoan, R.; Tosato, G.; Little, R. F., Therapy insight: AIDS-related malignancies-The influence of antiviral therapy on pathogenesis and management. *Nat. Clin. Pract. Oncol.* **2005**, *2* (8), 406-415.
134. CDC, 1997 Revised Guidelines for Performing CD4+ T-Cell Determinations in Persons Infected with Human Immunodeficiency Virus (HIV). *MMWR* **1997**, *46* (RR-2).
135. Bofill, M.; Janossy, G.; Lee, C. A.; MacDonald-Burns, D.; Phillips, A. N.; Sabin, C.; Timms, A.; Johnson, M. A.; Kernoff, P. B., Laboratory control values for CD4 and CD8 T lymphocytes. Implications for HIV-1 diagnosis. *Clin. Exp. Immunol.* **1992**, *88* (2), 243-52.
136. UNAIDS, W. H. O. a. *CD4+ T-Cell Enumeration Technologies*; 2005.
137. Zijenah, L. S.; Kadzirange, G.; Madzime, S.; Borok, M.; Mudiwa, C.; Tobaiwa, O.; Muccheche, M.; Rusakaniko, S.; Katzenstein, D. A., Affordable flow cytometry for enumeration of absolute CD4+ T-lymphocytes to identify subtype C HIV-1 infected adults requiring antiretroviral therapy (ART) and monitoring response to ART in a resource-limited setting. *J. Trans. Med.* **2006**, *4*.
138. Thorslund, S.; Larsson, R.; Nikolajeff, F.; Bergquist, J.; Sanchez, J., Bioactivated PDMS microchannel evaluated as sensor for human CD4+ cells-The concept of a point-of-care method for HIV monitoring. *Sens. Actuators, B.* **2007**, *B123* (2), 847-855.
139. Mishra, N. N.; Retterer, S.; Zieziulewicz, T. J.; Isaacson, M.; Szarowski, D.; Mousseau, D. E.; Lawrence, D. A.; Turner, J. N., On-chip micro-biosensor for the

- detection of human CD4⁺ cells based on AC impedance and optical analysis. *Biosens. Bioelectron.* **2005**, *21* (5), 696-704.
140. Truett April, A.; Letizia, A.; Malyangu, E.; Sinyangwe, F.; Morales Brandi, N.; Crum Nancy, F.; Crowe Suzanne, M., Efficacy of Cyto-Chex blood preservative for delayed manual CD4 testing using Dynal T4 Quant CD4 test among HIV-infected persons in Zambia. *J. Acquir. Immune Defic. Syndr.* **2006**, *41* (2), 168-74.
141. Cheng, X.; Irimia, D.; Dixon, M.; Sekine, K.; Demirci, U.; Zamir, L.; Tompkins, R. G.; Rodriguez, W.; Toner, M., A microfluidic device for practical label-free CD4⁺ T cell counting of HIV-infected subjects. *Lab Chip* **2007**, *7* (2), 170-178.
142. Ozcan, A.; Demirci, U., Ultra wide-field lens-free monitoring of cells on-chip. *Lab Chip* **2008**, *8* (1), 98-106.
143. Vilknor, T.; Janasek, D.; Manz, A., Micro total analysis systems. Recent developments. *Anal. Chem.* **2004**, *76* (12), 3373-3385.
144. Whitesides, G. M., The 'right' size in nanobiotechnology. *Nat. Biotechnol.* **2003**, *21* (10), 1161-1165.
145. Mattheakis, L. C.; Dias, J. M.; Choi, Y.-J.; Gong, J.; Bruchez, M. P.; Liu, J.; Wang, E., Optical coding of mammalian cells using semiconductor quantum dots. *Anal. Biochem.* **2004**, *327* (2), 200-208.
146. Hoshino, A.; Fujioka, K.; Kawamura, Y. I.; Toyama-Sorimachi, N.; Yasuhara, M.; Dohi, T.; Yamamoto, K., Immune cells tracing using quantum dots. *Proceedings of SPIE-The International Society for Optical Engineering* **2006**, *6096* (Colloidal Quantum Dots for Biomedical Applications), 609613/1-609613/8.
147. Rodriguez, W. R.; Christodoulides, N.; Floriano, P. N.; Graham, S.; Mohanty, S.; Dixon, M.; Hsiang, M.; Peter, T.; Zavahir, S.; Thior, I.; Romanovicz, D.; Bernard, B.; Goodey, A. P.; Walker, B. D.; McDevitt, J. T., A microchip CD4 counting method for HIV monitoring in resource-poor settings. *PLoS Med* **2005**, *2* (7), e182.
148. Rasband, W. Image J, image processing and analysis in Java. <http://rsb.info.nih.gov/ij/>.
149. The author strongly thanks Dr. Pierre Floriano for his extensive assistance in preparing the Java-based deconvolution macro from the ImageJ analysis software.
150. Harris, L. J.; Skaletsky, E.; McPherson, A., Crystallographic structure of an intact IgG1 monoclonal antibody. *J. Mol. Biol.* **1998**, *275* (5), 861-872.
151. Nardone, E.; Rosano, C.; Santambrogio, P.; Curnis, F.; Corti, A.; Magni, F.; Siccardi, A. G.; Paganelli, G.; Losso, R.; Apreda, B.; Bolognesi, M.; Sidoli, A.; Arosio, P., Biochemical characterization and crystal structure of a recombinant hen avidin and its acidic mutant expressed in *Escherichia coli*. *Eur. J. Biochem.* **1998**, *256* (2), 453-460.
152. Salomo, M.; Keyser, U. F.; Struhalla, M.; Kremer, F., Optical tweezers to study single Protein A/Immunoglobulin G interactions at varying conditions. *Eur. Biophys. J.* **2008**, *37* (6), 927-934.

153. Wessendorf, M. W.; Tallaksen-Greene, S. J.; Wohlhueter, R. M., A spectrophotometric method for determination of fluorophore-to-protein ratios in conjugates of the blue fluorophore 7-amino-4-methylcoumarin-3-acetic acid (AMCA). *The journal of histochemistry and cytochemistry official journal of the Histochemistry Society* **1990**, *38* (1), 87-94.
154. Sapan, C. V.; Lundblad, R. L.; Price, N. C., Colorimetric protein assay techniques. *Biotechnol. Appl. Biochem.* **1999**, *29* (Pt 2), 99-108.
155. Horiba A Guide to Recording Fluorescence Quantum Yields - Jobin Yvon (Horiba).
<http://www.jobinyvon.com/SiteResources/Data/MediaArchive/files/Fluorescence/applications/quantumyieldstrad.pdf> (accessed October 1, 2008).
156. Lakowicz, J. R., *Principles of Fluorescence Spectroscopy*. Kluwer Academic/Plenum Press: New York, 1999.
157. Yu, W. W.; Qu, L. H.; Guo, W. Z.; Peng, X. G., Experimental determination of the extinction coefficient of CdTe, CdSe, and CdS nanocrystals. *Chem. Mater.* **2003**, *15* (14), 2854-2860.
158. Resch-Genger, U.; Grabolle, M.; Cavaliere-Jaricot, S.; Nitschke, R.; Nann, T., Quantum dots versus organic dyes as fluorescent labels. *Nat. Meth.* **2008**, *5* (9), 763-775.
159. Ostuni, E.; Grzybowski, B. A.; Mrksich, M.; Roberts, C. S.; Whitesides, G. M., Adsorption of proteins to hydrophobic sites on mixed self-assembled monolayers. *Langmuir* **2003**, *19* (5), 1861-1872.
160. Xing, Y.; Chaudry, Q.; Shen, C.; Kong Koon, Y.; Zhau Haiyen, E.; Chung Leland, W.; Petros John, A.; O'Regan Ruth, M.; Yezhelyev Maksym, V.; Simons Jonathan, W.; Wang May, D.; Nie, S., Bioconjugated quantum dots for multiplexed and quantitative immunohistochemistry. *Nat Protoc FIELD Full Journal Title:Nature protocols* **2007**, *2* (5), 1152-65.
161. Breus, V. V.; Heyes, C. D.; Nienhaus, G. U., Quenching of CdSe-ZnS Core-Shell Quantum Dot Luminescence by Water-Soluble Thiolated Ligands. *J. Phys. Chem. C* **2007**, *111* (50), 18589-18594.
162. Davis, K. A.; Abrams, B.; Iyer, S. B.; Hoffman, R. A.; Bishop, J. E., Determination of CD4 antigen density on cells: Role of antibody valency, avidity, clones, and conjugation. *Cytometry* **1998**, *33* (2), 197-205.
163. Floriano, P. N.; Christodoulides, N.; Romanovicz, D.; Bernard, B.; Simmons, G. W.; Cavell, M.; McDevitt, J. T., Membrane-based on-line optical analysis system for rapid detection of bacteria and spores. *Biosens Bioelectron* **2005**, *20* (10), 2079-88.
164. Unpublished McDevitt Group data.
165. Loiko, V. A.; Ruban, G. I.; Gritsai, O. A.; Gruzdev, A. D.; Kosmacheva, S. M.; Goncharova, N. V.; Miskevich, A. A., Morphometric model of lymphocyte as applied to

scanning flow cytometry. *Journal of Quantitative Spectroscopy & Radiative Transfer* **2006**, *102* (1), 73-84.

166. Gao, X.; Nie, S., Quantum Dot-Encoded Mesoporous Beads with High Brightness and Uniformity: Rapid Readout Using Flow Cytometry. *Anal. Chem.* **2004**, *76* (8), 2406-2410.

167. Empedocles, S. A.; Norris, D. J.; Bawendi, M. G., Photoluminescence spectroscopy of single CdSe nanocrystallite quantum dots. *Phys. Rev. Lett.* **1996**, *77* (18), 3873-3876.

168. Cottingham, K., Quantum dots: leave the light on. *Analytical Chemistry* **2005**, *77* (17), 354A-357A.

169. Klostranec, J. M.; Xiang, Q.; Farcas, G. A.; Lee, J. A.; Rhee, A.; Lafferty, E. I.; Perrault, S. D.; Kain, K. C.; Chan, W. C. W., Convergence of Quantum Dot Barcodes with Microfluidics and Signal Processing for Multiplexed High-Throughput Infectious Disease Diagnostics. *Nano Lett* **2007**, *7* (9), 2812-2818.

170. Kyewski, B., A Breath of Aire for the Periphery. *Science* **2008**, *321* (5890), 776-777.

171. Dainiak, M. B.; Kumar, A.; Galaev, I. Y.; Mattiasson, B., Methods in cell separations. *Advances in Biochemical Engineering/Biotechnology* **2007**, *106* (Cell Separation), 1-18.

172. Tanabe, R.; Hata, S.; Shimokohbe, A., MEMS complete blood count sensors designed to reduce noise from electrolysis gas. *Microelectronic Engineering* **2006**, *83* (4-9), 1646-1650.

173. Zheng, S.; Lin, J. C.-H.; Kasdan, H. L.; Tai, Y.-C., Fluorescent labeling, sensing, and differentiation of leukocytes from undiluted whole blood samples. *Sensors and Actuators, B: Chemical* **2008**, *B132* (2), 558-567.

174. Chattopadhyay, P. K.; Price, D. A.; Harper, T. F.; Betts, M. R.; Yu, J.; Gostick, E.; Perfetto, S. P.; Goepfert, P.; Koup, R. A.; De Rosa, S. C.; Bruchez, M. P.; Roederer, M., Quantum dot semiconductor nanocrystals for immunophenotyping by polychromatic flow cytometry. *Nat. Med.* **2006**, *12* (8), 972-977.

175. Simonnet, C.; Groisman, A., High-Throughput and High-Resolution Flow Cytometry in Molded Microfluidic Devices. *Analytical Chemistry* **2006**, *78* (16), 5653-5663.

176. Jemal, A.; Siegel, R.; Ward, E.; Hao, Y.; Xu, J.; Murray, T.; Thun Michael, J., Cancer statistics, 2008. *CA a cancer journal for clinicians* **2008**, *58* (2), 71-96.

177. Lee, H. J.; Wark, A. W.; Corn, R. M., Microarray methods for protein biomarker detection. *Analyst* **2008**, *133* (8), 975-983.

178. Rasooly, A.; Jacobson, J., Development of biosensors for cancer clinical testing. *Biosens. Bioelectron.* **2006**, *21* (10), 1851-1858.

179. ACS *Cancer Facts and Figures 2008*; American Cancer Society: Atlanta, GA, 2008.
180. Ozols, R. F.; Herbst, R. S.; Colson, Y. L.; Gralow, J.; Bonner, J.; Curran, W. J., Jr.; Eisenberg, B. L.; Ganz, P. A.; Kramer, B. S.; Kris, M. G.; Markman, M.; Mayer, R. J.; Raghavan, D.; Reaman, G. H.; Sawaya, R.; Schilsky, R. L.; Schuchter, L. M.; Sweetenham, J. W.; Vahdat, L. T.; Winn, R. J., Clinical cancer advances 2006: major research advances in cancer treatment, prevention, and screening--a report from the American Society of Clinical Oncology. *J Clin Oncol* **2007**, *25* (1), 146-62.
181. Das, P. M.; Bast, R. C., Jr., Early detection of ovarian cancer. *Biomarkers Med.* **2008**, *2* (3), 291-303.
182. Haab, B. B., Antibody arrays in cancer research. *Mol. Cell. Proteomics* **2005**, *4* (4), 377-383.
183. Tainsky, M. A.; Chatterjee, M.; Levin, N. K.; Draghici, S.; Abrams, J., Multianalyte tests for the early detection of cancer: speedbumps and barriers. *Biomarker Insights* **2007**, 261-267.
184. Harris, L.; Fritsche, H.; Mennel, R.; Norton, L.; Ravdin, P.; Taube, S.; Somerfield, M. R.; Hayes, D. F.; Bast, R. C., Jr., American Society of Clinical Oncology 2007 update of recommendations for the use of tumor markers in breast cancer. *J. Clin. Oncol.* **2007**, *25* (33), 5287-5312.
185. Bhasin, S.; Zhang, A.; Coviello, A.; Jasuja, R.; Ulloor, J.; Singh, R.; Vesper, H.; Vasan, R. S., The impact of assay quality and reference ranges on clinical decision making in the diagnosis of androgen disorders. *Steroids* **2008**, *73* (13), 1311-1317.
186. Wong, D. T., *Salivary Diagnostics*. Wiley-Blackwell: Hoboken, NJ, 2008; p 301 pp.
187. Mandel, I. D., Salivary Diagnosis - More Than a Lick and a Promise. *Journal of the American Dental Association* **1993**, *124* (1), 85-87.
188. Malamud, D., Salivary diagnostics: the future is now. *J. Am. Dent. Assoc.* **2006**, *137* (3), 284-286.
189. Siqueira, W. L.; Salih, E.; Wan, D. L.; Helmerhorst, E. J.; Oppenheim, F. G., Proteome of human minor salivary gland secretion. *J. Dent. Res.* **2008**, *87* (5), 445-450.
190. Hu, S.; Arellano, M.; Boonthung, P.; Wang, J.; Zhou, H.; Jiang, J.; Elashoff, D.; Wei, R.; Loo, J. A.; Wong, D. T., Salivary Proteomics for Oral Cancer Biomarker Discovery. *Clin. Cancer Res.* **2008**, *14* (19), 6246-6252.
191. Hu, S.; Loo, J. A.; Wong, D. T., Human saliva proteome analysis. *Ann. N. Y. Acad. Sci.* **2007**, *1098* (Oral-Based Diagnostics), 323-329.
192. Oppenheim, F., G.; Salih, E.; Siqueira Walter, L.; Zhang, W.; Helmerhorst Eva, J., Salivary proteome and its genetic polymorphisms. *Ann. N.Y. Acad. Sci.* **2007**, *1098*, 22-50.

193. Herr, A. E.; Hatch, A. V.; Throckmorton, D. J.; Tran, H. M.; Brennan, J. S.; Giannobile, W. V.; Singh, A. K., Microfluidic immunoassays as rapid saliva-based clinical diagnostics. *PNAS* **2007**, *104* (13), 5268-5273.
194. Tan, W.; Sabet, L.; Li, Y.; Yu, T.; Klokkevold, P. R.; Wong, D. T.; Ho, C. M., Optical protein sensor for detecting cancer markers in saliva. *Biosens. Bioelectron.* **2008**, *24* (2), 266-71.
195. Streckfus, C. F.; Bigler, L. R.; Zwick, M., The use of surface-enhanced laser desorption/ionization time-of-flight mass spectrometry to detect putative breast cancer markers in saliva: A feasibility study. *J. Oral. Path. Med.* **2006**, *35* (5), 292-300.
196. Streckfus, C.; Bigler, L.; Dellinger, T.; Dai, X.; Cox, W. J.; McArthur, A.; Kingman, A.; Thigpen, J. T., Reliability assessment of soluble c-erbB-2 concentrations in the saliva of healthy women and men. *Oral Surg Oral Med Oral Pathol Oral Radiol Endol* **2001**, *91*, 174-9.
197. Gustavsson, P.-E.; Mosbach, K.; Nilsson, K.; Larsson, P.-O., Superporous agarose as an affinity chromatography support. *J. Chromatogr., A* **1997**, *776* (2), 197-203.
198. Gustavsson, P. E.; Mosbach, K.; Nilsson, K.; Larsson, P. O., Superporous agarose as an affinity chromatography support. *J Chromatography A* **1997**, *776*, 197-203.
199. Wong, J., *Ph.D. Dissertation - Bead Based Microreactors for Sensing Applications*. The University of Texas at Austin: Austin, TX, 2007.
200. Gustavsson, P.-E.; Larsson, P.-O., Superporous agarose, a new material for chromatography. *J. Chromatogr., A* **1996**, *734* (2), 231-240.
201. Borch, R. F.; Bernstein, M. D.; Durst, H. D., *J. Am. Chem. Soc* **1971**, *93*, 2897-2904.
202. Please see Appendix A
203. Ali, M. F.; Kirby, R.; Goodey, A. P.; Rodriguez, M. D.; Ellington, A. D.; Neikirk, D. P.; McDevitt, J. T., DNA hybridization and discrimination of single-nucleotide mismatches using chip-based microbead arrays. *Analytical Chemistry* **2003**, *75* (18), 4732-4739.
204. Christodoulides, N.; Mohanty, S.; Miller, C. S.; Langub, M. C.; Floriano, P. N.; Dharshan, P.; Ali, M. F.; Bernard, B.; Romanovicz, D.; Anslyn, E.; Fox, P. C.; McDevitt, J. T., Application of microchip assay system for the measurement of C-reactive protein in human saliva. *Lab Chip* **2005**, *5* (3), 261-9.
205. Ettre, L. S., Headspace-gas chromatography: an ideal technique for sampling volatiles present in non-volatile matrices. *Adv. Exp. Med. Biol.* **2001**, *488*, 9-32.
206. Boehm, M. K.; Perkins, S. J., Structural models for carcinoembryonic antigen and its complex with the single-chain Fv antibody molecule MFE23. *FEBS Lett.* **2000**, *475* (1), 11-16.

207. Narayanan, J.; Xiong, J.-Y.; Liu, X.-Y., Determination of agarose gel pore size: absorbance measurements vis a vis other techniques. *Journal of Physics: Conference Series* **2006**, *28*, 83-86.
208. Lakowicz, J. R., *Principles of Fluorescence Spectroscopy, 3rd Edition*. Springer: New York, 2006.
209. Crowther, J. R., *ELISA: Theory and Practice*. Method Mol.Biol.: Totowa, NJ, 1995.
210. Baron, T.; Boardman Cecelia, H.; Lafky Jacqueline, M.; Rademaker, A.; Liu, D.; Fishman David, A.; Podratz Karl, C.; Maihle Nita, J., Soluble epidermal growth factor receptor (sEGFR) [corrected] and cancer antigen 125 (CA125) as screening and diagnostic tests for epithelial ovarian cancer. *Cancer Epidemiol. Biomarkers Prev.* **2005**, *14* (2), 306-18.
211. Pallud, C.; Guinebretiere, J. M.; Guepratte, S.; Hacene, K.; Neumann, R.; Carney, W.; Pichon, M. F., Tissue expression and serum levels of the oncoprotein HER-2/neu in 157 primary breast tumours. *Anticancer Res.* **2005**, *25* (2B), 1433-40.
212. Mitchell, K. F., A carcinoembryonic antigen (CEA) specific monoclonal hybridoma antibody that reacts only with high-molecular-weight CEA. *Cancer Immunology Immunotherapy* **1980**, *10* (1), 1-5.
213. Aps, J. K.; Martens, L. C., Review: The physiology of saliva and transfer of drugs into saliva. *Forensic Sci. Int.* **2005**, *150* (2-3), 119-31.
214. Choi, D. H.; Katakura, Y.; Matsuda, R.; Hayashi, Y.; Ninomiya, K.; Shioya, S., Simulation model for predicting limit of detection and range of quantitation of competitive enzyme-linked immunosorbent assay. *J. Biosci. Bioeng.* **2007**, *103* (5), 427-431.
215. Nagler, R.; Bahar, G.; Shpitzer, T.; Feinmesser, R., Concomitant Analysis of Salivary Tumor Markers - A New Diagnostic Tool for Oral Cancer. *Clin. Cancer Res.* **2006**, *12* (13), 3979-3984.
216. Negri, L.; Pacchioni, D.; Calabrese, F.; Giacomasso, S.; Mastromatteo, V.; Fazio, M., Serum and salivary CEA and GICA levels in oral cavity tumours. *Int. J. Biol. Markers* **1988**, *3* (2), 107-12.
217. Hendriks, H. A.; Kortlandt, W.; Verweij, W. M., Analytical performance comparison of five new generation immunoassay analyzers. *Ned. Tijdschr. Klin. Chem.* **2000**, *25* (3), 170-177.
218. Murray, A.; Willsher, P.; Price, M. R.; Dixon, A. R.; Robertson, J. F. R., Evaluation of the IMMULITE BR-MA and CEA assays and comparison with immunoradiometric assays for CA15-3 and CEA in breast cancer. *Anticancer Res.* **1997**, *17* (3C), 1945-1949.
219. Limbut, W.; Kanatharana, P.; Mattiasson, B.; Asawatreratanakul, P.; Thavarungkul, P., A reusable capacitive immunosensor for carcinoembryonic antigen

(CEA) detection using thiourea modified gold electrode. *Anal. Chim. Acta* **2006**, *561* (1-2), 55-61.

220. Herr, A. E.; Hatch, A. V.; Giannobile, W. V.; Throckmorton, D. J.; Tran, H. M.; Brennan, J. S.; Singh, A. K., Integrated microfluidic platform for oral diagnostics. *Ann. N. Y. Acad. Sci.* **2007**, *1098* (Oral-Based Diagnostics), 362-374.

221. Jokerst, J. V.; Christodoulides, N.; Floriano, P. N.; Raamanthan, A.; Pollard, A.; Simmons, G. W.; Redding, S.; Furmaga, W.; McDevitt, J. T., Nano-Bio-Chips for High Performance Multiplexed Protein Detection: Determinations of Cancer Biomarkers in Serum and Saliva using Quantum Dot Bioconjugate Labels *Biosensors and Bioelectronics, In Press, Accepted March, 26, 2009.* **2009**.

222. I especially thank Jorge Wong for the use of the computer-generated imagery used in some of my dissertation figures.

223. Christodoulides, N.; Floriano, P. N.; Acosta, S. A.; Ballard, K. L. M.; Weigum, S. E.; Mohanty, S.; Dharshan, P.; Romanovicz, D.; McDevitt, J. T., Toward the development of a lab-on-a-chip dual-function leukocyte and C-reactive protein analysis method for the assessment of inflammation and cardiac risk. *Clin. Chem.* **2005**, *51* (12), 2391-2395.

224. Goluch, E. D.; Nam, J.-M.; Georganopoulou, D. G.; Chiesl, T. N.; Shaikh, K. A.; Ryu, K. S.; Barron, A. E.; Mirkin, C. A.; Liu, C., A bio-barcode assay for on-chip attomolar-sensitivity protein detection. *Lab on a Chip* **2006**, *6* (10), 1293-1299.

225. Ellis, W. J.; Vessella, R. L.; Noteboom, J. L.; Lange, P. H.; Wolfert, R. L.; Rittenhouse, H. G., Early detection of recurrent prostate cancer with an ultrasensitive chemiluminescent prostate-specific antigen assay. *Urology* **1997**, *50* (4), 573-9.

226. Black, M. H.; Giai, M.; Ponzzone, R.; Sismondi, P.; Yu, H.; Diamandis, E. P., Serum total and free prostate-specific antigen for breast cancer diagnosis in women. *Clin. Cancer Res.* **2000**, *6* (2), 467-473.

227. Malanoski, A. P.; Lin, B.; Stenger, D. A., A model of base-call resolution on broad-spectrum pathogen detection resequencing DNA microarrays. *Nucleic Acids Res.* **2008**, *36* (10), 3194-3201.

228. Sanchez-Carbayo, M., Discovery of cancer biomarkers using antibody arrays. *Exp. Op. Med. Diagn.* **2008**, *2* (3), 249-262.

229. Crowther, J. R.; Editor, *The ELISA Guidebook*. 2001; p 521 pp.

230. Engvall, E.; Perlmann, P., Enzyme-linked immunosorbent assay (ELISA). Quantitative assay of immunoglobulin G. *Immunochemistry* **1971**, *8* (9), 871-4.

231. Bonanno, L. M.; DeLouise, L. A., Steric Crowding Effects on Target Detection in an Affinity Biosensor. *Langmuir* **2007**, *23* (10), 5817-5823.

232. Butler, J. E.; Ni, L.; Nessler, R.; Joshi, K. S.; Suter, M.; Rosenberg, B.; Chang, J.; Brown, W. R.; Cantarero, L. A., The physical and functional behavior of capture antibodies adsorbed on polystyrene. *J. Immunol. Methods* **1992**, *150* (1-2), 77-90.

233. Rodriguez, M. D., *Ph.D. Dissertation - The Development of Microbead-based Immunoassays: Application of the "Electronic Taste Chip"* The University of Texas at Austin: Austin, TX, 2003.
234. Yan, B.; Martin, P. C.; Lee, J., Single-Bead Fluorescence Microspectroscopy: Detection of Self-Quenching in Fluorescence-Labeled Resin Beads. *J. Comb. Chem.* **1999**, *1* (1), 78-81.
235. Kress, J.; Rose, A.; Frey, J. G.; Brocklesby, W. S.; Ladlow, M.; Mellor, G. W.; Bradley, M., Site distribution in resin beads as determined by confocal Raman spectroscopy. *Chem.--Eur. J.* **2001**, *7* (18), 3880-3883.
236. Kress, J.; Zanaletti, R.; Rose, A.; Frey, J. G.; Brocklesby, W. S.; Ladlow, M.; Bradley, M., Which Sites React First? Functional Site Distribution and Kinetics on Solid Supports Investigated Using Confocal Raman and Fluorescence Microscopy. *J. Comb. Chem.* **2003**, *5*, 28-32.
237. Ali, M. F., *Ph.D. Dissertation - The Development of a Microbead Array for the Detection and Amplification of Nucleic Acids*. The University of Texas at Austin: Austin, TX, 2006.
238. Harlow, E.; Lane, D., *Antibodies: A Laboratory Manual*. Cold Spring Harbor Press: Cold Spring Harbor, NY, 1988.
239. Morino, K.; Katsumi, H.; Akahori, Y.; Iba, Y.; Shinohara, M.; Ukai, Y.; Kohara, Y.; Kurosawa, Y., Antibody fusions with fluorescent proteins: a versatile reagent for profiling protein expression. *J Immunol Methods* **2001**, *257* (1-2), 175-84.
240. Mariani, M.; Camagna, M.; Tarditi, L.; Seccamani, E., A new enzymic method to obtain high-yield F(ab)₂ suitable for clinical use from mouse IgG1. *Mol. Immunol.* **1991**, *28* (1-2), 69-77.
241. Song, S.-P.; Li, B.; Hu, J.; Li, M.-Q., Simultaneous multianalysis for tumor markers by antibody fragments microarray system. *Anal. Chim. Acta* **2004**, *510* (2), 147-152.
242. Angenendt, P.; Wilde, J.; Kijanka, G.; Baars, S.; Cahill, D. J.; Kreuzberger, J.; Lehrach, H.; Konthur, Z.; Glokler, J., Seeing better through a MIST: evaluation of monoclonal recombinant antibody fragments on microarrays. *Anal Chem* **2004**, *76* (10), 2916-21.
243. Borrebaeck, C. A. K.; Ekstrom, S.; Hager, A. C. M.; Nilsson, J.; Laurell, T.; Marko-Varga, G., Protein chips based on recombinant antibody fragments: a highly sensitive approach as detected by mass spectrometry. *Biotechniques* **2001**, *30* (5), 1126, 1128, 1130, 1132.
244. Song, S.; Li, B.; Wang, L.; Wu, H.; Hu, J.; Li, M.; Fan, C., A cancer protein microarray platform using antibody fragments and its clinical applications. *Molecular BioSystems* **2007**, *3* (2), 151-158.

245. Pernodet, N.; Maaloum, M.; Tinland, B., Pore size of agarose gels by atomic force microscopy. *Electrophoresis* **1997**, *18* (1), 55-58.
246. Belenky Alexander, S.; Wask-Rotter, E.; Sommer Michael, J., Absence of protein G-Fc interaction in ficin-derived mouse IgG1 digests. *J Immunoassay Immunochem* **2003**, *24* (3), 311-8.
247. Bradford, M. M., A rapid and sensitive method for the quantitation of microgram quantities of protein utilizing the principle of protein-dye binding. *Anal. Biochem.* **1976**, *72*, 248-54.
248. Bolte, S.; Cordelieres, F. P., A guided tour into subcellular colocalization analysis in light microscopy. *J. Microsc.* **2006**, *224* (Pt 3), 213-32.
249. Kohler, G.; Milstein, C., Continuous cultures of fused cells secreting antibody of predefined specificity. *Nature* **1975**, *256* (5517), 495-7.
250. Wilson, D. S.; Wu, J.; Peluso, P.; Nock, S., Improved method for pepsinolysis of mouse IgG1 molecules to F(ab')₂ fragments. *J. Immunol. Methods* **2002**, *260* (1-2), 29-36.
251. Liener, I. E.; Friedenson, B., Ficin. *Methods Enzymol.* **1970**, *19*, 261-273.
252. Devaraj, K. B.; Kumar, P. R.; Prakash, V., Purification, Characterization, and Solvent-Induced Thermal Stabilization of Ficin from *Ficus carica*. *J. Agric. Food Chem.* **2008**, *56* (23), 11417-11423.
253. Biotechnology, P., ImmunoPure[®] IgG1 Fab and F(ab')₂ Preparation Kit. Biotechnology, P., Ed. Rockford, IL, 2008.
254. Banfield, M. J.; King, D. J.; Mountain, A.; Brady, R. L., VL:VH domain rotations in engineered antibodies: crystal structures of the Fab fragments from two murine antitumor antibodies and their engineered human constructs. *Proteins* **1997**, *29* (2), 161-71.
255. Boehm, M. K.; Corper, A. L.; Wan, T.; Sohi, M. K.; Sutton, B. J.; Thornton, J. D.; Keep, P. A.; Chester, K. A.; Begent, R. H. J.; Perkins, S. J., Crystal structure of the anti-(carcinoembryonic antigen) single-chain Fv antibody MFE-23 and a model for antigen binding based on intermolecular contacts. *Biochem. J.* **2000**, *346* (2), 519-528.
256. Li, Q.; Lau, A.; Morris, T. J.; Guo, L.; Fordyce, C. B.; Stanley, E. F., A syntaxin 1, Galpha o, and N-type calcium channel complex at a presynaptic nerve terminal: analysis by quantitative immunocolocalization. *J. Neurosci.* **2004**, *24* (16), 4070-4081.
257. Lage, J. L., The fundamental theory of flow through permeable media from Darcy to turbulence. *Transp. Phenom. Porous Media* **1998**, 1-30.
258. Mattern, K. J.; Nakornchai, C.; Deen, W. M., Darcy permeability of agarose-glycosaminoglycan gels analyzed using fiber-mixture and donnan models. *Biophys. J.* **2008**, *95* (2), 648-56.

259. Clague, D. S.; Kandhai, B. D.; Zhang, R.; Sloot, P. M. A., Hydraulic permeability of (un)bounded fibrous media using the lattice Boltzmann method. *Phys. Rev. E: Stat. Phys., Plasmas, Fluids, Relat. Interdiscip. Top.* **2000**, *61* (1), 616-625.
260. Pluen, A.; Netti, P. A.; Jain, R. K.; Berk, D. A., Diffusion of Macromolecules in Agarose Gels: Comparison of Linear and Globular Configurations. *Biophys. J.* **1999**, *77*, 542-552.
261. Brinkman, H. C., A calculation of the viscous force exerted by a flowing fluid on a dense swarm of particles. *Appl. Sci. Res., Sect. A* **1947**, *A1*, 27-34.
262. Ogston, A. G.; Preston, B. N.; Wells, J. D.; Snowden, J. M., Transport of compact particles through solutions of chain-polymers. *Proc. Roy. Soc. London, Ser. A* **1973**, *333* (1594), 297-316.
263. James Camp. Unpublished data from 2008.
264. Adamek, D. H.; Guerrero, L.; Blaber, M.; Caspar, D. L. D., Structural and Energetic Consequences of Mutations in a Solvated Hydrophobic Cavity. *J. Mol. Biol.* **2005**, *346* (1), 307-318.
265. RCSB, Protein Data Base. 2009.
266. Sloane, N. J. A., Kepler's conjecture confirmed. *Nature (London)* **1998**, *395* (6701), 435-436.
267. Zeilberger, D., *Mathematics: To prove the optimal packing: Kepler's Conjecture. How Some of the Greatest Minds in History Helped solve on of the oldest math problem in the World*, by George G. Szpiro. 2003; Vol. 301, p 1186.
268. Iannone, M. A.; Consler, T. G., Effect of microsphere binding site density on the apparent affinity of an interaction partner. *Cytometry, Part A* **2006**, *69A* (5), 374-383.
269. Muller, K. M.; Arndt, K. M.; Pluckthun, A., Model and simulation of multivalent binding to fixed ligands. *Anal. Biochem.* **1998**, *261* (2), 149-158.
270. Engel, P. C., *Handbook of biochemical kinetics*, by D. L. Purich and R. D. Allison. 2000; Vol. 25, p 457.

Vita

Jesse Vincent Jokerst entered this world in the agrarian hamlet of Ste. Genevieve, Missouri, the oldest child of Thomas and Mary Ellen Jokerst. The son of a mathematician and an elementary school teacher, he received his first chemistry set in the late 1980s. He attended Valle Catholic for both elementary and high school education and flourished under the tutelage of Valle's dedicated staff. Truman State University awarded him full tuition, room, and board and he relocated to Kirksville, MO in 1999. Although a career in medicine was his initial intent, a summer of undergraduate research via the National Science Foundation's REU program, produced a change of heart. After earning his B.S. *cum laude* in chemistry from Truman, Jesse matriculated to The University of Texas at Austin in the autumn of 2003 where he quickly joined the research group of Professor John T. McDevitt. His work focuses on improving methods to measure biologically interesting analytes using advances in nanomaterials and microfluidics.

Permanent address: 20276 State Route B,
Ste. Genevieve, MO 63670

This dissertation was typed by author.